

AD-A252 576



1992

~~THESIS~~ DISSERTATION

Damage Detection in Concrete Elements with Surface Wave
Measurements

①

Britt Roderick Bowen, Captain

AFIT Student Attending: University of Texas, Austin

AFIT/CI/CIA- 92-002D

AFIT/CI
Wright-Patterson AFB OH 45433-6583

Approved for Public Release IAW 190-1
Distributed Unlimited
ERNEST A. HAYGOOD, Captain, USAF
Executive Officer

DTIC
ELECTE
JUL 09 1992
S A D

92

92-17924

DAMAGE DETECTION IN CONCRETE ELEMENTS

WITH SURFACE WAVE

MEASUREMENTS

Accession For	
NTIS CRA&I	<input checked="" type="checkbox"/>
DTIC TAB	<input type="checkbox"/>
Unannounced	<input type="checkbox"/>
Justification	
By	
Distribution /	
Availability Codes	
Dist	Avail and/or Special
A-1	

APPROVED BY

DISSERTATION COMMITTEE:

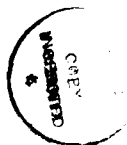
Joe W. Roesel

Kenneth H. Spence

Ronald Starnes

John L. Tassell

James O. Jones



DAMAGE DETECTION IN CONCRETE ELEMENTS
WITH SURFACE WAVE
MEASUREMENTS

by

BRITT RODERICK BOWEN, B.S.C.E., M.S.

DISSERTATION

Presented to the Faculty of the Graduate School of

The University of Texas at Austin

in Partial Fulfillment

of the Requirement

for the Degree of

Doctor of Philosophy

THE UNIVERSITY OF TEXAS AT AUSTIN

May, 1992

ACKNOWLEDGEMENTS

I would like to thank the U.S. Air Force for providing this opportunity and challenge. It has been a great opportunity to learn many new things and broaden my engineering capabilities and background.

I would like to acknowledge my committee members and express my appreciation and thanks for their time, effort, and patience. A special thanks goes out to:

Dr Roeset for spending countless hours helping me, his patience in explaining concepts, and his willingness to sharing his wealth of knowledge.

Dr Stokoe for his ideas, equipment, and time. His unending enthusiasm, optimism, and encouragement was appreciated.

Dr Jirsa for sending me the application for Admissions and who's "UT sales pitch" convinced me that Austin was the place for me. I have been very happy with my decision, UT had everything I wanted for my PhD program.

A special thanks goes out to my fellow graduate students of which I befriended many. Each and everyone brought new perspectives and attitudes about engineering and life, all of which expanded my view of the world. I will remember the long group projects that forced us to work together and tested our patience. I will also remember the "interesting" discussions on capitalism, communism, democracy, "new world order", use of force, rights, the environment, religion, and cultural traditions.

DAMAGE DETECTION IN CONCRETE ELEMENTS

WITH SURFACE WAVE

MEASUREMENTS

Publication No. _____

Britt Roderick Bowen, Ph.D.
The University of Texas at Austin, 1992

Supervisor: Jose M. Roesset

The objective of this research was to assess the ability of surface wave measurements and the SASW technique to detect crack damage in beam and column elements.

The damage was detected by a change in the surface wave dispersion curve (phase velocity vs frequency) between undamaged and damaged states. To calculate the dispersion curve, the SASW (Spectral Analysis of Surface Waves) technique was used with response records from two locations. Finite element analysis was used to analytically generate the response records. Experimentally, acceleration measurements were taken.

Results showed that the SASW method is one potential method to detect cracks.

TABLE OF CONTENTS

ACKNOWLEDGEMENTS	iii
ABSTRACT	iv
LIST OF TABLES	viii
LIST OF FIGURES	ix
1. INTRODUCTION	1
1.1 OBJECTIVES	
1.2 APPROACH	
1.3 SCOPE	
1.4 WHY	
1.5 ORGANIZATION	
2. THE SASW METHOD	5
2.1 OVERVIEW OF METHOD	
2.2 DERIVATION OF THE VELOCITY AND WAVELENGTH	
2.3 INTERPRETATION OF PHASE DIAGRAM	
2.4 UNFOLDING OF PHASE DIAGRAM	
2.5 WINDOWS	
2.6 RECOMMENDATIONS ON WINDOW LENGTH	
2.7 PARAMETERS INVOLVED	
3. ANALYTICAL FORMULATION	37
3.1 MODAL ANALYSIS OF SIMPLE SUPPORTED BEAM USING BEAM THEORY	
3.1.1 EQUATION OF MOTION	
3.1.2 MODAL SOLUTION	
3.1.3 SOLUTION OF FORCED VIBRATION PROBLEM	
3.1.4 SOLUTION OF FREE VIBRATION AFTER LOAD ENDS	
3.1.5 COMPARISON OF SASW WITH THEORETICAL DISPERSION CURVE FOR FLEXURAL WAVES IN A SIMPLE SUPPORTED BEAM.	
3.2 FINITE ELEMENTS	
3.2.1 NEWMARK BETA TIME ITERATION	
3.2.2 STIFFNESS MATRIX	

3.2.3	MASS MATRIX	
3.2.4	JACOBIAN	
3.2.5	SHAPE FUNCTIONS	
3.2.6	MESH SIZE CONSIDERATIONS	
3.3	BEAM BEHAVIOR	
3.4	ANALYTICAL FORMULATION OF A LAYER WITH AIR ON BOTH SIDES	
3.5	EFFECT OF BOUNDARY CONDITIONS	
3.6	TYPE OF MEASUREMENT	
4.	EXPERIMENTAL WORK	81
4.1	TEST MATRIX	
4.2	EQUIPMENT	
4.3	SPECIMENS	
4.4	TEST PROCEDURES	
4.5	RECOMMENDATIONS TO GET A GOOD PHASE DIAGRAM	
5.	UNDAMAGED BEAMS	88
5.1	EXPERIMENTAL AND ANALYTICAL DISPERSION CURVES	
5.2	LOAD DURATION	
5.3	ARRAY LOCATION ON BEAM	
5.4	SPACING	
6.	DAMAGED BEAMS	96
6.1	LOAD AND RECEIVER TO THE SAME SIDE OF CRACK	
6.2	CRACK BETWEEN THE TWO RECEIVERS	
6.2.1	CRACKS	
6.2.2	REPAIRED CRACKS	
6.3	CRACK BETWEEN THE LOAD AND FIRST RECEIVER	
6.4	LOAD AND RECEIVERS ON OPPOSITE FACE OF CRACK	
6.5	LOAD AND RECEIVERS ON LATERAL SIDE OF BEAM	
7.	SUMMARY, CONCLUSIONS AND RECOMMENDATIONS	147
7.1	SUMMARY	
7.2	CONCLUSIONS	
7.3	RECOMMENDATIONS	

APPENDIX A. STRESS WAVE BASICS	151
A.1 TERMINOLOGY	
A.2 TYPES OF WAVES	
A.3 PHENOMENA AND DEFINITIONS	
A.4 STRESS WAVES IN A ROD	
A.5 DERIVATION OF EQUATION OF MOTION (HALF SPACE)	
A.6 SOLUTION OF EQUATION OF MOTION	
A.7 RAYLEIGH WAVE VELOCITY	
A.8 RAYLEIGH WAVE DISPLACEMENT	
A.9 VELOCITIES	
A.10 ENERGY PARTITION	
A.11 ATTENUATION	
A.12 REFLECTION	
APPENDIX B. FOURIER TRANSFORMS	175
B.1 CONTINUOUS FOURIER TRANSFORM	
B.2 DISCRETE FOURIER TRANSFORM	
B.3 CONVOLUTION AND CORRELATION	
B.4 WINDOWS	
B.5 CROSS POWER SPECTRUM	
B.6 COHERENCE	
APPENDIX C. OTHER APPROACHES TO DAMAGE DETECTION AND CRACK SIZING	182
C.1 P-WAVE ARRIVAL	
C.2 IMAGING SYSTEM	
C.3 SEPARATION OF WAVES IN WAVEFORM	
C.4 PERIODIC VARIATION IN HIGH FREQUENCY SPECTRUM	
BIBLIOGRAPHY	186
VITA	

LIST OF TABLES

3.1.5 - 1	Wavelength Comparison: Theory Vs SASW	48
3.2.6 - 1	Effect of Mesh Size: Arrival Times	58
3.2.6 - 2	Effect of Mesh Size: Highest Frequency in Response	58
3.3 - 1	Maximum Displacement for Beam: 20' x 2' x 1'	70
3.3 - 2	Maximum Displacement for Beam: 48" x 6" x 6"	70
3.3 - 3	Maximum Displacement for Beam: 21" x 6" x 6"	71
A.4 - 1	Wave Propagation in a Rod: Mode Shapes and Natural Frequencies	153
A.11 - 1	Geometric Damping	168
A.12 - 1	Definition for Reflected and Transmitted Amplitude Ratios	171
A.12 - 2	Displacement and Stress Amplitudes for Different Impedance Ratios	172

LIST OF FIGURES

2.1 - 1	Overview of SASW Method	6
2.1 - 2	Cross Power Spectrum Phase, Unfolded Phase, and Coherence Diagrams	7
2.1 - 3	Phase Velocity vs Frequency, Wavelength Vs Frequency, and Phase Velocity vs Wavelength Diagrams	8
2.3 - 1	Unfolded Linear Spectrum Phase and Cross Power Spectrum Phase	10
2.4 - 1	Cross Power Spectrum Phase and Coherence Diagram of Data with Good Coherence	13
2.4 - 2	Cross Power Spectrum Phase and Coherence Diagram of Data with Poor Coherence at 12 kHz	14
2.4 - 3	Unfolded Cross Power Spectrum Phase and Dispersion Curve from Phase Diagrams in Figures 2.4-1 and 2.4-2	15
2.4 - 4	Unfolded Cross Power Spectrum Phase and Dispersion Curve from Phase Diagrams with Phase Masked around 12 kHz, Point of Low Coherence	16
2.5 - 1	Hanning Window: Time and Frequency Diagrams	19
2.5 - 2	Rectangular Window: Time and Frequency Diagrams	20
2.5 - 3	Exponential Window: Time and Frequency Diagrams	21
2.5 - 4	Hanning Window (1024 μ sec) Windowed Time Record, Frequency Diagram and Phase vs Frequency: Beam (21" x 6" x 6"), XL-XR1-XR2 (14 - 11 - 8), Analytical Data.	22
2.5 - 5	Hanning Window (512 μ sec) Windowed Time Record, Frequency Diagram and Phase vs Frequency: Beam (21" x 6" x 6"), XL-XR1-XR2 (14 - 11 - 8), Analytical Data.	23

2.5 - 6	Hanning Window (256 μ sec) Windowed Time Record, Frequency Diagram and Phase vs Frequency: Beam (21" x 6" x 6"), XL-XR1-XR2 (14 - 11 - 8), Analytical Data.	24
2.5 - 7	Rectangular Window (1024 μ sec) Windowed Time Record, Frequency Diagram and Phase vs Frequency: Beam (21" x 6" x 6"), XL-XR1-XR2 (14 - 11 - 8), Analytical Data.	25
2.5 - 8	Rectangular Window (512 μ sec) Windowed Time Record, Frequency Diagram and Phase vs Frequency: Beam (21" x 6" x 6"), XL-XR1-XR2 (14 - 11 - 8), Analytical Data.	26
2.5 - 9	Rectangular Window (256 μ sec) Windowed Time Record, Frequency Diagram and Phase vs Frequency: Beam (21" x 6" x 6"), XL-XR1-XR2 (14 - 11 - 8), Analytical Data.	27
2.5 - 10	Exponential Window (256 μ sec) Windowed Time Record, Frequency Diagram and Phase vs Frequency: Beam (21" x 6" x 6"), XL-XR1-XR2 (14 - 11 - 8), Analytical Data.	28
2.5 - 11	Exponential Window (128 μ sec) Windowed Time Record, Frequency Diagram and Phase vs Frequency: Beam (21" x 6" x 6"), XL-XR1-XR2 (14 - 11 - 8), Analytical Data.	29
2.5 - 12	Exponential Window (64 μ sec) Windowed Time Record, Frequency Diagram and Phase vs Frequency: Beam (21" x 6" x 6"), XL-XR1-XR2 (14 - 11 - 8), Analytical Data.	30
2.5 - 13	Frequency Diagram: Comparison of Three Different Time Duration Using a Hanning Window, Beam (21" x 6" x 6"), XL-XR1-XR2 (14 - 11 - 8), Experimental Data, Instrumented Hammer.	31
2.5 - 14	Frequency Diagram: Comparison of Three Different Time Duration Using a Rectangular Window, Beam (21" x 6" x 6"), XL-XR1-XR2 (14 - 11 - 8), Experimental Data, Instrumented Hammer.	32

2.5 - 15	Frequency Diagram: Comparison of Three Different Time Duration Using a Exponential Window, Beam (21" x 6" x 6"), XL-XR1-XR2 (14 - 11 - 8), Experimental Data, Instrumented Hammer.	33
2.6 - 1	Linear Spectra Phase and Cross Power Spectrum Phase with Proper Exponential Window, Beam (21" x 6" x 6"), XL-XR1-XR2 (14 - 11 - 8), Experimental Data, Instrumented Hammer	35
2.6 - 2	Linear Spectra Phase and Cross Power Spectrum Phase with an Exponential Window which is too Short, Beam (21" x 6" x 6"), XL-XR1-XR2 (14 - 11 - 8), Experimental Data, Instrumented Hammer.	35
3.1.5 - 1	Configuration and Load Pulse	43
3.1.5 -2	Time Records: 11' and 12'	44
3.1.5 - 3	Time Records: 12' and 14'	45
3.1.5 - 4	Time Records: 13' and 16'	46
3.1.5 - 5	Dispersion Curve: Theory vs SASW for Modal Analysis Data	47
3.2.6 - 1	Mesh Diagram	59
3.2.6 - 2	Mesh Size 3 x 21; Acceleration Diagram, Frequency Diagram and Dispersion Curve; Beam (21" x 6" x 6"), XL-XR1-XR2 (14-11-8), Exponential Window	60
3.2.6 - 3	Mesh Size 3 x 168; Acceleration Diagram, Frequency Diagram and Dispersion Curve; Beam (21" x 6" x 6"), XL-XR1-XR2 (14-11-8), Exponential Window	61
3.2.6 - 4	Mesh Size 3 x 336; Acceleration Diagram, Frequency Diagram and Dispersion Curve; Beam (21" x 6" x 6"), XL-XR1-XR2 (14-11-8), Exponential Window	62
3.2.6 - 5	Mesh Size 6 x 21; Acceleration Diagram, Frequency Diagram and Dispersion Curve; Beam (21" x 6" x 6"), XL-XR1-XR2 (14-11-8), Exponential Window	63

3.2.6 - 6	Mesh Size 6 x 168; Acceleration Diagram, Frequency Diagram and Dispersion Curve; Beam (21" x 6" x 6"), XL-XR1-XR2 (14-11-8), Exponential Window	64
3.2.6 - 7	Mesh Size 6 x 336; Acceleration Diagram, Frequency Diagram and Dispersion Curve; Beam (21" x 6" x 6"), XL-XR1-XR2 (14-11-8), Exponential Window	65
3.2.6 - 8	Mesh Size 12 x 21; Acceleration Diagram, Frequency Diagram and Dispersion Curve; Beam (21" x 6" x 6"), XL-XR1-XR2 (14-11-8), Exponential Window	66
3.2.6 - 9	Mesh Size 12 x 168; Acceleration Diagram, Frequency Diagram and Dispersion Curve; Beam (21" x 6" x 6"), XL-XR1-XR2 (14-11-8), Exponential Window	67
3.2.6 - 10	Mesh Size 12 x 336; Acceleration Diagram, Frequency Diagram and Dispersion Curve; Beam (21" x 6" x 6"), XL-XR1-XR2 (14-11-8), Exponential Window	68
3.3 - 1	Modal Analysis and Finite Element Analysis; Displacement Diagram, Frequency Diagram and Dispersion Curve; $TD / T_0 = 10$, Beam (21" x 6" x 6"), XL-XR1-XR2 (14-11-8), Exponential Window	72
3.3 - 2	Modal Analysis and Finite Element Analysis; Displacement Diagram, Frequency Diagram and Dispersion Curve; $TD / T_0 = 5$, Beam (21" x 6" x 6"), XL-XR1-XR2 (14-11-8), Exponential Window	73
3.3 - 3	Modal Analysis and Finite Element Analysis; Displacement Diagram, Frequency Diagram and Dispersion Curve; $TD / T_0 = 1$, Beam (21" x 6" x 6"), XL-XR1-XR2 (14-11-8), Exponential Window	74
3.3 - 4	Modal Analysis and Finite Element Analysis; Displacement Diagram, Frequency Diagram and Dispersion Curve; $TD / T_0 = .5$, Beam (21" x 6" x 6"), XL-XR1-XR2 (14-11-8), Exponential Window	75
3.3 - 5	Modal Analysis and Finite Element Analysis; Displacement Diagram, Frequency Diagram and Dispersion Curve; $TD / T_0 = .1$, Beam (21" x 6" x 6"), XL-XR1-XR2 (14-11-8), Exponential Window	76

3.4 - 1	Dispersion Curve Comparison: SASW (using Finite Element Data) Vs Analytical (Finite Layer with Air on Both Sides)	78
3.5 - 1	Dispersion Curve: Boundary Conditions Analytical Data, Mesh Size 12 x 168, Beam (21" x 6" x 6"), XL-XR1-XR2 (14-11-8), Exponential Window	79
3.6 - 1	Dispersion Curve: Acceleration vs Displacement, Analytical Data, Mesh Size 12 x 168, Beam (21" x 6" x 6"), XL-XR1-XR2 (14-11-8), Exponential Window	80
4.1 - 1	Relative Location of Damage and Source-Receiver Array	83
4.2 - 1	Test Set Up	85
5.1 - 1	Dispersion Curve: Experimental vs Analytical Mesh Size 12 x 168, Beam (21" x 6" x 6"), XL-XR1-XR2 (14-11-8), Exponential Window	89
5.2 - 1	Dispersion Curve: Load Duration Varied, Analytical Data, Mesh Size 12 x 168, Beam (21" x 6" x 6"), XL-XR1-XR2 (14-11-8), Exponential Window	90
5.2 - 2	Dispersion Curve: Load Duration Varied, Experimental Data, Beam (21" x 6" x 6"), XL-XR1-XR2 (14-11-8), Exponential Window	91
5.3 - 1	Dispersion Curve: Array Location Varied, Analytical Data, Mesh Size 12 x 168, Beam (21" x 6" x 6"), Exponential Window	92
5.3 - 2	Dispersion Curve: Array Location Varied, Experimental Data, Beam (21" x 6" x 6"), Exponential Window	93
5.4 - 1	Dispersion Curve: Spacing Varied, Analytical Data, Mesh Size 12 x 168, Beam (21" x 6" x 6"), Exponential Window	94
5.4 - 2	Dispersion Curve: Spacing Varied, Experimental Data, Beam (21" x 6" x 6"), Exponential Window	95
6 - 1	SASW Test Configurations	97
6.1 - 1	Test Configuration 1	98

6.1 - 2	Phase Diagrams, 3" Spacing, Experimental Data, Test Configuration 1 : No Damage, 1", 2" and 3" Deep Crack	99
6.1 - 3	Unfolded Phase Diagrams, 3" Spacing, Experimental Data, Test Configuration 1 : No Damage, 1", 2" and 3" Deep Crack	100
6.1 - 4	Dispersion Curve, 3" Spacing, Experimental Data, Test Configuration 1: No Damage, 1", 2" and 3" Deep Crack	101
6.1 - 5	Dispersion Curve, 3" Spacing, Analytical Data, Test Configuration 1: No Damage, 1", 2" and 3" Deep Crack	101
6.1 - 6	Phase Diagrams, 6" Spacing, Experimental Data, Test Configuration 1 : No Damage, 1", 2" and 3" Deep Crack	103
6.1 - 7	Unfolded Phase Diagrams, 6" Spacing, Experimental Data, Test Configuration 1 : No Damage, 1", 2" and 3" Deep Crack	104
6.1 - 8	Dispersion Curve, 6" Spacing, Experimental Data, Test Configuration 1: No Damage, 1", 2" and 3" Deep Crack	105
6.1 - 9	Dispersion Curve, 6" Spacing, Analytical Data, Test Configuration 1: No Damage, 1", 2" and 3" Deep Crack	105
6.2.1 - 1	Test Configuration 2	106
6.2.1 - 2	Phase Diagrams, 3" Spacing, Experimental Data, Test Configuration 2 : No Damage, 1", 2" and 3" Deep Crack	108
6.2.1 - 3	Unfolded Phase Diagrams, 3" Spacing, Experimental Data, Test Configuration 2 : No Damage, 1", 2" and 3" Deep Crack	109
6.2.1 - 4	Dispersion Curve, 3" Spacing, Experimental Data, Test Configuration 2: No Damage, 1", 2" and 3" Deep Crack	110
6.2.1 - 5	Dispersion Curve, 3" Spacing, Analytical Data, Test Configuration 2: No Damage, 1", 2" and 3" Deep Crack	110
6.2.1 - 6	Phase Diagrams, 6" Spacing, Experimental Data, Test Configuration 2 : No Damage, 1", 2" and 3" Deep Crack	111

6.2.1 - 7	Unfolded Phase Diagrams, 6" Spacing, Experimental Data, Test Configuration 2 : No Damage, 1", 2" and 3" Deep Crack	112
6.2.1 - 8	Dispersion Curve, 6" Spacing, Experimental Data, Test Configuration 2: No Damage, 1", 2" and 3" Deep Crack	113
6.2.1 - 9	Dispersion Curve, 6" Spacing, Analytical Data, Test Configuration 2: No Damage, 1", 2" and 3" Deep Crack	113
6.2.1 - 10	Unfolded Phase Diagrams, 3" Spacing, Experimental Data, Test Configuration 2, 2" Deep Crack, Array Location Varied	114
6.2.1 - 11	Dispersion Curve, 3" Spacing, Experimental Data, Test Configuration 2, 2" Deep Crack, Array Location Varied	115
6.2.1 - 12	Dispersion Curve, 3" Spacing, Analytical Data, Test Configuration 2, 2" Deep Crack, Array Location Varied	115
6.2.1 - 13	Unfolded Phase Diagrams, 6" Spacing, Experimental Data, Test Configuration 2, 2" Deep Crack, Array Location Varied	116
6.2.1 - 14	Dispersion Curve, 6" Spacing, Experimental Data, Test Configuration 2, 2" Deep Crack, Array Location Varied	117
6.2.1 - 15	Dispersion Curve, 6" Spacing, Analytical Data, Test Configuration 2, 2" Deep Crack, Array Location Varied	117
6.2.2 - 1	Phase Diagrams from Repaired Beams, 3" Spacing, Experimental Data, Test Configuration 2 : No Damage, 1", 2" and 3" Deep Crack	119
6.2.2 - 2	Unfolded Phase Diagrams from Repaired Beams, 3" Spacing, Experimental Data, Test Configuration 2 : No Damage, 1", 2" and 3" Deep Crack	120
6.2.2 - 3	Dispersion Curve from Repaired Beams, 3" Spacing, Experimental Data, Test Configuration 2: No Damage, 1", 2" and 3" Deep Crack	121
6.2.2 - 4	Phase Diagrams from Repaired Beams, 6" Spacing, Experimental Data, Test Configuration 2 : No Damage, 1", 2" and 3" Deep Crack	122

6.2.2 - 5	Unfolded Phase Diagrams from Repaired Beams, 6" Spacing, Experimental Data, Test Configuration 2 : No Damage, 1", 2" and 3" Deep Crack	123
6.2.2 - 6	Dispersion Curve from Repaired Beams, 6" Spacing, Experimental Data, Test Configuration 2: No Damage, 1", 2" and 3" Deep Crack	124
6.3 - 1	Test Configuration 3	125
6.3 - 2	Phase Diagrams, 3" Spacing, Experimental Data, Test Configuration 3 : No Damage, 1", 2" and 3" Deep Crack	127
6.3 - 3	Unfolded Phase Diagrams, 3" Spacing, Experimental Data, Test Configuration 3 : No Damage, 1", 2" and 3" Deep Crack	128
6.3 - 4	Dispersion Curve, 3" Spacing, Experimental Data, Test Configuration 3: No Damage, 1", 2" and 3" Deep Crack	129
6.3 - 5	Dispersion Curve, 3" Spacing, Analytical Data, Test Configuration 3: No Damage, 1", 2" and 3" Deep Crack	129
6.3 - 6	Phase Diagrams, 6" Spacing, Experimental Data, Test Configuration 3 : No Damage, 1", 2" and 3" Deep Crack	130
6.3 - 7	Unfolded Phase Diagrams, 6" Spacing, Experimental Data, Test Configuration 3 : No Damage, 1", 2" and 3" Deep Crack	131
6.3 - 8	Dispersion Curve, 6" Spacing, Experimental Data, Test Configuration 3: No Damage, 1", 2" and 3" Deep Crack	132
6.3 - 9	Dispersion Curve, 6" Spacing, Analytical Data, Test Configuration 3: No Damage, 1", 2" and 3" Deep Crack	132
6.4 - 1	Test Configuration 4	133
6.4 - 2	Phase Diagrams, 3" Spacing, Experimental Data, Test Configuration 4 : No Damage, 1", 2" and 3" Deep Crack	134
6.4 - 3	Unfolded Phase Diagrams, 3" Spacing, Experimental Data, Test Configuration 4 : No Damage, 1", 2" and 3" Deep Crack	135

6.4 - 4	Dispersion Curve, 3" Spacing, Experimental Data, Test Configuration 4: No Damage, 1", 2" and 3" Deep Crack	136
6.4 - 5	Dispersion Curve, 3" Spacing, Analytical Data, Test Configuration 4: No Damage, 1", 2" and 3" Deep Crack	136
6.4 - 6	Phase Diagrams, 6" Spacing, Experimental Data, Test Configuration 4 : No Damage, 1", 2" and 3" Deep Crack	137
6.4 - 7	Unfolded Phase Diagrams, 6" Spacing, Experimental Data, Test Configuration 4 : No Damage, 1", 2" and 3" Deep Crack	138
6.4 - 8	Dispersion Curve, 6" Spacing, Experimental Data, Test Configuration 4: No Damage, 1", 2" and 3" Deep Crack	139
6.4 - 9	Dispersion Curve, 6" Spacing, Analytical Data, Test Configuration 4: No Damage, 1", 2" and 3" Deep Crack	139
6.5 - 1	Test Configuration 5	140
6.5 - 2	Phase Diagrams, 3" Spacing, Experimental Data, Test Configuration 5 : No Damage, 1", 2" and 3" Deep Crack	141
6.5 - 3	Unfolded Phase Diagrams, 3" Spacing, Experimental Data, Test Configuration 5 : No Damage, 1", 2" and 3" Deep Crack	142
6.5 - 4	Dispersion Curve, 3" Spacing, Experimental Data, Test Configuration 5: No Damage, 1", 2" and 3" Deep Crack	143
6.5 - 5	Phase Diagrams, 6" Spacing, Experimental Data, Test Configuration 5 : No Damage, 1", 2" and 3" Deep Crack	144
6.5 - 6	Unfolded Phase Diagrams, 6" Spacing, Experimental Data, Test Configuration 5 : No Damage, 1", 2" and 3" Deep Crack	145
6.5 - 7	Dispersion Curve, 6" Spacing, Experimental Data, Test Configuration 5: No Damage, 1", 2" and 3" Deep Crack	146

CHAPTER ONE

INTRODUCTION

1.1 OBJECTIVE

The objective of this research was to assess the ability of surface wave measurements and the SASW technique to determine the elastic properties and detect crack damage in beam and column concrete elements.

1.2 APPROACH

The modulus of elasticity was detected from the phase velocity given by the dispersion curve as a function of frequency. Damage was detected by a change in the dispersion curve between undamaged and damaged states. The SASW (Spectral Analysis of Surface Waves) technique was used to calculate the surface wave dispersion curve (phase velocity vs frequency).

1.3 SCOPE

This work was made up of both an analytical study and an experimental study. The goal of the analytical study was to determine the model sophistication necessary to represent a surface wave propagating in a beam. Two models were used. The first model was a time domain solution of beam theory using modal analysis. The second model was a two dimensional finite element model which used constant average acceleration, plane stress constitutive equations, eight noded quadratic rectangular elements, and a consistent mass matrix.. After determining the necessary modelling sophistication, a crack was introduced in the beam and a parametric study, similar to the experimental study, was run.

Experimentally, a parametric study was run on 21" x 6" x 6" concrete test specimens. The damage form studied was vertical cracks. Crack depths of 1", 2", and 3" were used. Two receiver spacing were used: 3" and 6". The location of the source-receiver array relative to the crack was varied, such that the crack was either outside the array, between the receivers, between the source and first receiver, or on the bottom face with the array on the top face.

The goal was to determine how the crack affected the dispersion curve and evaluate if the change in the dispersion curve could be used for detecting damage.

1.4 WHY

There are many forms of damage to reinforced concrete members such as cracking and crushing of the concrete, yielding and fracture of the reinforcement, loss of bond between the concrete and steel, honeycombing and voids as well as deterioration due to the environment.

Most forms of damaged due to structural overload and deterioration result in cracking. The need to study damage detection has been identified by several authors. In 1989, a working group on "Global Structural Diagnostics", at the conference on the Nondestructive Evaluation for Performance of Civil Structures, identified the need for "Better techniques for detection of flaws or defects inside structural members". At the same conference, the group on "Controlling the Construction Process", identified the need to "Develop methods to check, automatically, dimensional accuracy and presence of cracks in precast members."

When assessing the ability of surface waves and the ability of the SASW technique to detect damage, crack damage was chosen as the initial damage form because it represents a limiting case. If the method cannot detect cracks, then the method would probably not detect other forms of damage such as honeycombing and

voids.

In the report, "Impact Echo: A Method for Flaw Detection in Concrete Using Transient Stress Waves", Sansalone and Carino showed that compression waves could be used to detect imperfections. Hence the use of stress waves is a viable technique.

Surface waves and the SASW method have several features which make the technique attractive. They include:

1. When an impact is used to create the source wave, the majority of energy from the impact is imparted in the form of surface waves with the remainder going into body waves.
2. The damping due to geometrical spreading for surface waves (cylindrical) is smaller than for body waves (spherical).
3. The SASW method only requires access to one side of the member.
4. SASW also provides information about the depth of the beam; due to the dispersive nature of the surface wave, different wave lengths sample different depths. Impact-echo and through transmission techniques only provide information about the ray path between the source and receiver.
5. The SASW method does not require estimation of the compression wave velocity as the impact-echo method does.

1.5 ORGANIZATION

This dissertation consists of seven chapters and three appendices. Chapter Two

provides background on the SASW method. Chapter Three reviews the analytical methods used to model the problem. Chapter Four presents data on generating the waveform experimentally. It includes the test matrix and a review of the equipment and test procedures used experimentally. Chapter Five shows data on an intact section. Chapter Six shows the effect of vertical crack damage on the dispersion curve for various source receiver crack configurations. Chapter Seven contains the conclusions and makes recommendations for future research. Appendix A is a review of the basics of stress waves. Appendix B is a review of Fourier transforms. Appendix C is a review of other stress wave methods for crack detection and sizing.

CHAPTER TWO

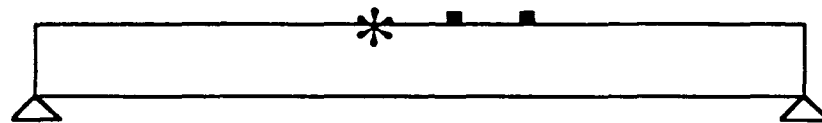
SASW (Spectral Analysis of Surface Waves)

2.1 OVERVIEW OF THE METHOD

SASW stands for Spectral Analysis of Surface Waves. The goal of SASW is to determine the dispersion curve which is a plot of the phase velocity versus wavelength or frequency. (It is implied that there is a one to one correspondence between the wavelength and the frequency)

The process considers two simultaneous time records resulting from an impact generated surface wave and at a given separation. Using the time records, the phase of the cross power spectrum can be calculated. In this form, the cross power spectrum phase varies between π and $-\pi$ and must be unfolded to get the proper phase diagram (This is discussed in section 2.4). The unfolded phase diagram represents the phase difference between the linear spectra of the two records. The unfolded cross power spectrum phase is then used to calculate the velocity and wavelength for each frequency. This process is shown schematically in Figure 2.1 - 1 and a graphical example of the phase, unfolded phase, and coherence (coherence is a measure the data quality) is given in Figure 2.1 - 2. Figure 2.1 - 3 shows the resulting velocity vs frequency, wavelength vs frequency, and velocity vs wavelength diagrams.

In this work, the dispersion curve used will be velocity vs frequency. This is because in the range of interest of 30 kHz to 100 kHz the results are better on the velocity vs frequency diagram than on the velocity vs wavelength plot.



TIME RECORD 1

TIME RECORD 2

CROSS POWER
SPECTRUM
PHASE

$$\text{VELOCITY} = \frac{(\text{REC_SPACING} * 360 * \text{FREQ})}{\text{PHASE}}$$

$$\text{WAVELENGTH} = \frac{(\text{REC_SPACING} * 360)}{\text{PHASE}}$$

Figure 2.1 - 1 Overview of SASW Method

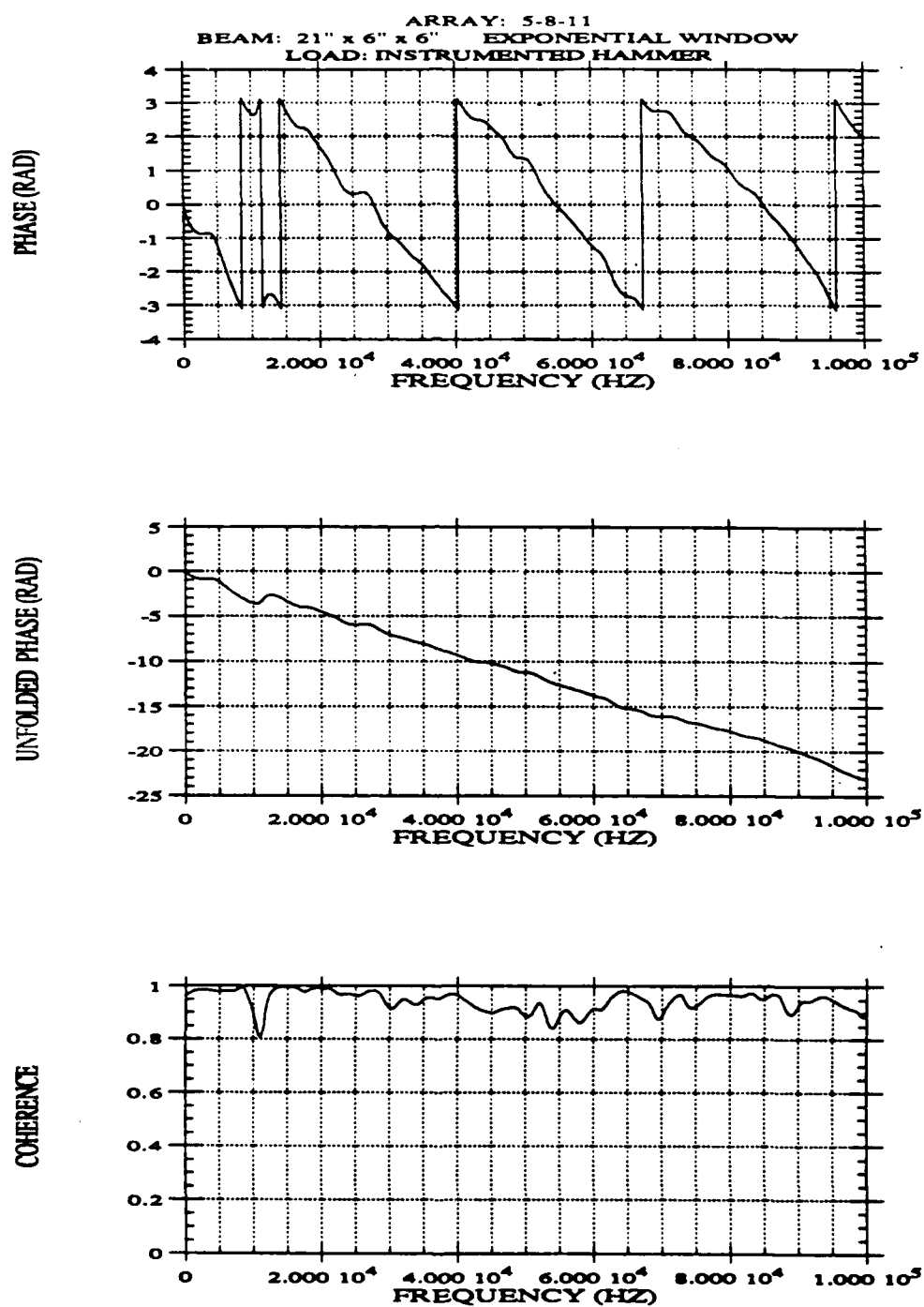


Figure 2.1 - 2 Cross Power Spectrum Phase, Unfolded Phase, and Coherence Diagrams

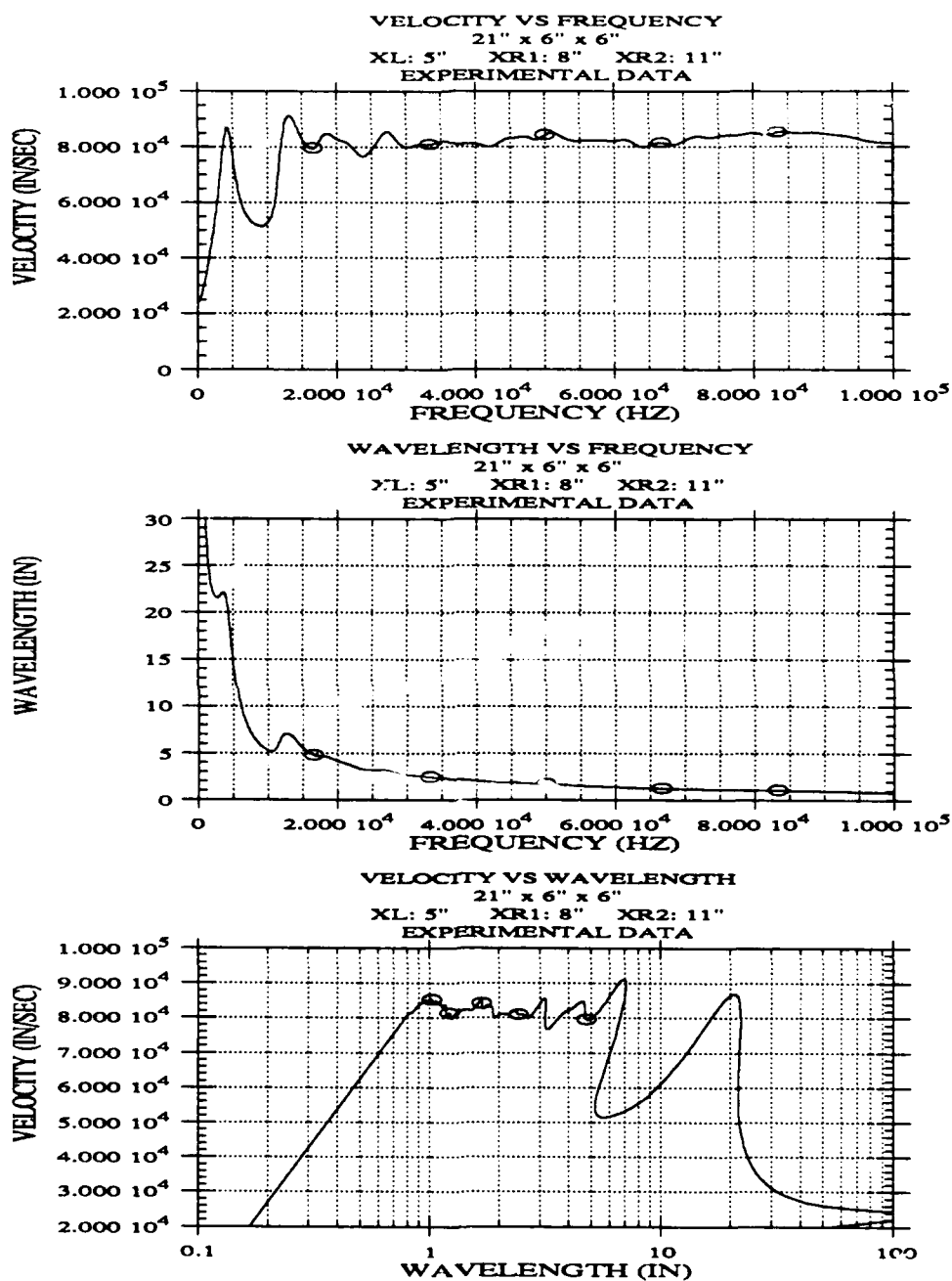


Figure 2.1 - 3 Phase Velocity vs Frequency, Wavelength Vs Frequency, and Phase Velocity vs Wavelength Diagrams

2.2 DERIVATION OF THE VELOCITY AND WAVELENGTH

Given the phase shift (calculated from the cross power spectrum) and the frequency, the time to transverse the path can be calculated as:

$$t(f) = \frac{\phi(f)}{\omega(f)} = \frac{\phi(f)}{2 \pi f}$$

where $\phi(f)$ is the phase in radians. Since the distance, d , is known between the receivers. The velocity can be calculated as:

$$V(f) = \frac{d}{t(f)} = \frac{d 2 \pi f}{\phi(f)}$$

Finally, using the relationship, $V = \lambda * \text{frequency}$, the wavelength is calculated:

$$\lambda = \frac{V}{f} = \frac{d 2 \pi}{\phi(f)}$$

2.3 INTERPRETATION OF THE PHASE DIAGRAM

The cross power spectrum is a complex number which can be represented by its amplitude and phase, where

$$S_{12}(f) = |S_{12}(f)| \exp(i \phi_{12}(f))$$

and

$$|S_{12}(f)| = \sqrt{\text{Imag } S_{12}(f)^2 + \text{Real } S_{12}(f)^2}$$

$$\phi_{12}(f) = \tan^{-1} \left[\frac{\text{Imag } S_{12}(f)}{\text{Real } S_{12}(f)} \right]$$

The phase information, $\phi_{12}(f)$, is the phase difference as a function of frequency between the two measuring points. That is

$$\phi_{12}(f) = \phi_2(f) - \phi_1(f)$$

where $\phi_1(f)$ and $\phi_2(f)$ denote the phases of the Fourier transform of time records 1 and 2 respectively. Figure 2.3 -1 illustrated this point using the the unfolded phase diagram.

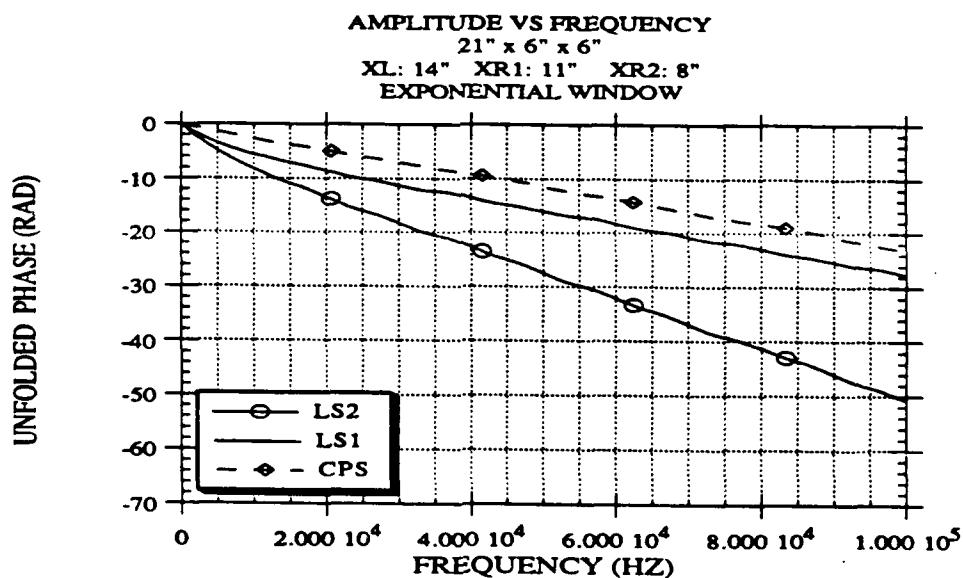


Figure 2.3 - 1 Unfolded Linear Spectrum Phase and Cross Power Spectrum Phase

2.4 UNFOLDING THE PHASE DIAGRAM

In the SASW method, determining the proper phase shift for each frequency is important. The proper phase is the actual number of cycles of a given wavelength for a given distance between two points.

As the wavelength decreases (frequency increases) for a homogeneous material, the smaller wavelengths must go through more cycles to transverse a given distance. Hence the cross power spectrum phase diagram should increase/decrease monotonically. However, when the cross power spectrum is calculated, it only varies between π and $-\pi$ as seen in Figure 2.1 - 2. There are points in the phase diagram where there is a jump discontinuity as the phase diagram goes from $-\pi$ to π . These jump discontinuities are referred to as 2π phase ambiguities. As such the cross power spectrum phase cannot be used "as is" to calculate the velocity and wavelength. The phase diagram must be unfolded and the 2π phase ambiguities eliminated. The phase in the unfolded phase diagram is equal to the calculated phase plus $n2\pi$ where n is an integer and must be determined at each frequency. Figure 2.1 - 2 also shows the unfolded phase, where the 2π phase ambiguities are eliminated.

In addition to 2π phase ambiguities, low coherence affects the way a phase diagram is unfolded. Coherence is a measure of the data quality. When the coherence is low, a decision to include or exclude that data must be made and is based on judgement. In the range of low coherence, additional 2π phase ambiguities are generally introduced. As a result, if the data is excluded, the proper phase ambiguities must be accounted for before the unfolded phase is used to calculate the dispersion curve.

Figure 2.4 - 1 shows a good phase diagram with good coherence. Figure 2.4 - 2 shows a phase diagram with low coherence at 10 kHz. Figure 2.4 - 3 shows the unfolded phases from Figures 2.4 - 1 and 2.4 - 2 and the subsequent dispersion curves. In the comparison of the unfolded phase diagram, there is a 2π phase shift

around 10 kHz, the point of low coherence, between the data with good coherence and the data with poor coherence. The data with good coherence gives the proper velocities and wavelengths. The data with poor coherence overestimate the phase by 2π for frequencies over 10 kHz and hence, underestimate the corresponding velocities and wavelengths. To deal with these data, the data with low coherence would be masked in the record. This will insure the proper phase diagram by eliminating the additional 2π introduced at the point of low coherence. Figure 2.4 - 4 shows the masked unfolded phase diagram and subsequent dispersion curve.

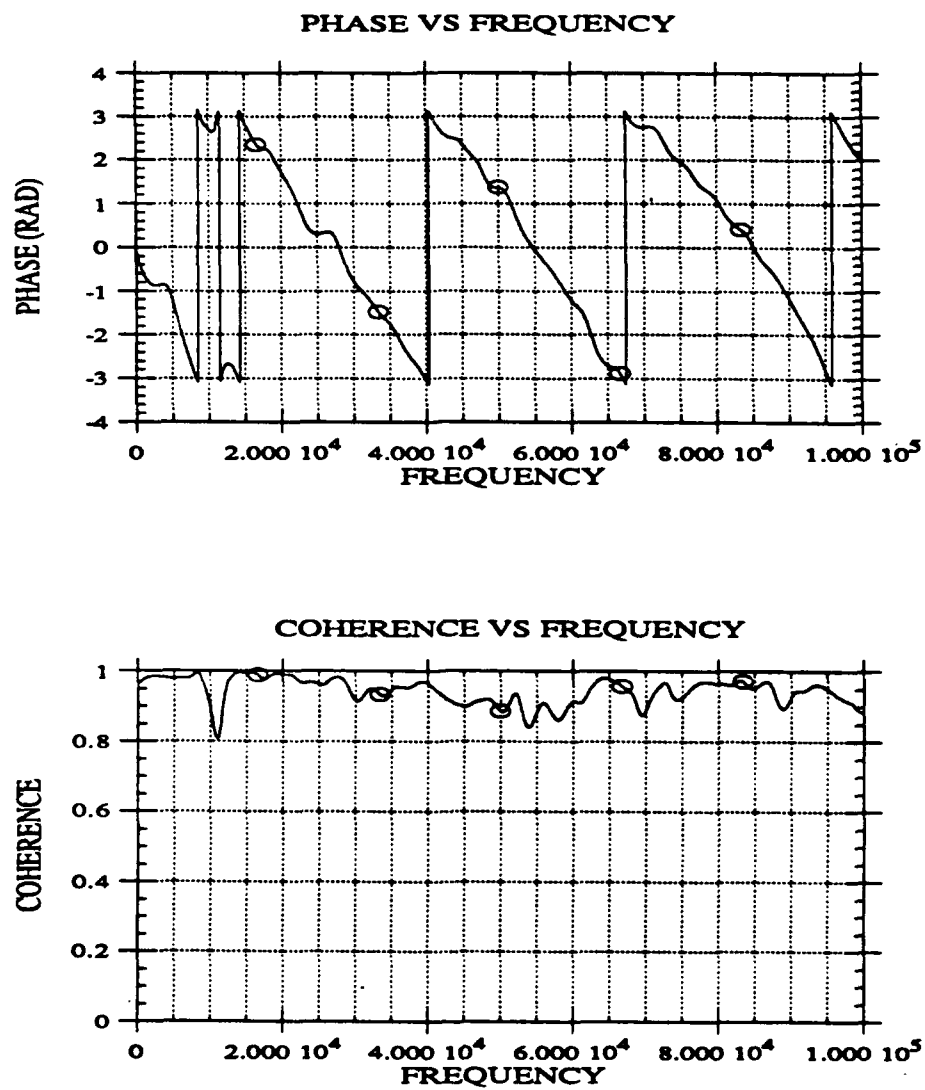


Figure 2.4 - 1 Cross Power Spectrum Phase and Coherence Diagram of Data with Good Coherence

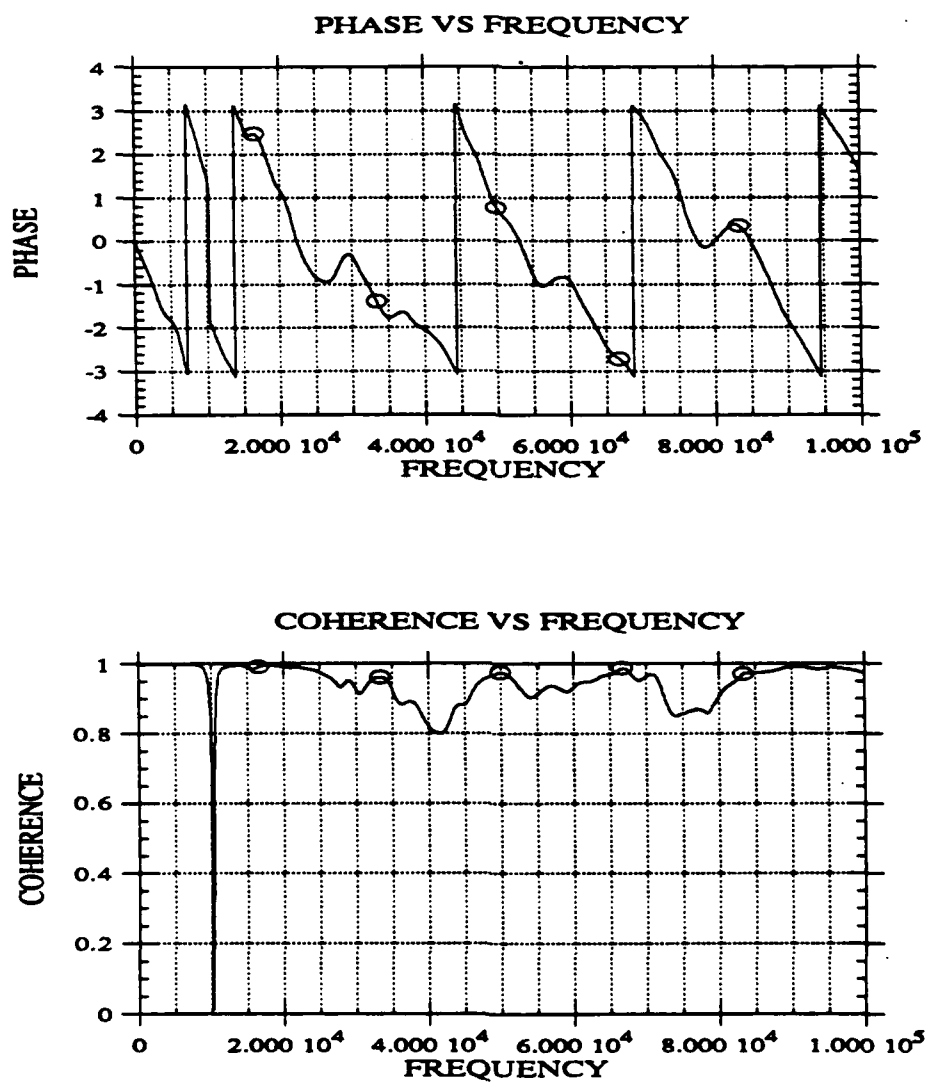


Figure 2.4 - 2 Cross Power Spectrum Phase and Coherence Diagram of Data with Poor Coherence at 10 kHz

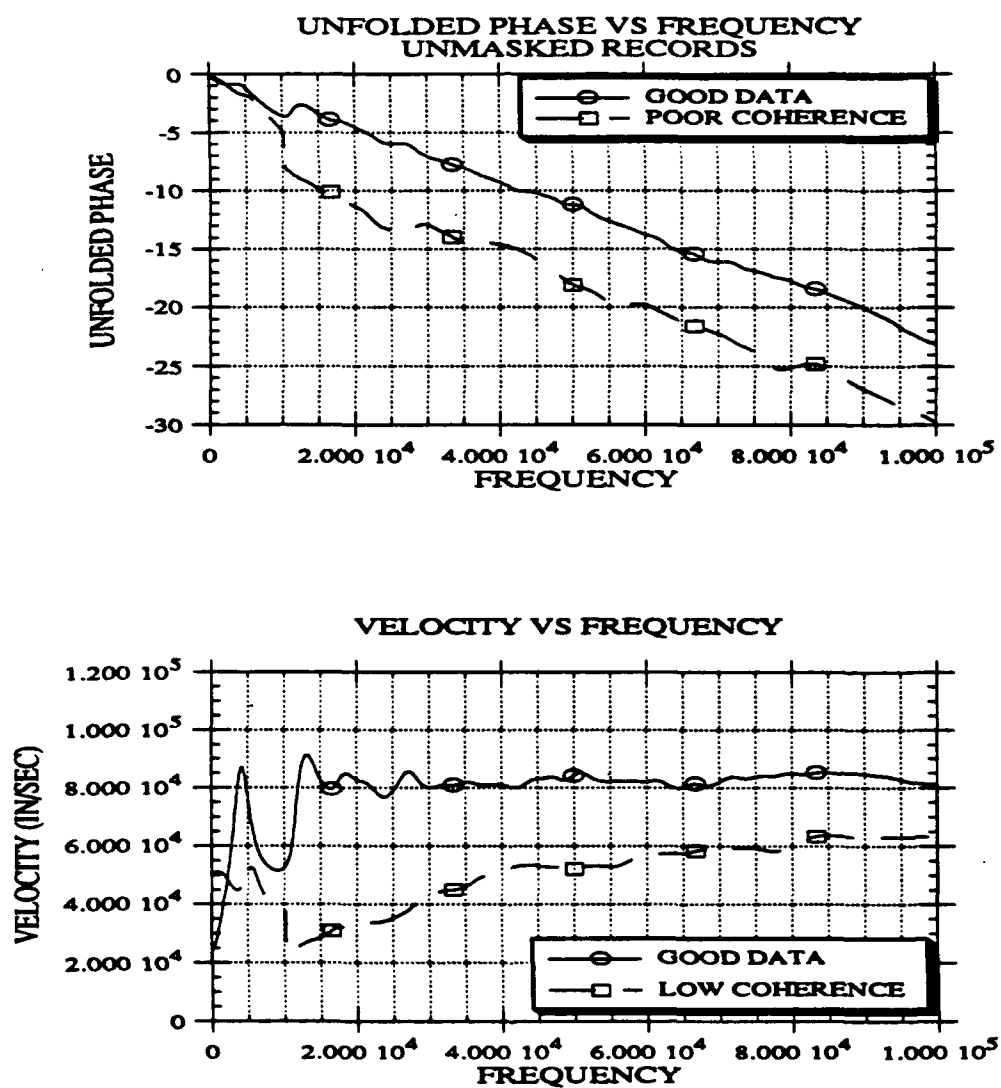


Figure 2.4 - 3 Unfolded Cross Power Spectrum Phase and Dispersion Curve from Phase Diagrams in Figures 2.4 - 1 and 2.4 - 2

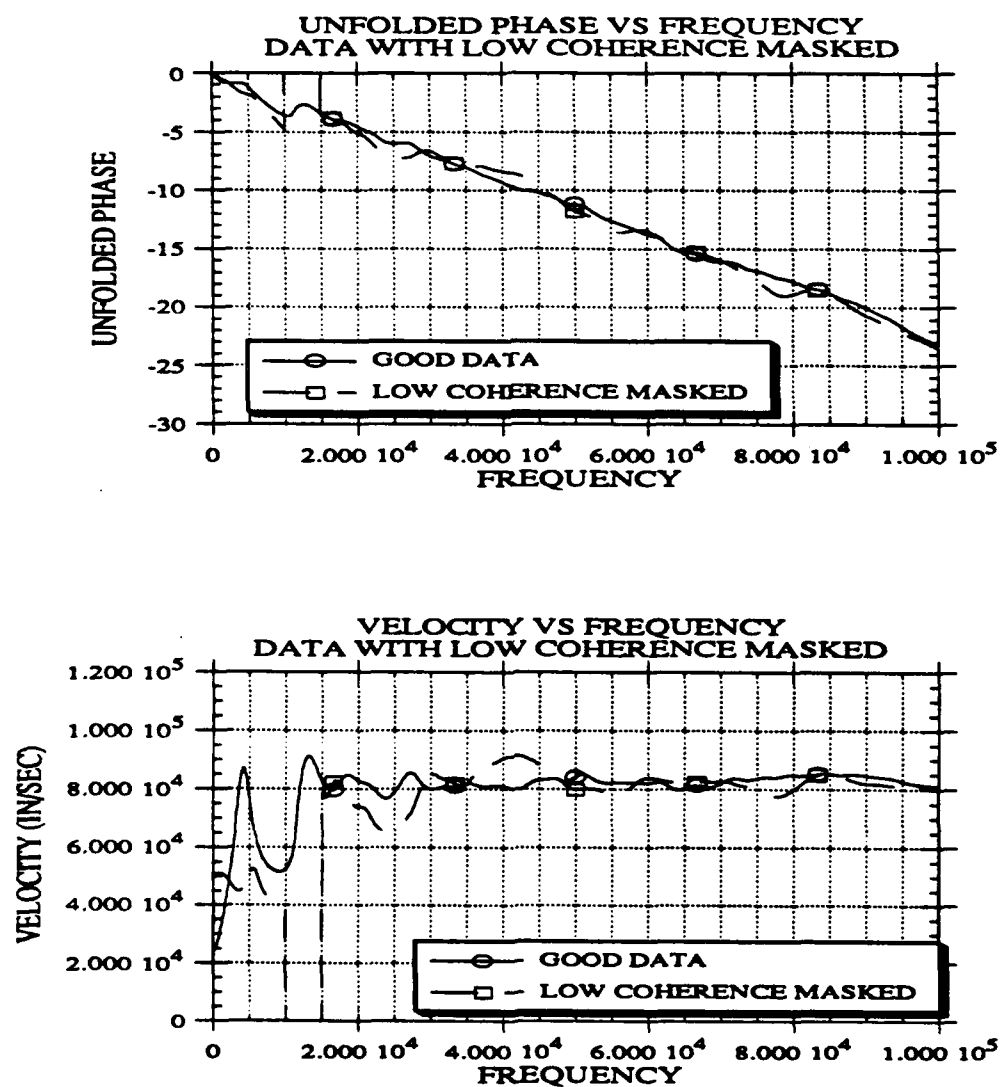


Figure 2.4 - 4 Unfolded Cross Power Spectrum Phase and Dispersion Curve from Phase Diagrams with Phase masked around 10 kHz, Point of Low Coherence

2.5 WINDOWS

Windows are necessary to get the proper phase diagram and affect the smoothness and magnitude of the spectrum. Time records are multiplied by the window to reduce leakage before the discrete Fourier transform is applied (The discrete Fourier transform is performed using an efficient algorithm called a Fast Fourier Transform (FFT)). Leakage is a result of taking a finite length record in the discrete Fourier transform and is always present for finite length data. The types of windows most often used are the Hanning, uniform, and exponential windows defined below:

$$\text{Hanning:} \quad = \frac{1}{2} \left(1 - \cos \left(\frac{2\pi t}{T} \right) \right)$$

$$\begin{aligned} \text{Rectangular:} \quad &= 1 \quad 0 < t < T \\ &= 0 \quad \text{O.W.} \end{aligned}$$

$$\text{Exponential} \quad = \text{Exp} \left(- \frac{t}{\tau} \right)$$

where T is total record length, t is time, and τ is a parameter to shape the exponential record.

The Hanning window is used for periodic and random data. The exponential window is used for decaying processes.

To better understand the effect of windows, an example is given in graphical form, to show the window shape in time and frequency, how the window affects the amplitude and magnitude of the linear spectrum, and finally how the cross power spectrum phase is affected.

The time domain representation and the FFT of the Hanning, rectangular (uniform), and exponential windows are given in Figure 2.5 - 1, Figure 2.5 - 2,

and Figure 2.5 - 3, respectively.

The cross power spectrum phase diagram was calculated using the Hanning window with lengths of 1024, 512, and 256 micro seconds, a rectangular window with lengths of 1024, 512, and 256 microseconds, and an exponential window with $\tau = 256, 128,$ and 64 microseconds. The time data used for this example is acceleration data from finite element analysis of a $21'' \times 6''$ beam. The load is at $14''$ from the left end. The first receiver is at $11''$ and the second receiver is at $8''$. For each case, only the windowed time record for the first receiver, the FFT of that time record and the phase diagram are presented in Figures 2.5 - 4 to 2.5 - 12. The best cross power spectrum phase diagram was calculated using an exponential window with $\tau = 64$ microseconds

Figures 2.5 - 13 to 2.5 - 15 show a comparison of the Fourier amplitude spectrum for three different window lengths for the Hanning, rectangular and exponential windows respectively. From this it can be seen that windows affect the smoothness and magnitude of the linear spectrum.

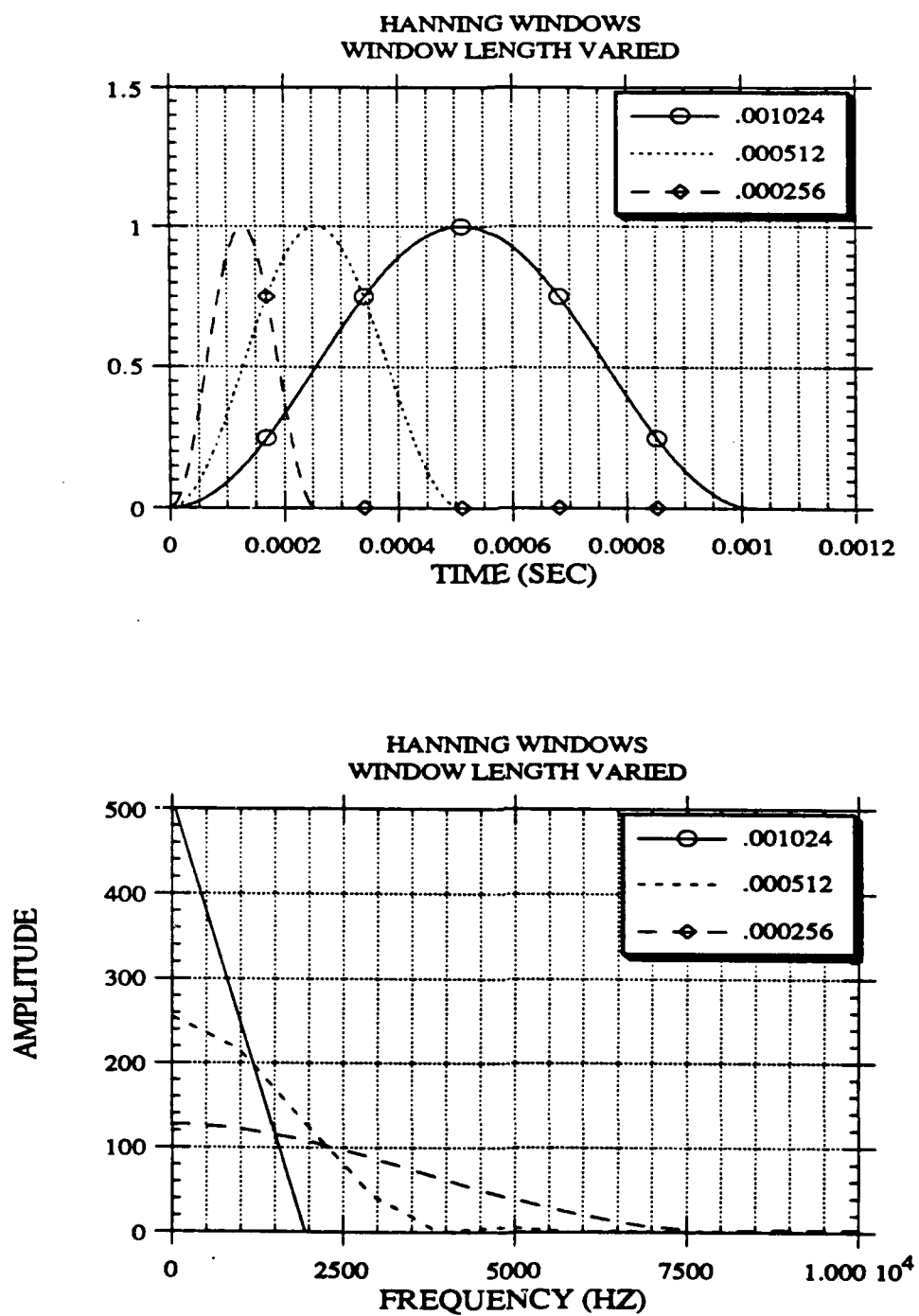


Figure 2.5 - 1 Hanning Window: Time and Frequency Diagrams

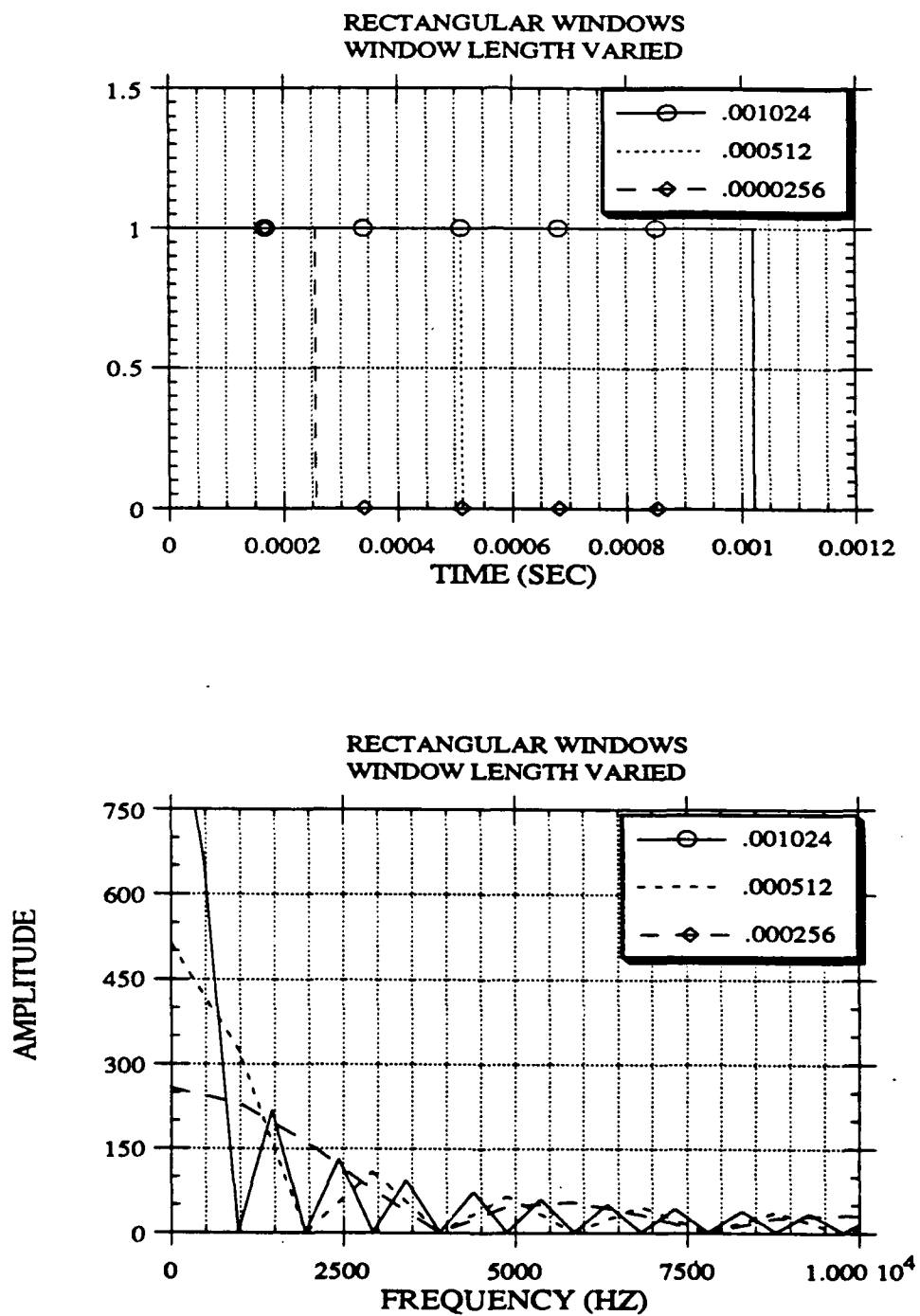


Figure 2.5 - 2 Rectangular Window: Time and Frequency Diagrams

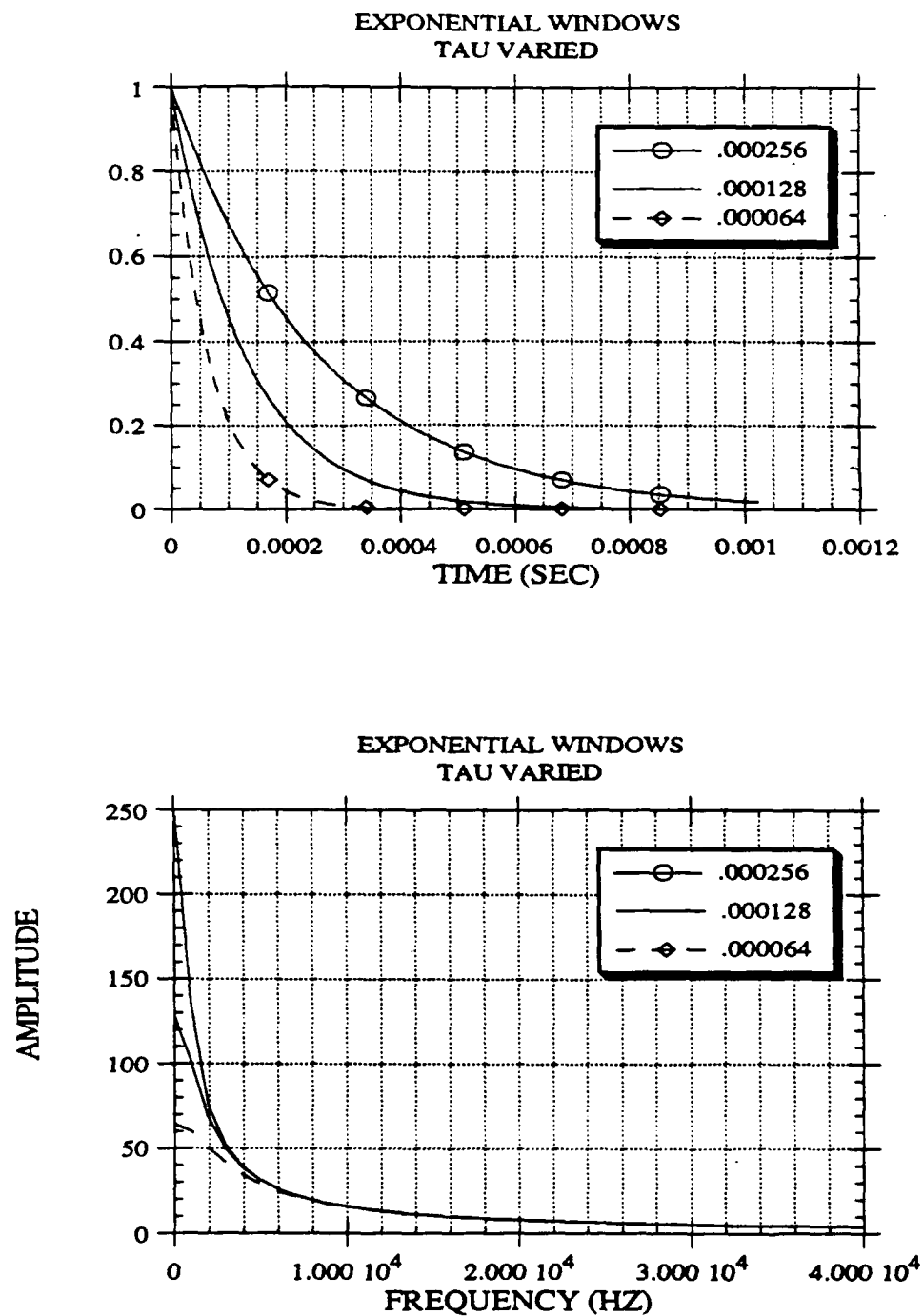


Figure 2.5 - 3 Exponential Window: Time and Frequency Diagrams

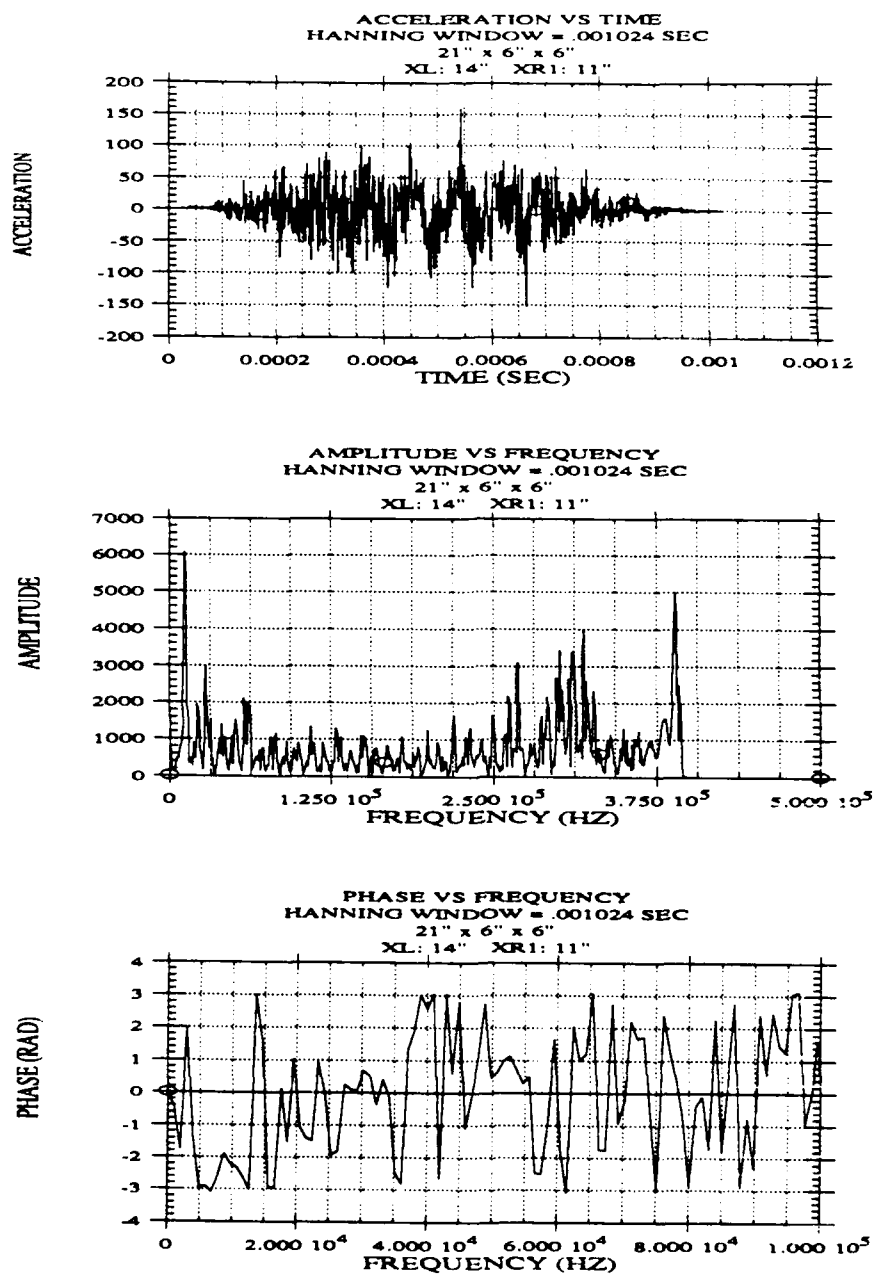


Figure 2.5 - 4 Hanning Window (1024 μ sec) Windowed Time Record, Frequency Diagram and Phase vs Frequency: Beam (21" x 6" x 6"), XL-XR1-XR2 (14 - 11 - 8), Analytical Data.

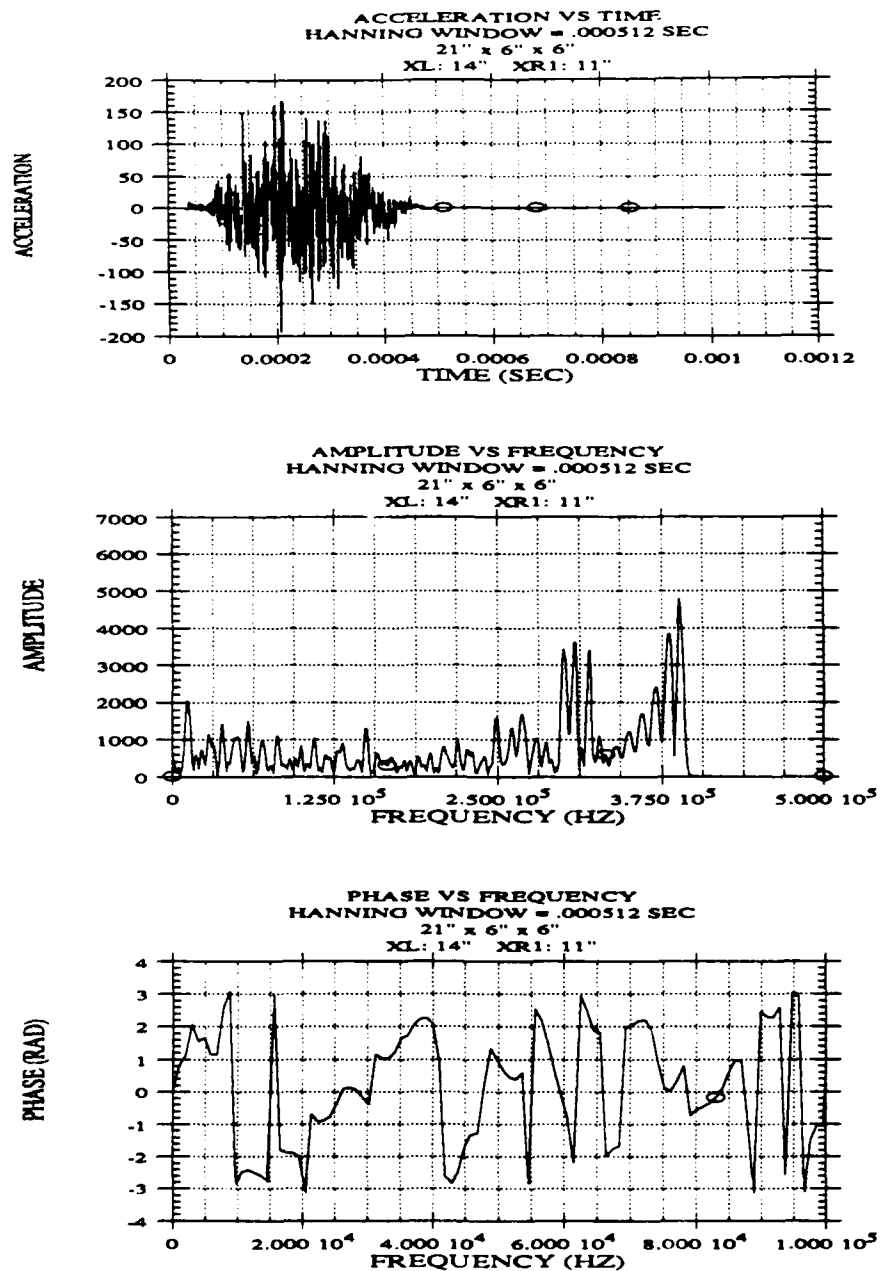


Figure 2.5 - 5 Hanning Window (512 μ sec) Windowed Time Record, Frequency Diagram and Phase vs Frequency: Beam (21" x 6" x 6"), XL-XR1-XR2 (14 - 11 - 8), Analytical Data.

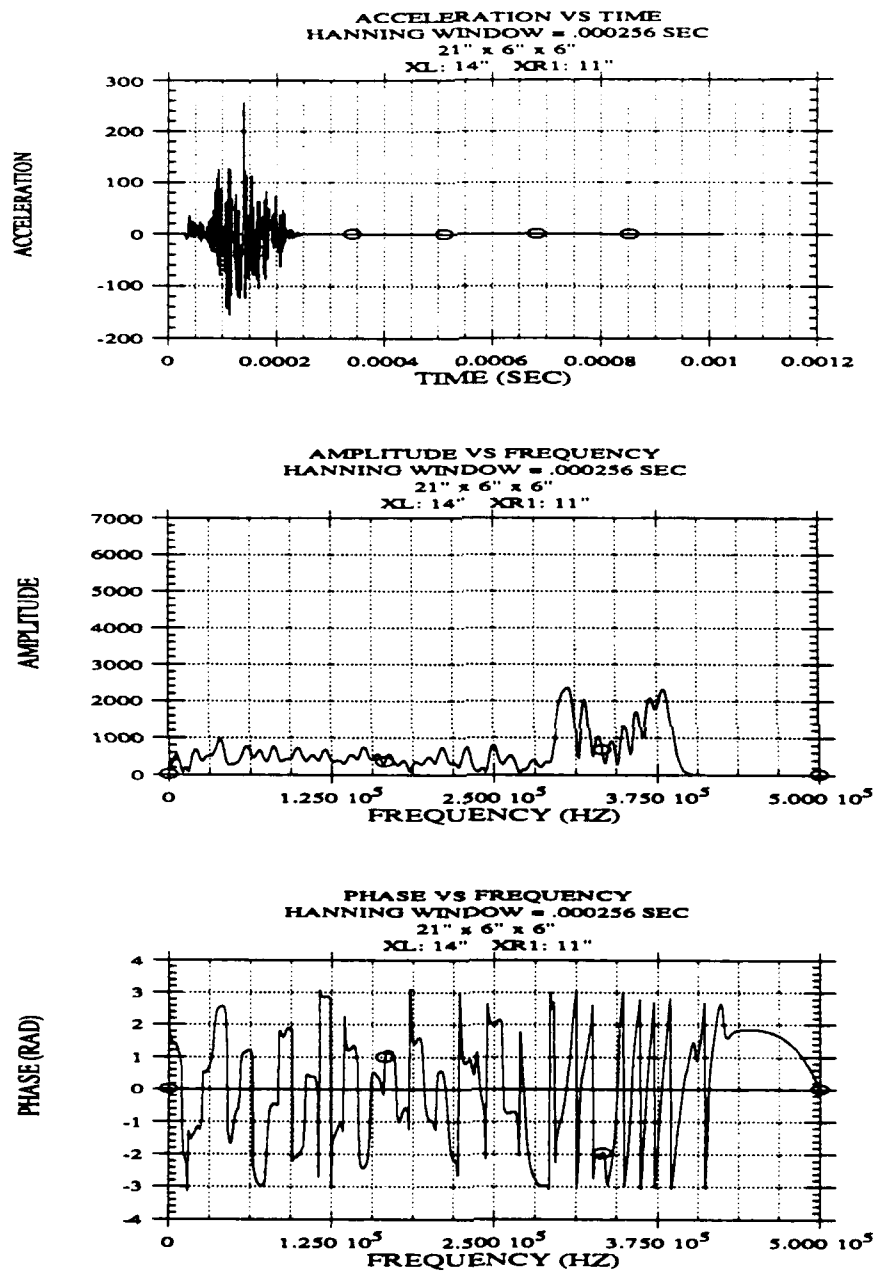


Figure 2.5 - 6 Hanning Window (256 μ sec) Windowed Time Record, Frequency Diagram and Phase vs Frequency: Beam (21" x 6" x 6"), XL-XR1-XR2 (14 - 11 - 8), Analytical Data.

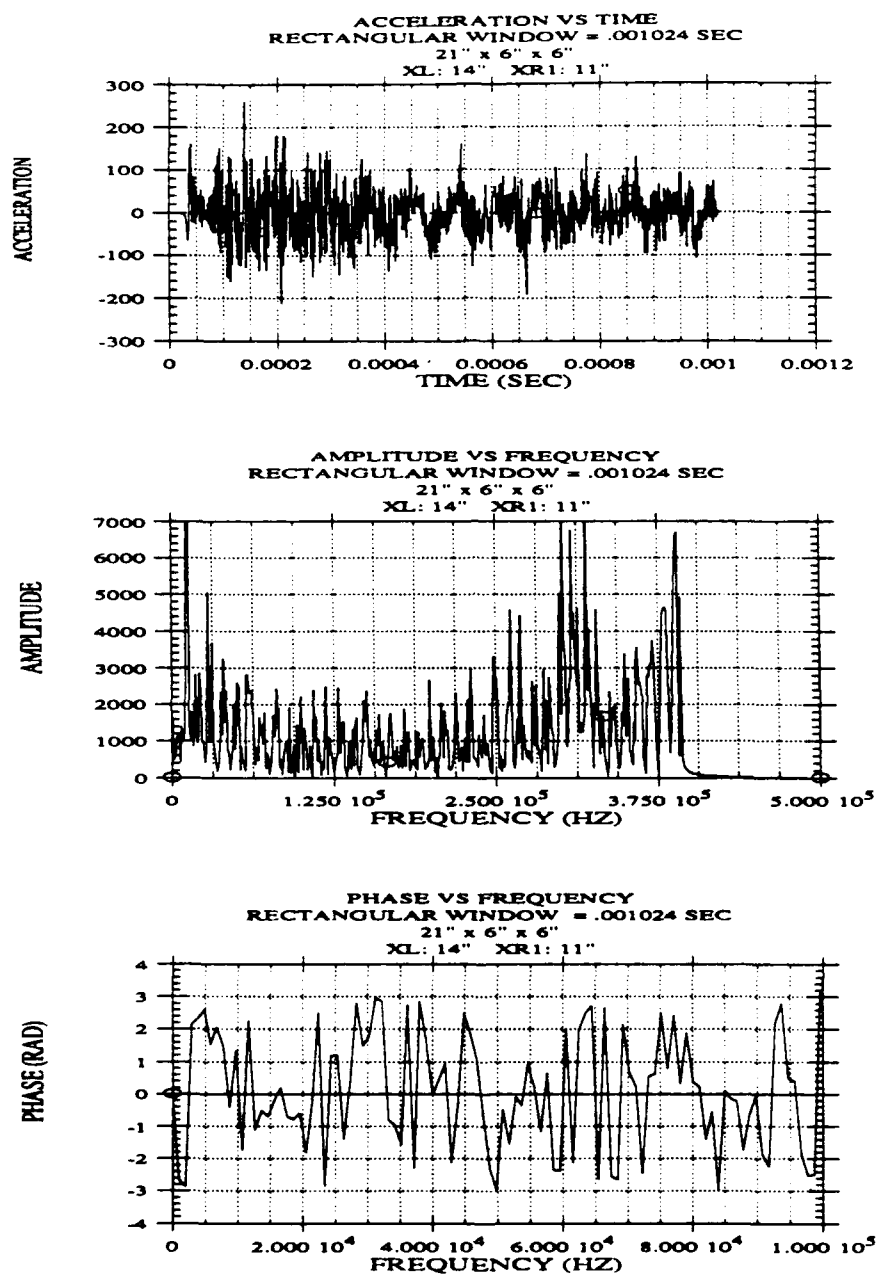


Figure 2.5 - 7 Rectangular Window (1024 μ sec) Windowed Time Record, Frequency Diagram and Phase vs Frequency: Beam (21" x 6" x 6"), XL-XR1-XR2 (14 - 11 - 8), Analytical Data.

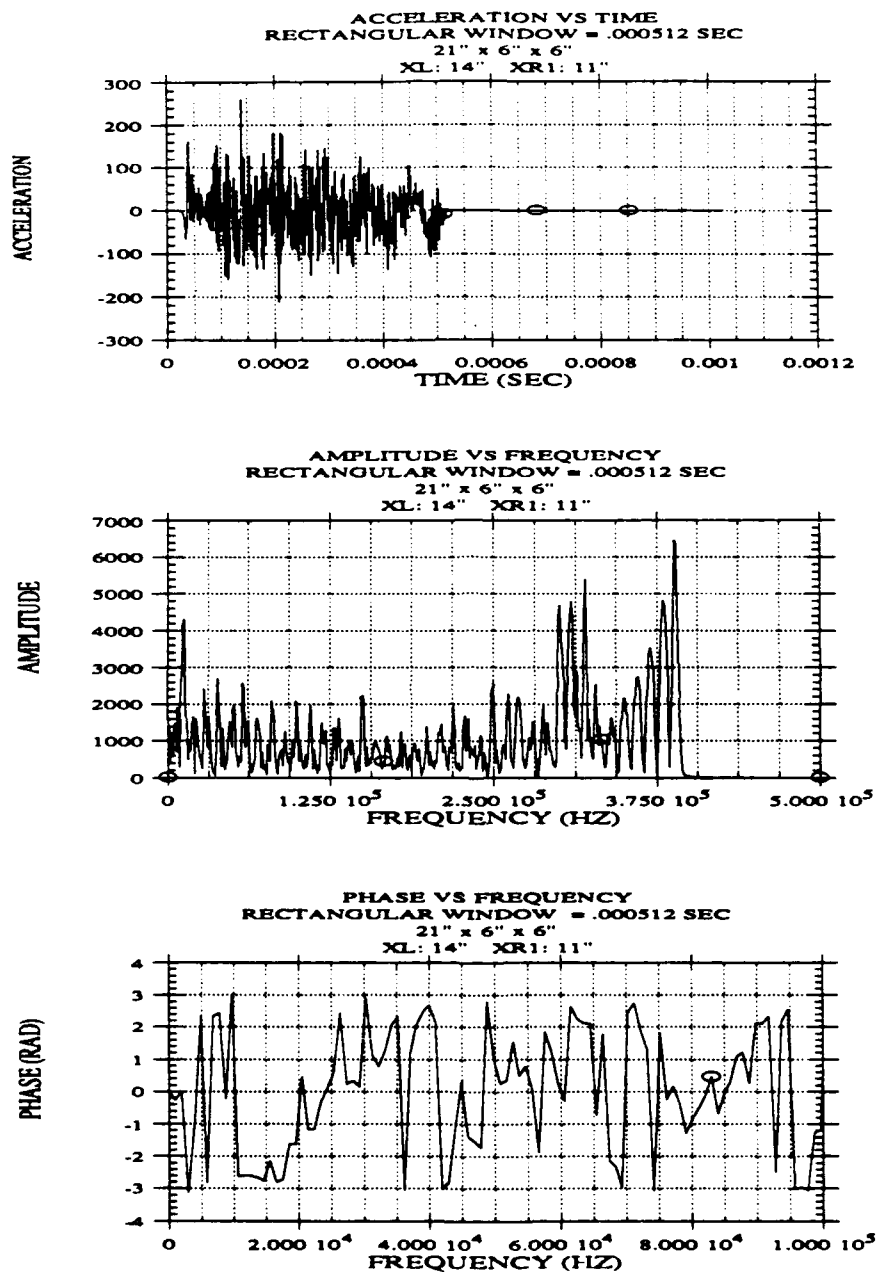


Figure 2.5 - 8 Rectangular Window (512 μ sec) Windowed Time Record, Frequency Diagram and Phase vs Frequency: Beam (21" x 6" x 6"), XL-XR1-XR2 (14 - 11 - 8), Analytical Data.

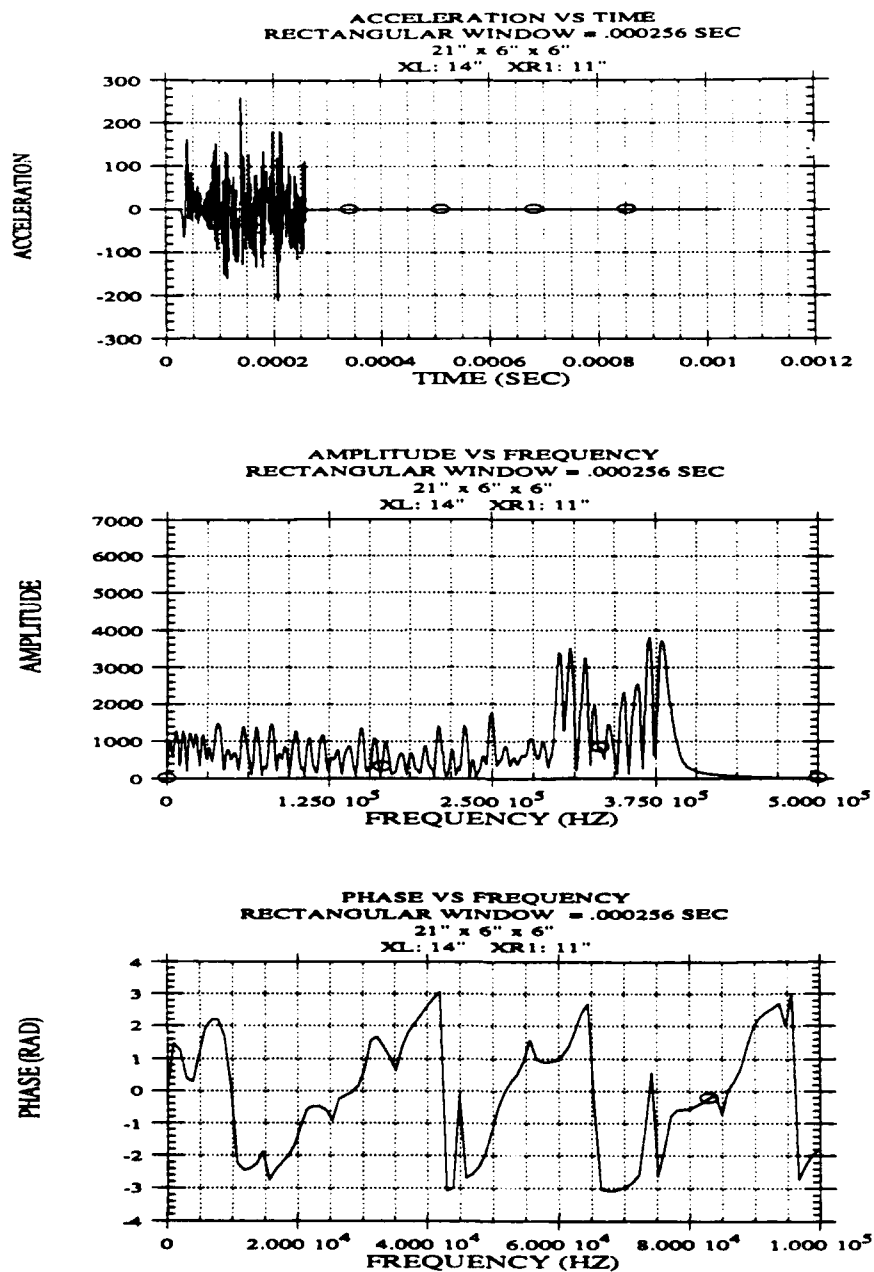


Figure 2.5 - 9 Rectangular Window (256 μ sec) Windowed Time Record, Frequency Diagram and Phase vs Frequency: Beam (21" x 6" x 6"), XL-XR1-XR2 (14 - 11 - 8), Analytical Data.

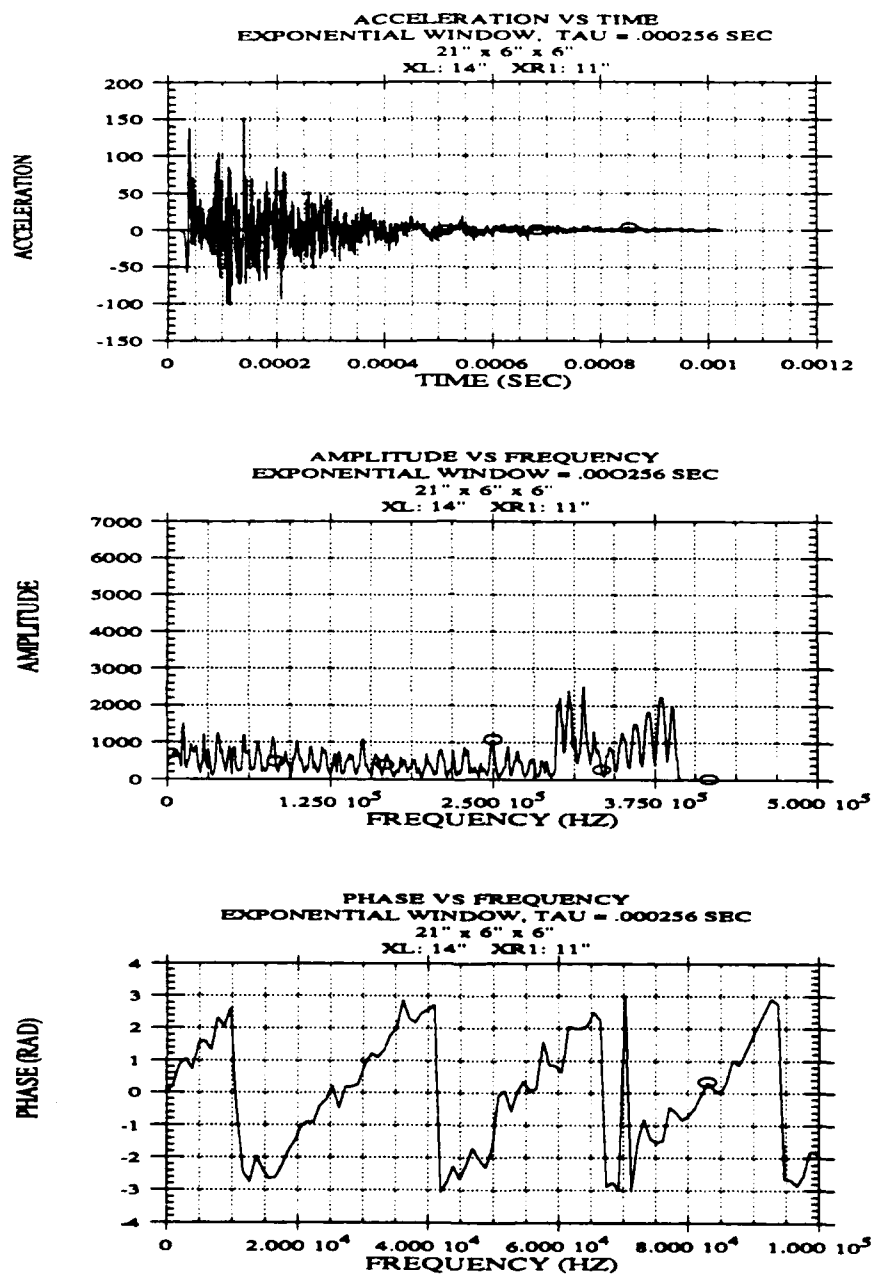


Figure 2.5 - 10 Exponential Window (256 μ sec) Windowed Time Record, Frequency Diagram and Phase vs Frequency: Beam (21" x 6" x 6"), XL-XR1-XR2 (14 - 11 - 8), Analytical Data.

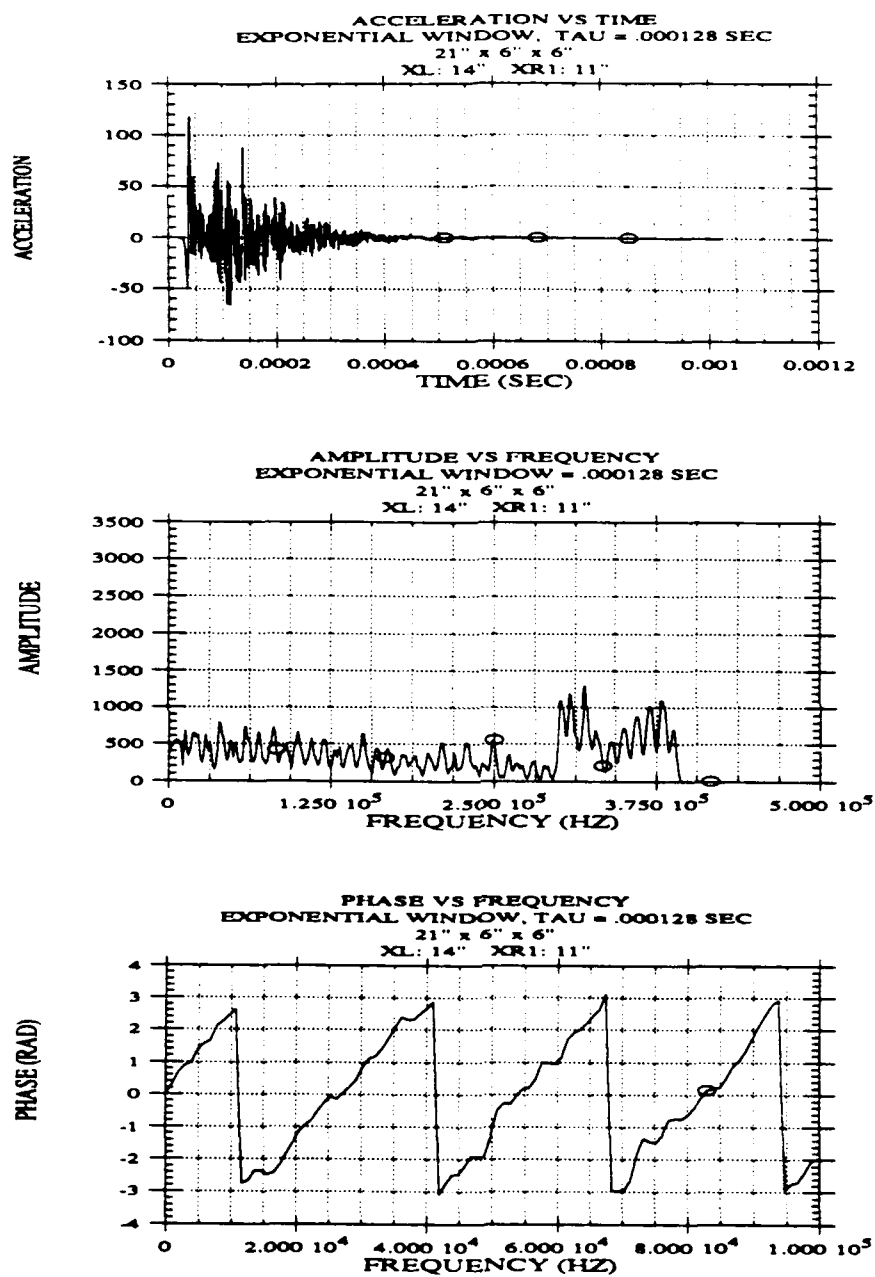


Figure 2.5 - 11 Exponential Window (128 μ sec) Windowed Time Record, Frequency Diagram and Phase vs Frequency: Beam (21" x 6" x 6"), XL-XR1-XR2 (14 - 11 - 8), Analytical Data.

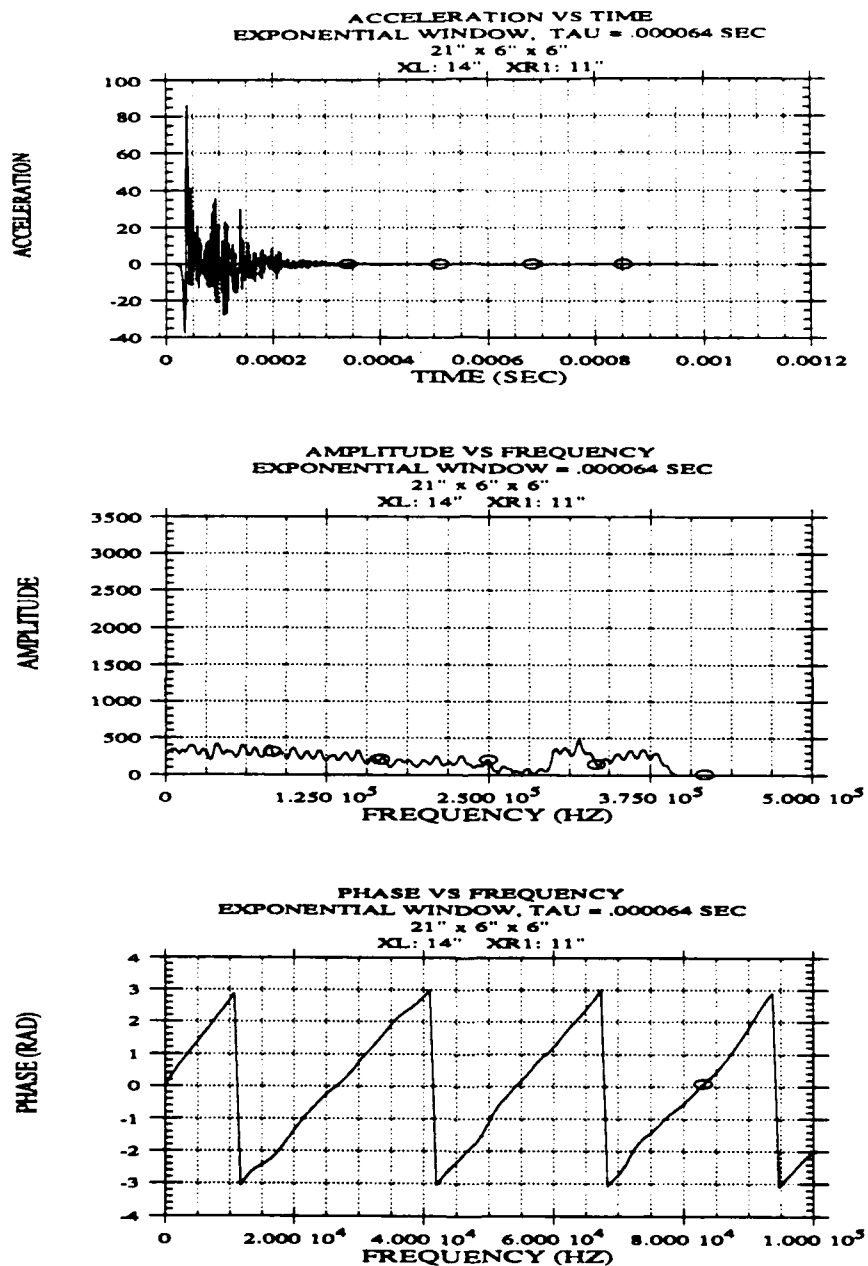


Figure 2.5 - 12 Exponential Window (64 μ sec) Windowed Time Record, Frequency Diagram and Phase vs Frequency: Beam (21" x 6" x 6"), XL-XR1-XR2 (14 - 11 - 8), Analytical Data.

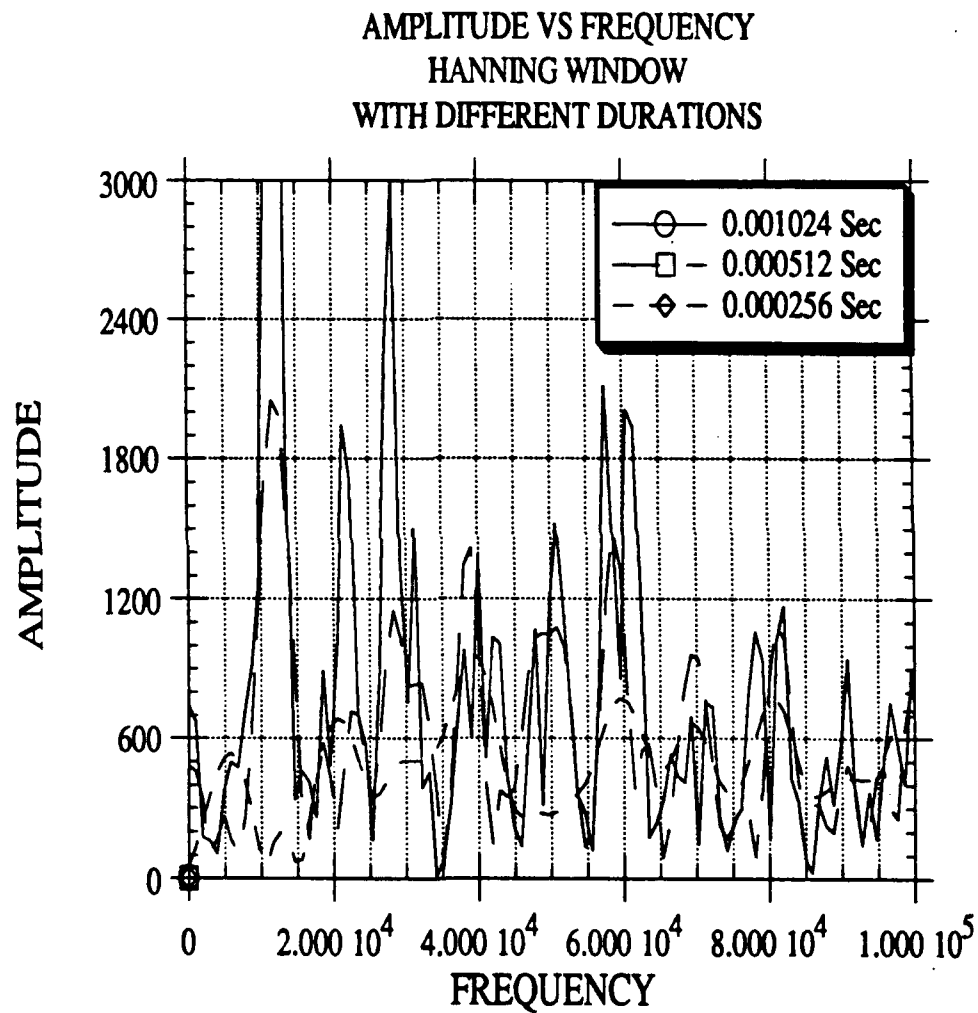


Figure 2.5 - 13 Frequency Diagram: Comparison of Three Different Time Duration Using a Hanning Window, Beam (21" x 6" x 6"), XL-XR1-XR2 (14 - 11 - 8), Experimental Data, Instrumented Hammer.

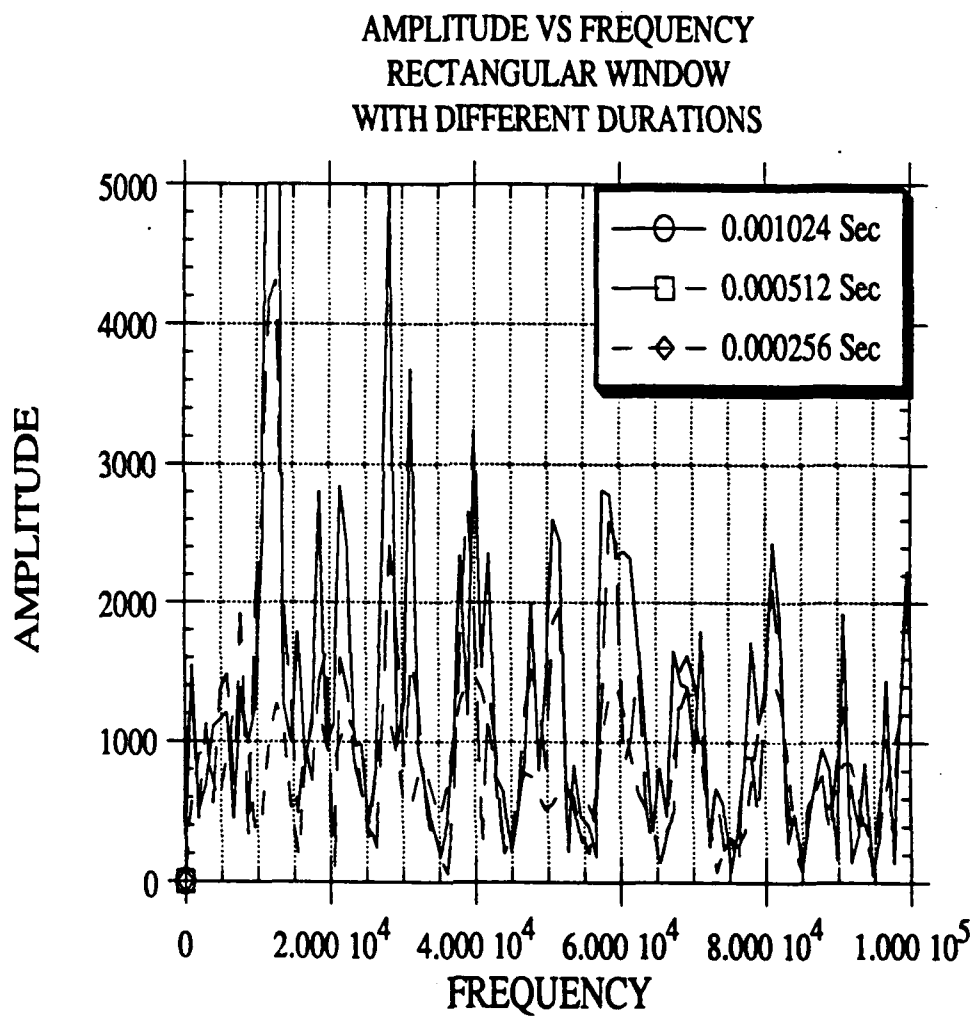


Figure 2.5 - 14 Frequency Diagram: Comparison of Three Different Time Duration Using a Rectangular Window, Beam (21" x 6" x 6"), XL-XR1-XR2 (14 - 11 - 8), Experimental Data, Instrumented Hammer.

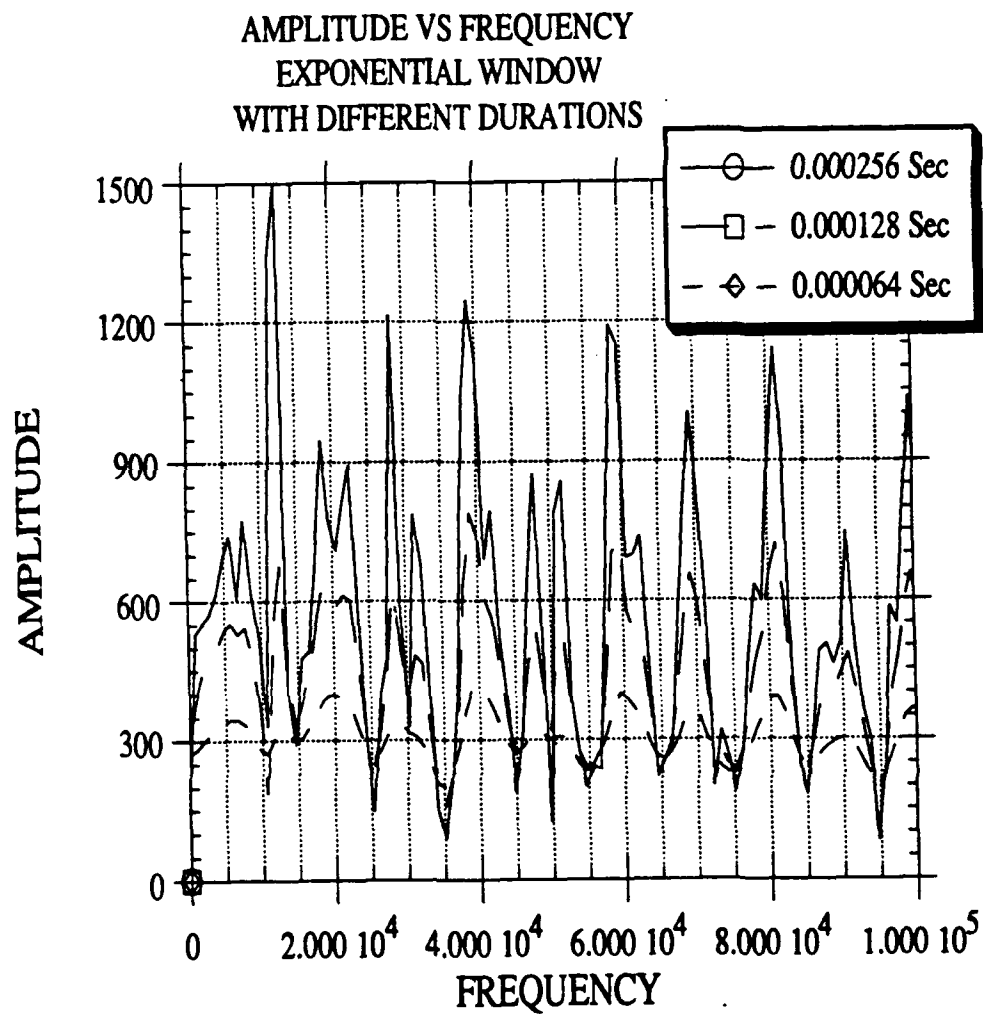


Figure 2.5 - 15 Frequency Diagram: Comparison of Three Different Time Duration Using a Exponential Window, Beam (21" x 6" x 6"), XL-XR1-XR2 (14 - 11 - 8), Experimental Data, Instrumented Hammer.

2.6 RECOMMENDATION ON WINDOW LENGTH

The primary window used in this dissertation was an exponential window, with $\tau = 80$ to 150 micro seconds. Two criteria were used in selecting, τ . The first was the smoothness of the cross power phase diagram. The second criterion was a monotonically increasing/decreasing phase diagram for linear spectra of each record. The cross power spectrum phase diagram is very erratic when using a long τ , and this makes it hard to determine the proper 2π phase shifts. If a very short τ is used, the linear spectrum phase diagram will not be monotonically increasing/decreasing at the higher frequencies. When this happens, the phase no longer monotonically increases, but essentially has a constant value over the range of frequencies in which there is no energy. Figure 2.6 - 1 shows the linear spectrum phase diagram and the cross power phase diagram when proper windows are used. Notice also that the cross power spectrum is equal to the difference between the linear spectra. Figure 2.6 - 2 gives an example where τ is too short. In this case, linear spectrum one is properly windowed but linear spectrum two is not and the record starts to fall apart at about 25000 Hz. The cross power spectrum in this figure is an average of five measurements with improper windowing.

Hence, the recommended window length for each record should be just long enough to insure sufficient energy in the linear spectrum over the entire frequency range. This, in turn, will also insure the smoothest possible cross power spectrum phase diagram.

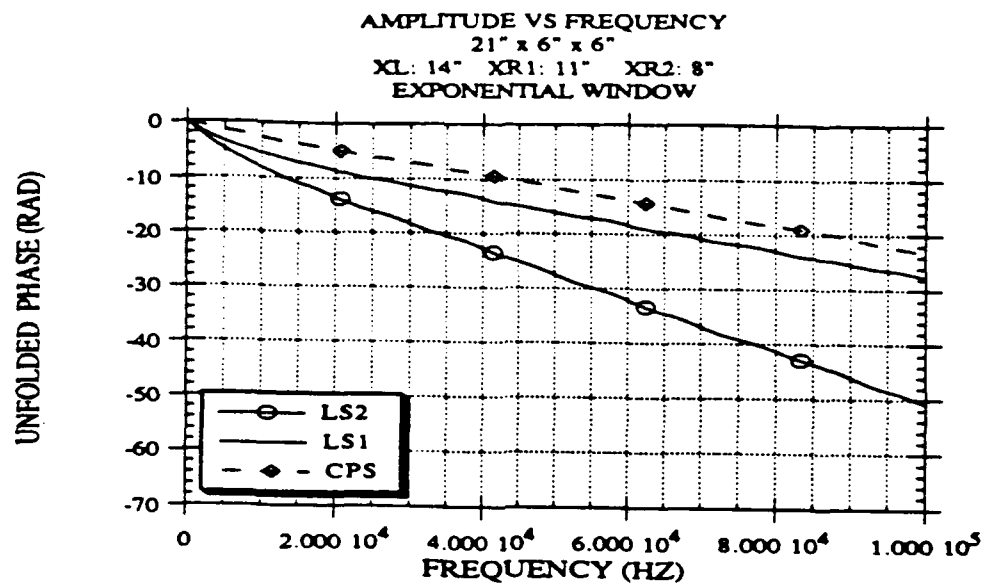


Figure 2.6 - 1 Linear Spectra Phase and Cross Power Spectrum Phase with a Proper Exponential Window Duration. Beam (21" x 6" x 6"), XL-XR1-XR2 (14 - 11 - 8), Experimental Data, Instrumented Hammer.

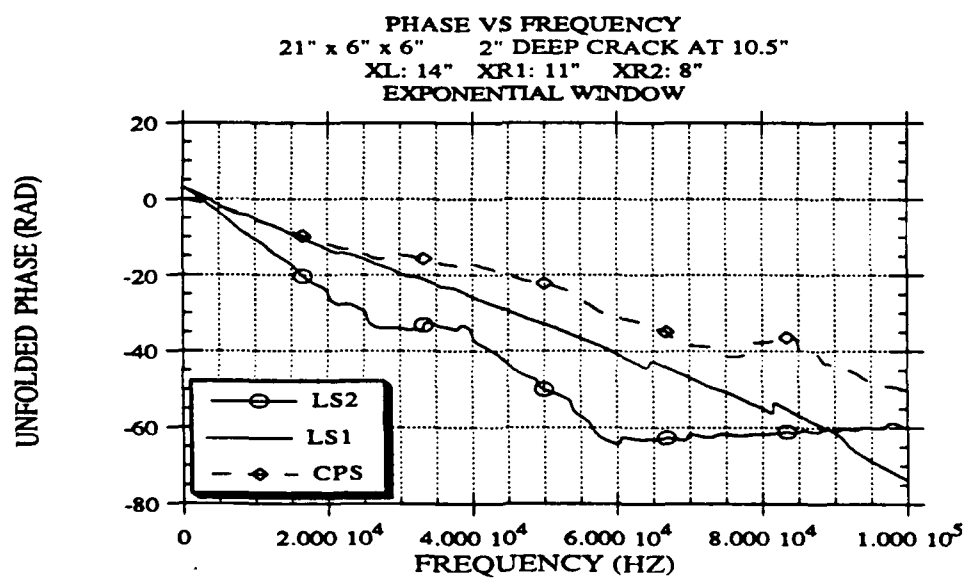


Figure 2.6 - 2 Linear Spectra Phase and Cross Power Spectrum Phase with Too Short of a Exponential Window Duration. Beam (21" x 6" x 6"), XL-XR1-XR2 (14 - 11 - 8), Experimental Data, Instrumented Hammer.

2.7 PARAMETERS INVOLVED

The operator's objective is to set up the equipment and process the data in a manner which will enhance the detection of damage. As such, the operator must know how the different variables affect the measurement.

For any testing situation, the geometric and material properties are those insitu. The test operator has control over the load location and duration, the type of receivers (acceleration, velocity, or displacement transducers), receiver spacing, and location with respect to other surfaces. The operator also controls the data processing which includes the frequency range of interest, the type and length of the windows used, and the number of repetitions per measurement. Finally the operator controls the interpretation of the data. The effect of each parameter on the dispersion curve is investigated in the following sections.

The dispersion curve is often defined as the Velocity vs. Wavelength, but throughout this report, Velocity vs Frequency will be used.

CHAPTER THREE

ANALYTICAL FORMULATION

To use the SASW technique two simultaneous time records are necessary. In this study time response records were generated analytically and experimentally. The analytical techniques used include a modal analysis of a conventional one dimensional beam model, a two dimensional finite element model and a two dimensional plane stress analysis of surface waves in a homogeneous plate of finite thickness. The modal analysis solution is discussed first and the results obtained applying the SASW technique to the computed records are compared with the theoretical dispersion curve for flexural waves. The finite element formulation is presented next. The effect of mesh size, boundary conditions and position of source and receivers is investigated. The results are then compared to those of the plane surface wave solution.

3.1 MODAL ANALYSIS OF A SIMPLY SUPPORTED BEAM

Modal analysis of a simply supported beam was used first to assess the validity of a one dimensional model and the difference between flexural and surface waves. a review of the equations of motion and their solution for steady state condition (forced vibration) as well as for a transient (including the free vibration terms) is presented. Finally a comparison is made of an SASW derived dispersion curve compared to the theoretical dispersion curve for flexural waves in a simply supported beam using beam theory.

3.1.1 EQUATION OF MOTION

The equation of motion for a beam is:

$$EI \frac{\partial^4 y}{\partial x^4} + \bar{M} \frac{\partial^2 y}{\partial t^2} = p(x,t)$$

where:

E: elastic modulus

I: area moment of Inertia

\bar{M} : mass per unit length

$p(x,t) = \delta(x_1) \sin\left(\frac{\pi t}{TD}\right)$ for $0 < t < TD$

x_1 : load location

TD: load duration

3.1.2 SOLUTION

To solve for $y(x,t)$, the forced vibration problem must be solved. This gives the solution up to $t=TD$. After $t=TD$, the free vibration problem must be solved. The initial conditions for the free vibration problem are the displacement and velocity at $t=TD$ from the forced vibration problem.

In general, the free vibration solution is:

$$y(x,t) = \sum_{n=1}^{\infty} \sin\left(\frac{n\pi x}{L}\right) [(C_1)_n \cos \omega_n t + (C_2)_n \sin \omega_n t]$$

Given $y(x,0) = \rho(x)$ and $\dot{y}(x,0) = \Psi(x)$

$$(C_1)_n = \frac{2}{L} \int_0^L \rho(x) \sin\left(\frac{n\pi x}{L}\right) dx$$

$$(C_2)_n = \frac{2}{\omega_n L} \int_0^L \Psi(x) \sin\left(\frac{n\pi x}{L}\right) dx$$

$$\omega_n = (n\pi)^2 \sqrt{\frac{EI}{\bar{M} L^4}}$$

3.1.3 SOLUTION OF FORCED VIBRATION PROBLEM

For the forced vibration problem, where $t < TD$:

$$Y(x,t) = \sum_{n=1}^{\infty} \sin\left(\frac{n\pi x}{L}\right) K_n \left[\sin \Omega t + \frac{\Omega}{\omega_n} \sin \omega_n t \right]$$

$$\dot{Y}(x,t) = \sum_{n=1}^{\infty} \sin\left(\frac{n\pi x}{L}\right) K_n \left[\Omega \cos \Omega t - \Omega \cos \omega_n t \right]$$

$$\ddot{Y}(x,t) = \sum_{n=1}^{\infty} \sin\left(\frac{n\pi x}{L}\right) K_n \left[-\Omega^2 \sin \Omega t + \Omega \omega_n \sin \omega_n t \right]$$

where

$$K_n = \left[\frac{\sin\left(\frac{n\pi x_1}{L}\right) \frac{2}{\bar{M} L}}{(\omega_n^2 - \Omega^2)} \right]$$

$$\Omega = \frac{\pi}{TD} \quad \omega_n = (n\pi)^2 \sqrt{\frac{EI}{\bar{M} L^4}}$$

3.1.4 SOLUTION OF FREE VIBRATION AFTER LOAD ENDS

For the free vibration problem after the impulse, $t > TD$:

$$Y(x,t) = \sum_{n=1}^{\infty} \sin\left(\frac{n\pi x}{L}\right) [(C_1)_n \cos \omega_n t_1 + (C_2)_n \sin \omega_n t_1]$$

$$\dot{Y}(x,t) = \sum_{n=1}^{\infty} \sin\left(\frac{n\pi x}{L}\right) [-\omega_n (C_1)_n \sin \omega_n t_1 + \omega_n (C_2)_n \cos \omega_n t_1]$$

$$\ddot{Y}(x,t) = \sum_{n=1}^{\infty} \sin\left(\frac{n\pi x}{L}\right) [-\omega_n^2 (C_1)_n \cos \omega_n t_1 - \omega_n^2 (C_2)_n \sin \omega_n t_1]$$

where

$$(C_1)_n = K_n \left(-\frac{\Omega}{\omega_n} \sin(\omega_n TD) \right)$$

$$(C_2)_n = -\frac{\Omega}{\omega_n} K_n [1 + \cos(\omega_n TD)]$$

$$K_n = \left[\frac{\sin\left(\frac{n\pi x_1}{L}\right) \frac{2}{\bar{M} L}}{(\omega_n^2 - \Omega^2)} \right]$$

$$\Omega = \frac{\pi}{TD} \quad \omega_n = (n\pi)^2 \sqrt{\frac{EI}{\bar{M} L^4}}$$

TD = Load duration

$t_1 = t - TD$

x_1 : Load location

3.1.5 COMPARISON OF SASW WITH THEORETICAL DISPERSION CURVE FOR FLEXURAL WAVES IN A SIMPLE SUPPORTED BEAM.

A comparison was made between the dispersion curve determined from the SASW method with the time records generated using modal analysis of beam theory and the theoretical dispersion curve for flexural waves in a simply supported beam. This allows the verification of the SASW method. Verification of the process shows that it works, inspires confidence, and provides the ability to evaluate the limitations of the process.

The theoretical dispersion curve is given by (Meirovich,pg355)

$$\text{Velocity} = \frac{2\pi}{\lambda} \sqrt{\frac{EI}{M}} \quad (3.1.5 - 1)$$

substituting

$$\text{Velocity} = \lambda * \text{frequency}$$

and rearranging, velocity as function of frequency is,

$$\text{Velocity} = \sqrt{2\pi f} \sqrt{\frac{EI}{M}}$$

For this example, a twenty foot , simply supported beam was used, as shown in Figure 3.1.5 - 1. A half pulse of a sine function was used for loading purposes. The time duration (TD) was 50 micro seconds. One hundred and fifty modes were used in the calculation. The time step was 1 micro second and 1024 points were calculated, resulting in a FFT resolution of 976.6 Hz. Three different spacings were used to calculate a dispersion curve and compared to the theoretical dispersion curve (Figure 3.1.5 - 5). For a one foot spacing, the beam was loaded at $x=10'$ and the receivers were at $x=11'$ and $x=12'$. The response at $x=11'$ and $x=12'$ is

given in Figure 3.1.5 - 2. For a two foot spacing, the beam was loaded at $x=10'$ and the receivers were at $x=12'$ and $x=14'$. The response at $x=12'$ and $x=14'$ is given in Figure 3.1.5 - 3. For a three foot spacing, the beam was loaded at $x=10'$ and the receivers were at $x=13'$ and $x=16'$. The response at $x=13'$ and $x=16'$ is given in Figure 3.1.5 - 4. After processing the time records, the dispersion curves were calculated and compared to the theoretical dispersion curve. The comparison is shown in Figure 3.1.5 - 5.

As can be seen, there is very good agreement between the theoretical dispersion curve and the dispersion curve determined from modal data using the SASW method.

For the first four frequencies in the FFT, Table 3.1.5 -1 gives a wavelength comparison between theory and SASW. It shows the range of error for this example. The greatest errors are at the lowest frequencies, and the error decreases as the frequency increases. It should also be noticed that the agreement is perfect for a 3' spacing and deteriorates as the spacing becomes smaller. This is true up to approximately 50 kHz at which point the SASW dispersion curve shows minor fluctuations about the theoretical curve.

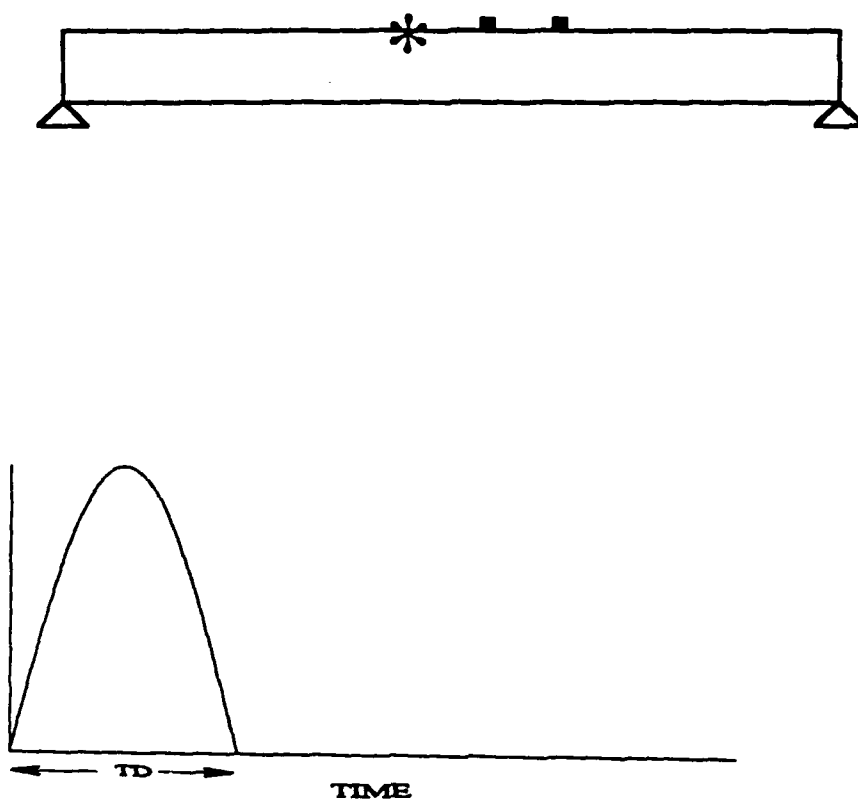


Figure 3.1.5 - 1 Configuration and Load Pulse

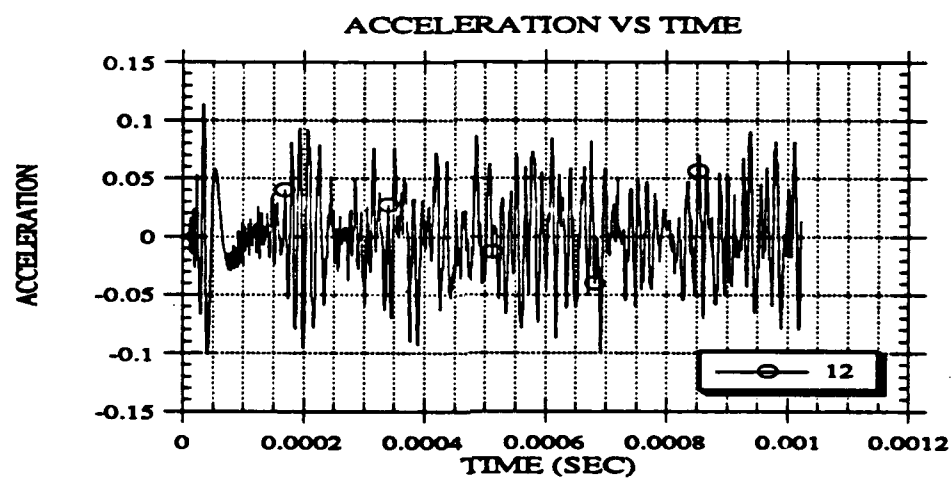
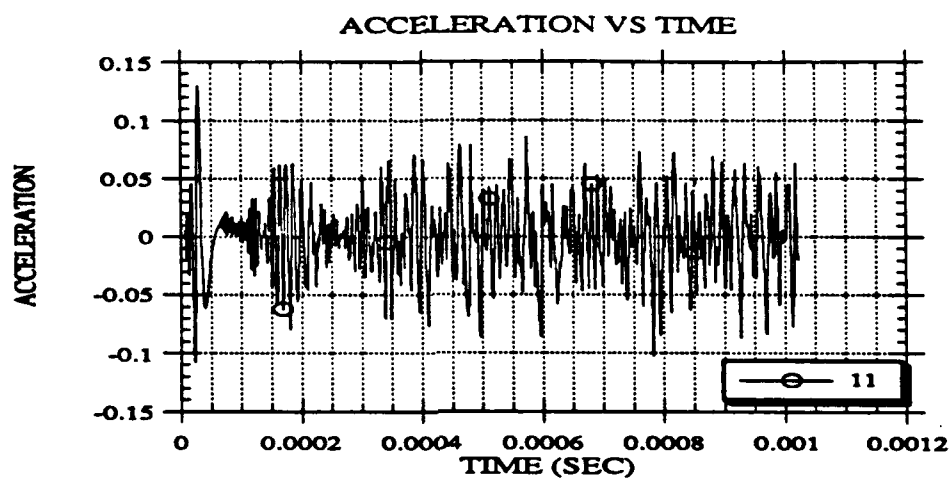


Figure 3.1.5 - 2 Time Records: 11' and 12'

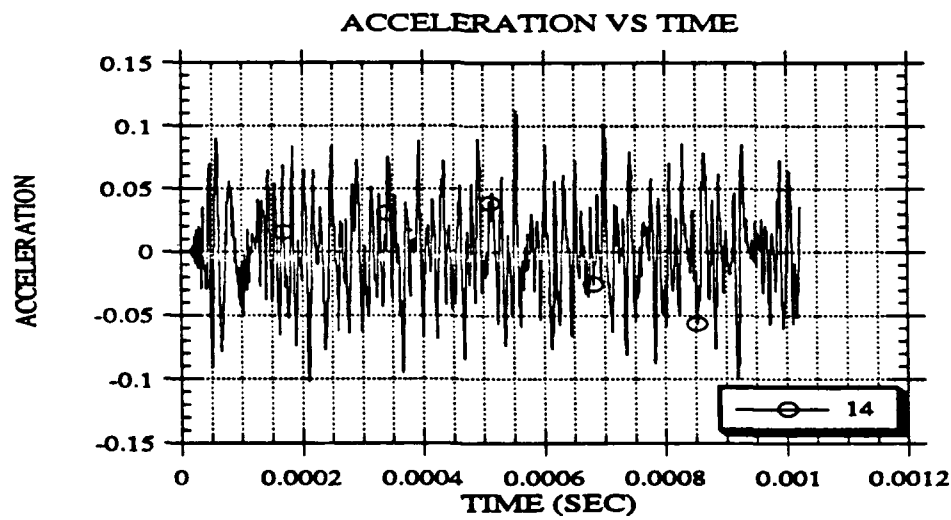
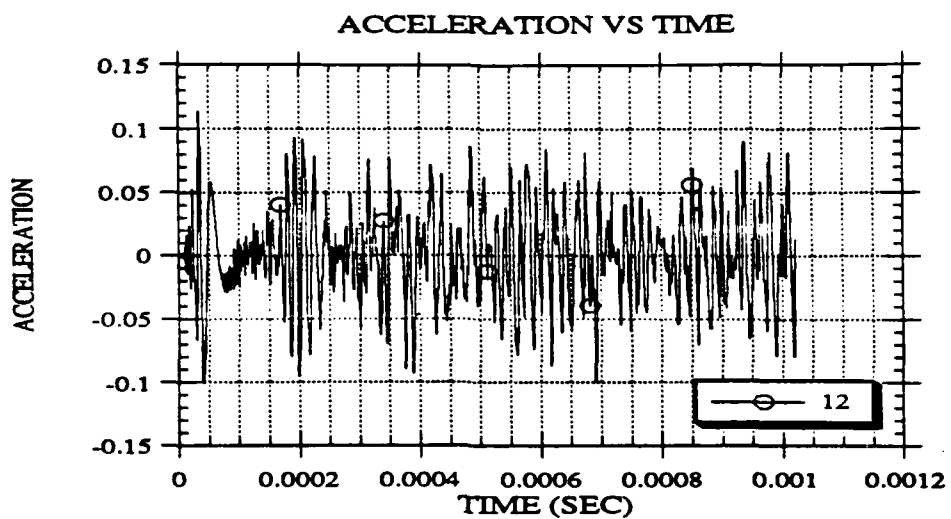


Figure 3.1.5 - 3 Time Records: 12' and 14'

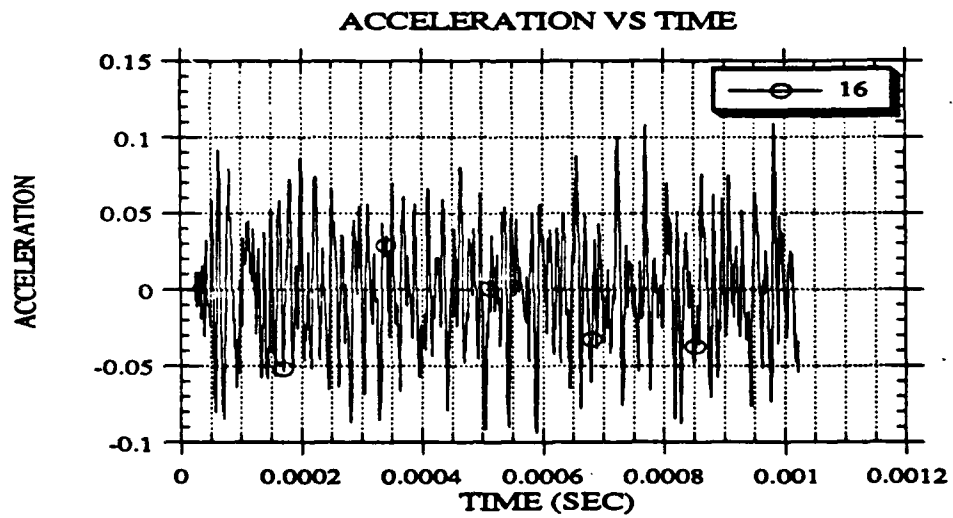
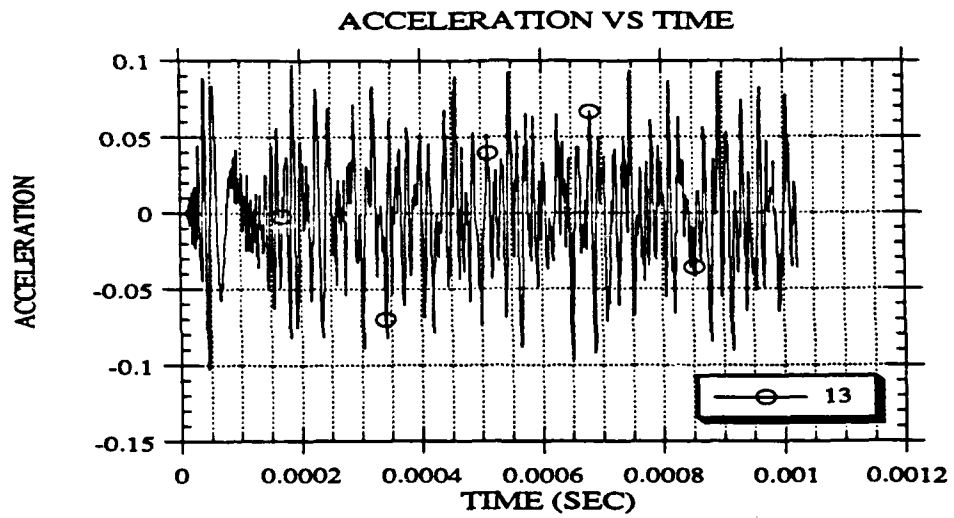


Figure 3.1.5 - 4 Time Records: 13' and 16'

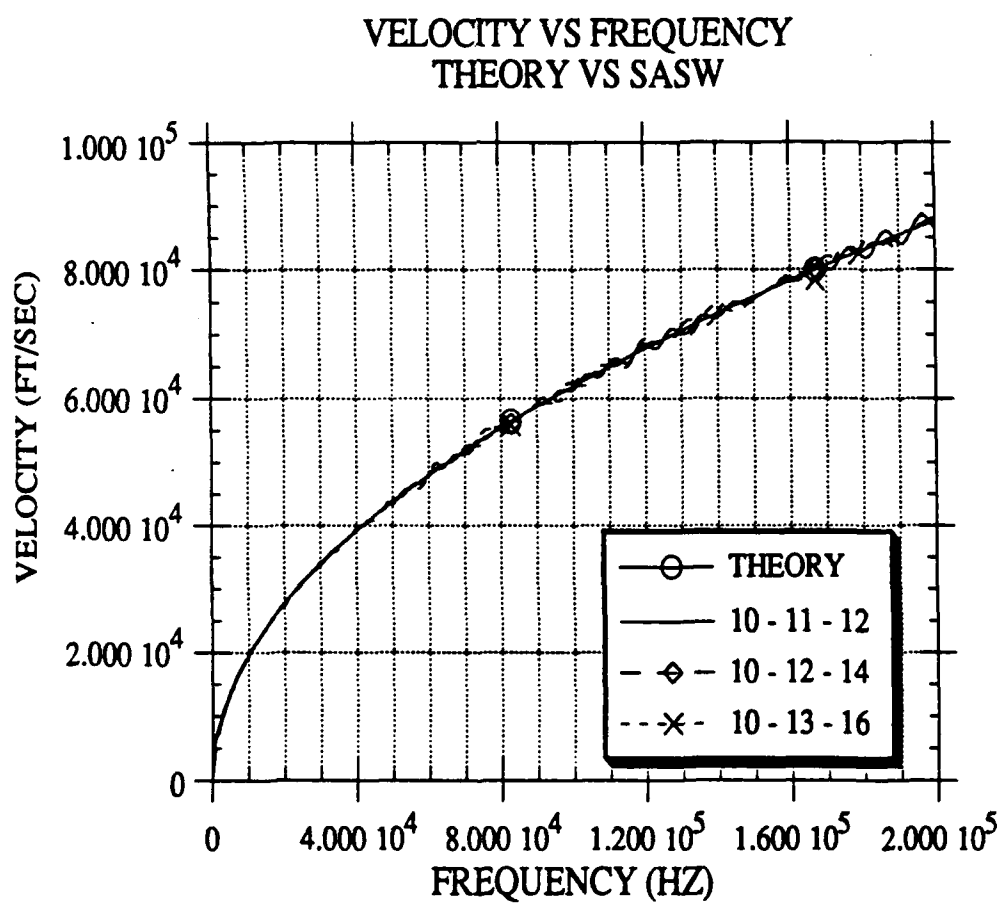


Figure 3.1.5 - 5 Dispersion Curve: Theory vs SASW for Modal Analysis Data

Table 3.1.5 -1 Wavelength Comparison between Theoretical and SASW data

FREQ	1'		2'		3'		Theory
(HZ)	λ	$\frac{\text{SASW}}{\text{Theory}}$	λ	$\frac{\text{SASW}}{\text{Theory}}$	λ	$\frac{\text{SASW}}{\text{Theory}}$	λ
977	6.95	1.53	4.39	0.96	4.55	1.0	4.55
1953	4.39	1.09	3.85	0.95	4.04	1.0	4.04
2929	3.5	1.01	3.33	0.96	3.46	1.0	3.46
3096	3.01	0.997	2.96	0.98	3.02	1.0	3.02

As can be seen by these comparisons, the SASW method is a viable method for calculating the dispersion curve from response records. It also shows the dispersion curve determined using modal analysis data is the dispersion curve of the flexural waves in the beam and not the surface waves.

3.2 FINITE ELEMENT MODEL

The finite element method was also used to model the beam in two dimensions and to evaluate the effectiveness of the method to get a surface wave dispersion curve. To solve wave propagation and dynamics problems, one approach is to discretize in time and in space. Newmark's β method was used to discretize in time, and the finite element method was used to discretize in space. A two dimensional finite element program was written. It used eight noded quadratic rectangular elements, plane stress constitutive equations, the constant average acceleration method of step by step integration, and a consistent mass matrix.

Background on the finite element method is given and a discussion of the importance of the mesh size is also presented.

3.2.1 NEWMARK BETA TIME ITERATION

Newmark's β method is a time step iteration technique to solve dynamic and wave propagation problems, where the next time step is based on current displacement, velocity and acceleration data. Given the equilibrium equation:

$$M \ddot{U}_{n+1} + K U_{n+1} = F_{n+1} \quad (3.2.1 - 1)$$

and

$$\dot{U}_{n+1} = \dot{U}_n + [(1-\alpha) \ddot{U}_n + \alpha \ddot{U}_{n+1}] \Delta t \quad (3.2.1 - 2)$$

$$U_{n+1} = U_n + \dot{U}_n \Delta t + \left[\left(\frac{1}{2} - \beta \right) \ddot{U}_n + \beta \ddot{U}_{n+1} \right] \Delta t^2 \quad (3.2.1 - 3)$$

where

M: Mass Matrix

K: Stiffness Matrix

F: Force Vector

U_n : Displacement Vector at time "n"

\dot{U}_n : Velocity Vector at time "n"

\ddot{U}_n : Acceleration Vector at time "n"

Solving (3.2.1 - 3) for \ddot{U}_{n+1} , gives:

$$\ddot{U}_{n+1} = \frac{1}{\beta \Delta t^2} \left[U_{n+1} - U_n - \dot{U}_n \Delta t - \left(\frac{1}{2} - \beta \right) \ddot{U}_n \right] \quad (3.2.1 - 4)$$

(3.2.1 - 4) into (3.2.1 - 1) leads to

$$M \left[\frac{1}{\beta \Delta t^2} \left(U_{n+1} - U_n - \dot{U}_n \Delta t - \left(\frac{1}{2} - \beta \right) \Delta t^2 \ddot{U}_n \right) \right] + K U_{n+1} = F_{n+1} \quad (3.2.1 - 5)$$

Solving (3.2.1 - 5) for U_{n+1} , leads to (3.2.1 - 6) a system of equations where the only unknowns are U_{n+1} :

$$\begin{aligned} \left[K + \frac{1}{\beta \Delta t^2} M \right] U_{n+1} \\ = F_{n+1} + M \left[\frac{1}{\beta \Delta t^2} \left(U_n + \dot{U}_n \Delta t + \left(\frac{1}{2} - \beta \right) \Delta t^2 \ddot{U}_n \right) \right] \end{aligned} \quad (3.2.1 - 6)$$

The system of equations (3.2.1 - 6) is solved using Gauss Elimination. After solving for U_{n+1} , (3.2.1 - 7) and (3.2.1 - 8) are used to solve for \ddot{U}_{n+1} , \dot{U}_{n+1}

$$\ddot{U}_{n+1} = \frac{1}{\beta \Delta t^2} \left[U_{n+1} - U_n - \dot{U}_n \Delta t - \left(\frac{1}{2} - \beta \right) \ddot{U}_n \right] \quad (3.2.1 - 7)$$

$$\dot{U}_{n+1} = \dot{U}_n + \left[(1-\alpha) \ddot{U}_n + \alpha \ddot{U}_{n+1} \right] \Delta t \quad (3.2.1 - 8)$$

For the next time step, equations (3.2.1 - 6) through (3.2.1 - 8) are repeated.

A number of different methods are included in the Newmark β technique. For instance:

Constant Average Acceleration : $\alpha=\frac{1}{2}$ $\beta=\frac{1}{4}$: Unconditionally Stable

Linear Average Acceleration : $\alpha=\frac{1}{2}$ $\beta=\frac{1}{6}$: Conditionally Stable

The constant average acceleration method is unconditionally stable numerically, while the linear average acceleration is conditionally stable. The stability condition for the linear average acceleration requires that the time step, Δt , be less than the period of the highest frequency divided by π . ($\Delta t < \frac{T_{\text{highest frequency}}}{\pi}$)

3.2.2 STIFFNESS MATRIX

Using the energy expression for the strain energy:

$$\int_{\text{vol}} \epsilon^T \sigma \, d\text{vol}$$

and substituting

$$\sigma = D \epsilon$$

$$\epsilon = B U$$

$$\epsilon^T = U^T B^T$$

results in

$$\text{Strain energy} = \frac{1}{2} U^T \left[\int_{\text{vol}} B^T D B \, d\text{vol} \right] U$$

where the stiffness matrix is

$$K = \int_{\text{vol}} B^T D B \, d\text{vol}$$

and U,B,D are defined below and f_i is a shape function defined in section 3.2.6

$$U = \begin{bmatrix} u_1 \\ v_1 \\ u_1 \\ v_1 \\ \dots \\ \dots \\ \dots \\ u_n \\ v_n \end{bmatrix}$$

$$B = \begin{bmatrix} \frac{\partial}{\partial x} & 0 \\ 0 & \frac{\partial}{\partial y} \\ \frac{\partial}{\partial y} & \frac{\partial}{\partial x} \end{bmatrix} \begin{bmatrix} f_1 & 0 & f_2 & 0 & f_3 & 0 & f_4 & 0 & f_5 & 0 & f_6 & 0 & f_7 & 0 & f_8 & 0 \\ 0 & f_1 & 0 & f_2 & 0 & f_3 & 0 & f_4 & 0 & f_5 & 0 & f_6 & 0 & f_7 & 0 & f_8 \end{bmatrix}$$

$$D = \begin{bmatrix} \frac{E}{(1-\nu^2)} & \frac{\nu E}{(1-\nu^2)} & 0 \\ \frac{\nu E}{(1-\nu^2)} & \frac{E}{(1-\nu^2)} & 0 \\ 0 & 0 & \frac{E}{2(1+\nu)} \end{bmatrix}$$

Given a uniform thickness, the volume integral can be changed to an area integral resulting in

$$K = \text{thickness} \int \int B^T D B \, dx \, dy = \text{thickness} \int_{\text{area}} B^T D B \, dA$$

To make integration easier, a coordinate transformation is performed to transform the area of the finite element to a unit square, resulting in:

$$K = \text{thickness} \int_{-1}^1 \int_{-1}^1 B^T D B |J| d\xi d\eta$$

where $|J|$ is the Jacobian discussed in section 3.2.5. The integration is done numerically using Gaussian integration which leads to:

$$K = \text{thickness} \sum_{l=1}^3 \sum_{m=1}^3 [B^T D B |J|] \xi_l \eta_m$$

3.2.3 MASS MATRIX

Using the expression for the kinetic energy to calculate the mass matrix, results in

$$\text{Kinetic energy} = \frac{1}{2} \dot{U}^T \left[\int_{\text{vol}} N^T \rho N d\text{vol} \right] \dot{U}$$

where the mass matrix is

$$M = \left[\int_{\text{vol}} N^T \rho N d\text{vol} \right]$$

and N is defined below, ρ is mass density, and f_i is a shape function defined in section 3.2.6.

$$N = \begin{bmatrix} f_1 & 0 & f_2 & 0 & f_3 & 0 & f_4 & 0 & f_5 & 0 & f_6 & 0 & f_7 & 0 & f_8 & 0 \\ 0 & f_1 & 0 & f_2 & 0 & f_3 & 0 & f_4 & 0 & f_5 & 0 & f_6 & 0 & f_7 & 0 & f_8 \end{bmatrix}$$

Given a uniform thickness, the volume integral can be changed to an area integral resulting in

$$M = \text{thickness} \int \int N^T \rho N \, dx \, dy = \text{thickness} \int_{\text{area}} N^T \rho N \, dA$$

To make integration easier, a coordinate transformation is performed as before resulting in:

$$M = \text{thickness} \int_{-1}^1 \int_{-1}^1 N^T \rho N |J| \, d\xi \, d\eta$$

using Gaussian Integration leads to:

$$M = \text{thickness} \sum_{l=1}^3 \sum_{m=1}^3 [N^T \rho N |J|] \xi_l \eta_m$$

3.2.4 JACOBIAN

The Jacobian is used in the coordinate transformation. The shape functions are written in terms of the natural coordinates and not the actual x and y coordinates. For a given element the displacements are approximated by

$$U = \sum_{i=1}^8 u_i f_i \quad \text{and} \quad V = \sum_{i=1}^8 v_i f_i$$

The derivatives of displacement with respect to x and y are

$$\frac{\partial U}{\partial x} = \sum_{i=1}^8 u_i f_{i,x}$$

$$\frac{\partial V}{\partial x} = \sum_{i=1}^8 v_i f_{i,x}$$

$$\frac{\partial U}{\partial y} = \sum_{i=1}^8 u_i f_{i,y}$$

$$\frac{\partial V}{\partial y} = \sum_{i=1}^8 v_i f_{i,y}$$

Given:

$$\begin{bmatrix} \frac{\partial f_i}{\partial \xi} \\ \frac{\partial f_i}{\partial \eta} \end{bmatrix} = \begin{bmatrix} \frac{\partial x}{\partial \xi} & \frac{\partial y}{\partial \xi} \\ \frac{\partial x}{\partial \eta} & \frac{\partial y}{\partial \eta} \end{bmatrix} \begin{bmatrix} \frac{\partial f_i}{\partial x} \\ \frac{\partial f_i}{\partial y} \end{bmatrix}$$

and letting

$$J_{11} = \sum_{i=1}^8 x_i f_{i,\xi}$$

$$J_{12} = \sum_{i=1}^8 y_i f_{i,\xi}$$

$$J_{21} = \sum_{i=1}^8 x_i f_{i,\eta}$$

$$J_{22} = \sum_{i=1}^8 y_i f_{i,\eta}$$

the determinant of the matrix becomes

$$|J| = J_{11} J_{22} - J_{12} J_{21}$$

inverting the matrix and solving for $f_{i,x}$ and $f_{i,y}$ leads to:

$$\begin{bmatrix} \frac{\partial f_i}{\partial x} \\ \frac{\partial f_i}{\partial y} \end{bmatrix} = \frac{1}{|J|} \begin{bmatrix} J_{22} & -J_{12} \\ -J_{21} & J_{11} \end{bmatrix} \begin{bmatrix} \frac{\partial f_i}{\partial \xi} \\ \frac{\partial f_i}{\partial \eta} \end{bmatrix} \quad (3.2.5 - 1)$$

Therefore, $f_{i,x}$ and $f_{i,y}$ can be obtained since the right hand side is defined.

3.2.5 SHAPE FUNCTIONS

The shape function are defined below in terms of the natural coordinates.

$$f_1 = \frac{1}{4} (1-\xi) (1-\eta) (-1-\xi-\eta)$$

$$f_2 = \frac{1}{4} (1+\xi) (1-\eta) (-1+\xi-\eta)$$

$$f_3 = \frac{1}{4} (1+\xi) (1+\eta) (-1+\xi+\eta)$$

$$f_4 = \frac{1}{4} (1-\xi) (1+\eta) (-1-\xi+\eta)$$

$$f_5 = \frac{1}{2} (1-\xi^2) (1-\eta)$$

$$f_6 = \frac{1}{2} (1+\xi) (1-\eta^2)$$

$$f_7 = \frac{1}{2} (1-\xi^2) (1+\eta)$$

$$f_8 = \frac{1}{2} (1-\xi) (1-\eta^2)$$

3.2.6 MESH SIZE CONSIDERATIONS AND ITS EFFECT ON THE DISPERSION CURVE

This section presents the results of a number of parametric studies on the mesh size for finite element analysis and the effect of mesh size on the dispersion curve.

Modal analysis using beam theory gave good maximum displacement values but did not match the experimental dispersion curve. Finite elements, with the proper mesh size, models the dispersion curve well for a beam with no damage.

The importance of mesh size is shown by example in this section. Nine different meshes are compared. The number of elements through the depth was varied using 3, 6 and 12 elements. The number of elements along the length was varied using 21, 168, and 336 elements. This resulted in a test matrix 3×21 , 3×168 , 3×336 , 6×21 , 6×168 , 6×336 , 12×21 , 12×168 , and 12×336 . Figure 3.2.6 - 1 shows diagrams of the meshes. For each case, the arrival time, the highest frequency in FFT, and the dispersion curve were calculated. The dispersion curves were calculated with the load at $x=14"$, the first receiver at $x=11"$, and the second receiver at $x=8"$. Table 3.2.6 - 1 gives the arrival times from the acceleration time records at $x=11"$ for each mesh. Table 3.2.6 - 2 gives the highest frequency in the acceleration time record at $x=11"$ for each mesh. Figures 3.2.6 - 2 through 3.2.6 - 10 show the acceleration time records, the FFT of the time records, and the calculated dispersion curves for each mesh. The time records show that there is a visible difference between the time records of coarse meshes and fine meshes. This difference is seen in the arrival times of the pulse as well as the shape of the response records. Only the first 200 microseconds are shown in the time record to see the shape of the record better, the time record is 1024 microseconds long. In calculating the dispersion curve, the entire time record was used and exponentially windowed.

As can be seen the mesh size is important to insure the proper dispersion curve is calculated. If the mesh is too coarse, higher frequencies are filtered out of the time record, and the arrival time are smaller than they should be.

A mesh size of 12 x 168 elements was selected for all subsequent analysis. The dispersion curve was equal to the dispersion curve using 12 x 336 mesh.

Table 3.2.6 - 1 Arrival Time of Impulse, Beam: 21" x 6", XL: 14", XR1: 11"

Number of Elements through Depth	Number Elements along Length		
	21	168	336
3	5 μ sec	20 μ sec	20 μ sec
6	5 μ sec	20 μ sec	20 μ sec
12	5 μ sec	20 μ sec	20 μ sec

Table 3.2.6 - 2 Highest Frequency in FFT of Acceleration Record, Beam: 21" x 6", XL: 14", XR1: 11"

Number of Elements through Depth	Number Elements along Length		
	21	168	336
3	120 kHz	390 kHz	445 kHz
6	170 kHz	395 kHz	445 kHz
12	270 kHz	395 kHz	445 kHz

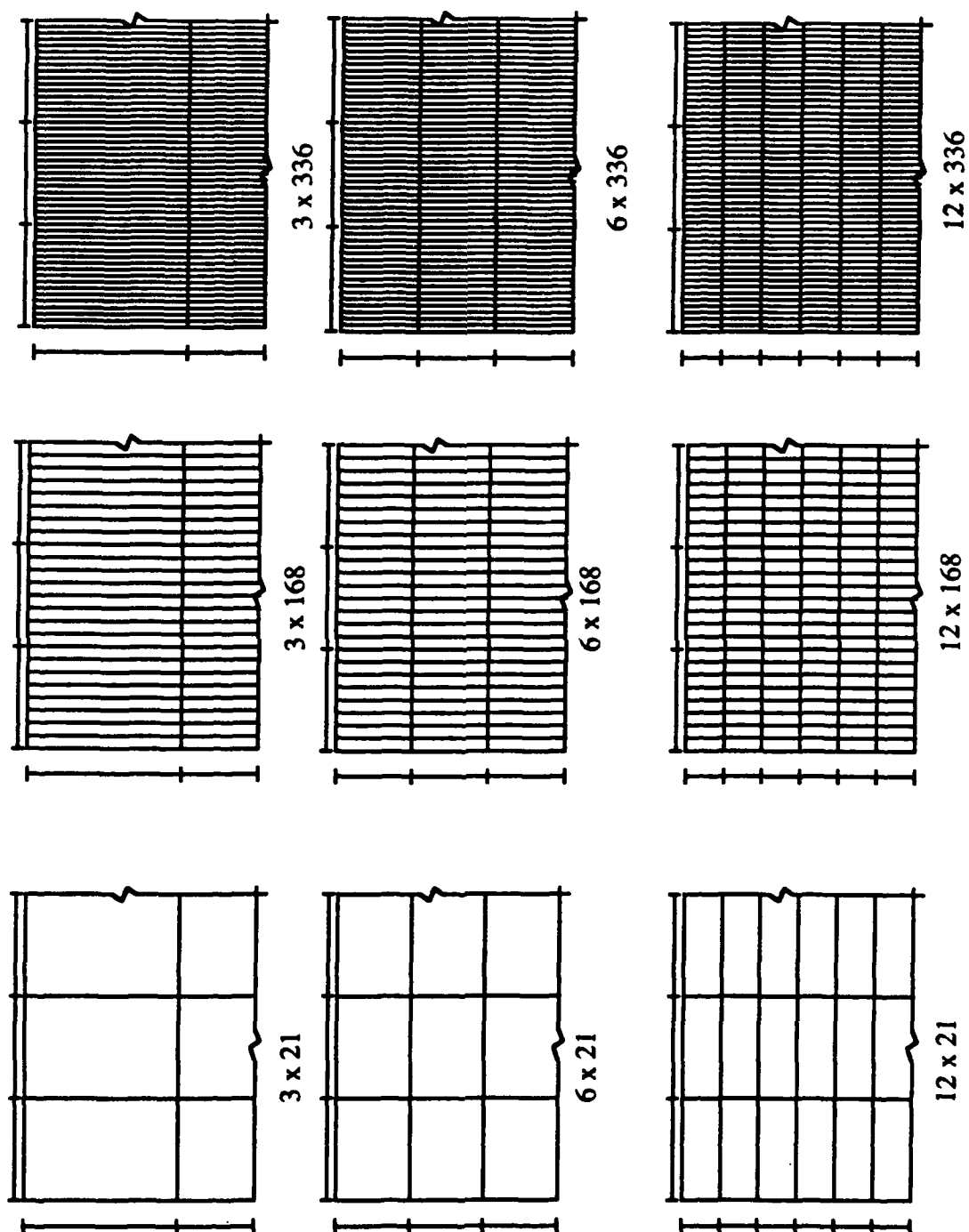


Figure 3.2.6 - 1 Mesh Diagram

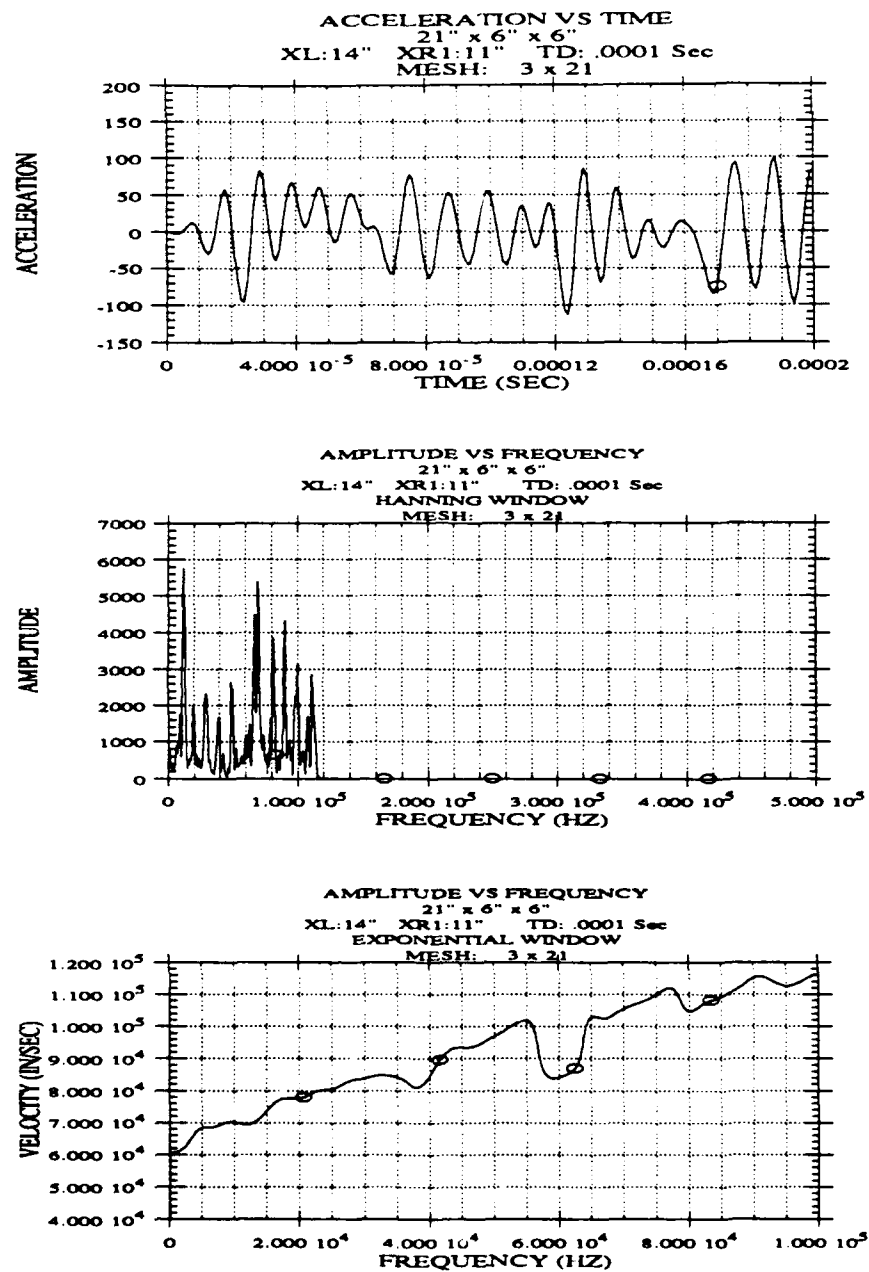


Figure 3.2.6 - 2 Mesh Size 3 x 21; Acceleration Diagram, Frequency Diagram and Dispersion Curve; Beam (21" x 6" x 6"), XL-XR1-XR2 (14-11-8), Exponential Window

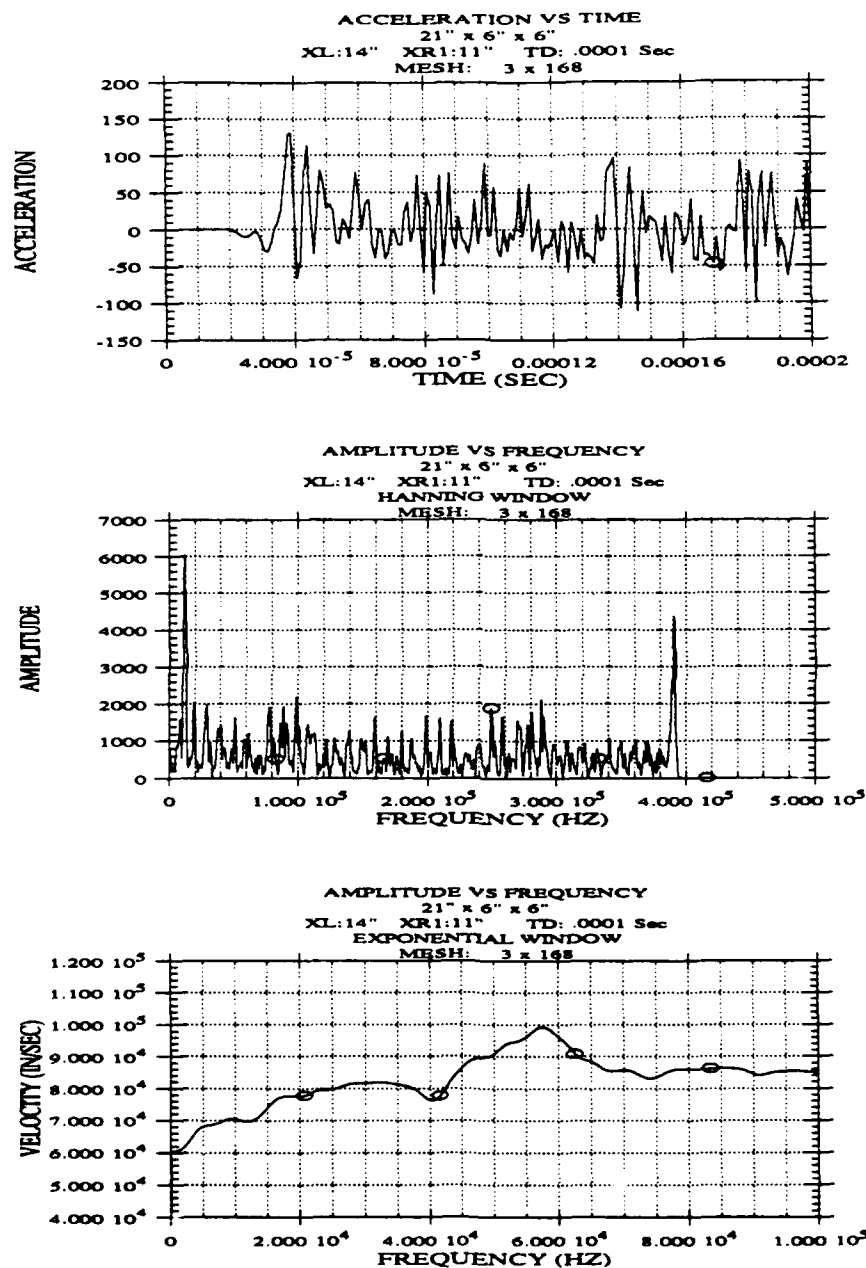


Figure 3.2.6 - 3 Mesh Size 3 x 168; Acceleration Diagram, Frequency Diagram and Dispersion Curve; Beam (21" x 6" x 6"), XL-XR1-XR2 (14-11-8), Exponential Window

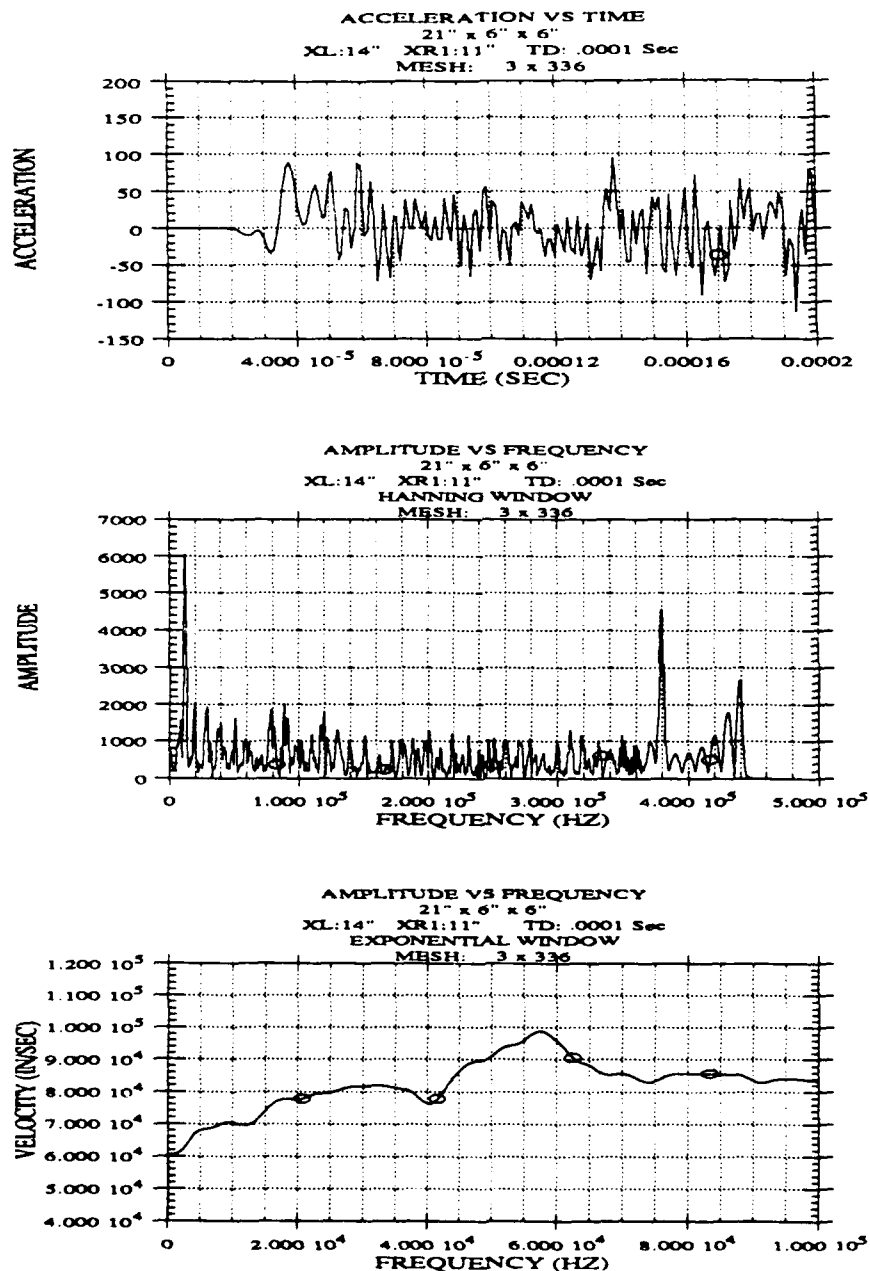


Figure 3.2.6 - 4 Mesh Size 3 x 336; Acceleration Diagram, Frequency Diagram and Dispersion Curve; Beam (21" x 6" x 6"), XL-XR1-XR2 (14-11-8), Exponential Window

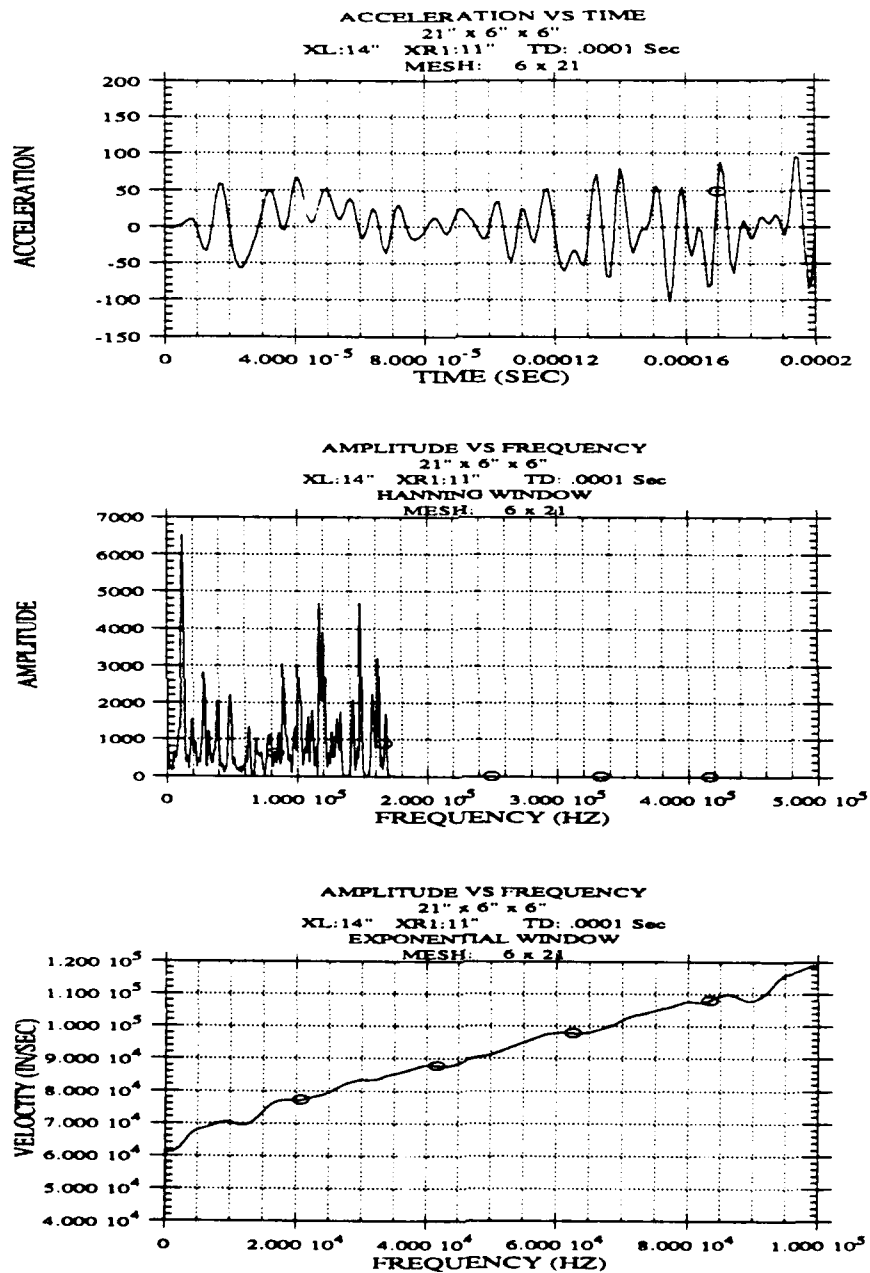


Figure 3.2.6 - 5 Mesh Size 6 x 21; Acceleration Diagram, Frequency Diagram and Dispersion Curve; Beam (21" x 6" x 6"), XL-XR1-XR2 (14-11-8), Exponential Window

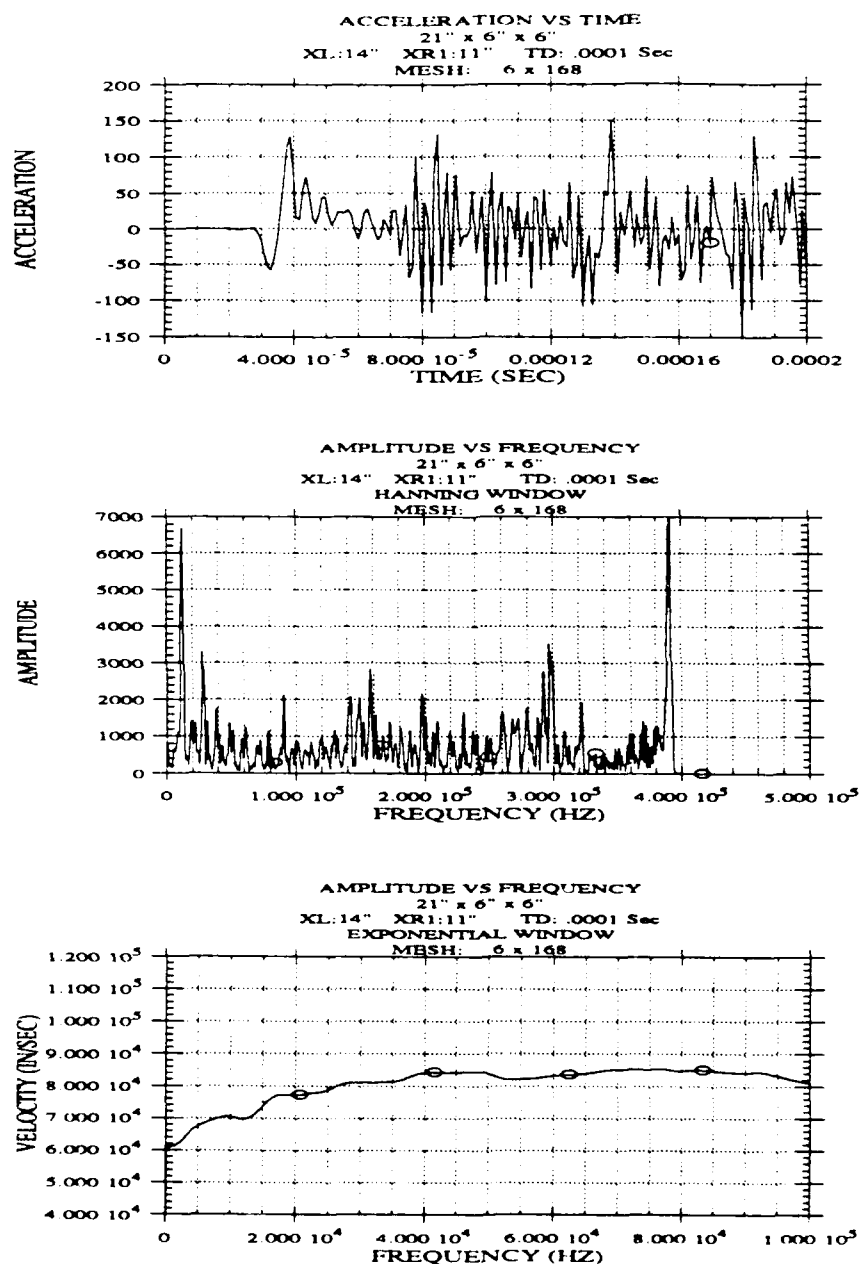


Figure 3.2.6 - 6 Mesh Size 6 x 168; Acceleration Diagram, Frequency Diagram and Dispersion Curve; Beam (21" x 6" x 6"), XL-XR1-XR2 (14-11-8), Exponential Window

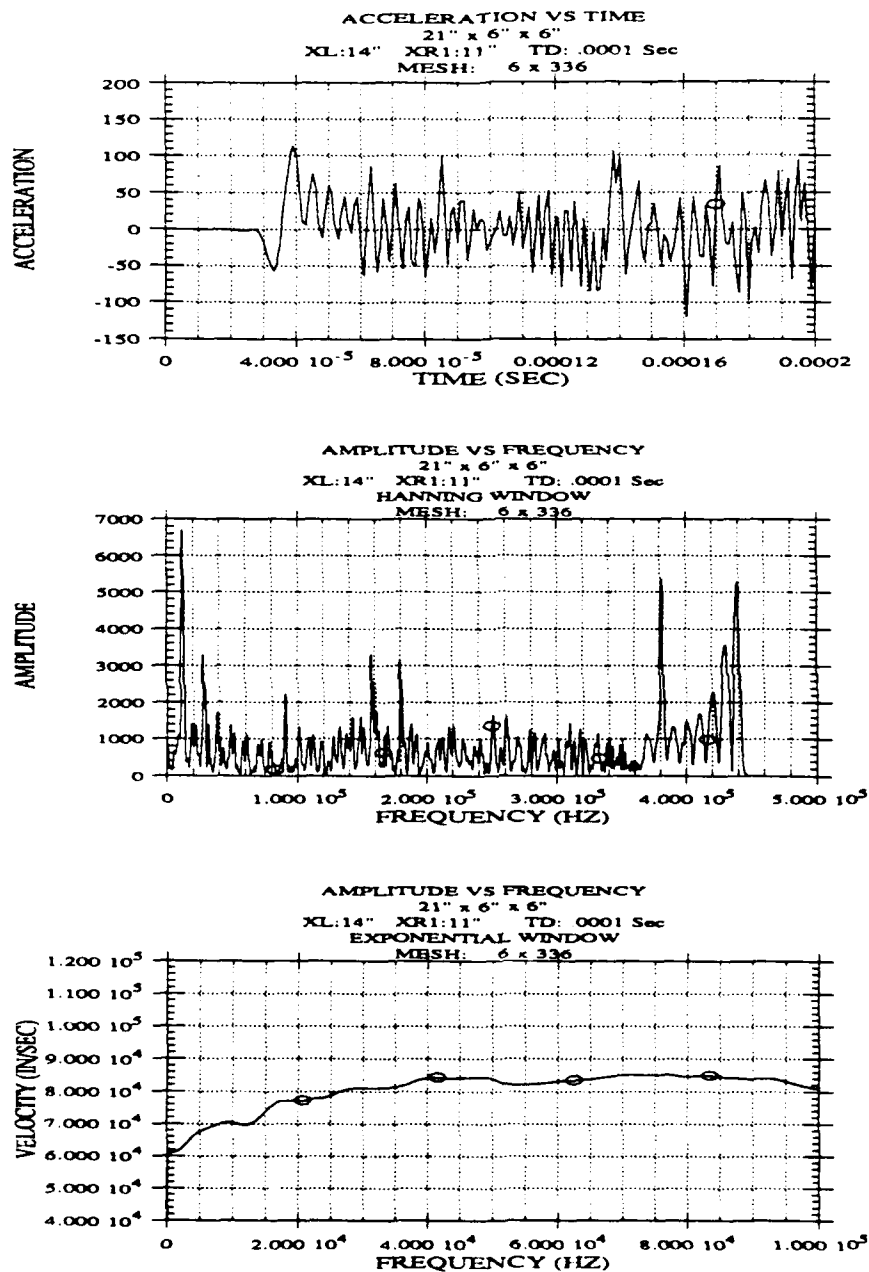


Figure 3.2.6 - 7 Mesh Size 6 x 336; Acceleration Diagram, Frequency Diagram and Dispersion Curve; Beam (21" x 6" x 6"), XL-XR1-XR2 (14-11-8), Exponential Window

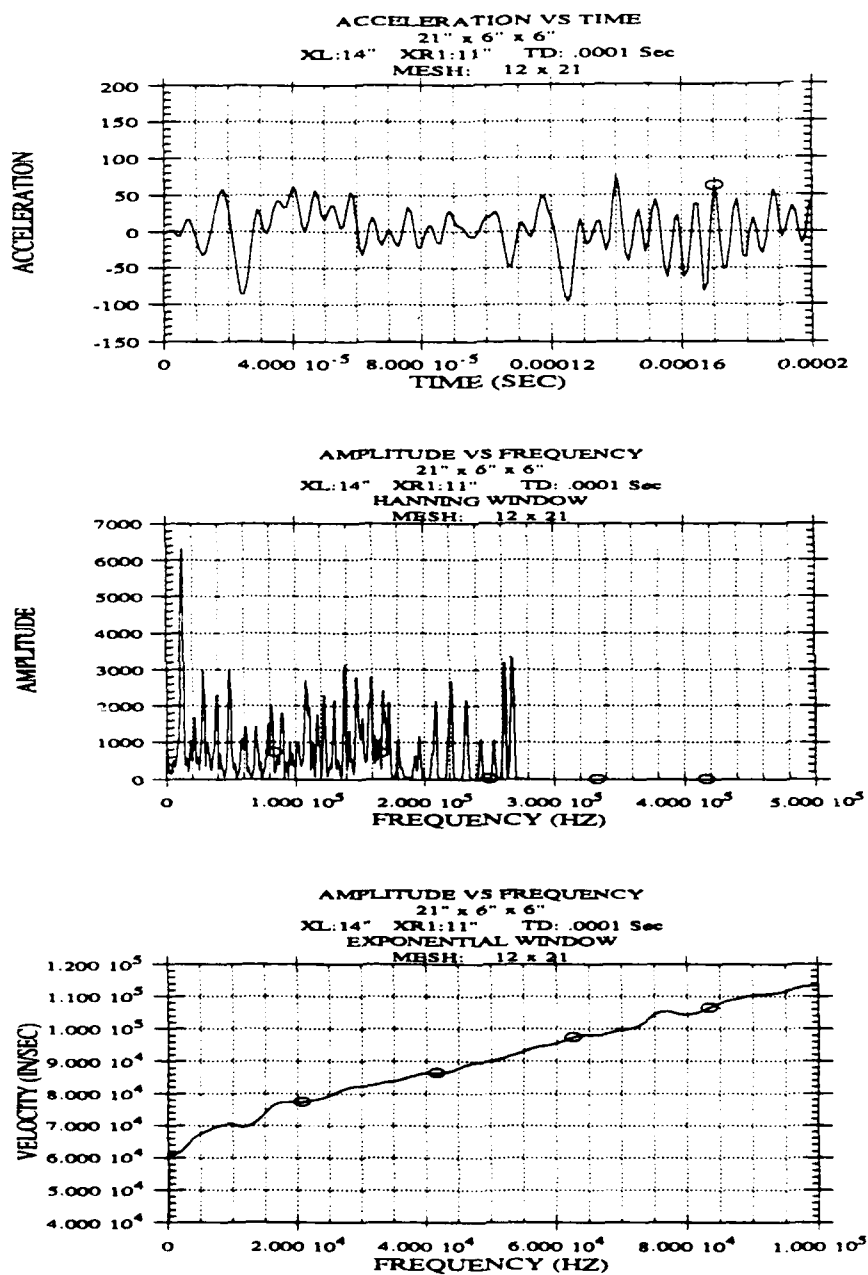


Figure 3.2.6 - 8 Mesh Size 12 x 21; Acceleration Diagram, Frequency Diagram and Dispersion Curve; Beam (21" x 6" x 6"), XL-XR1-XR2 (14-11-8), Exponential Window

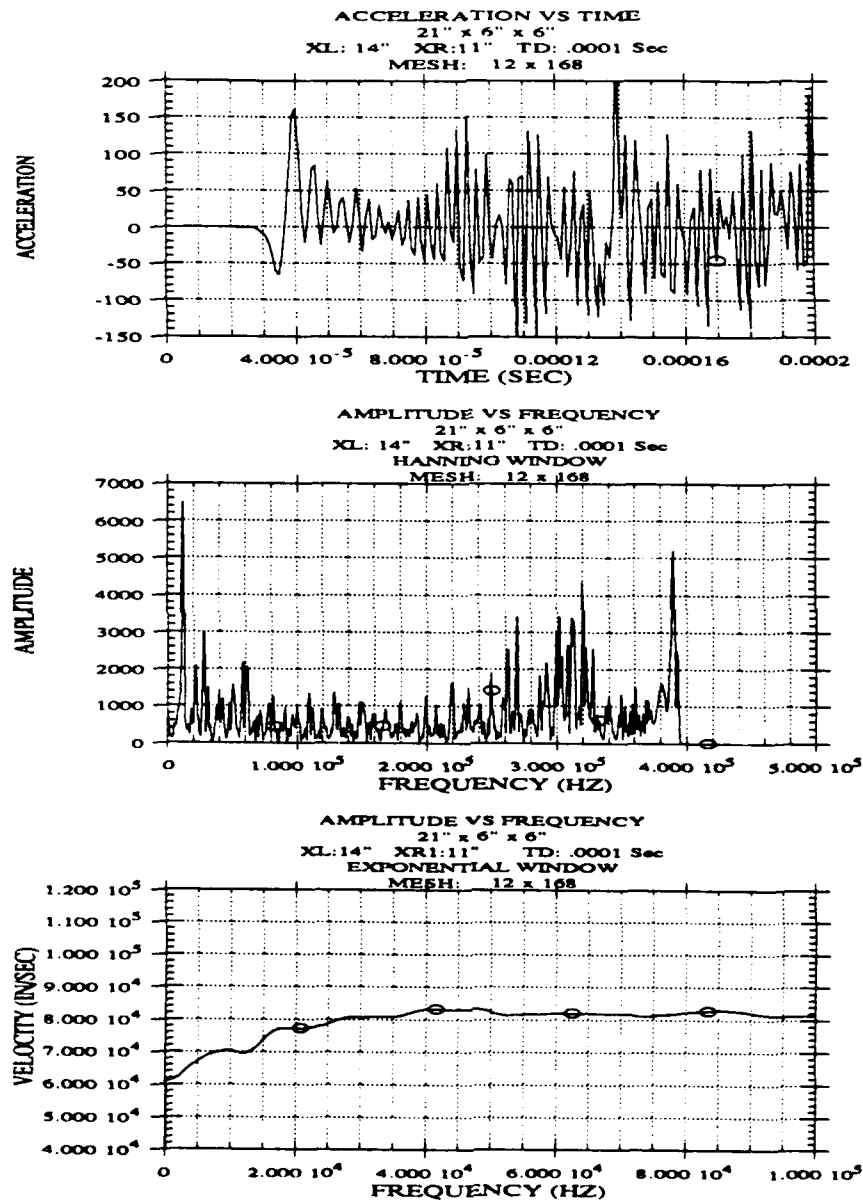


Figure 3.2.6 - 9 Mesh Size 12 x 168; Acceleration Diagram, Frequency Diagram and Dispersion Curve; Beam (21" x 6" x 6"), XL-XR1-XR2 (14-11-8), Exponential Window

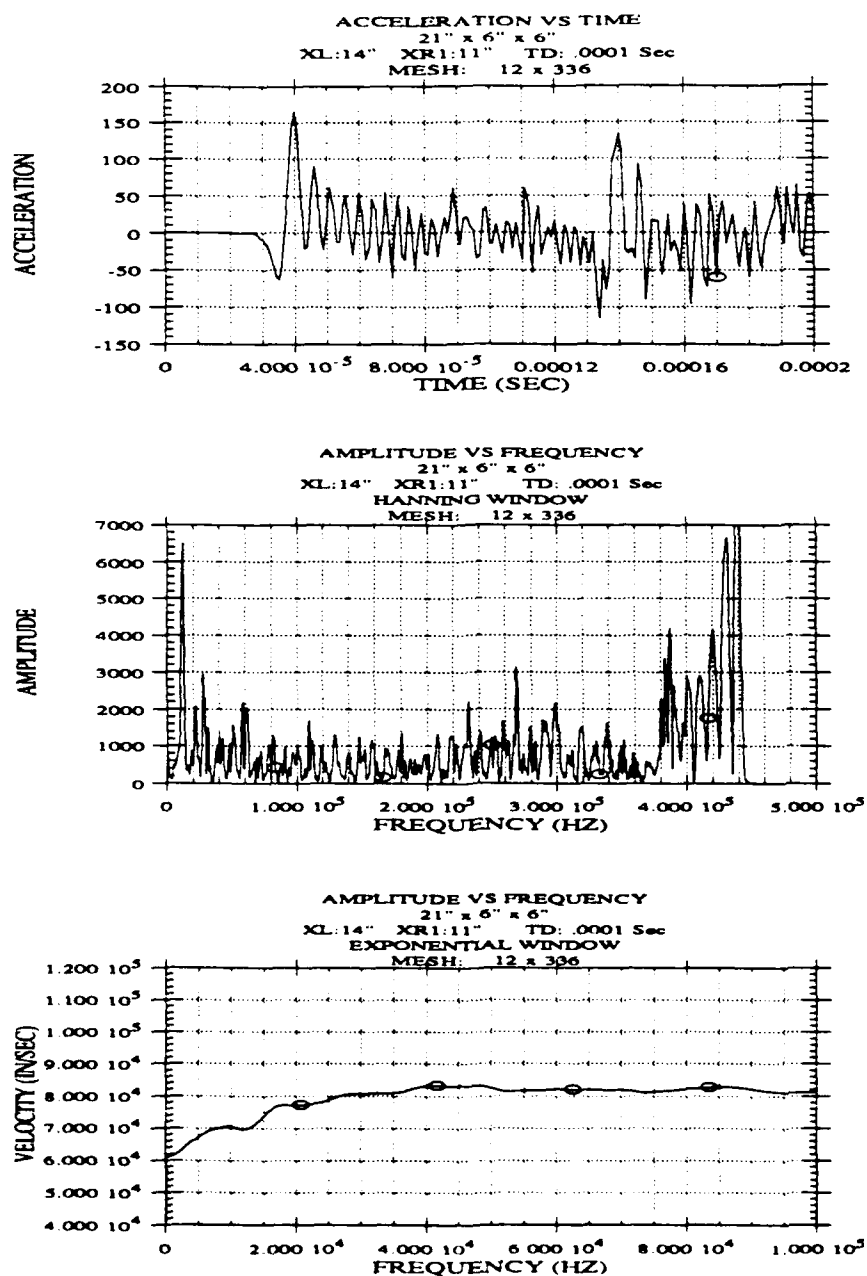


Figure 3.2.6 - 10 Mesh Size 12 x 336; Acceleration Diagram, Frequency Diagram and Dispersion Curve; Beam (21" x 6" x 6"), XL-XR1-XR2 (14-11-8), Exponential Window

3.3 BEHAVIOR AS FUNCTION OF $\frac{TD}{T_0}$

The main goal of this section is to describe the behavior of a beam's response as a function of the duration (TD) of the pulse load relative to the fundamental natural period (T_0) of the beam. A second goal is to identify the sophistication necessary to model the behavior. Three different beams were analyzed with dimensions, 20' x 2' x 1', 48" x 6" x 6", and 21" x 6" x 6". For the 20' x 2' x 1' beam only modal analysis was done. For the 48" x 6" x 6" and 21" x 6" x 6" beams, modal and finite element analyses were conducted. For the finite element studies, a convergence study was performed to determine the proper mesh. These data are presented in section 3.2.6. A summary of maximum and free vibration response is given in Tables 3.3 - 1 through 3.3 - 3. The load pulse length was varied based on the natural fundamental period and the shortest pulse physically possible. As such, the load varied from about 100 microseconds to 10 T_0 .

A graphical comparison of modal and finite element displacement response is given in Figures 3.3 - 1 through 3.3 - 5 for the different values of $\frac{TD}{T_0}$ and the 21" x 6" beam. The load is at x=14" the first receiver is at x=11" and the second receiver at x=8". Each figure shows a time record (x=11"), the Fourier transform (x=11") and the dispersion curve determined from the data. From these data the following conclusions can be drawn. Based on $\frac{TD}{T_0}$ there are three realms of response:

- | | |
|--------------------------|----------------------------|
| 1. Static response | $5 < \frac{TD}{T_0}$ |
| 2. Dynamic Magnification | $0.1 < \frac{TD}{T_0} < 5$ |
| 3. Fraction of Static | $\frac{TD}{T_0} < 0.1$ |

Table 3.3 - 1 Maximum Response for 20' x 2' x 1' Beam For Load at 10' and Response at 11' Using Modal Analysis

	BEAM: 20' x 2' x 1'	
	MODAL	
$\frac{TD}{T_0}$	MAXIMUM (FT)	STEADY STATE (FT)
10	4.75 (10 ⁻⁷)	0.2 (10 ⁻⁷)
5	5.0 (10 ⁻⁷)	1.0 (10 ⁻⁷)
2	5.9 (10 ⁻⁷)	2.3 (10 ⁻⁷)
1	7.5 (10 ⁻⁷)	6.0 (10 ⁻⁷)
.5	7.0 (10 ⁻⁷)	6.3 (10 ⁻⁷)
.1	1.85 (10 ⁻⁷)	1.85 (10 ⁻⁷)
.01	2.0 (10 ⁻⁸)	2.0 (10 ⁻⁸)
.001	1.95 (10 ⁻⁹)	1.95 (10 ⁻⁹)
STATIC	4.55 (10 ⁻⁷)	

Table 3.3 - 2 Maximum Response for 48" x 6" x 6" Beam For Load at 18" and Response at 30" Using Modal and Finite Element Analysis

	BEAM: 48" x 6" x 6"	
	FINITE ELEMENT AND MODAL	
$\frac{TD}{T_0}$	MAXIMUM (IN)	STEADY STATE (IN)
10	5.0 (10 ⁻⁶)	.5 (10 ⁻⁶)
5	5.4 (10 ⁻⁶)	1.0 (10 ⁻⁶)
2	6.2 (10 ⁻⁶)	2.7 (10 ⁻⁶)
1	8.5 (10 ⁻⁶)	7.0 (10 ⁻⁶)
.5	7.9 (10 ⁻⁶)	7.9 (10 ⁻⁶)
.1	2.1 (10 ⁻⁶)	2.1 (10 ⁻⁶)
.01	2.3 (10 ⁻⁷)	2.3 (10 ⁻⁷)
STATIC	4.8 (10 ⁻⁶)	

Table 3.3 - 3 Maximum Response for 21" x 6" x 6" Beam For Load at 14" and Response at 11" Using Modal and Finite Element Analysis

$\frac{TD}{T_0}$	BEAM: 21" x 6" x 6" FINITE ELEMENT		BEAM: 21" x 6" x 6" MODAL	
	MAXIMUM (IN)	STEADY STATE (IN)	MAXIMUM (IN)	STEADY STATE (IN)
10	4.4 (10^{-7})	0.15 (10^{-7})	3.4 (10^{-7})	0.4 (10^{-7})
5	4.7 (10^{-7})	0.8 (10^{-7})	3.8 (10^{-7})	0.8 (10^{-7})
1	7.5 (10^{-7})	6.5 (10^{-7})	6.0 (10^{-7})	4.5 (10^{-7})
.5	6.0 (10^{-7})	5.75 (10^{-7})	5.5 (10^{-7})	5.5 (10^{-7})
.1	1.35 (10^{-7})	1.35 (10^{-7})	1.35 (10^{-7})	1.35 (10^{-7})
STATIC	3.396 (10^{-7})		3.396 (10^{-7})	

Note that the true demarcation lines between each realm of response were not specifically determined. The above values give a guideline as to the types of behavior and where they begin.

Both the modal beam analysis and the finite element analysis give comparable maximum displacement values. There is good agreement between modal and finite element data with the 48" long beam. For the 21", there is a difference in the maximum values obtained, due to the fact that the beam is short and shear should be considered. The modal analysis solution does not account for shear. As a result the Fourier transform shows a different fundamental frequency for the system for modal analysis and finite elements (smaller natural frequency for the latter). For the short duration loads ($\frac{TD}{T_0} = 0.1$ or 114 microseconds), the arrival times of the wave are also different from both models

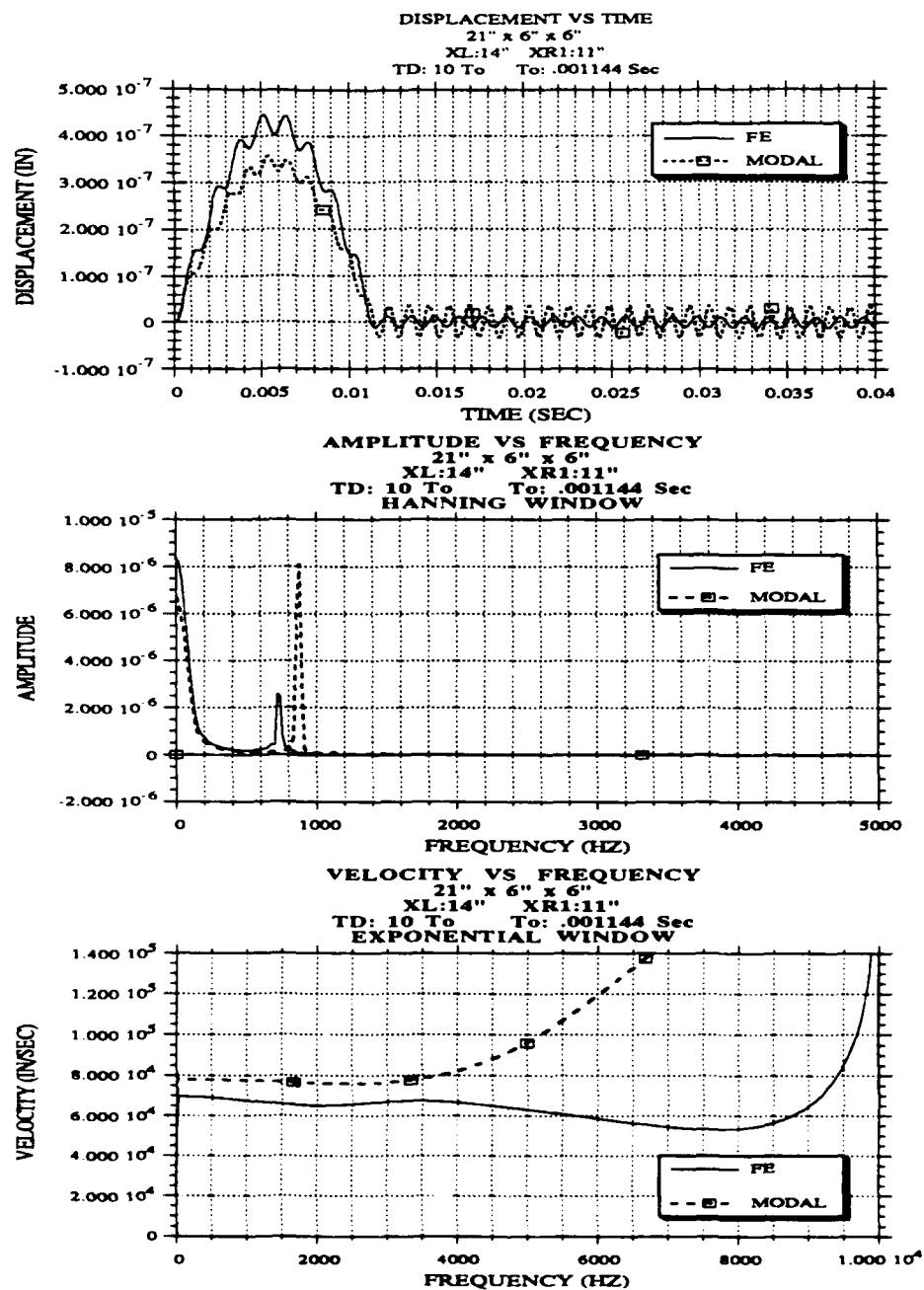


Figure 3.3 - 1 Modal Analysis and Finite Element Analysis; Displacement Diagram, Frequency Diagram and Dispersion Curve; $T_D / T_0 = 10$, Beam (21" x 6" x 6"), XL-XR1-XR2 (14-11-8), Exponential Window

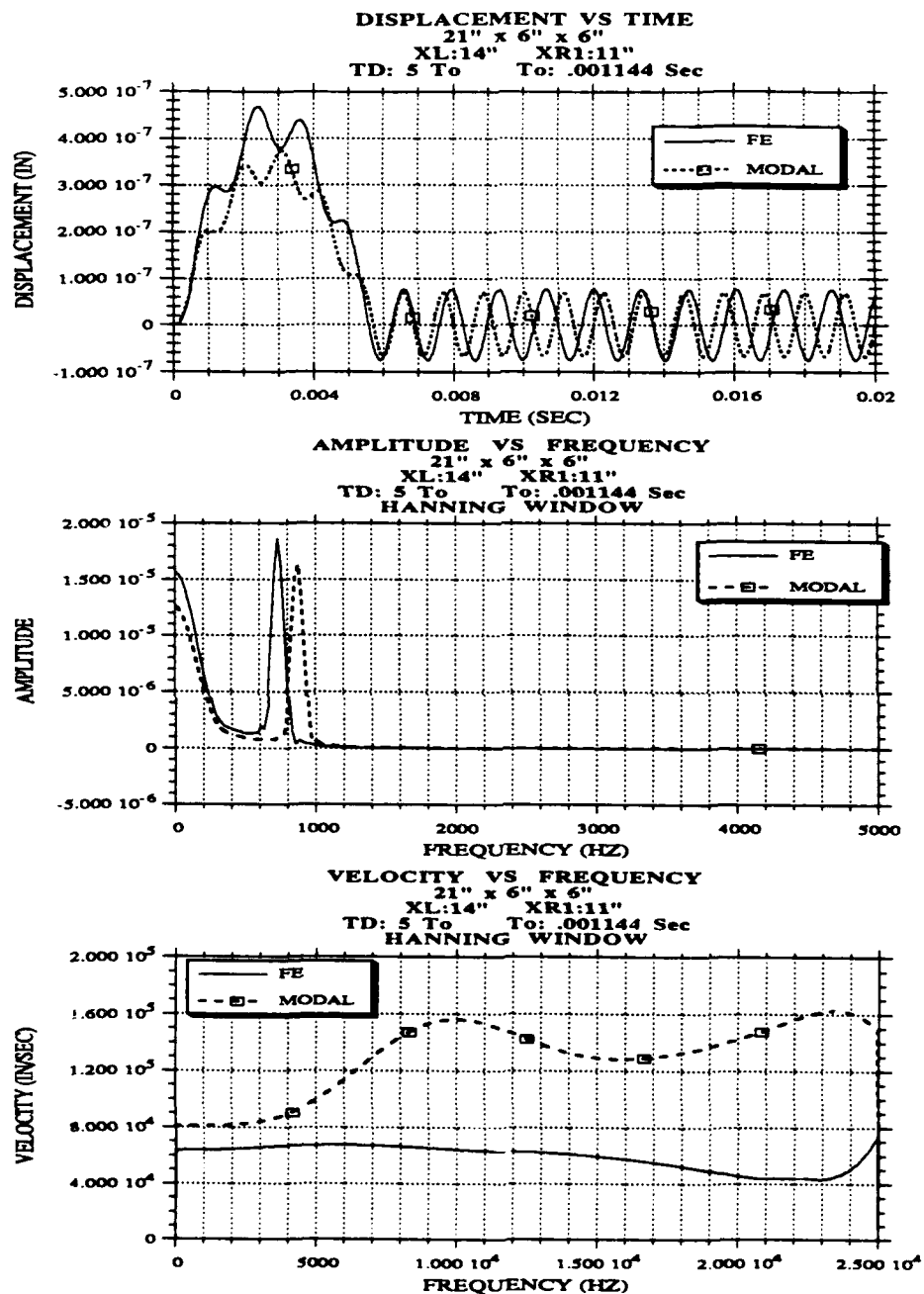


Figure 3.3 - 2 Modal Analysis and Finite Element Analysis; Displacement Diagram, Frequency Diagram and Dispersion Curve; $TD / T_0 = 5$, Beam (21" x 6" x 6"), XL-XR1-XR2 (14-11-8), Exponential Window

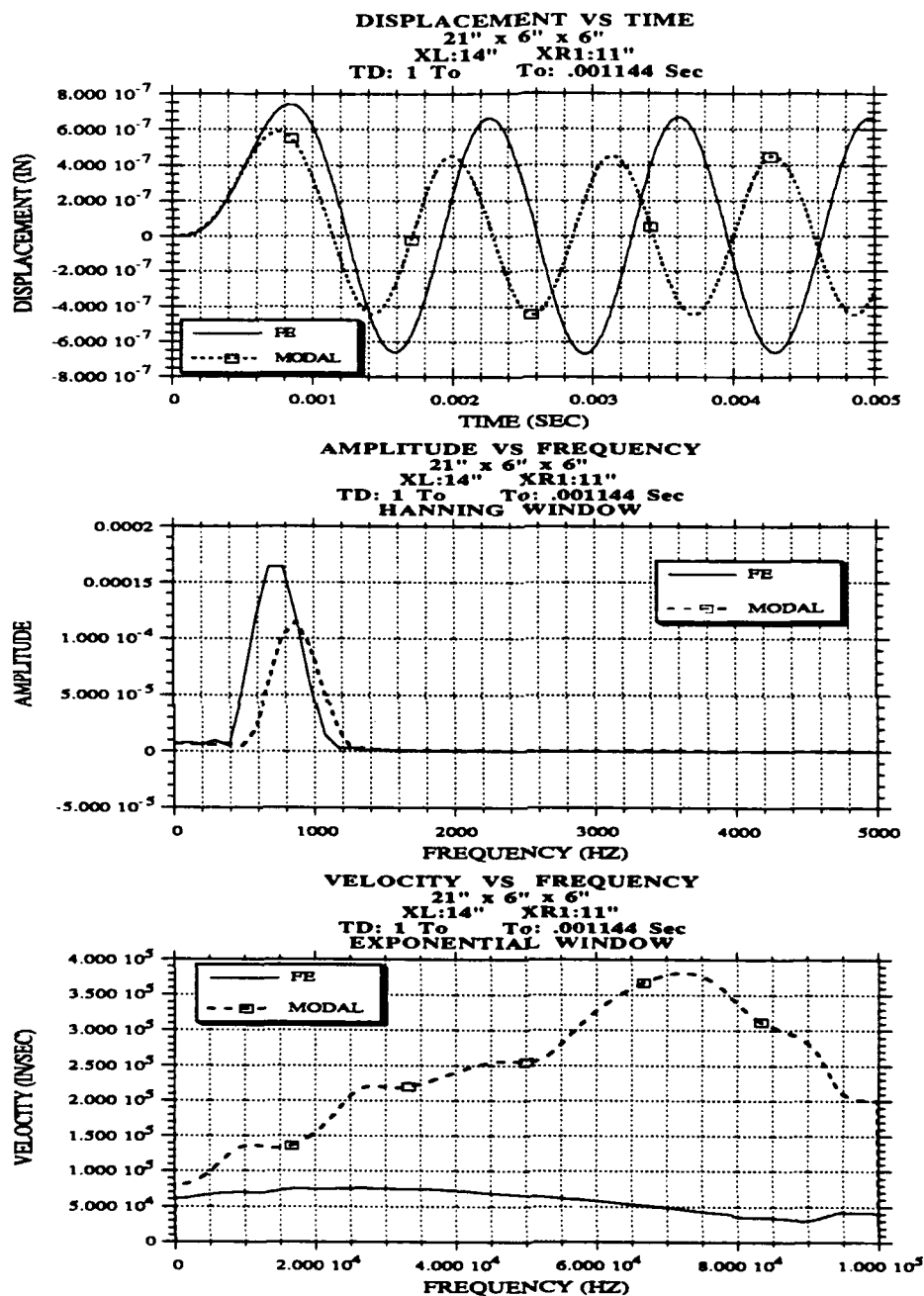


Figure 3.3 - 3 Modal Analysis and Finite Element Analysis; Displacement Diagram, Frequency Diagram and Dispersion Curve; $T_D / T_0 = 1$, Beam (21" x 6" x 6"), XL-XR1-XR2 (14-11-8), Exponential Window

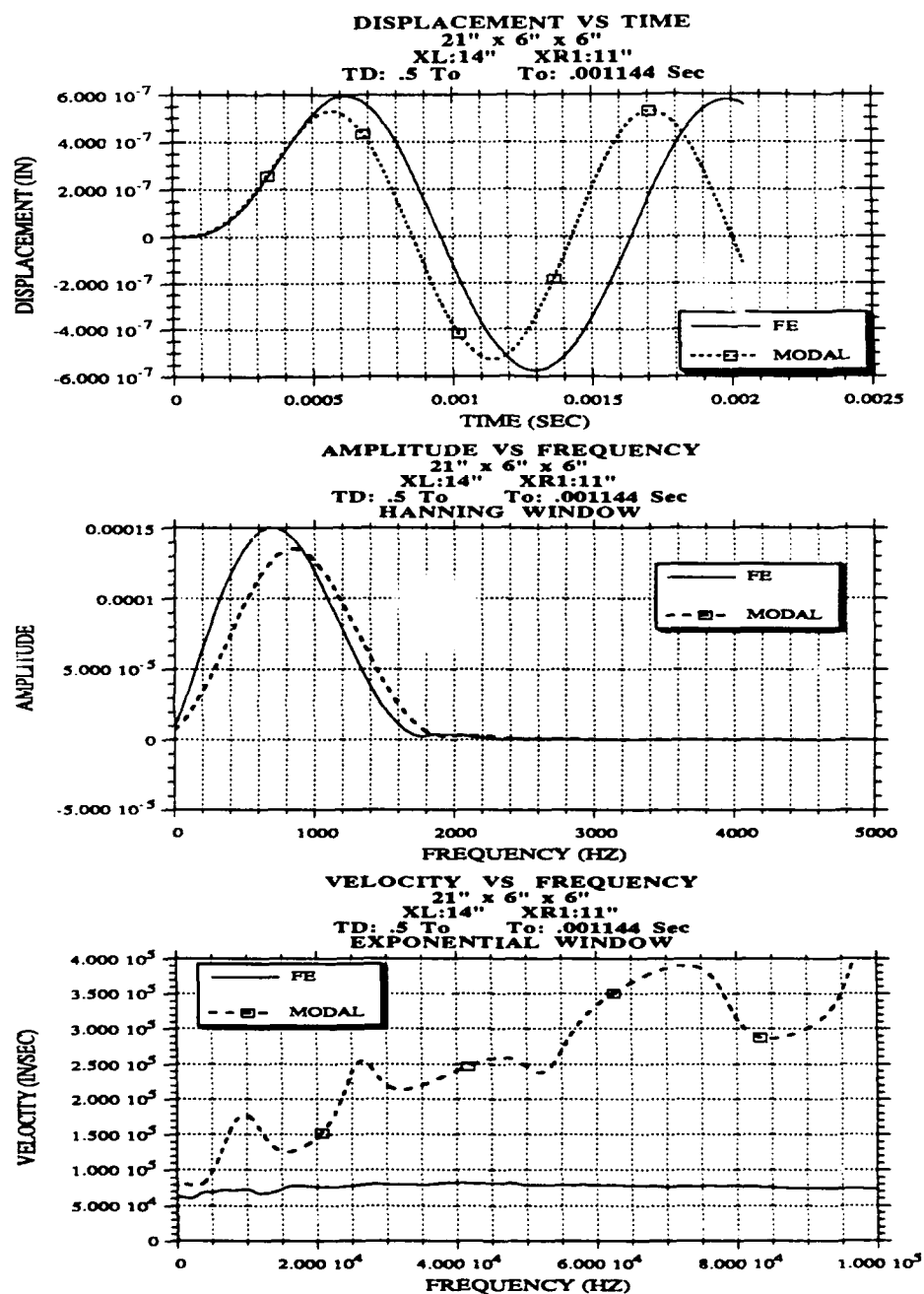


Figure 3.3 - 4 Modal Analysis and Finite Element Analysis; Displacement Diagram, Frequency Diagram and Dispersion Curve; $T_D / T_0 = 0.5$, Beam (21" x 6" x 6"), XL-XR1-XR2 (14-11-8), Exponential Window

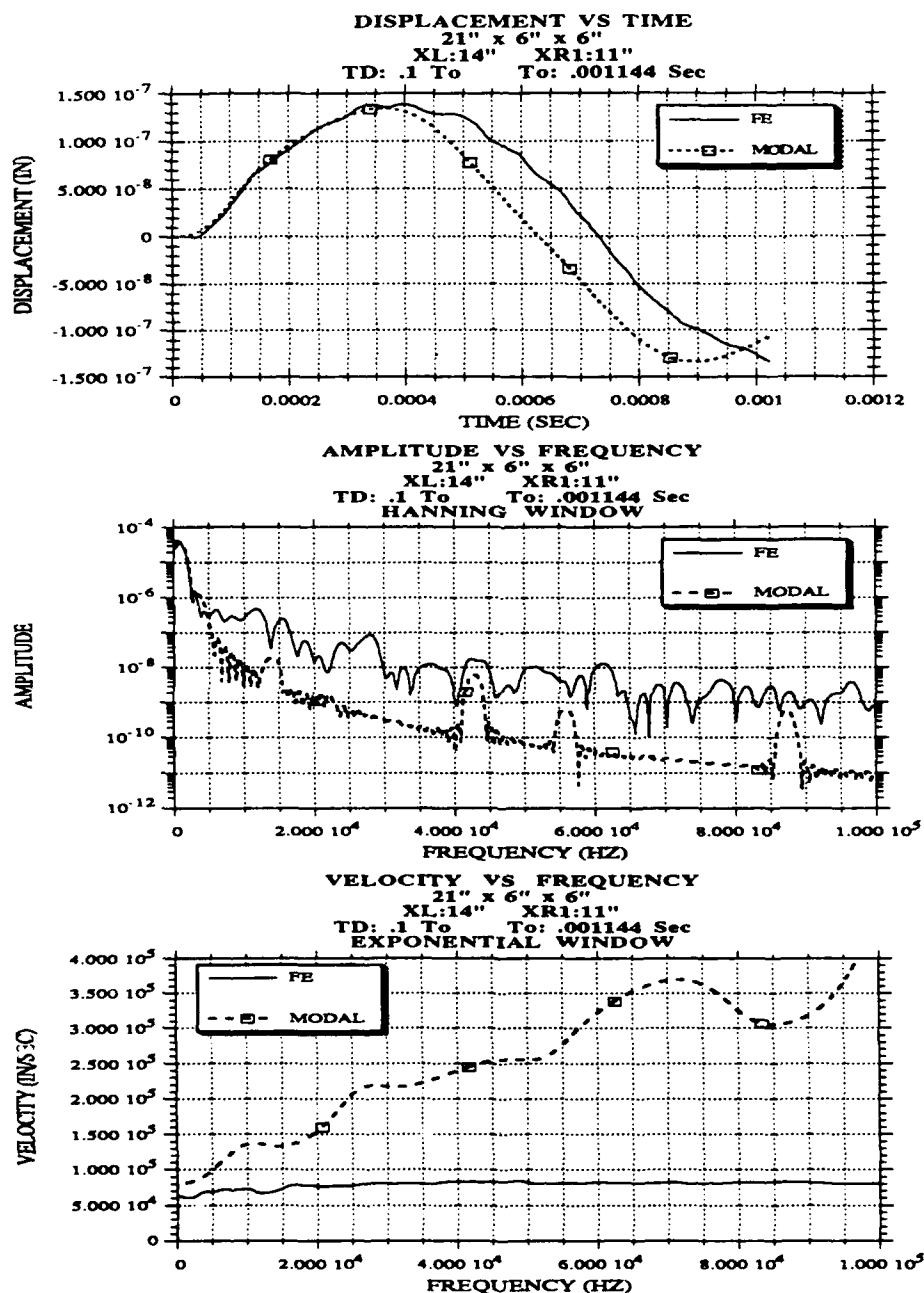


Figure 3.3 - 5 Modal Analysis and Finite Element Analysis; Displacement Diagram, Frequency Diagram and Dispersion Curve; $T_D/T_0 = 0.1$, Beam (21" x 6" x 6"), XL-XR1-XR2 (14-11-8), Exponential Window

The amplitude of the Fourier spectrum is larger for the finite element model than for the beam solution for the higher frequencies. This can be seen better on a log scale, as shown in Figure 3.3 - 5. The high frequency component is important in obtaining the proper phase diagram.

The dispersion curves determined from the finite element and modal data consequently do not match each other. The modal data oscillates about the theoretical dispersion curve for flexural waves in a simple supported beam as given by Equation 3.1.5 - 1. The finite element data dispersion curve gives a curve which resembles the experimental data. (A comparison of experimental and analytical data is presented in section 5.1)

3.4 ANALYTICAL FORMULATION WITH AIR ON BOTH SIDES

The dispersion curve was also calculated directly (not using SASW) for a finite thick layer with air on both sides, and a comparison was made with a SASW derived dispersion curve using finite element data. If instead of a half space, there is a layer of finite thickness with air on both sides the Rayleigh wave speed equation is

$$[s^2 + K^2]^4 - 8 K^2 [s^2 + K^2]^2 q s \left[\frac{C_1 C_2 - 1}{S_1 S_2} \right] + 16 q^2 s^2 K^4 = 0 \quad (3.4 - 1)$$

where

$$C_1 = \cosh(qh)$$

$$S_1 = \sinh(qh)$$

$$C_2 = \cosh(sh)$$

$$S_2 = \sinh(sh)$$

h is the depth of the layer

$$K = \frac{2\pi}{\lambda}$$

$$q^2 = \left(K^2 - \frac{\omega^2}{V_p^2} \right) \qquad s^2 = \left(K^2 - \frac{\omega^2}{V_s^2} \right)$$

Solving equation 3.4 - 1 for the normalized velocity ($\frac{V_r}{V_s}$) as a function of normalized frequency ($\frac{\text{Depth}}{\lambda}$), the dispersion curve can be calculated. For comparison purposes, the results are converted to velocity vs frequency by using the same material properties ($E = 4515000$ psi, $\nu = .2$, depth = 6") input into the finite element program to calculate the time records used in the SASW method. Figure 3.4 - 1 shows the comparison between the dispersion curve determine from solving Equation 3.4 - 1 and the SASW derived dispersion curves using finite element data.

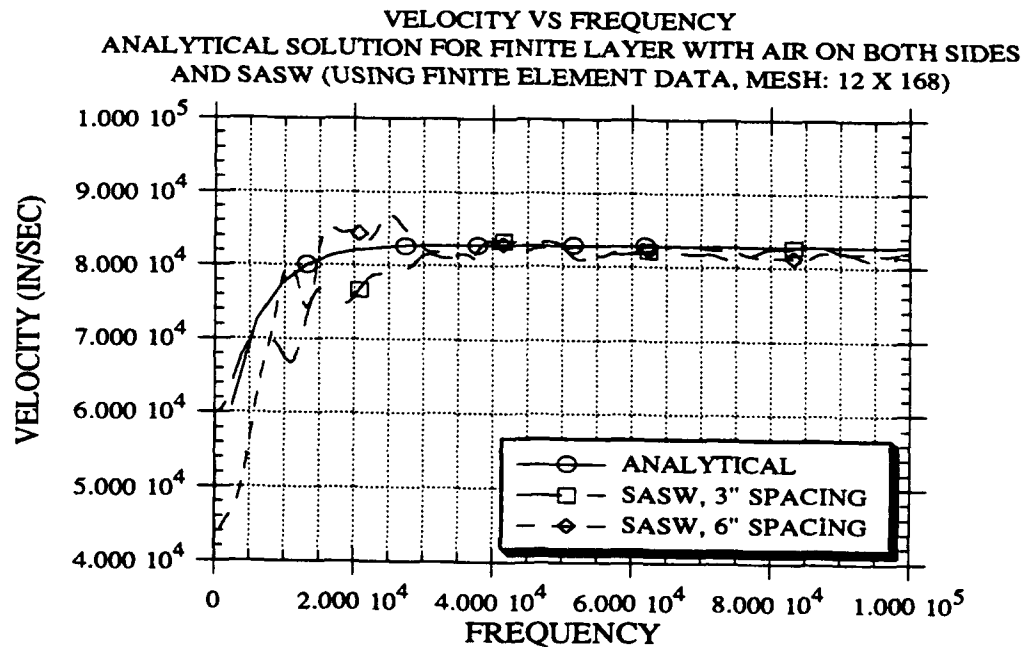


Figure 3.4 - 1 Dispersion Curve Comparison: SASW (using Finite Element Data) Vs Analytical (Finite Layer with Air on Both Sides)

3.5 BOUNDARY CONDITIONS

To determine if the boundary conditions at the end of the beam affected the dispersion curve a numerical study was conducted for different end conditions. Figure 3.5 - 1 compares the dispersion curves determined using Fixed-Fixed, Fixed-Free, Fixed-Simple, and Simple-Simple boundary conditions. These results show that above 30 kHz, in the range where the phase velocity is properly reproduced, the boundary conditions do not affect the dispersion curve. This is due to the exponential window used on the data, which "zeroes-out" the time record before the reflections from the boundaries arrive.

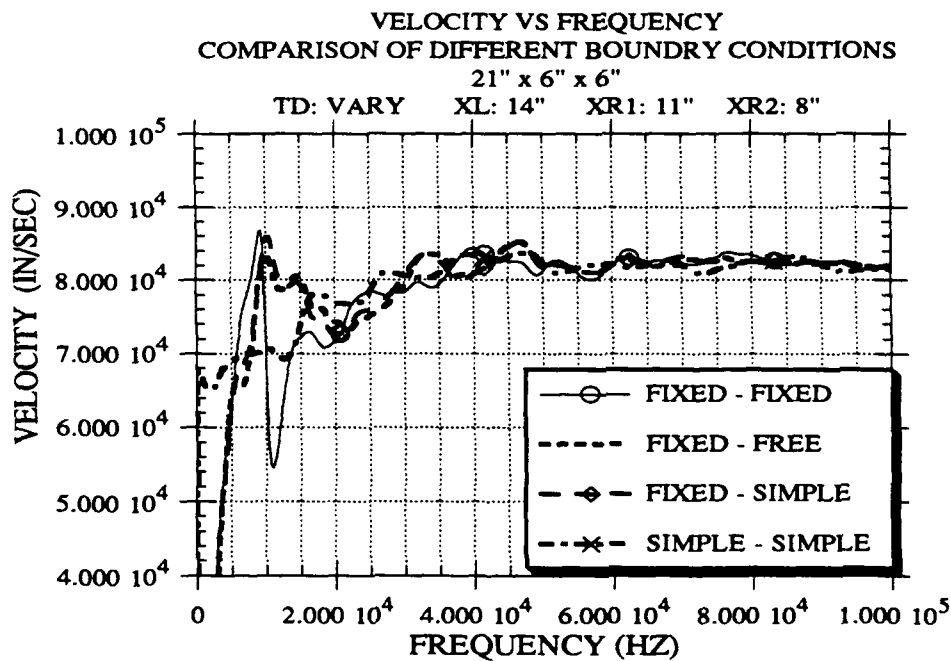


Figure 3.5 - 1 Dispersion Curve: Boundary Conditions
Analytical Data, Mesh Size 12 x 168, Beam (21" x 6" x 6"), XL-XR1-XR2 (14-11-8), Exponential Window

3.6 TYPE OF MEASUREMENT

For a given impact one can obtain either acceleration, velocity, or displacement time records. The effect of the type of record was only investigated analytically. Only acceleration measurements were made experimentally. Figure 3.6 - 1 compares the dispersion curve determined using acceleration and displacement data. It can be seen that acceleration and displacement records give essentially the same dispersion curve, particularly above 20 kHz and therefore over the complete range of interest.

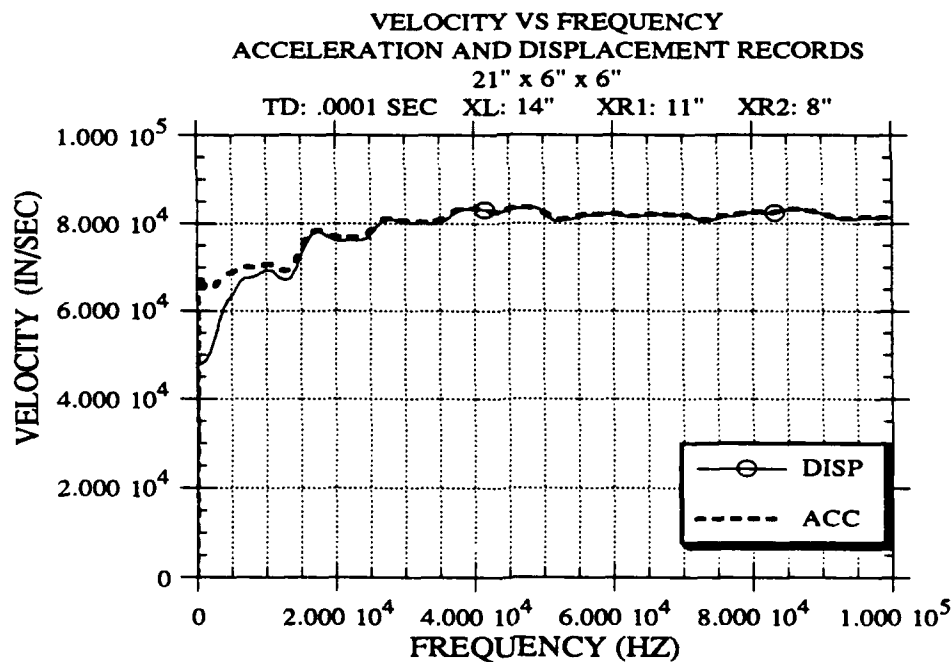


Figure 3.6 - 1 Dispersion Curve: Acceleration vs Displacement
Analytical Data, Mesh Size 12 x 168, Beam (21" x 6" x 6"), XL-XR1-XR2 (14-11-8), Exponential Window

CHAPTER FOUR

EXPERIMENTAL WORK

The objective of the SASW method is to calculate the surface wave dispersion curve. The key to the dispersion curve is an accurate cross power phase diagram. This chapter covers the experimental test matrix, the equipment used, test specimens, test procedures, and gives recommendations on how to get a good phase diagram.

4.1 TEST MATRIX

Four factors were considered in making up the test matrix: type of damage, face on which the source-receiver array is located, spacing of the source-receiver array, and relative location with respect to the damage of the source receiver array. The source-receiver spacings used were 3" and 6".

Damage was limited to vertical cracks. The damage levels were No Damage, 1", 2", and 3" deep vertical cracks at 10.5" from the left end of the test specimen. The cracks were saw cut to control the depth. The width of the cut was 1/8".

There were three possible faces on which to place the source-receiver array. They are the top of the beam with the crack opening at the same face, the bottom of the beam with the crack opening at the top, and on the side of the beam with the crack opening at the top.

Several source-receiver array locations were tested. The array location was moved across the beam from the left end to the right. When possible, symmetry was used to reduce the number of times the accelerometer needed to be moved. As the source-receiver array was moved across the beam with the crack fixed at 10.5"

from the left end, three different situations arose. The first is when the source and receivers are all on the same side of the crack. The second is when the crack is between the receivers; and the third when the crack is between the source and first receiver. Listed below are the different source-receiver locations tested; the first number is the location of the source, the second and third number are location of receivers one and two. Each location is the distance from the left end of the beam. Figure 4.1 - 1 shows the different relative locations of damage and source-receiver array.

3" SPACING

3	6	9
5	8	11
6	9	12
15	12	9
14	11	8
12	9	6
9	6	3

6" SPACING

1	2	8
1	5	11
1	6	12
1	7	13
19	13	7
18	12	6
17	11	5
14	8	2
10	8	2

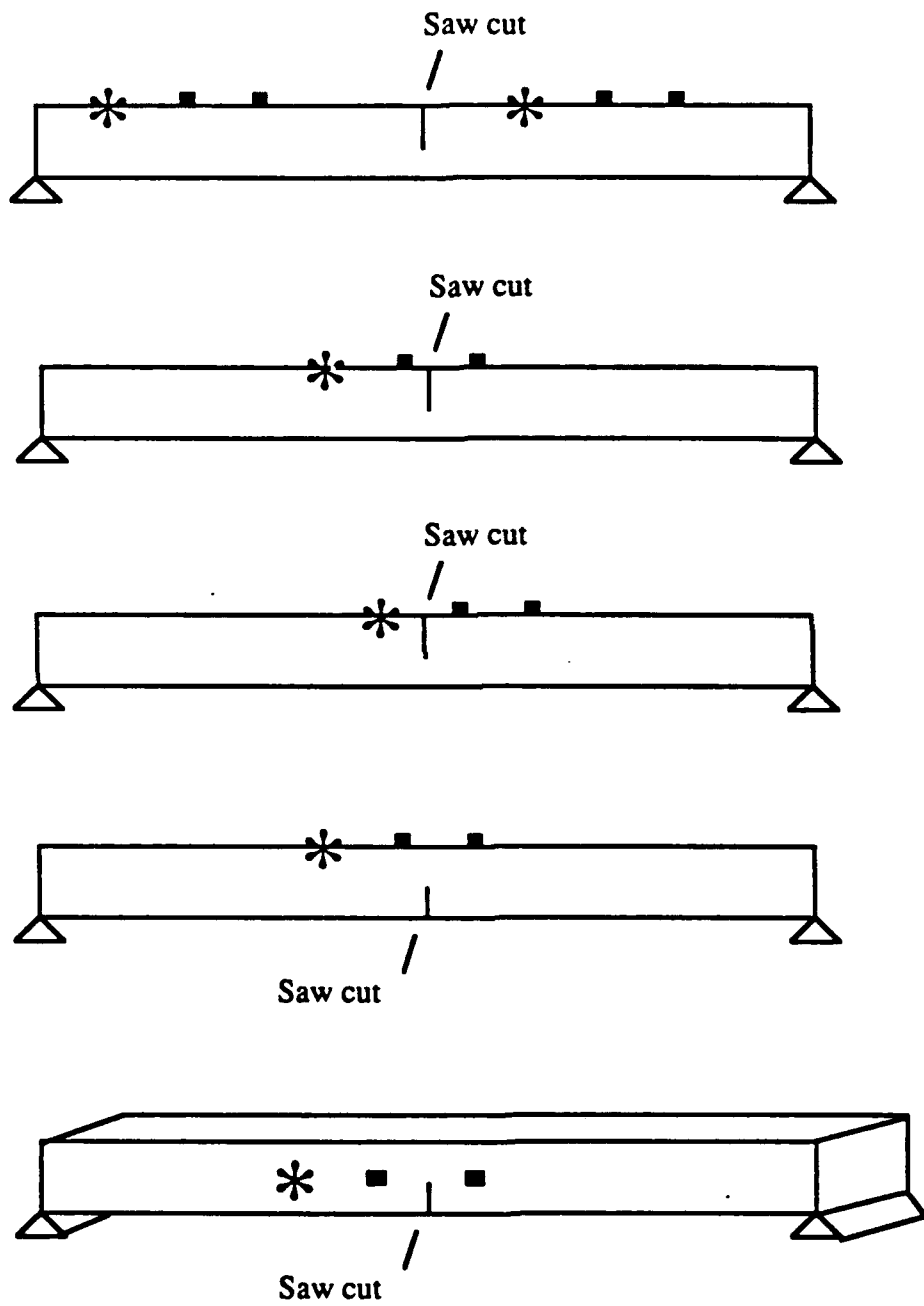


Figure 4.1 - 1 Relative Location of Damage and Source-Receiver Array

4.2 EQUIPMENT

Experimentally, two simultaneous acceleration measurements were made at a known distance apart. The instrumentation, used to make the acceleration measurements, included PCB 303A12 accelerometers powered by a PCB Piezotronic Amplifier Model 483A07 which connected into a HP3562A Dynamic Signal Analyzer. The data were stored on a 3.5" floppy disk via a HP9122 disk drive. This is diagramed in Figure 4.2 - 1

The dynamic signal analyzer had dual channel capability with a frequency range from 0 - 100 kHz and dual channel display of 801 data points. The analyzer is capable of capturing the acceleration time records and doing a variety of calculations afterwards. The calculations used were the cross power spectrum, linear spectrum of each record, coherence, and the captured time records.

The stress waves were generated by an impact of either an instrumented hammer or a ball bearing dropped from a given height. The ball bearing diameters used were 7/16", 5/16", 5/32", and 5/64".

4.3 TEST SPECIMENS

The test specimens were 21" x 6" x 6" . For this research, no coarse aggregate was used. The specimens were made of only cement and sand. The moist curing time was 90 days, minimum. Some of the specimens cured longer. Since this study only looked at detecting damage, the strength of the elements was not a concern.

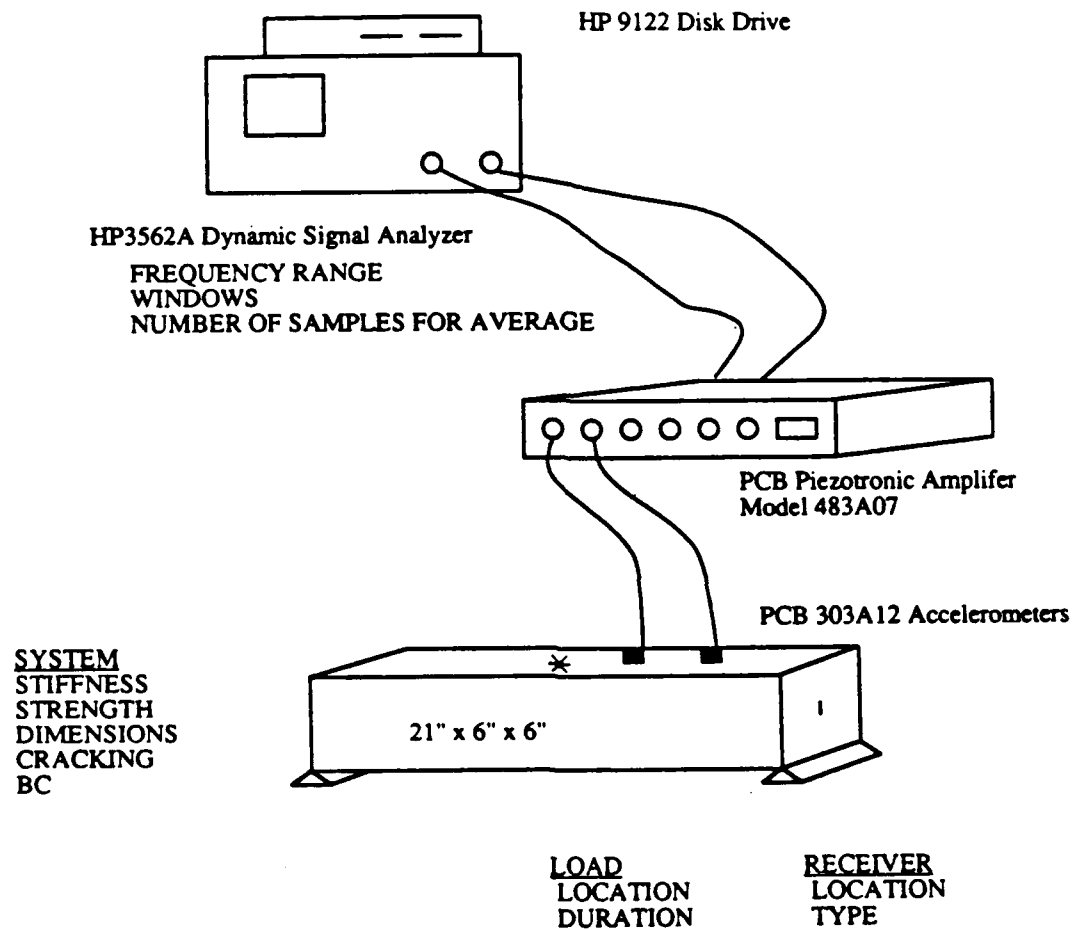


Figure 4.2 - 1 Test Set-Up

4.4 TEST PROCEDURES

The testing procedure for a given configuration was:

1. Attach the accelerometer to the test specimen at the proper location. The accelerometers were installed by attaching a nut to the stud at the base of the accelerometer and then gluing the accelerometer to the concrete with super glue.
2. Set up the analyzer to capture the time records and calculate the cross power spectrum phase.
3. Determine a reliable trigger, so a consistent time record could be captured. This was accomplished by finding a consistent feature in one of the time records and then using that feature to trigger the recording of the time records.
4. Change the window duration until a satisfactory phase diagram is determined. There is usually a range of window durations where the phase diagram will converge. The goal is to find this range of window durations for each measurement configuration.
5. If the measurement is still not satisfactory, increase the number of samples in the average measurement. Typically, five samples per measurement were sufficient.
6. Save the cross power spectrum, the coherence, the linear spectrum for each record, and each time record to a floppy disk.
7. Calculate the dispersion curve from the phase of the cross power spectrum.

4.5 RECOMMENDATION TO GET A GOOD PHASE DIAGRAM

To obtain an accurate dispersion curve, an accurate phase diagram must be determined. As such, the key to the dispersion curve is the phase diagram. A good phase diagram is monotonically increasing/decreasing, with clear 2π phase shifts (phase shifts in the correct places). To calculate a good phase diagram, the following observations were made:

1. For each record, in the frequency domain, it is desirable to have energy at every frequency in the range of interest. To increase energy level for a given frequency range, there are three alternatives: to hit harder with a given source, to use a source which generates the frequencies of interest, or to change the window duration.

2. The resolution in the frequency domain becomes more important as the spacing increases. The resolution is controlled by the sampling rate, Δt , and the number of points used in the FFT. Analytically, the typical resolution was 122 Hz. Experimentally, the resolution used was 125 Hz.

CHAPTER FIVE

UNDAMAGED BEAM

In this chapter, the dispersion curve for an undamaged beam is discussed. A comparison of the analytically generated and experimentally determined dispersion curves is made. The effect of load duration (or use of different sources) on the calculated dispersion curve is discussed. The effect of source-array location on the beam is shown. Finally, a comparison of dispersion curves determined from different receiver spacings is given. It is important to know, if the load duration, array location, and array spacing affect the dispersion curve in an undamaged medium. If they do, this effect must be accounted for when testing in a damaged medium, to insure that any change in the dispersion curve is a result of damage and not due to the use of a different source, array location on the beam, or array spacing. It should be noted that in this chapter and chapter six, any experimental data with low coherence was masked.

5.1 ANALYTICAL VS EXPERIMENTAL DISPERSION CURVES

Figure 5.1 - 1 shows the velocity of propagation vs frequency for a three inch load-receiver spacing. Experimental and analytical data are plotted together. There are two interesting aspects of the graph. First, the experimental and analytical results are in very good agreement over the range of frequencies of interest (above 30 kHz). The second is that in this frequency range the velocity is approximately constant.

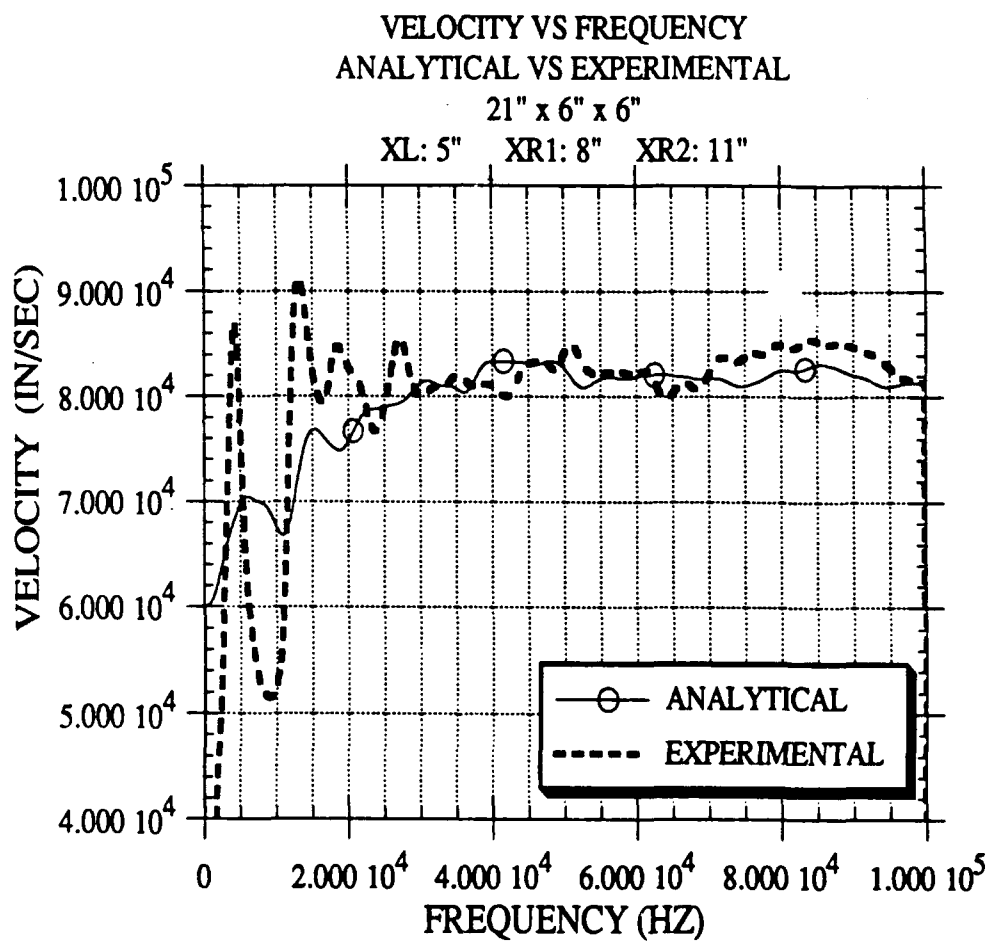


Figure 5.1 - 1 Dispersion Curve: Experimental vs Analytical
Mesh Size 12 x 168, Beam (21" x 6" x 6"), XL-XR1-XR2 (14-11-8),
Exponential Window

5.2 LOAD DURATION

The effect of load duration was explored both analytically and experimentally. Longer duration load pulses have less high frequency component. It was of interest to determine if the dispersion curve for higher frequencies was affected when there was less high frequency component in the load. Analytically, time durations (TD) of 50, 100, and 200 microseconds were used. Figure 5.2 - 1 shows that the results are not affected by the duration, provided there is sufficient energy in the frequency range of interest. Experimentally, this was investigated using an instrumented hammer and several sizes of ball bearings. Figure 5.2 - 2 shows the experimental data. Again the dispersion curve was insensitive to the load duration used. It should be noted that the load duration of the instrumented hammer with concrete varies between 100 - 150 microseconds and is the longest load duration used experimentally. Long duration pulses have less high frequency energy in them, which makes the hammer the critical case for experimental data.

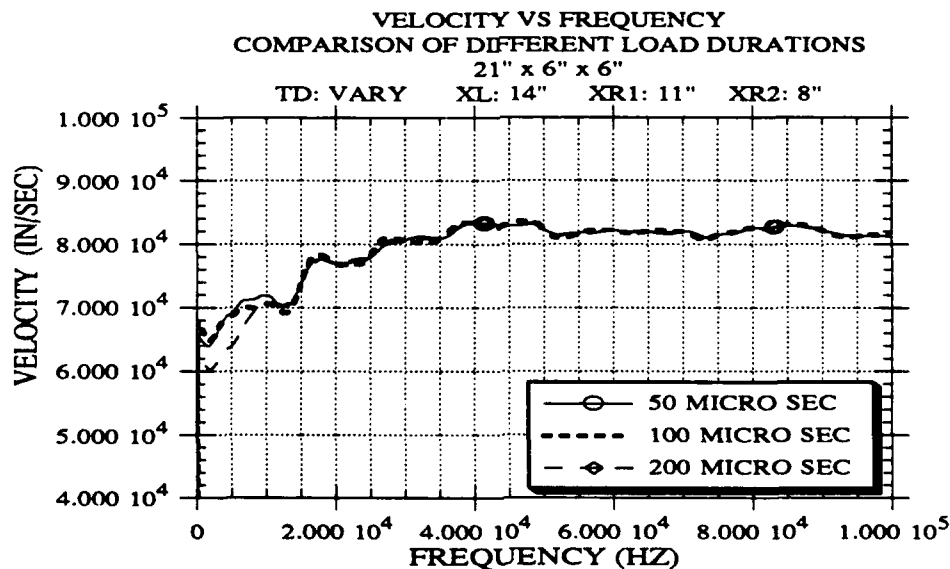


Figure 5.2 - 1 Dispersion Curve: Load Duration Varied
Analytical Data, Mesh Size 12 x 168, Beam (21" x 6" x 6"), XL-XR1-XR2 (14-11-8), Exponential Window

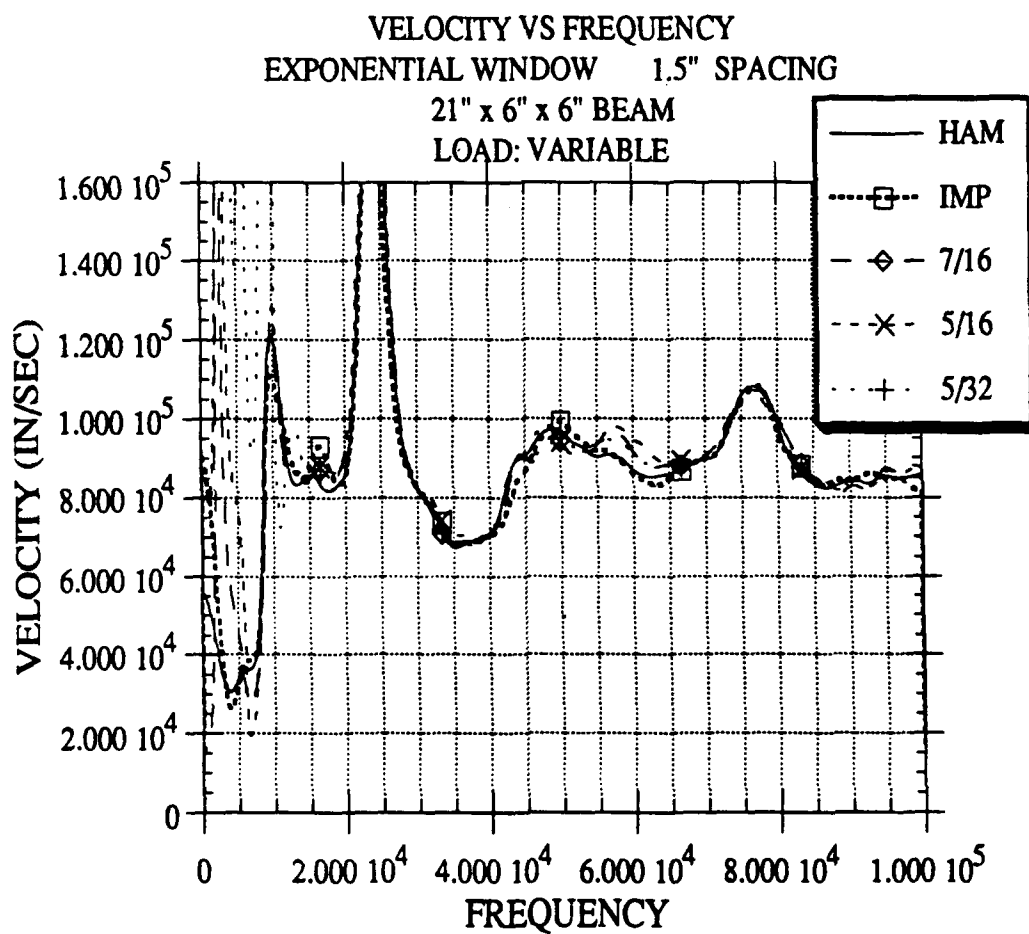


Figure 5.2 - 2 Dispersion Curve: Load Duration Varied
Experimental Data, Beam (21" x 6" x 6"), XL-XR1-XR2 (14-11-8), Exponential Window

5.3 ARRAY LOCATION ON BEAM

Since the beam was not considered a half space, it was of interest to determine if the source-receiver location affected the dispersion curve. Figure 5.3 - 1 shows the results of a number of numerical studies with different source and receivers locations (but constant spacing). Figure 5.3 - 2 shows corresponding experimental data. These figures show that for a given spacing, the source-receiver array location does not appreciably affect the dispersion curve. It is interesting to notice that the location affects the experimental results more when the source is near the edge but only for frequencies smaller than 30 kHz, below the range of interest.

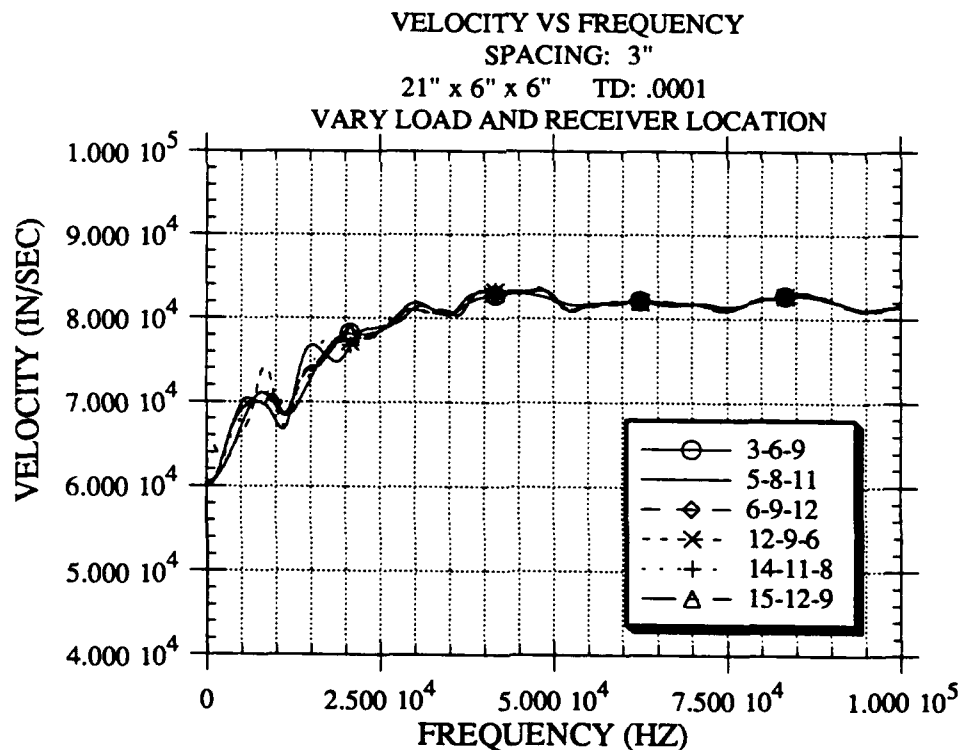


Figure 5.3 - 1 Dispersion Curve: Array Location Varied
Analytical Data, Mesh Size 12 x 168, Beam (21" x 6" x 6"), Exponential Window

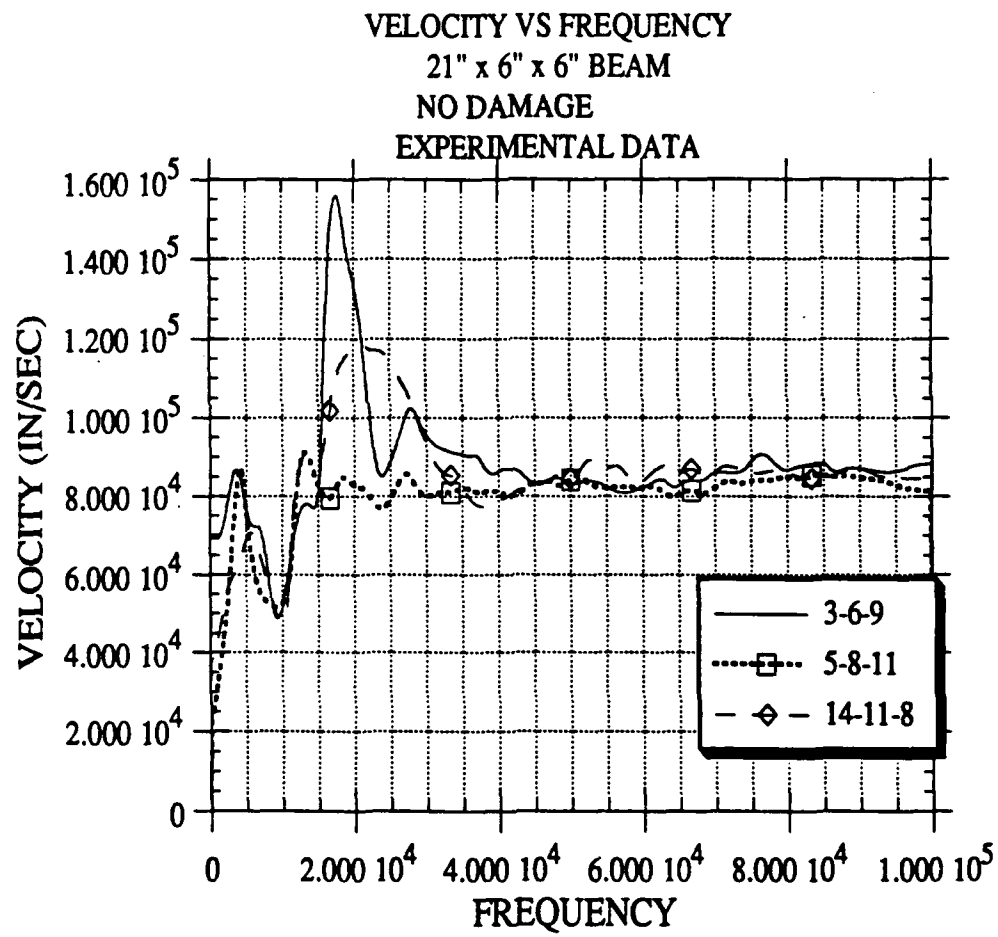


Figure 5.3 - 2 Dispersion Curve: Array Location Varied
Experimental Data, Beam (21" x 6" x 6"), Exponential Window

5.4 SPACING

Different array spacings give similar velocities for wavelengths less than the spacing. This can be seen in Figure 5.4 - 1, where 6", 3" and 1" array spacings are compared analytically and in Figure 5.4 - 2 for experimental data. It should be noted that a six inch wave length corresponds to about 12 kHz, a three inch wave length corresponds to about 28 kHz, and a one inch wave length corresponds to about 83 kHz.

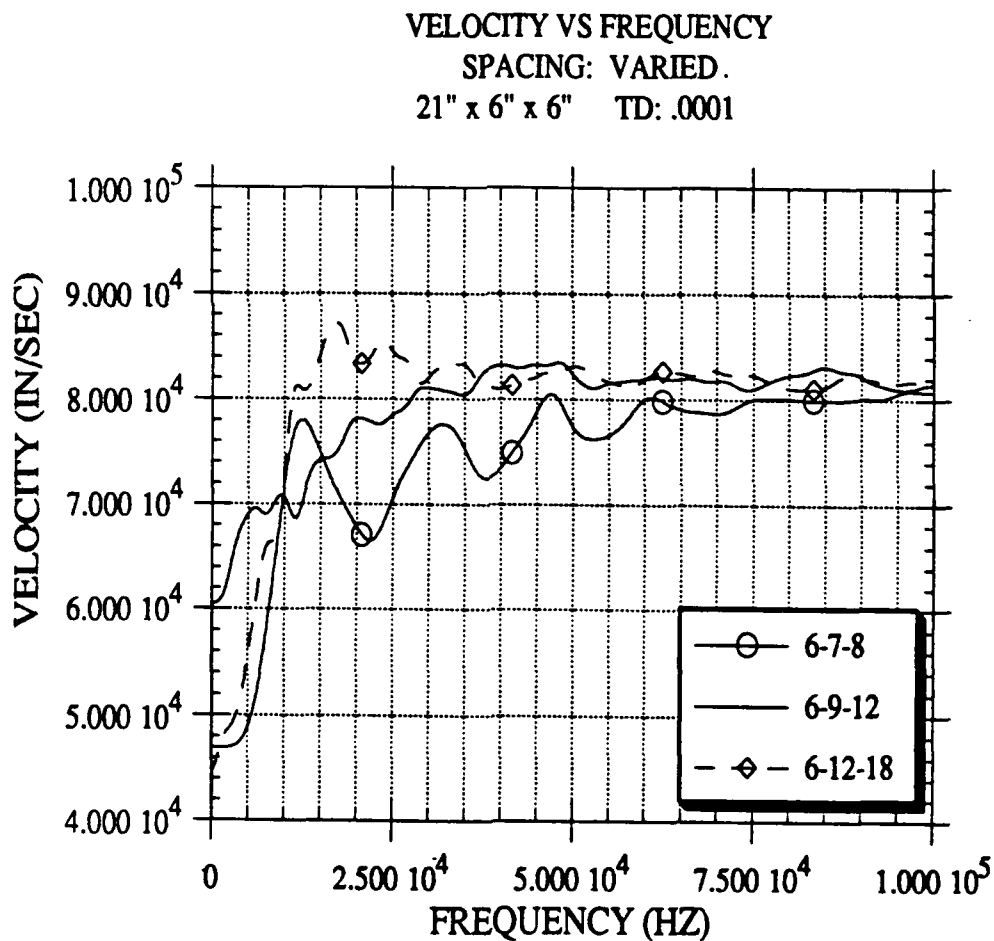


Figure 5.4 - 1 Dispersion Curve: Spacing Varied
 Analytical Data, Mesh Size 12 x 168, Beam (21" x 6" x 6"), Exponential Window

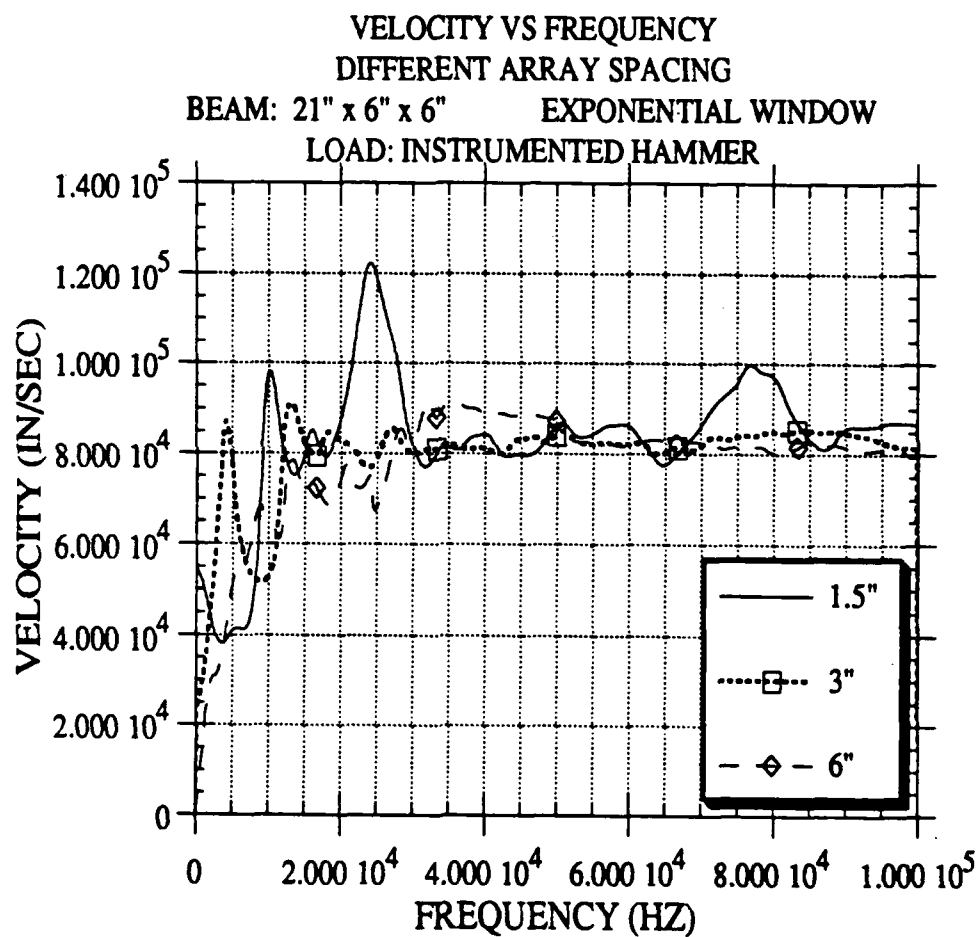


Figure 5.4 - 2 Dispersion Curve: Spacing Varied
Experimental Data, Beam (21" x 6" x 6"), Exponential Window

CHAPTER SIX

DAMAGED BEAMS

The objective of this research was to evaluate the effectiveness of the SASW method for the detection of cracks. This section presents analytical and experimental data for five different source-receiver-crack configurations and discusses the effect of the crack on the dispersion curve.

The five configurations investigated, shown in Figure 6 - 1, include load and receivers to one side of the crack (left or right), crack between the two receivers, crack between the source and receivers on the same face of the crack (top and bottom of element) and source and receivers on the side face.

Tests were conducted on a beam 21" x 6" x 6". Two array spacings were used: 3" and 6". Because the specimens were short (21"), it was often impossible to get the full 6" spacing between the load and first receiver; when this happened the distance between the load and first receiver was moved as close to 6" as possible. The cracks were cut in three different beams to depths of 1", 2" and 3". The width of the saw cut was an eighth of an inch. After the cracked beams were tested, the beams were repaired and retested. Acceleration measurements were used to calculate the dispersion curve, both analytically and experimentally.

Given the cross power phase diagram, there is a variety of ways to present the data, such as phase, unfolded phase, coherence, velocity vs frequency, velocity vs wavelength, and wavelength vs frequency. Each form presents the data in a different light and may highlight different features. The phase diagram, unfolded phase diagram and velocity vs frequency diagram will be presented. No coherence data are presented. Throughout this section the notation of array location (XL-XR1-XR2) stands for the location of the source from the left end, location of receiver one from the left end and location of receiver two from the left end of the

beam.

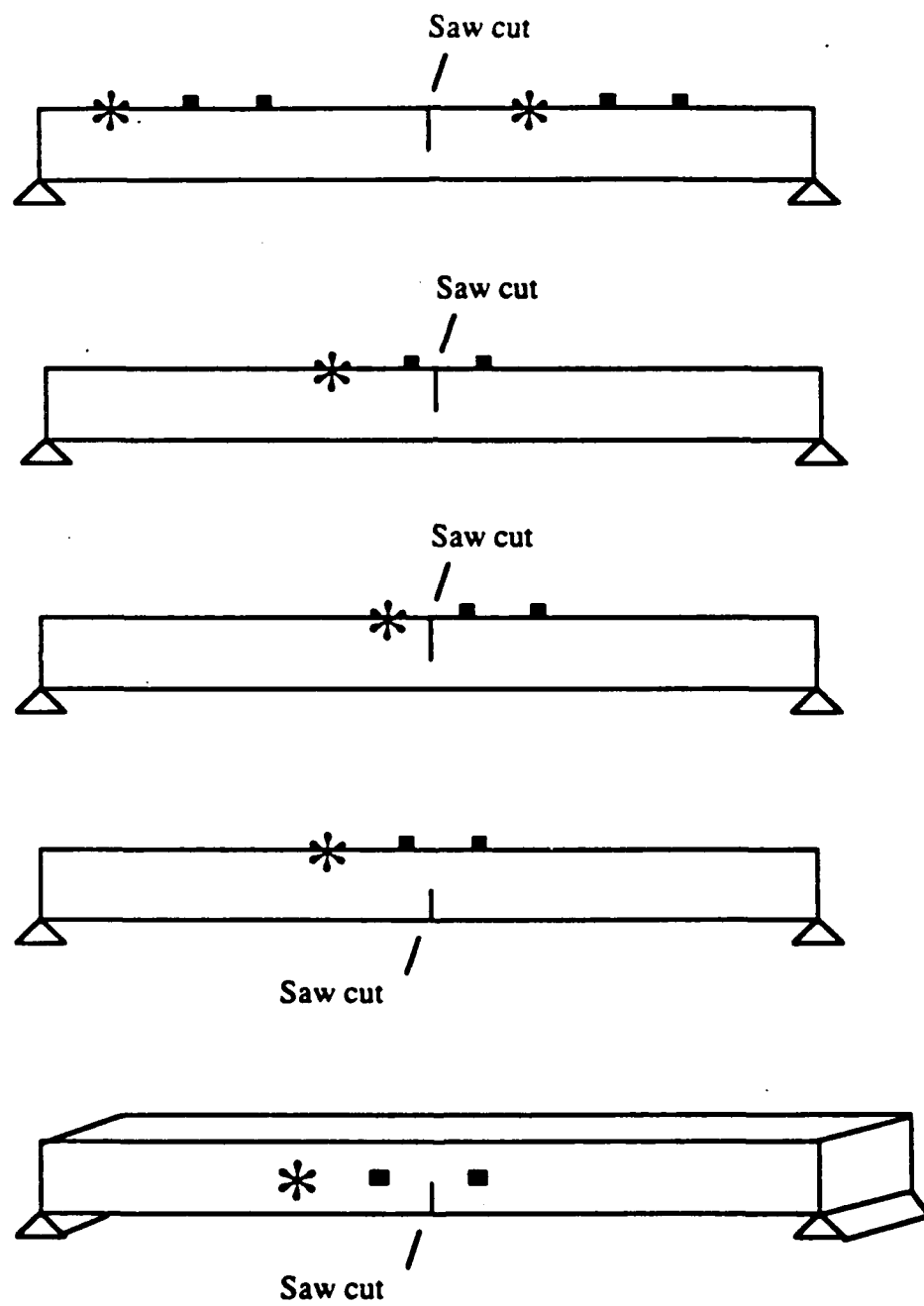


Figure 6 - 1 SASW Test Configurations

6.1 LOAD AND RECEIVERS TO THE SAME SIDE OF CRACK

When the load-receiver array is left or right of the crack as shown in Figure 6.1 -1 the dispersion curve is not affected by the crack. This will be shown for the three inch and six inch spacings, as well as for experimental and analytical data. Since the dispersion curve is not affected by the crack, this configuration is not effective for detecting or sizing the crack

Figure 6.1 - 2 shows the experimental phase diagrams for array location 3-6-9 (3" receiver spacing) for the beam with no damage, and the beams with 1", 2", 3" vertical cut at 10.5" from the left end (midpoint). Figure 6.1 - 3 compares the unfolded phase diagrams and Figures 6.1 - 4 and 6.1 - 5 show the experimental and analytical dispersion curves for this array location.

As can be seen in the comparison of the phase diagrams and dispersion curves, the crack does not affect the measurement for this configuration.

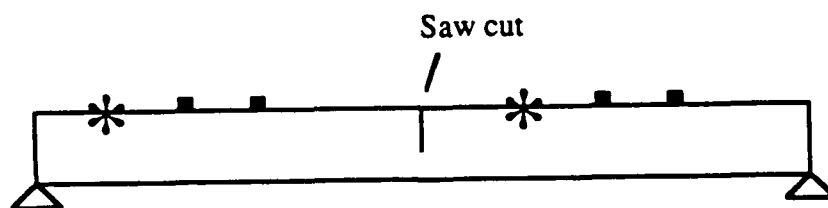


Figure 6.1 - 1 Test Configuration 1

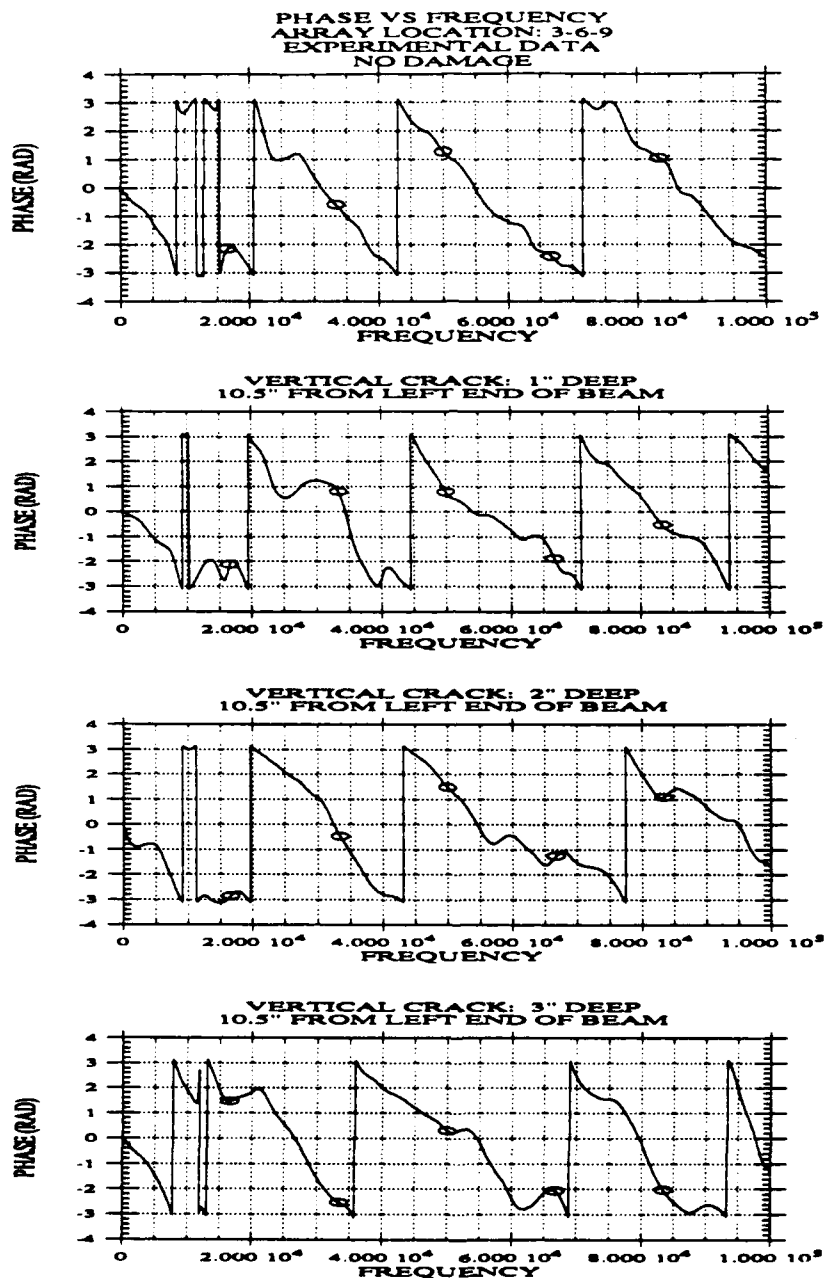


Figure 6.1 - 2 Phase Diagrams, 3" Spacing, Experimental Data, Test Configuration 1 : No Damage, 1", 2" and 3" Deep Crack

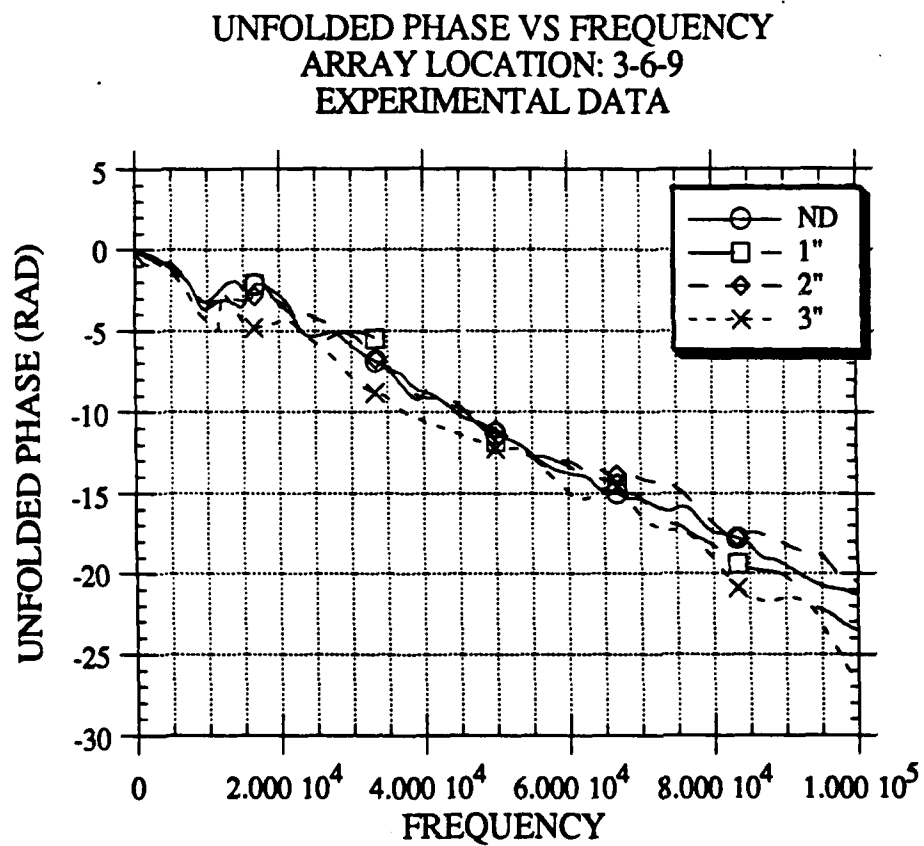


Figure 6.1 - 3 Unfolded Phase Diagrams, 3" Spacing, Experimental Data, Test Configuration 1 : No Damage, 1", 2" and 3" Deep Crack

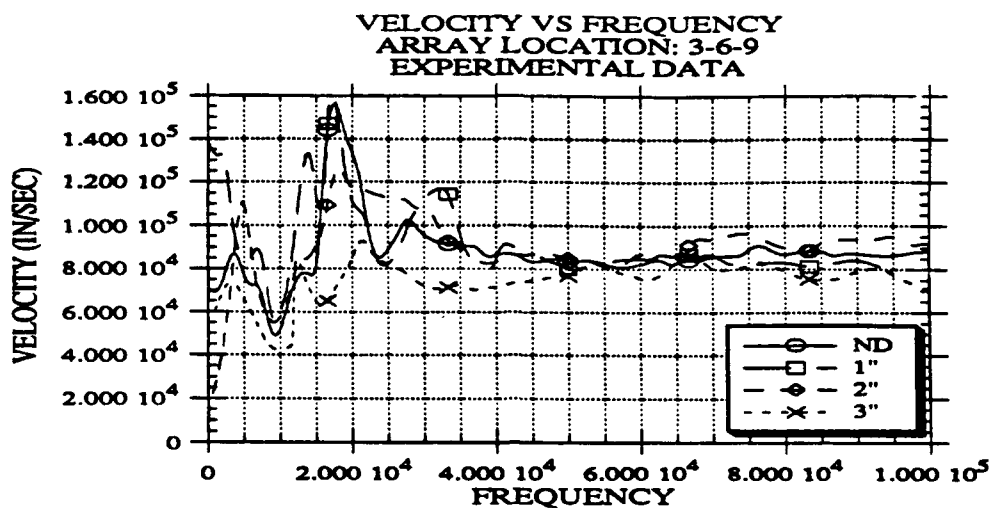


Figure 6.1 - 4 Dispersion Curve, 3" Spacing, Experimental Data, Test Configuration 1 : No Damage, 1", 2" and 3" Deep Crack

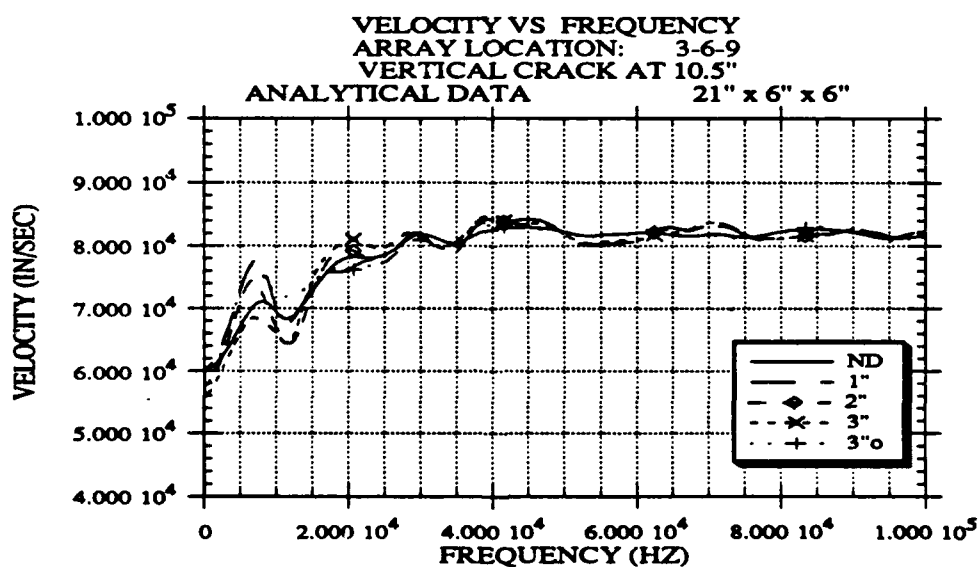


Figure 6.1 - 5 Dispersion Curve, 3" Spacing, Analytical Data, Test Configuration 1: No Damage, 1", 2" and 3" Deep Crack

Figure 6.1 - 6 shows the experimental phase diagrams for array location 1-2-8 (6" receiver spacing) for the beam with no damage, and the beams with 1", 2", 3" vertical cut at 10.5" from the left end. For the frequency range of 0 - 35 kHz the phase diagrams are not consistent. There are 2π phase shift at points of low coherence, usually around 12 kHz and 28 kHz, which must be taken into account when unfolding the phase diagram. For the frequency range above 35 kHz, the phase diagrams are consistent. Figure 6.1 - 7 shows the masked unfolded phase diagrams where the unfolded phase is masked from 10 - 18 kHz for the records from no damage, 1" and 2" beams. Figure 6.1 - 8 shows the experimental dispersion curve using the masked phase diagram. Figure 6.1 - 9 shows the analytical dispersion curve for same location. For the analytical data, the coherence was always high and 2π phase ambiguities due to low coherence were not a problem. Again, the six inch spacing shows that when the source-receiver array is to one side of the crack, the crack does not affect the measurement, hence this configuration is not effective at detecting the crack.

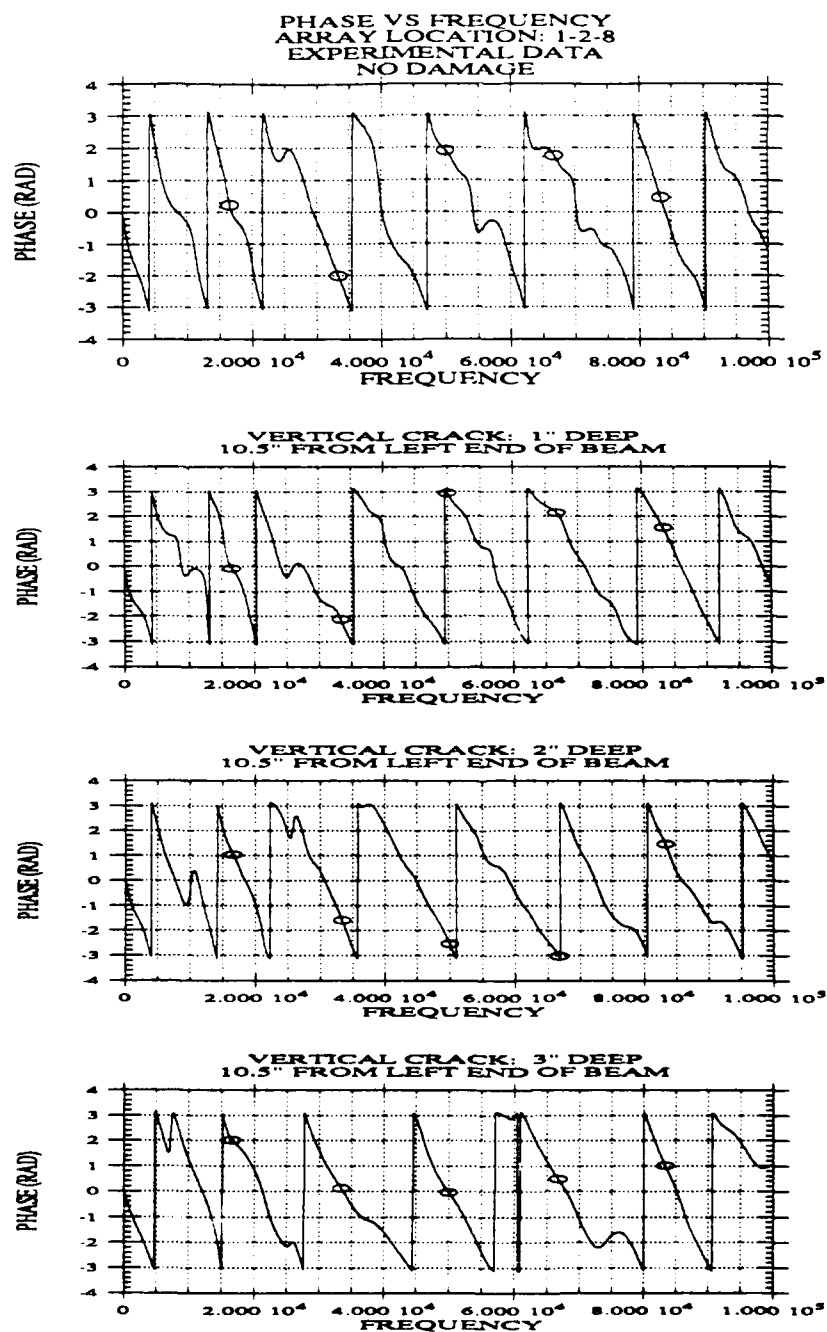


Figure 6.1 - 6 Phase Diagrams, 6" Spacing, Experimental Data, Test Configuration 1 : No Damage, 1", 2" and 3" Deep Crack

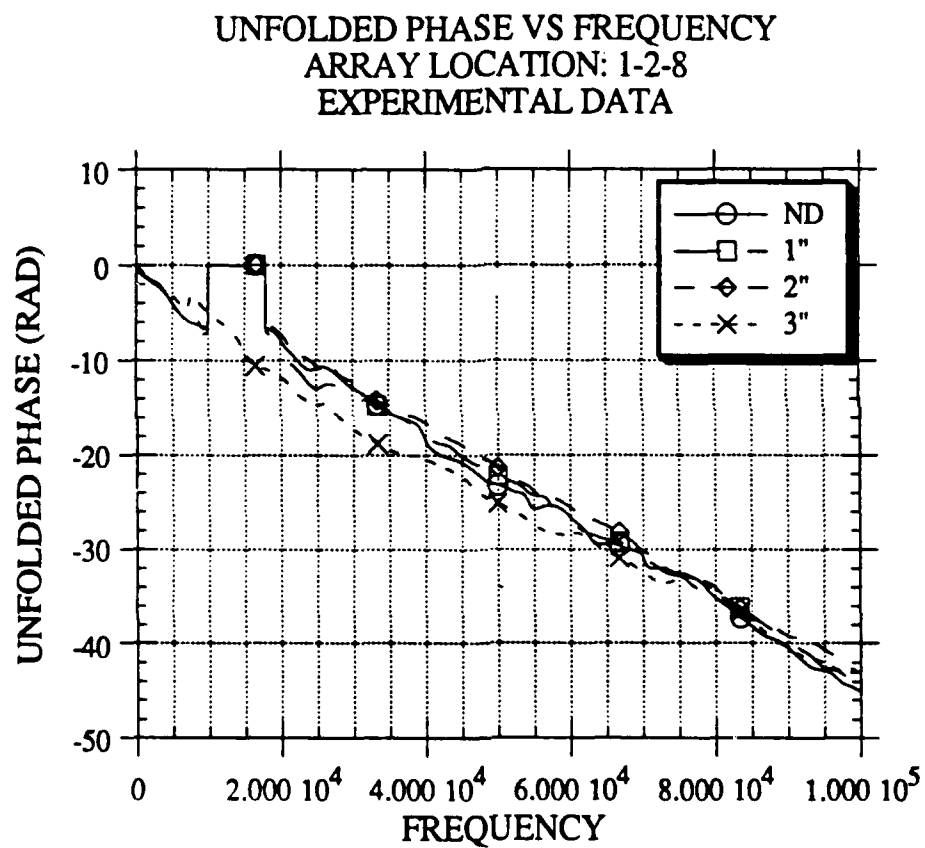


Figure 6.1 - 7 Unfolded Phase Diagrams, 6" Spacing, Experimental Data, Test Configuration 1 : No Damage, 1", 2" and 3" Deep Crack

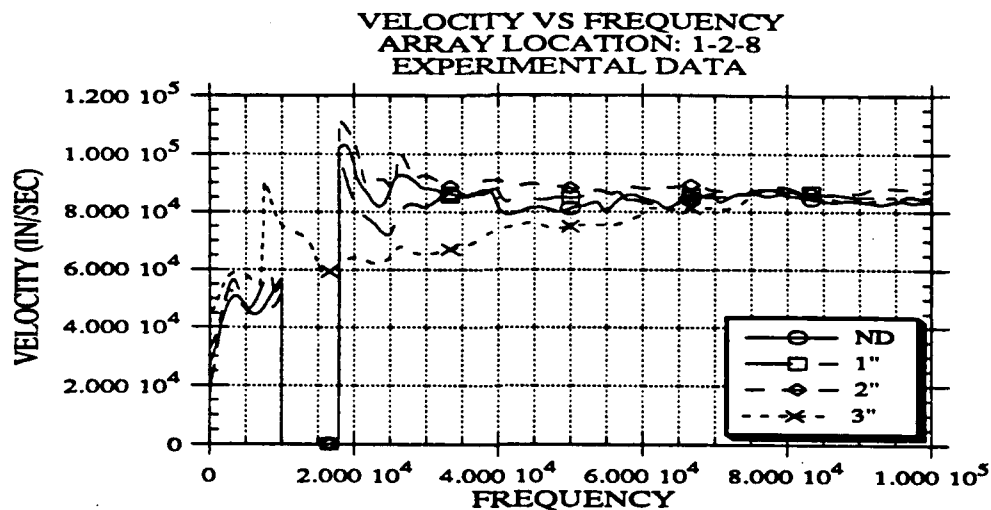


Figure 6.1 - 8 Dispersion Curve, 6" Spacing, Experimental Data, Test Configuration 1: No Damage, 1", 2" and 3" Deep Crack

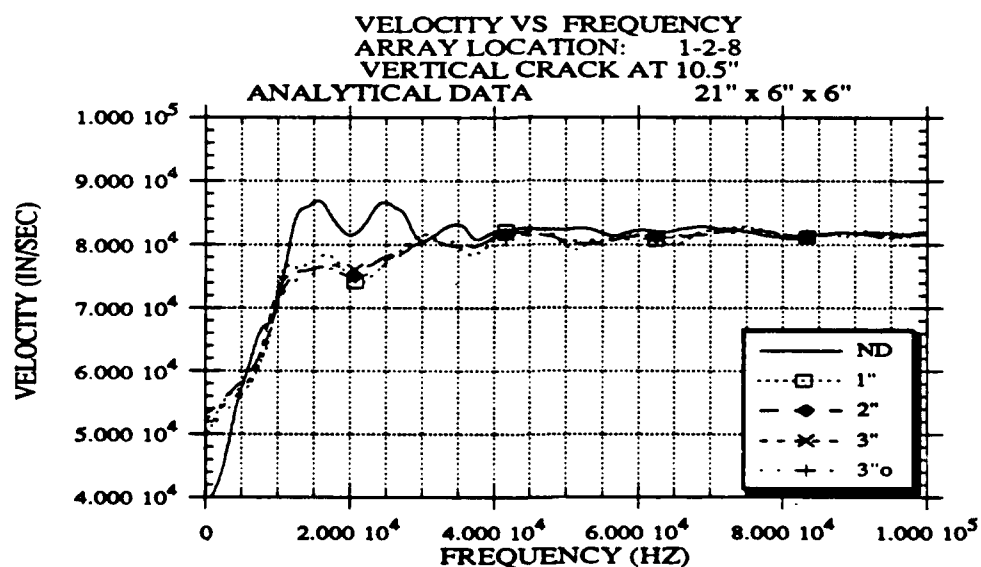


Figure 6.1 - 9 Dispersion Curve, 6" Spacing, Analytical Data, Test Configuration 1: No Damage, 1", 2" and 3" Deep Crack

6.2 CRACK BETWEEN THE TWO RECEIVERS

6.2.1 CRACKS

When the the crack is between the two receivers and on the same face, as shown in Figure 6.2.1 - 1, the phase is greater for the cracked condition than that for the uncracked condition. Greater phase implies a lower velocity of propagation. This trend is true for both analytical and experimental results.

This configuration (crack between the receivers) is effective at detecting cracks, as seen in the following figures. This is true for the three inch and six inch spacings, but the results are different for the two cases. The three inch spacing predicts lower apparent velocity of propagation than the six inch spacing, and both spacings predict lower apparent velocity of propagation than for the undamaged case.

As the depth of the crack changes, the changes in the dispersion curve as predicted from finite element data and measured experimentally do not show good agreement, also they do show the same trend.

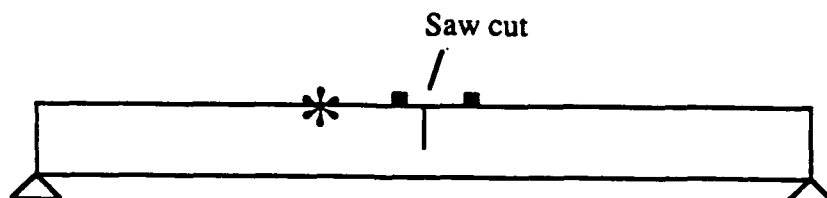


Figure 6.2.1 - 1 Test Configuration 2

Figures 6.2.1 - 2 to 6.2.1 - 5 show phase, unfolded phase, and the dispersion curve for the three inch receiver spacing with the source-receiver array at 5-8-11. It should be noted that for the records taken on the damaged beams the coherence was low for all frequencies, as such no masking was attempted on the data and the data was unfolded as measured. Figure 6.2.1 - 2 shows that the phase diagram from a damaged section is different from that of an undamaged section. This difference manifests itself in the dispersion curve, as shown in Figure 6.2.1 - 4, by a lower apparent velocity of propagation for the damaged sections.

Figures 6.2.1 - 6 to 6.2.1 -9 show phase, unfolded phase, and the dispersion curve for the six inch receiver spacing with the source-receiver array at 1-5-11. Again the coherence was low throughout each of the damaged records and the records were unfolded as measured. Figure 6.2.1 - 8 shows that the apparent velocity of propagation is lower for the damaged beams than for the undamaged ones.

In an attempt to size the crack, the array configuration was chosen so that the second receiver was just past the crack. In Vu's dissertation, it was shown that for the location just past the crack, the transmission coefficient at that point (as compared to other locations) had the greatest sensitivity to crack depth. As such the array configuration of 5 - 8 - 11 and 1 - 5 - 11 were used, as this put the second receiver just past the crack. For these array locations, the dispersion curve did show the greatest variation with crack depth as compared to other array locations. However, as can be seen in Figure 6.2.1 - 4 and Figure 6.2.1 -8, the dispersion curve does not change in a consistent manner with change in crack depth, which makes it hard to use the change in the dispersion curve to size the crack.

The effect of the actual position of the crack between the two receivers, is shown in Figures 6.2.1 - 10 to 6.2.1 - 15 for both the three inch and six inch spacing. These figures show that the calculated dispersion curve is not affected by the actual crack position relative to the two receivers for a given spacing. Again, there is poor agreement between the experimental and the numerical data.

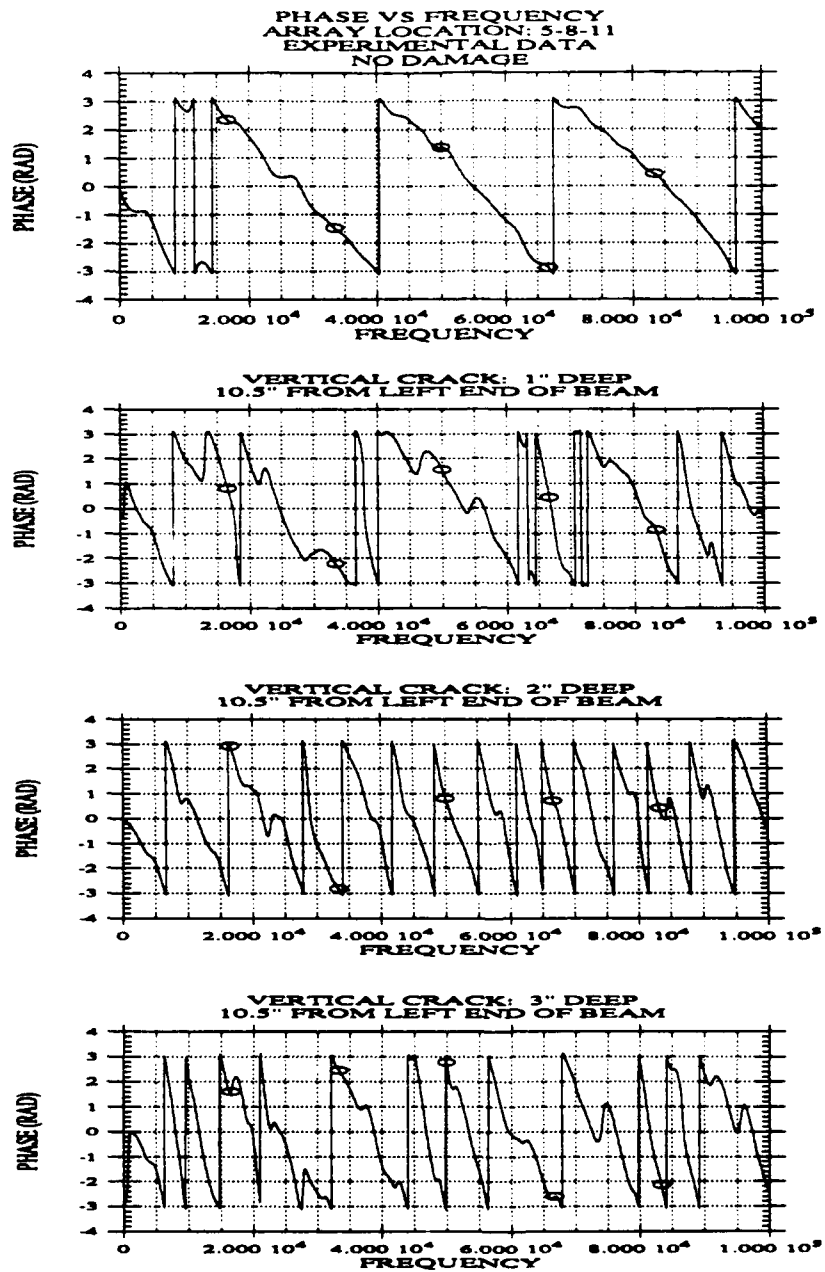


Figure 6.2.1 - 2 Phase Diagrams, 3" Spacing, Experimental Data, Test Configuration 2 : No Damage, 1", 2" and 3" Deep Crack

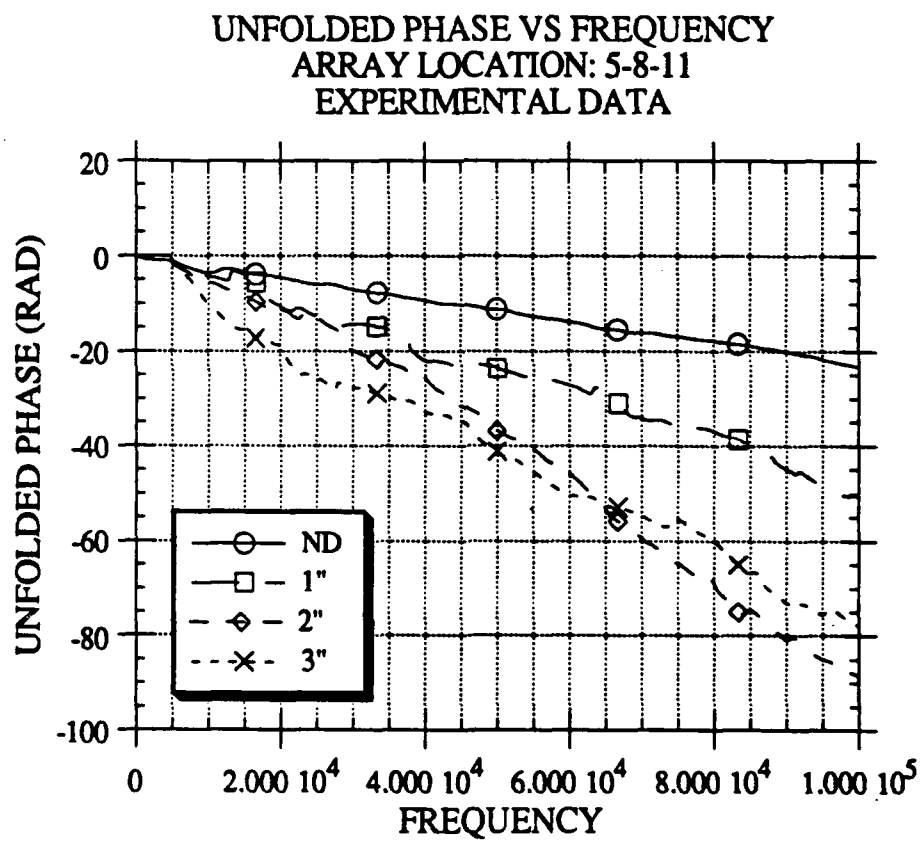


Figure 6.2.1 - 3 Phase Diagrams, 3" Spacing, Experimental Data, Test Configuration 2 : No Damage, 1", 2" and 3" Deep Crack

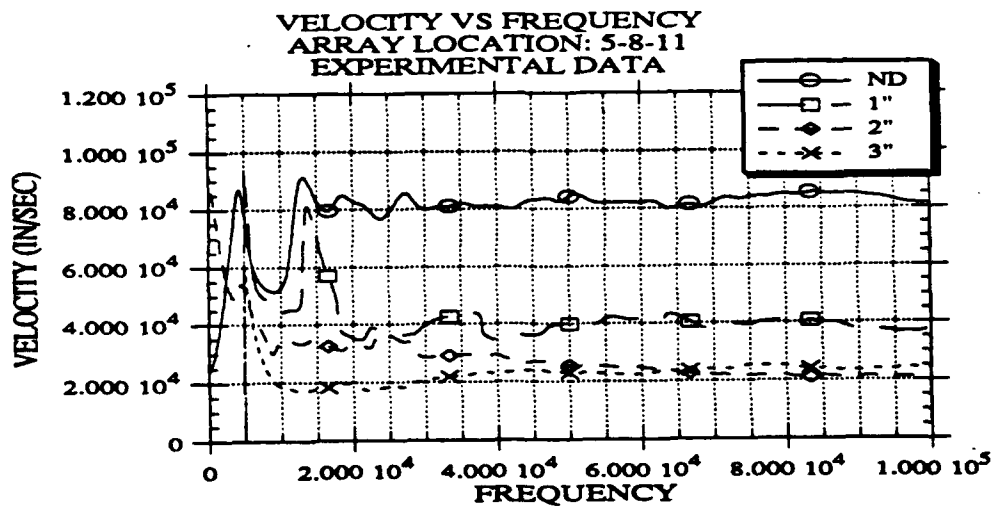


Figure 6.2.1 - 4 Dispersion Curve, 3" Spacing, Experimental Data, Test Configuration 2 : No Damage, 1", 2" and 3" Deep Crack

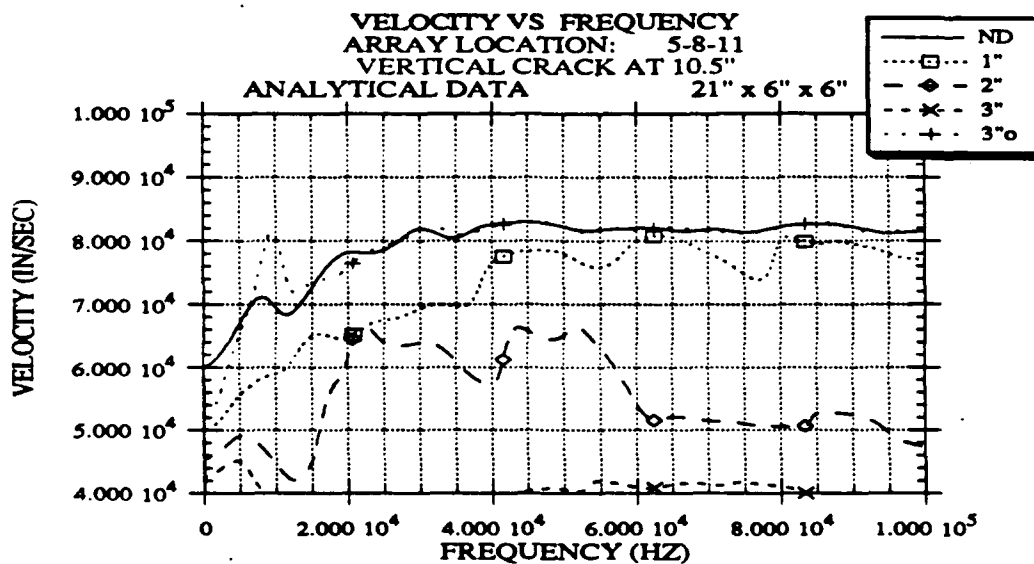


Figure 6.2.1 - 5 Dispersion Curve, 3" Spacing, Analytical Data, Test Configuration 2: No Damage, 1", 2" and 3" Deep Crack

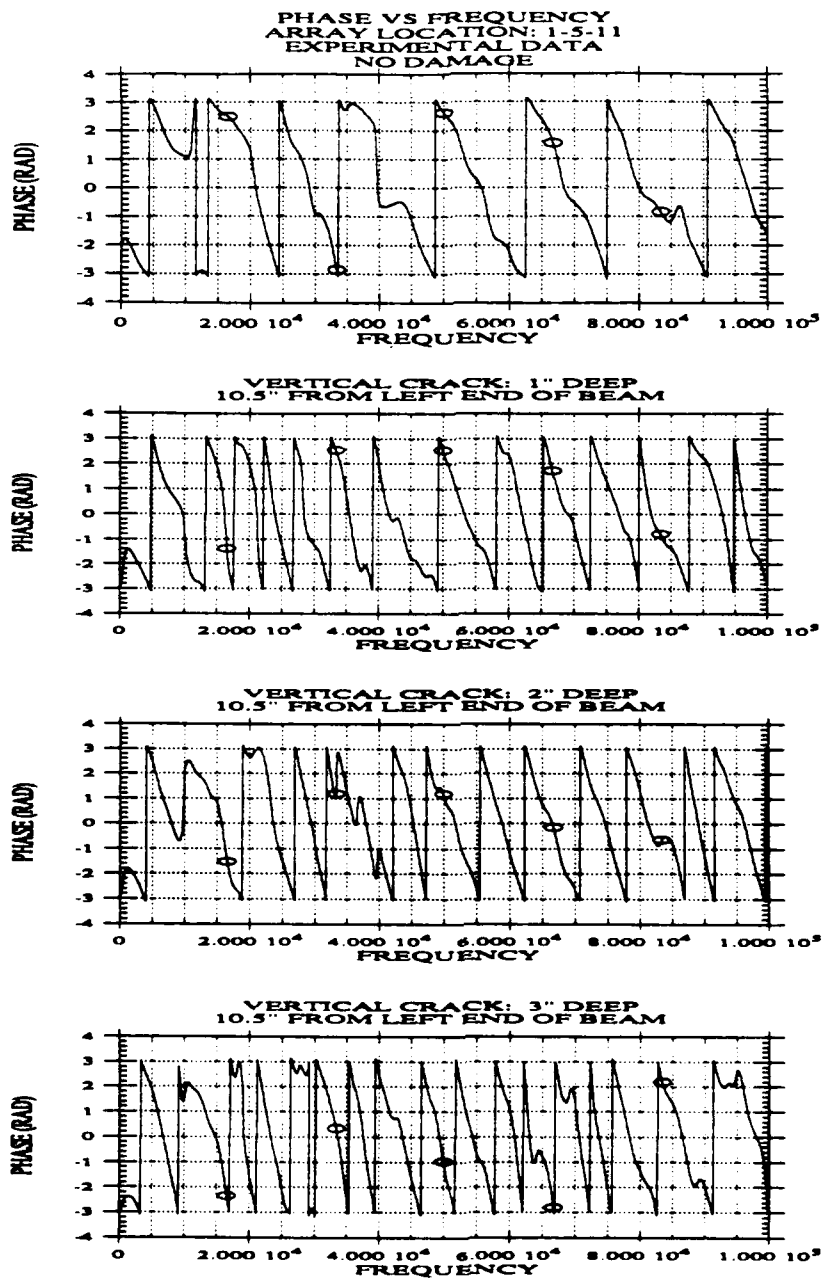


Figure 6.2.1 - 6 Phase Diagrams, 6" Spacing, Experimental Data, Test Configuration 2: No Damage, 1", 2" and 3" Deep Crack

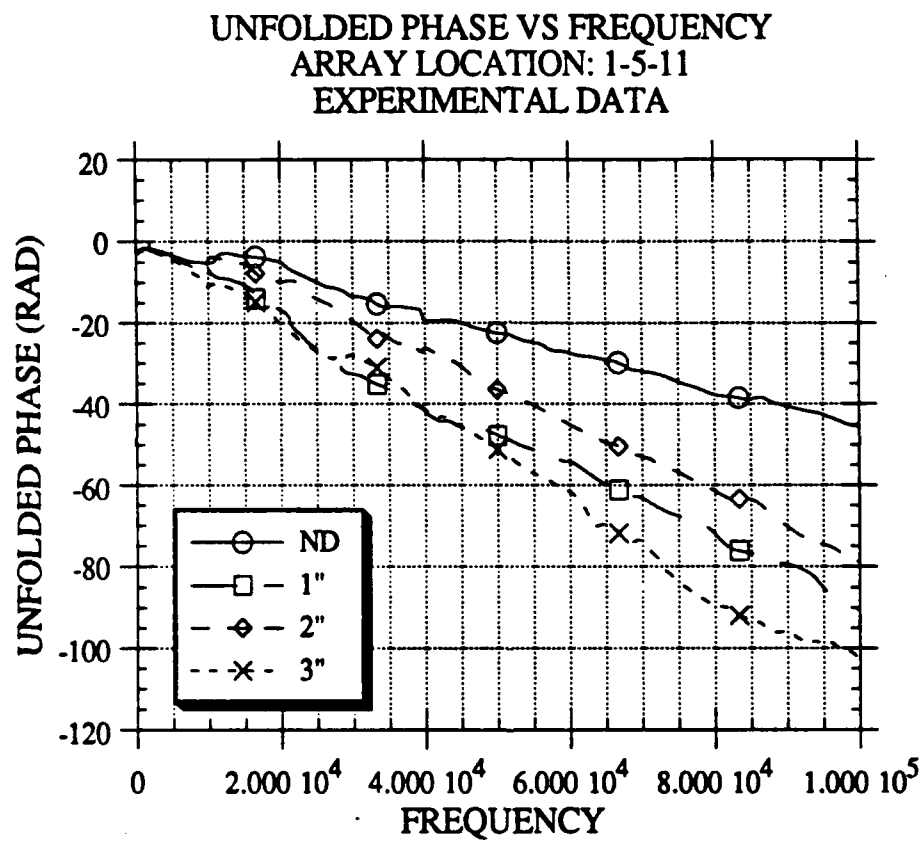


Figure 6.2.1 - 7 Phase Diagrams, 6" Spacing, Experimental Data, Test Configuration 2 : No Damage, 1", 2" and 3" Deep Crack

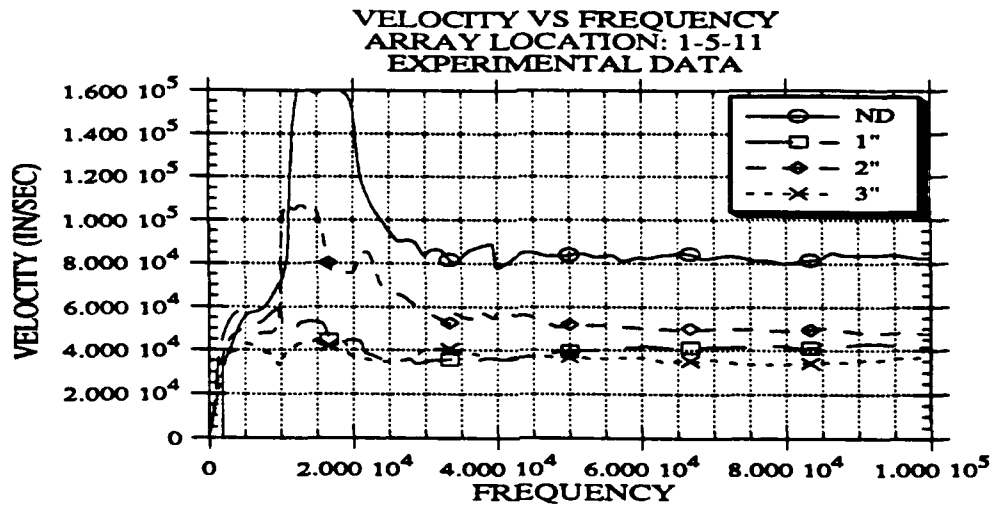


Figure 6.2.1 - 8 Dispersion Curve, 6" Spacing, Experimental Data, Test Configuration 2: No Damage, 1", 2" and 3" Deep Crack

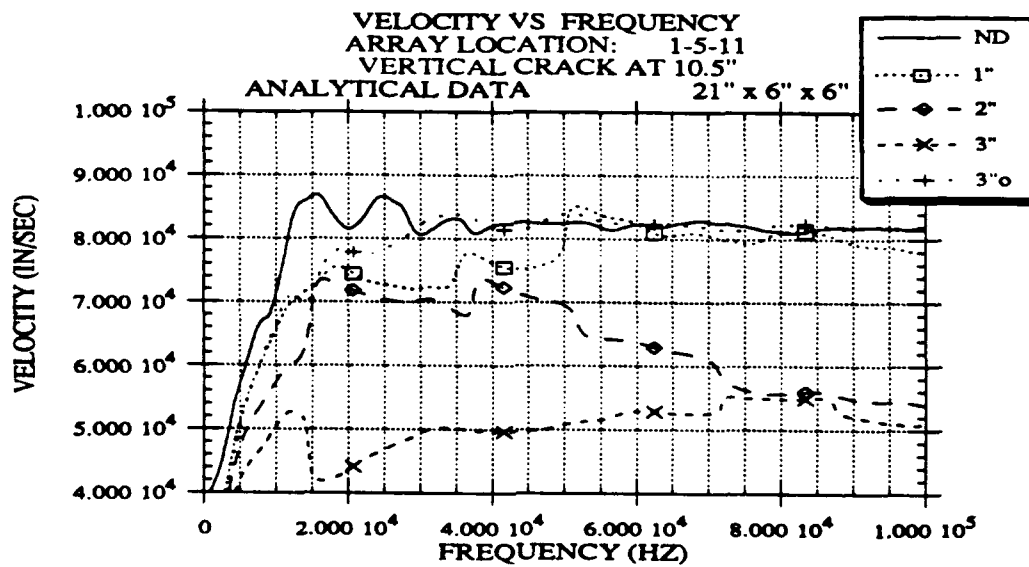


Figure 6.2.1 - 9 Dispersion Curve, 6" Spacing, Analytical Data, Test Configuration 2: No Damage, 1", 2" and 3" Deep Crack

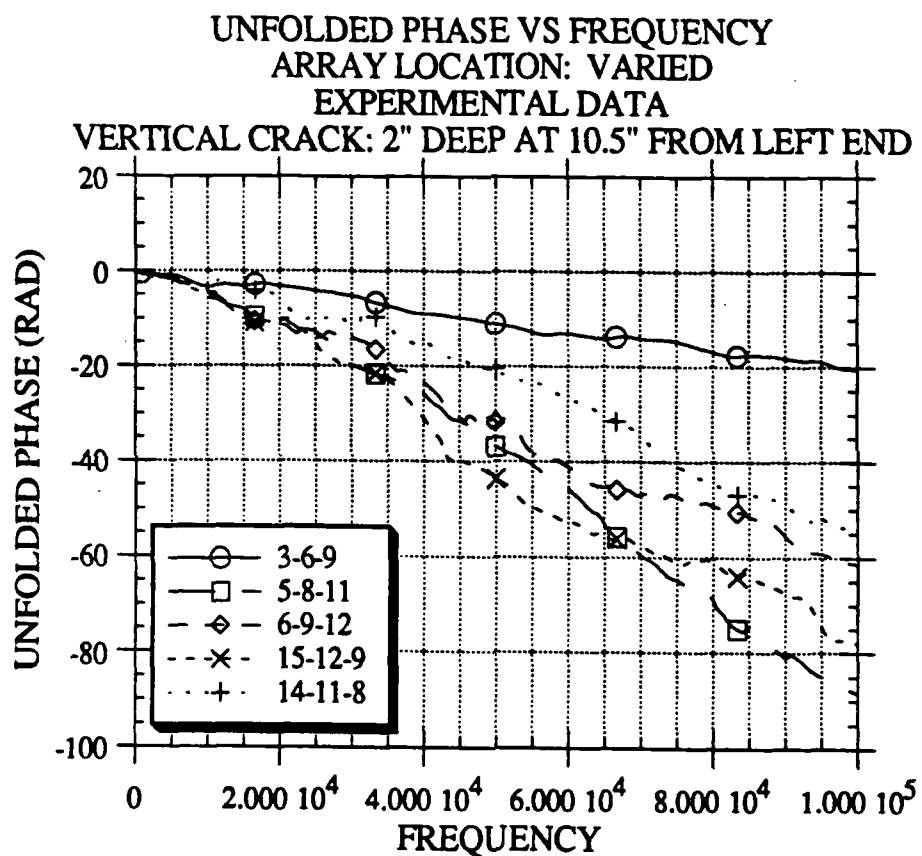


Figure 6.2.1 - 10 Phase Diagrams, 3" Spacing, Experimental Data, Test Configuration 2, 2" Deep Crack, Array Location Varied

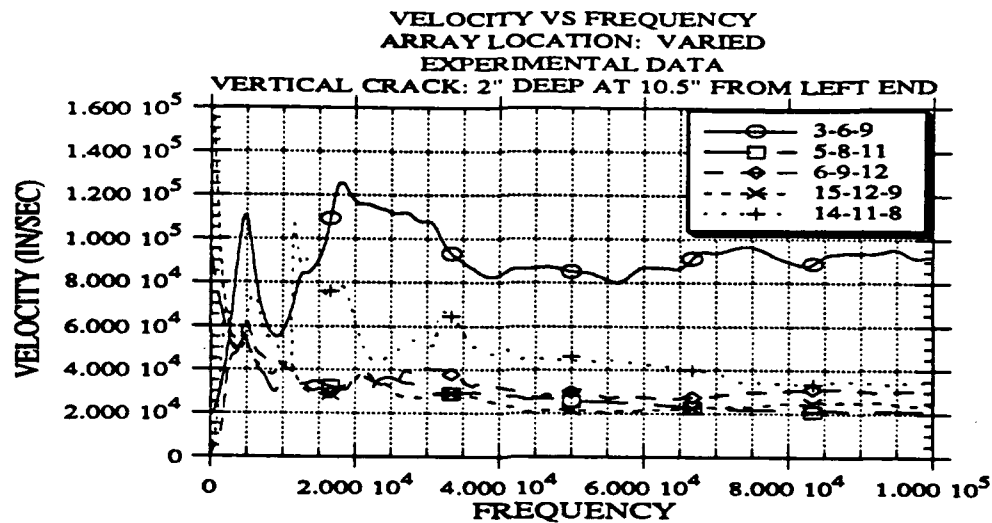


Figure 6.2.1 - 11 Dispersion Curve, 3" Spacing, Experimental Data, Test Configuration 2, 2" Deep Crack, Array Location Varied

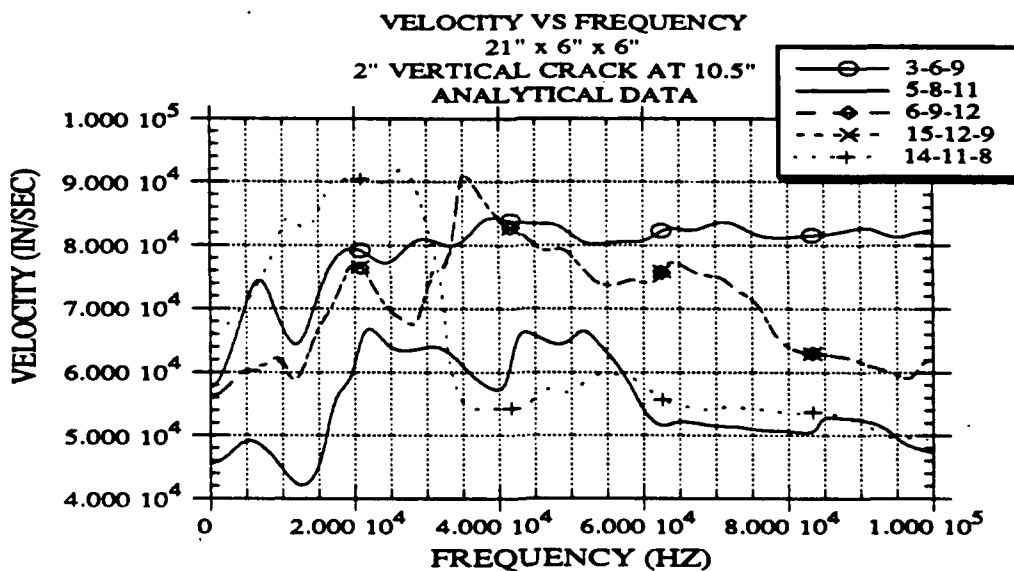


Figure 6.2.1 - 12 Dispersion Curve, 3" Spacing, Analytical Data, Test Configuration 2, 2" Deep Crack, Array Location Varied

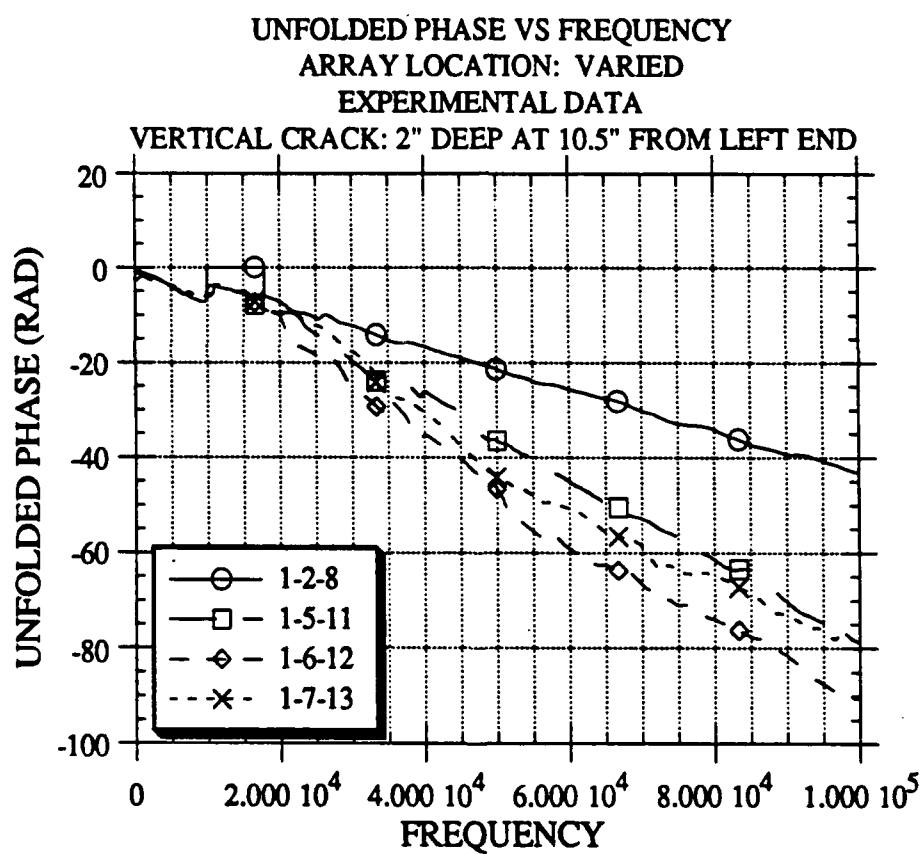


Figure 6.2.1 - 13 Phase Diagrams, 6" Spacing, Experimental Data, Test Configuration 2, 2" Deep Crack, Array Location Varied

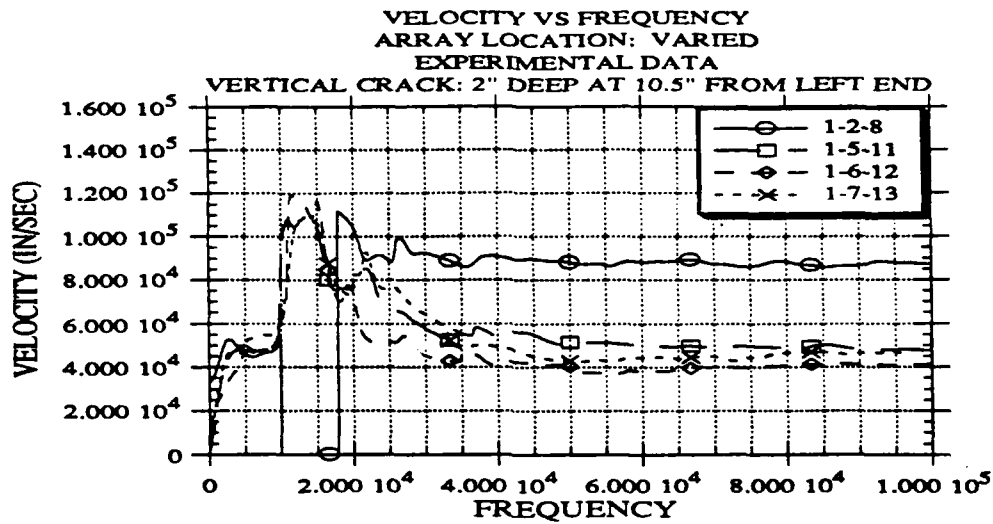


Figure 6.2.1 - 14 Dispersion Curve, 6" Spacing, Experimental Data, Test Configuration 2, 2" Deep Crack, Array Location Varied

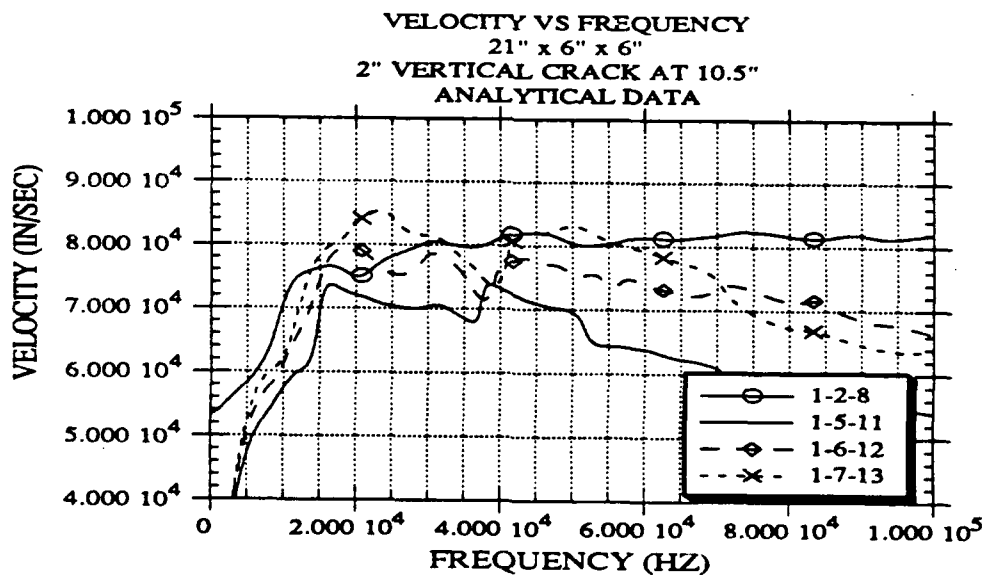


Figure 6.2.1 - 15 Dispersion Curve, 6" Spacing, Analytical Data, Test Configuration 2, 2" Deep Crack, Array Location Varied

6.2.2 REPAIRED CRACKS

After the beams were tested, they were repaired filling the cracks with Quikcrete - Fast Setting Cement. The beams were retested with the crack between the receivers. The dispersion curve from the repaired beams were similar to those of the undamaged case for the 3" spacing and the 6" spacing.

Figure 6.2.2 - 1 shows the experimental phase diagrams for array location 5-8-11 (3" receiver spacing) for the beam with no damage, and the repaired beams with 1", 2", 3" vertical cut at 10.5" from the left end. Figure 6.2.2 - 2 compares the unfolded phase diagrams and Figures 6.2.2 - 3 shows the experimental dispersion curves for this array location. This shows the dispersion curve for the repaired beams, where the second receiver was just past the repair, give the same results as the undamaged beam.

Figures 6.2.2 - 4 to 6.2.1 -6 show phase, unfolded phase, and the dispersion curve for the six inch receiver spacing with the source-receiver array at 1-5-11 on the repaired beams. In unfolding the phase diagrams, the data was masked for the 10 - 15 kHz range in the 2" record, and 25 - 30 kHz range for the 1", 2" and 3" records. Again, the dispersion curve for the repaired beams, where the second receiver was just past the repair, give the same results as the undamaged beam.

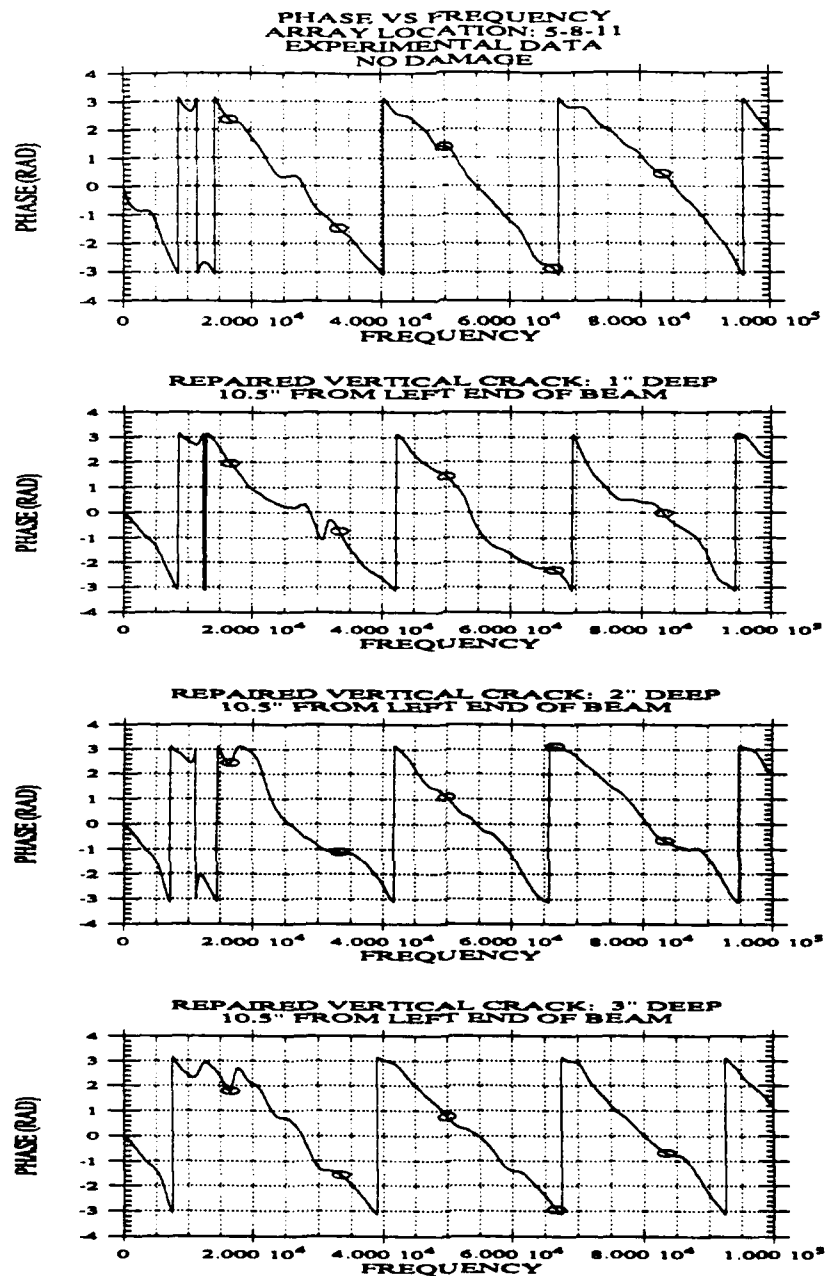


Figure 6.2.2 - 1 Phase Diagrams from Repaired Beams, 3" Spacing, Experimental Data, Test Configuration 2 : No Damage, 1", 2" and 3" Deep Crack

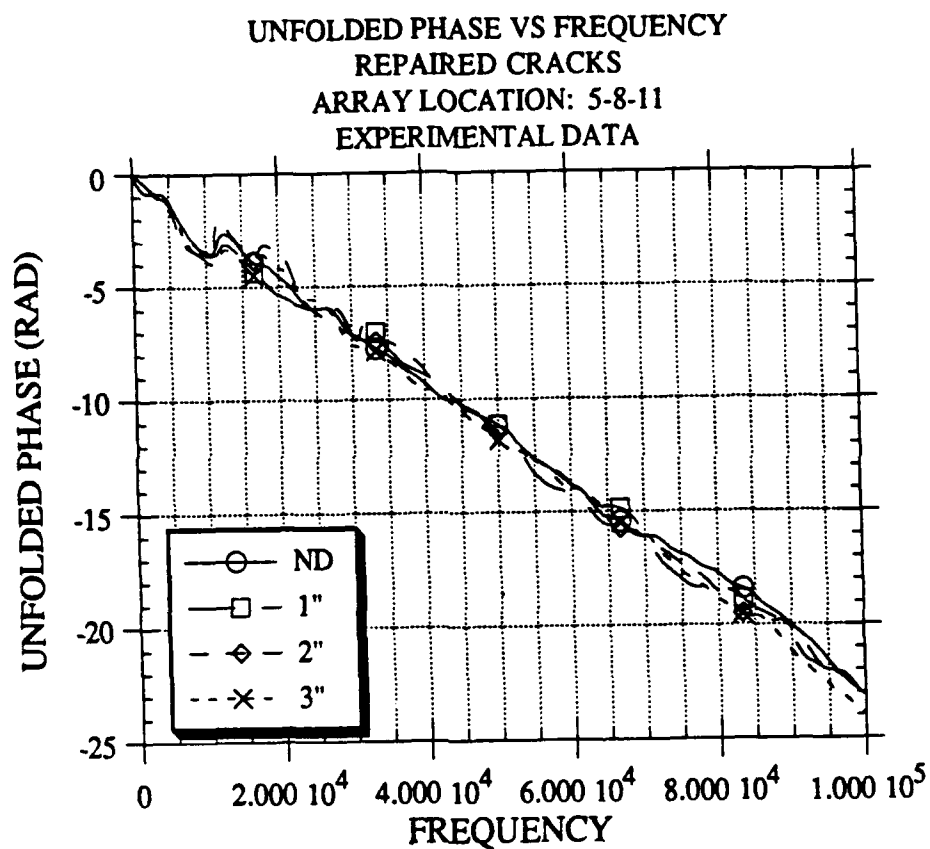


Figure 6.2.2 - 2 Phase Diagrams from Repaired Beams, 3" Spacing, Experimental Data, Test Configuration 2 : No Damage, 1", 2" and 3" Deep Crack

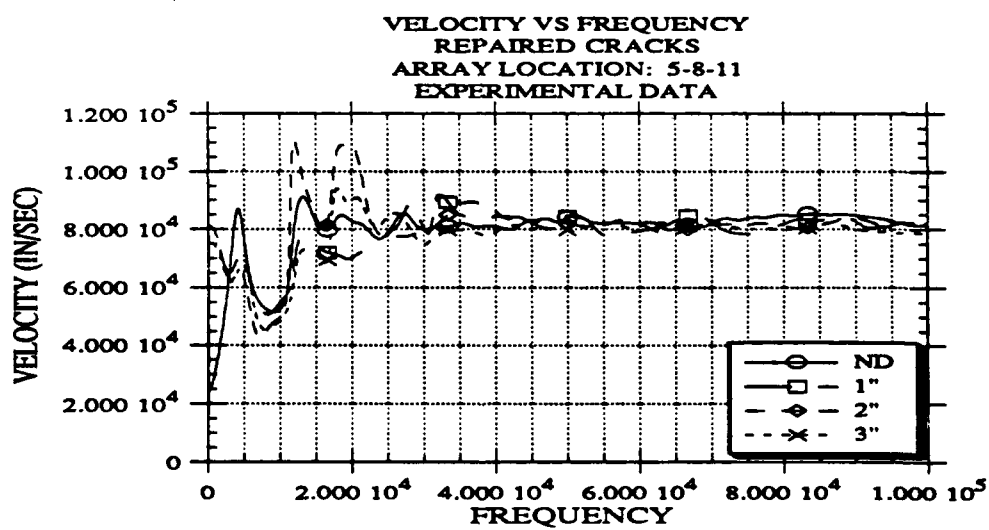


Figure 6.2.2 - 3 Dispersion Curve from Repaired Beams, 3" Spacing,
Experimental Data, Test Configuration 2 : No Damage, 1", 2" and 3" Deep Crack

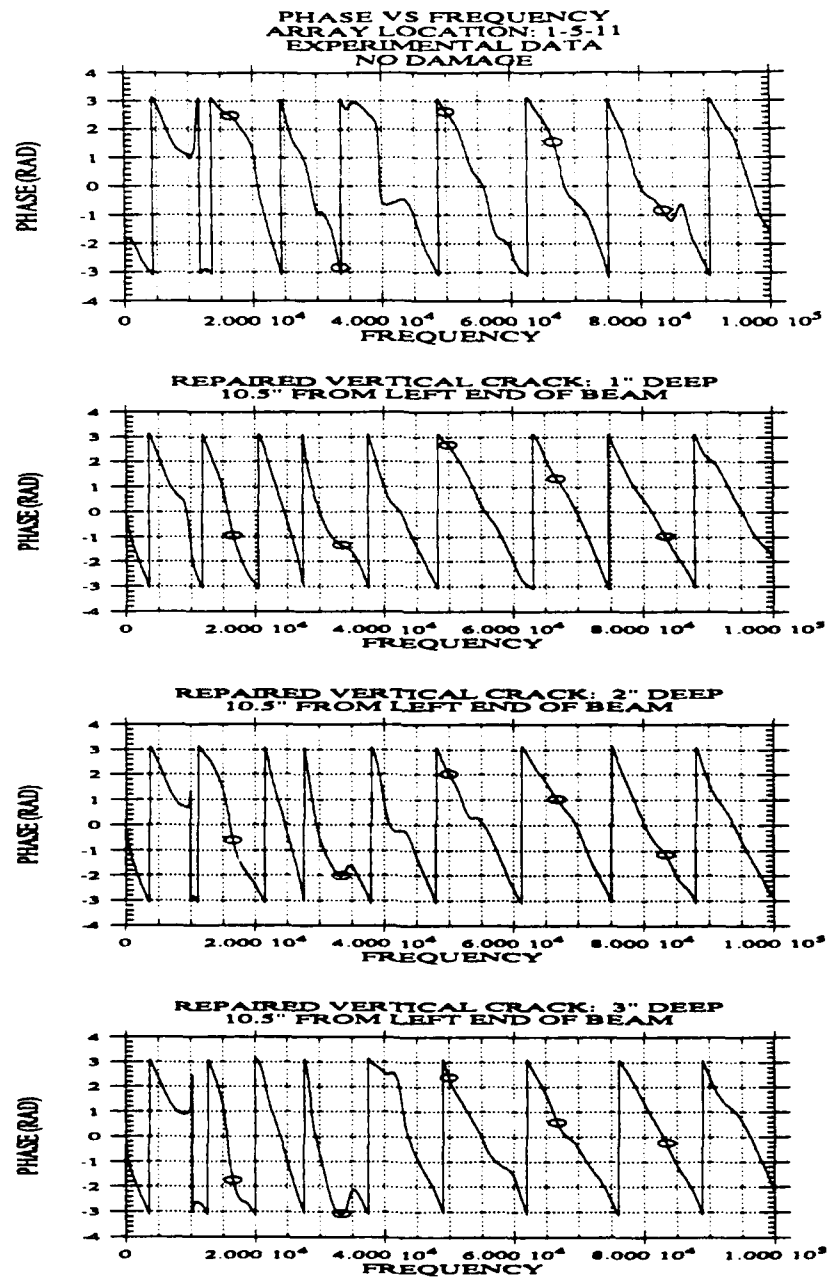


Figure 6.2.2 - 4 Phase Diagrams from Repaired Beams, 6" Spacing, Experimental Data, Test Configuration 2 : No Damage, 1", 2" and 3" Deep Crack

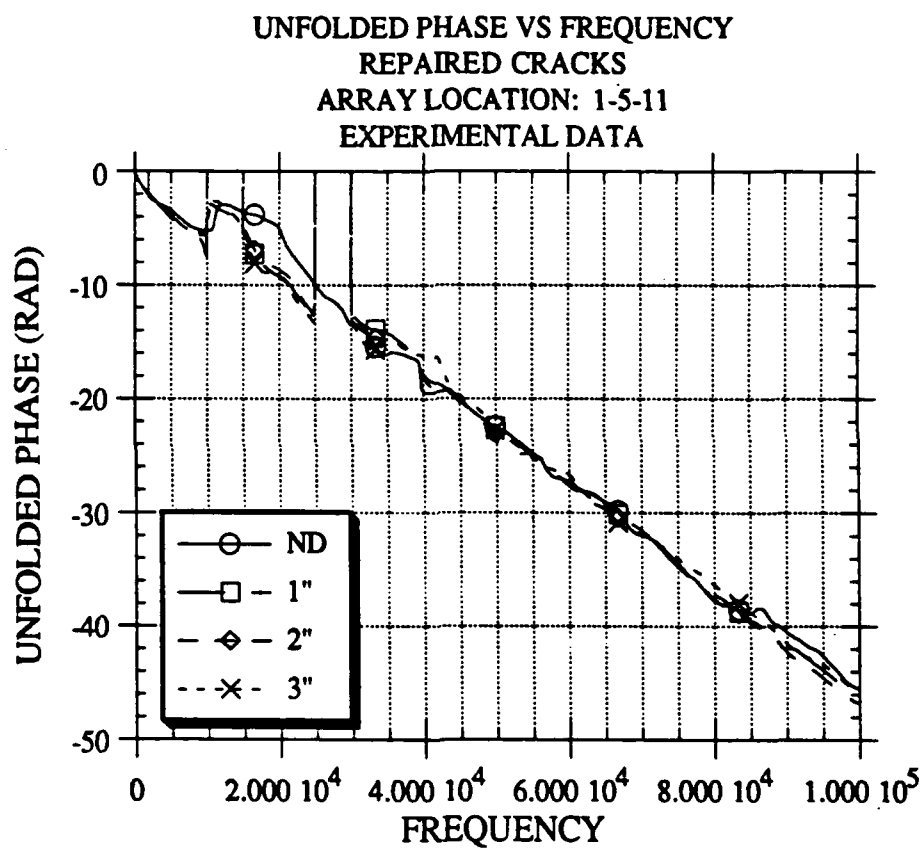


Figure 6.2.2 - 5 Phase Diagrams from Repaired Beams, 6" Spacing, Experimental Data, Test Configuration 2 : No Damage, 1", 2" and 3" Deep Crack

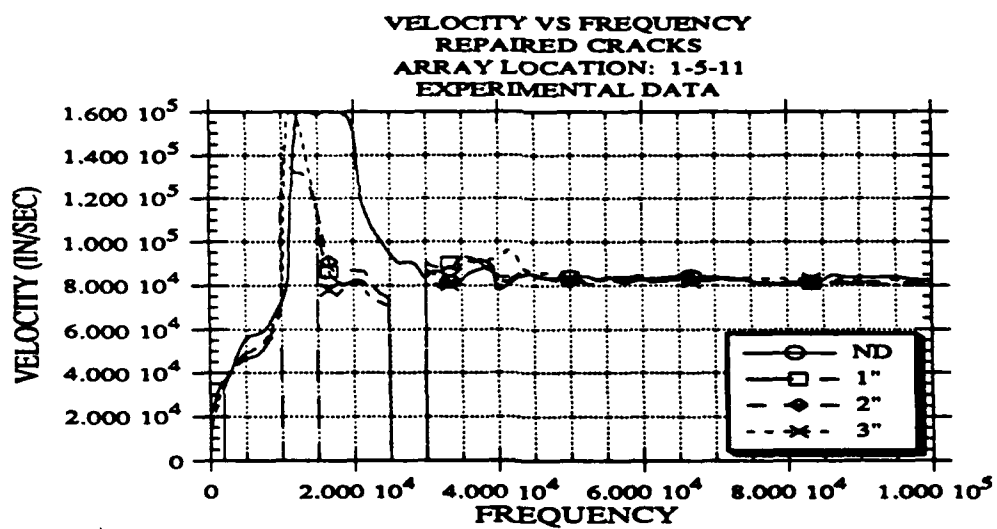


Figure 6.2.2 - 6 Dispersion Curve from Repaired Beams, 6" Spacing,
Experimental Data, Test Configuration 2: No Damage, 1", 2" and 3" Deep Crack

6.3 CRACK BETWEEN LOAD AND FIRST RECEIVER

When the load is left of the crack and the receivers are right of the crack, as shown in Figure 6.3 - 1, the dispersion curve is affected and the difference between undamaged and damaged condition is evident. This configuration detects the crack. The dispersion curve does not change in a consistent pattern with crack depth, and thus the changes in the dispersion curve cannot be easily used to size the crack. It is interesting to notice that in this case, the effect of the crack is to decrease the phase and as such to increase the apparent velocity of propagation. The agreement between the analytical and the experimental results is again poor although they both show the same trend.

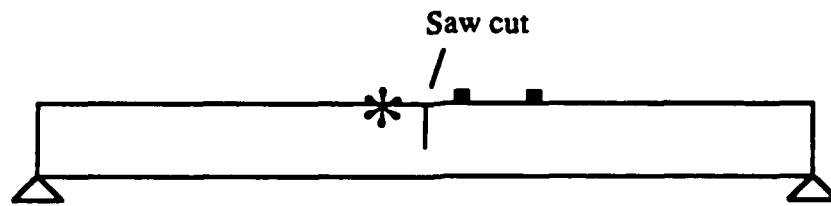


Figure 6.3 - 1 Test Configuration 3

Figures 6.3 - 2 to 6.3 - 5 show phase, unfolded phase, and the dispersion curve for the three inch receiver spacing with the source-receiver array at 12-9-6. It should be noted that for the records taken on the damaged beams the coherence was low for all frequencies; as such no masking was attempted and the data was unfolded as measured. Figure 6.3 - 2 shows that the phase diagrams from a damaged section is different from that of an undamaged section. This difference manifests itself in the dispersion curve, as shown in Figure 6.3 - 4, by a higher apparent velocity of propagation in the high frequencies for the damaged sections.

Figures 6.3 - 6 to 6.3 - 9 show phase, unfolded phase, and the dispersion curve for the six inch receiver spacing with the source-receiver array at 14-8-2. Again the coherence was low throughout each of the damaged records and the records were unfolded as measured. Figure 6.3 - 8 shows that the apparent velocity of propagation is higher for the high frequencies in the damaged records.

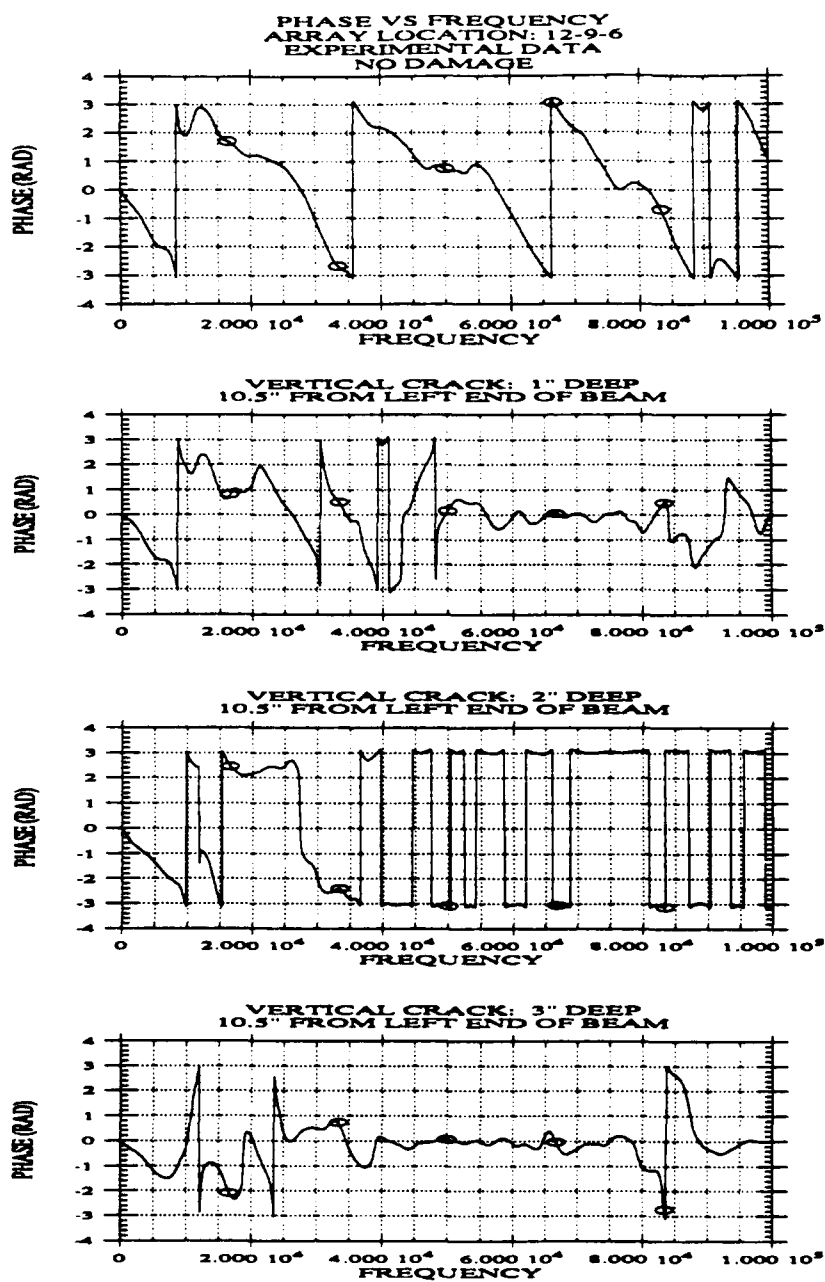


Figure 6.3 - 2 Phase Diagrams, 3" Spacing, Experimental Data, Test Configuration 3 : No Damage, 1", 2" and 3" Deep Crack

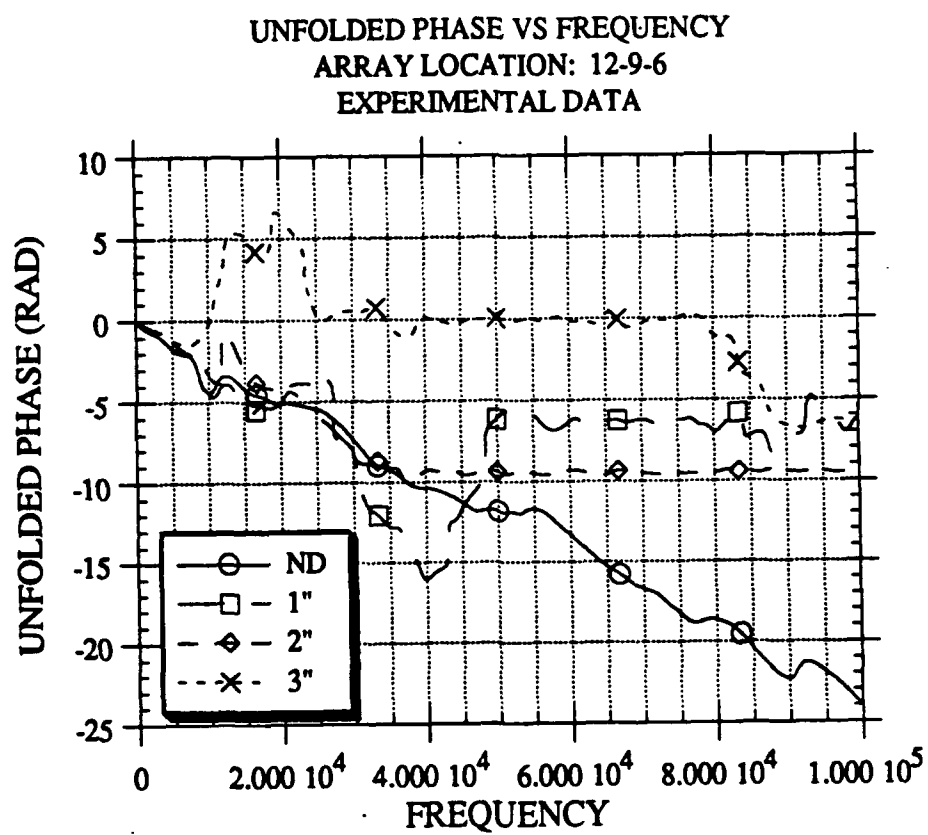


Figure 6.3 - 3 Phase Diagrams, 3" Spacing, Experimental Data, Test Configuration 3 : No Damage, 1", 2" and 3" Deep Crack

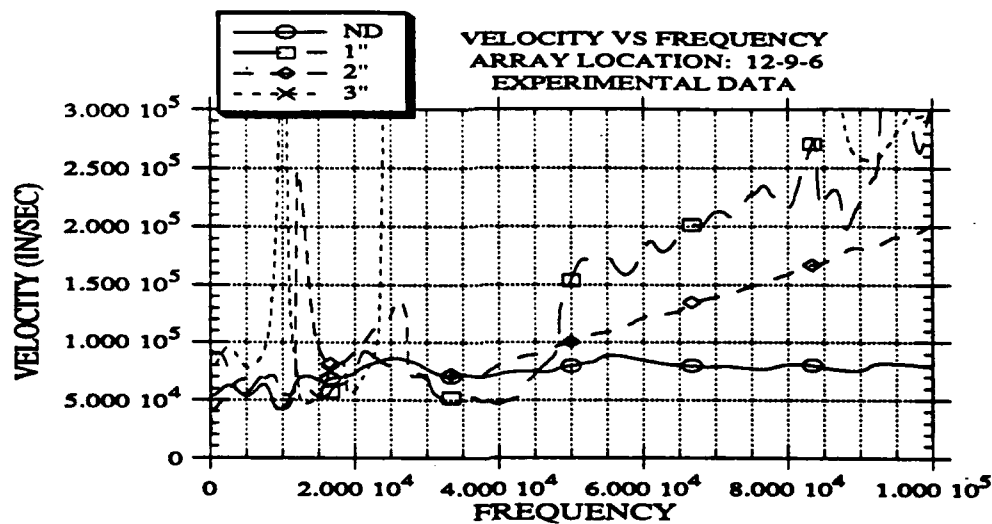


Figure 6.3 - 4 Dispersion Curve, 3" Spacing, Experimental Data, Test Configuration 3 : No Damage, 1", 2" and 3" Deep Crack

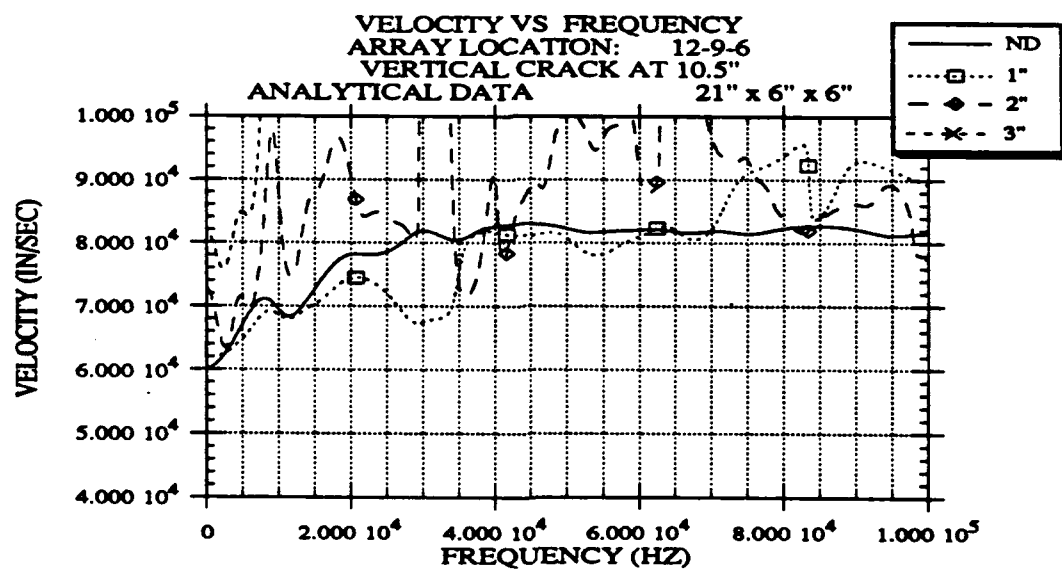


Figure 6.3 - 5 Dispersion Curve, 3" Spacing, Analytical Data, Test Configuration 3: No Damage, 1", 2" and 3" Deep Crack

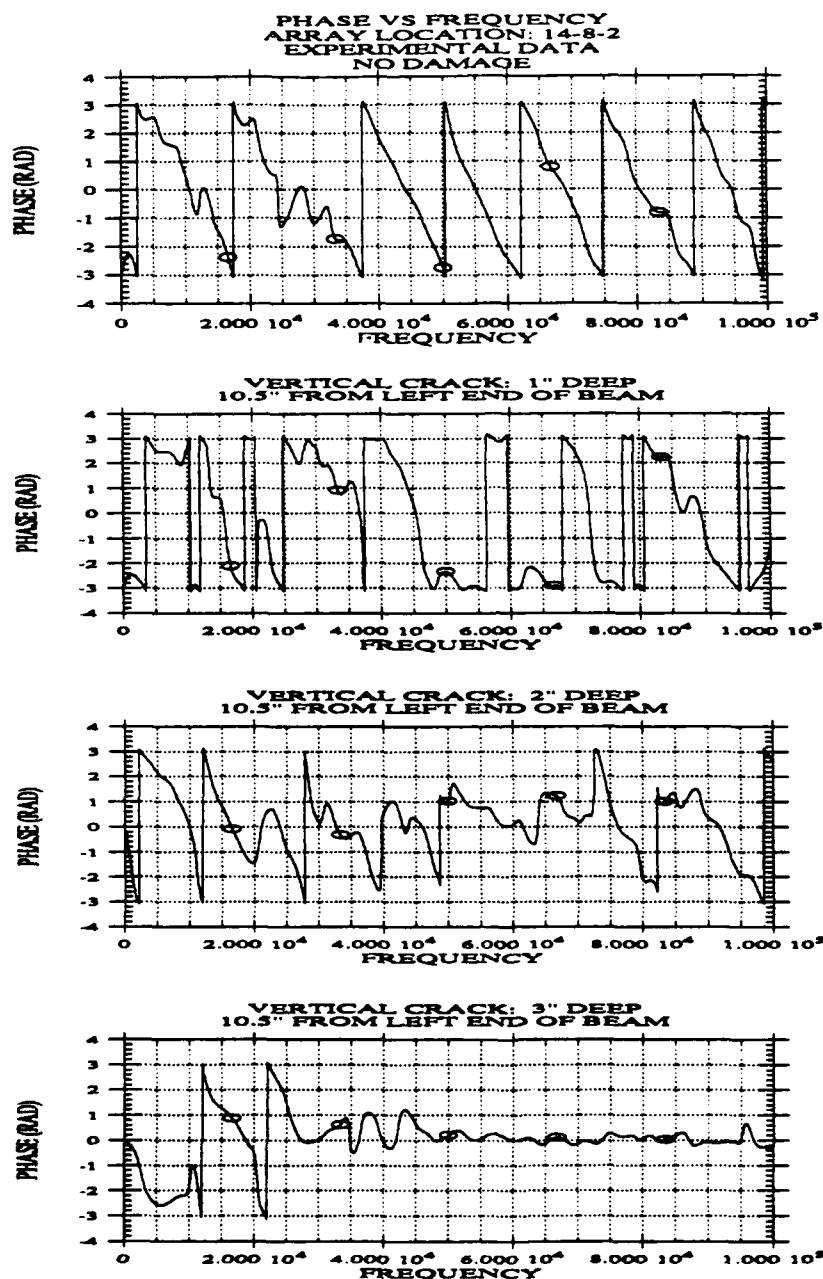


Figure 6.3 - 6 Phase Diagrams, 6" Spacing, Experimental Data, Test Configuration 3 : No Damage, 1", 2" and 3" Deep Crack

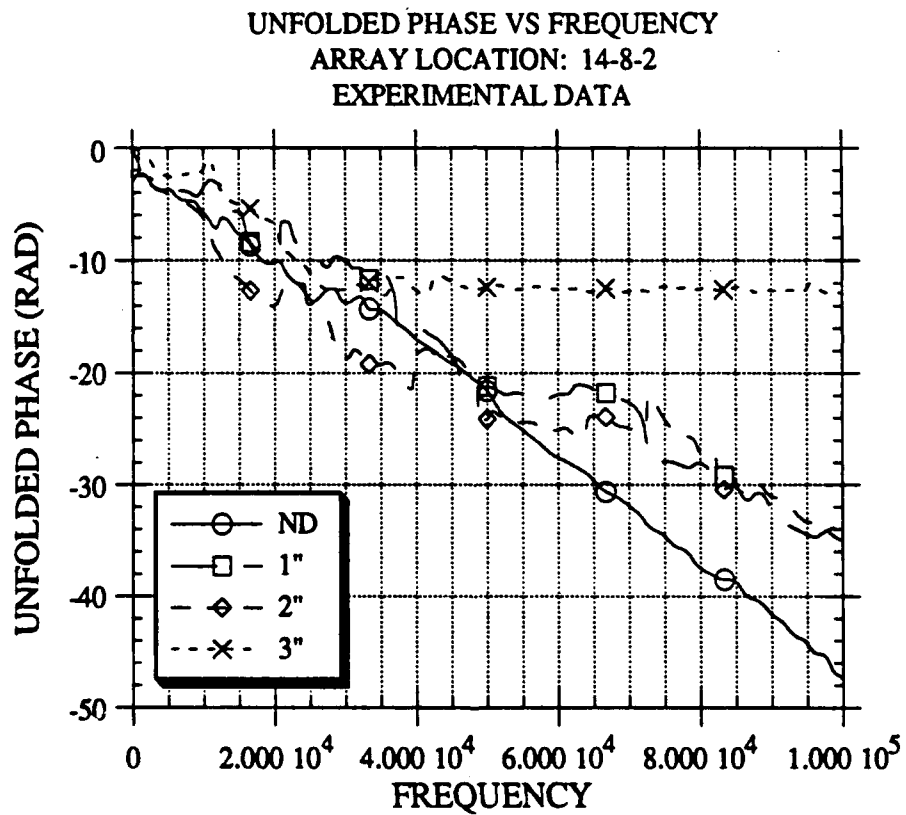


Figure 6.3 - 7 Phase Diagrams, 6" Spacing, Experimental Data, Test Configuration 3 : No Damage, 1", 2" and 3" Deep Crack

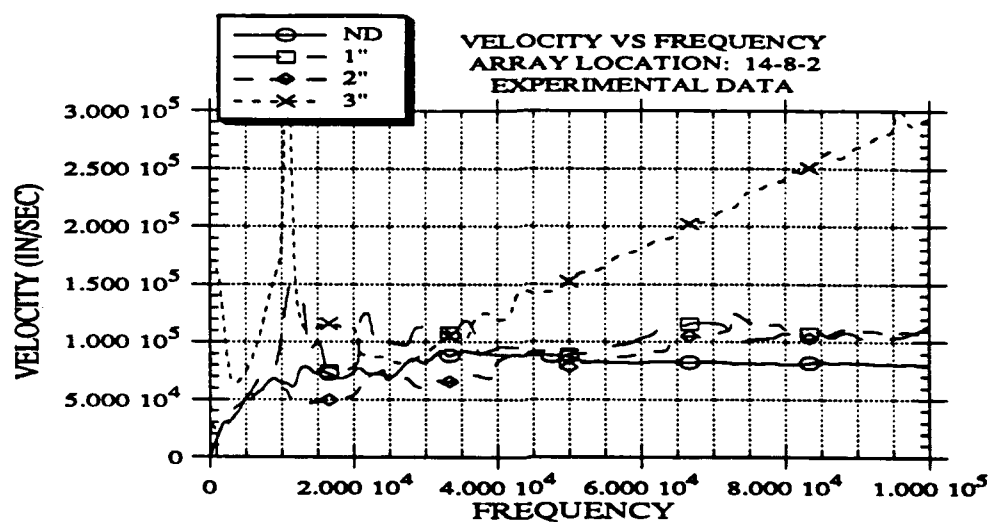


Figure 6.3 - 8 Dispersion Curve, 6" Spacing, Experimental Data, Test Configuration 3: No Damage, 1", 2" and 3" Deep Crack

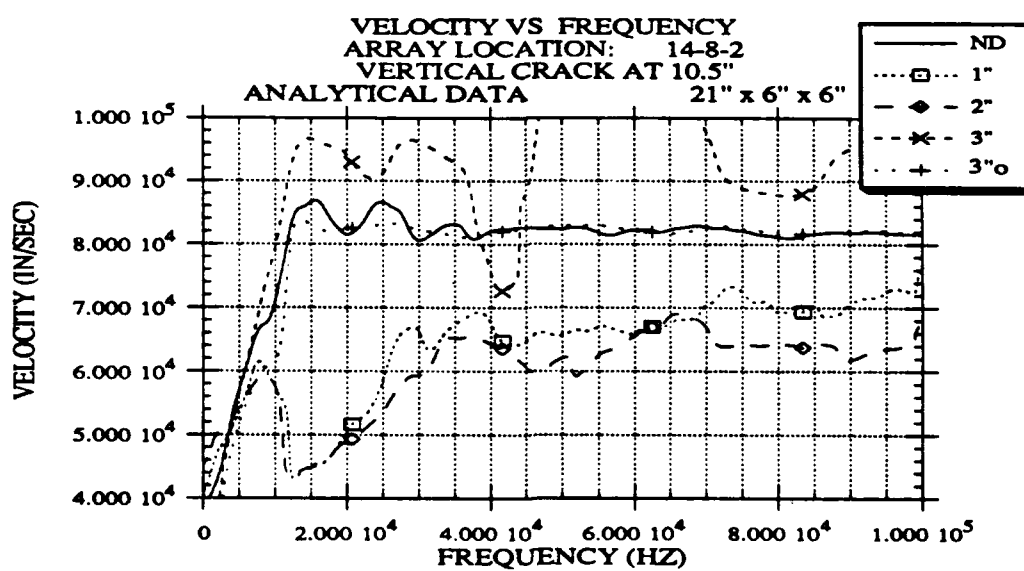


Figure 6.3 - 9 Dispersion Curve, 6" Spacing, Analytical Data, Test Configuration 3: No Damage, 1", 2" and 3" Deep Crack

6.4 LOAD AND RECEIVER ON OPPOSITE FACE OF CRACK

When the load and the receivers are on top of the beam and the crack is on the bottom, as shown in Figure 6.4 - 1, the analytical results predict no change in the dispersion curve over the range of frequencies of interest (where the results are reliable). Also the experimental results show little change in the dispersion curve. As such this configuration was not effective at detecting the crack.

Figure 6.4 - 2 shows the experimental phase diagrams for several array location with a 3" receiver spacing for the beam with a 3" deep vertical cut at 10.5" from the left end. The phase diagram for 15-12-9 is not shown in Figure 6.4 - 2, but shown in the unfolded state in Figure 6.4 - 3. Figure 6.4 - 3 compares the unfolded phase diagrams. In the 14-11-8 record, the phase was masked from 10 - 15 kHz where there was a range of low coherence. Figures 6.4 - 4 and 6.4 - 5 show the experimental and analytical dispersion curves.

Similar results are seen for the 6" receiver spacings, and this configuration does not detect the crack as shown in Figures 6.4 - 6 through 6.4 - 9. In unfolding the phase diagrams, ranges of low coherence were masked. In the 1-5-11 record, the data masked was 20 - 30 kHz. In the 1-7-13 record, the data masked was 11 - 15 kHz.

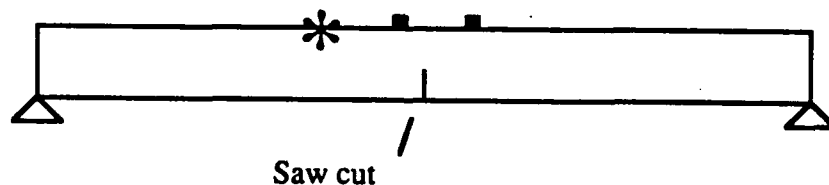


Figure 6.4 - 1 Test Configuration 4

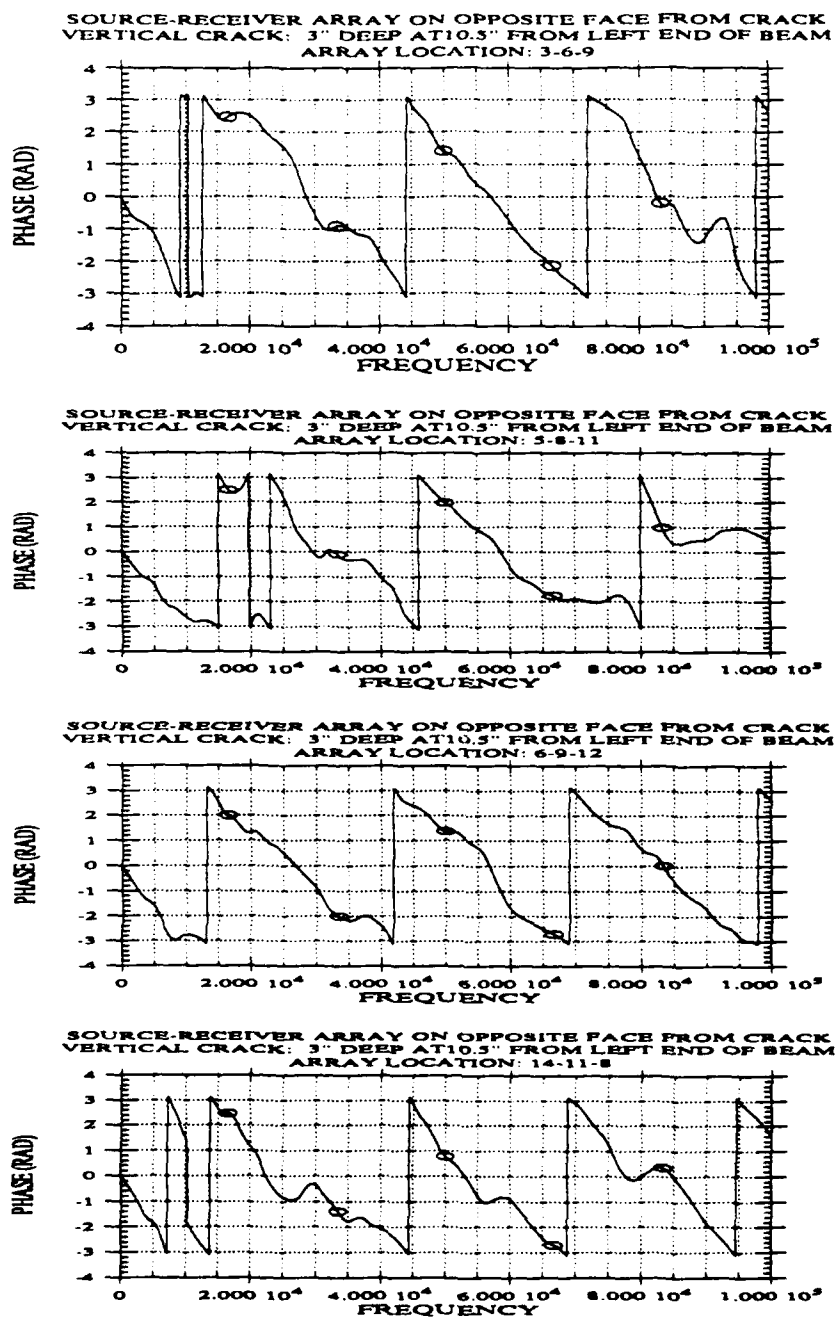


Figure 6.4 - 2 Phase Diagrams, 3" Spacing, Experimental Data, Test Configuration 4, 3" Deep Crack, Array Location Varied

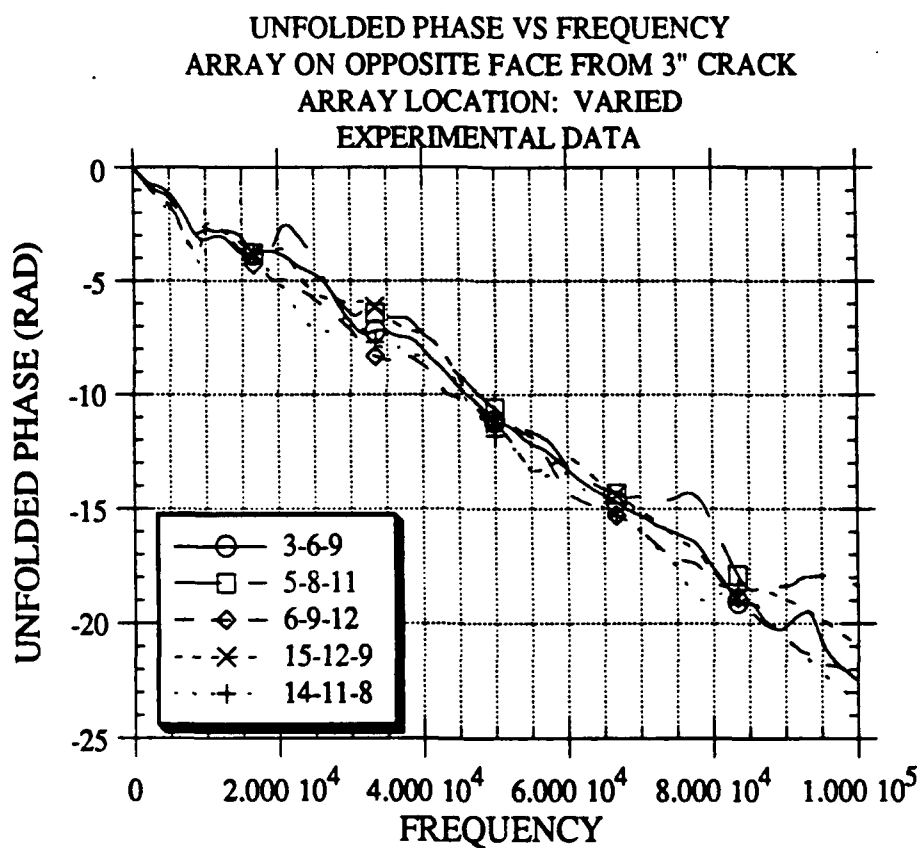


Figure 6.4 - 3 Unfolded Phase Diagrams, 3" Spacing, Experimental Data, Test Configuration 4, 3" Deep Crack, Array Location Varied

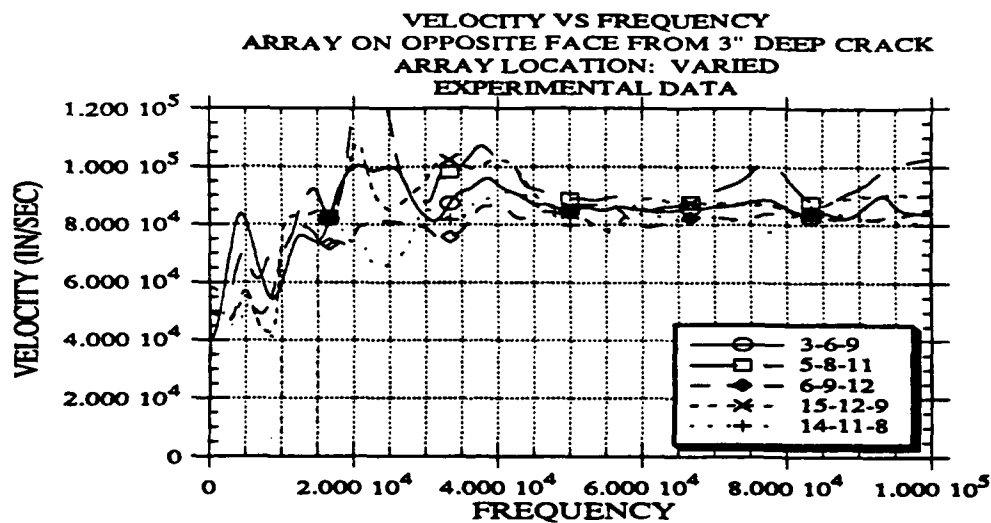


Figure 6.4 - 4 Dispersion Curve, 3" Spacing, Experimental Data, Test Configuration 4, 3" Deep Crack, Array Location Varied

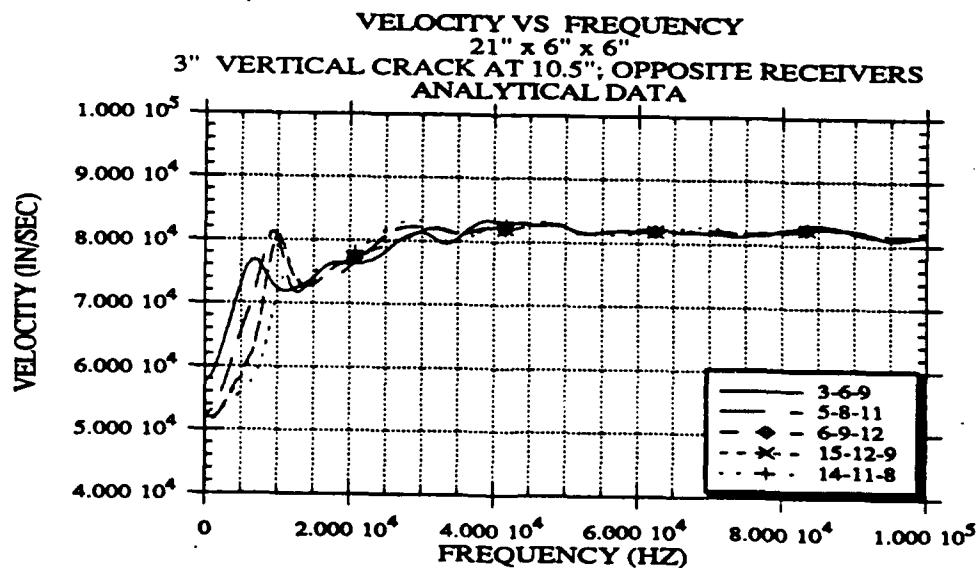


Figure 6.4 - 5 Dispersion Curve, 3" Spacing, Analytical Data, Test Configuration 4, 3" Deep Crack, Array Location Varied

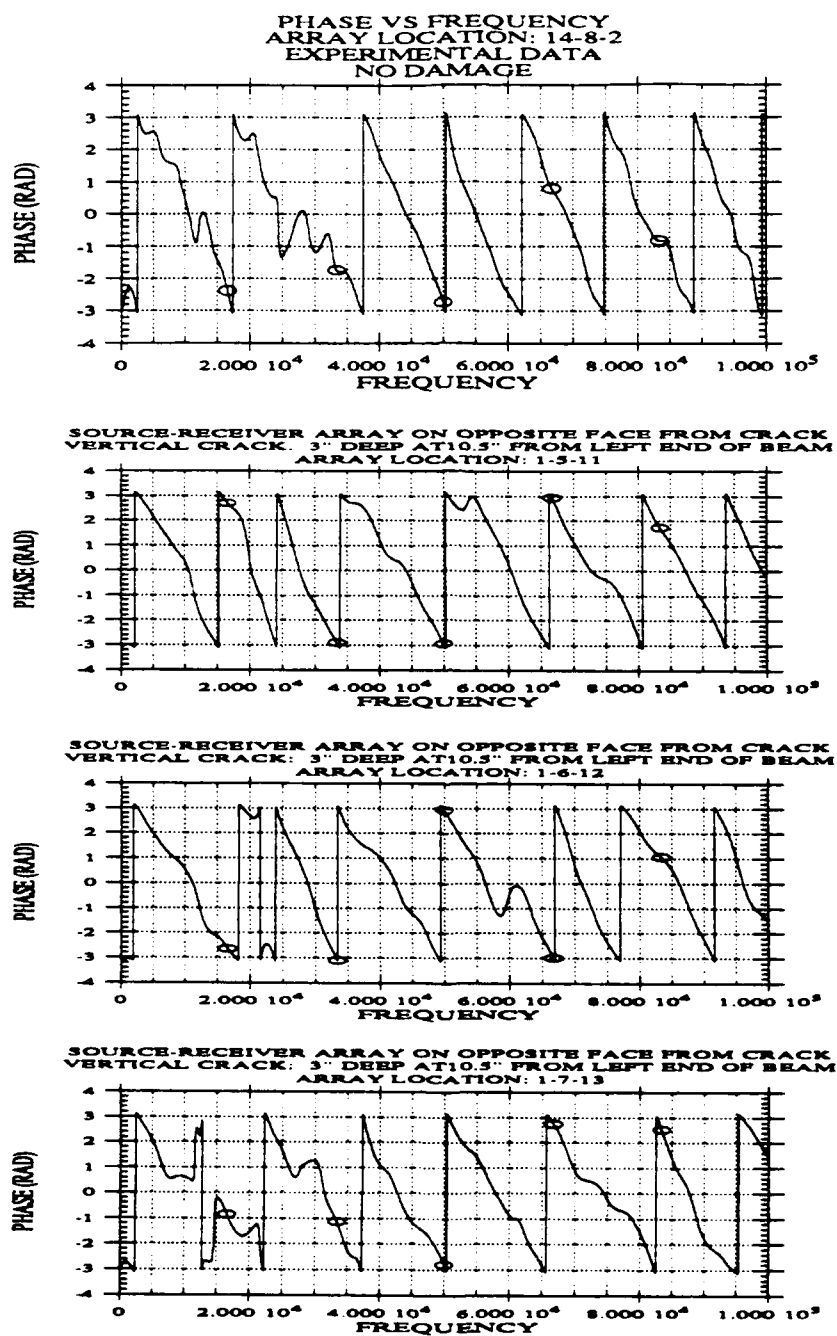


Figure 6.4 - 6 Phase Diagrams, 6" Spacing, Experimental Data, Test Configuration 4, 3" Deep Crack, Array Location Varied

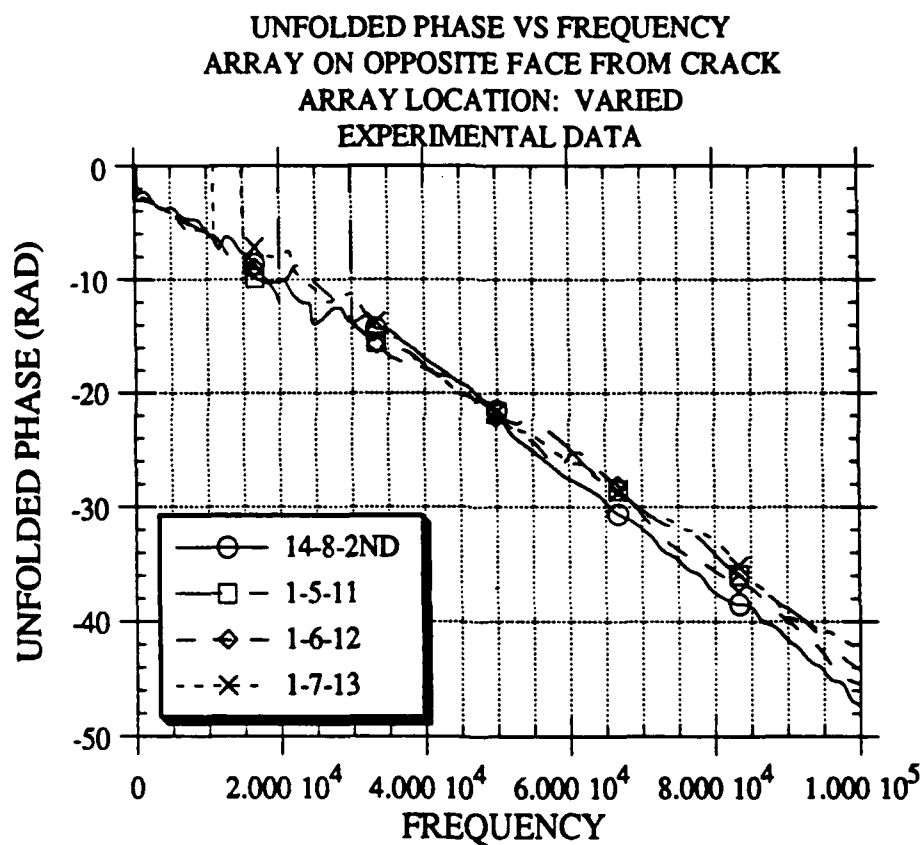


Figure 6.4 - 7 Unfolded Phase Diagrams, 6" Spacing, Experimental Data, Test Configuration 4, 3" Deep Crack, Array Location Varied

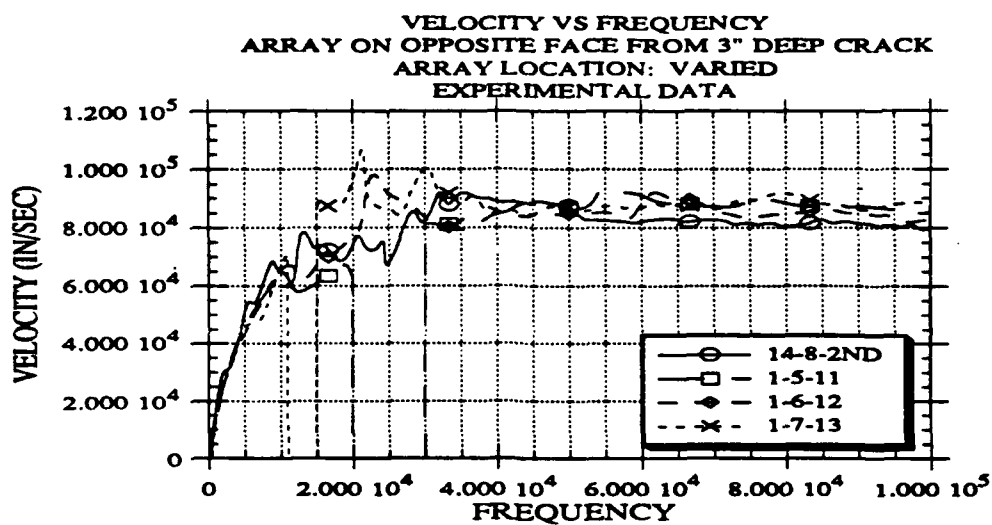


Figure 6.4 - 8 Dispersion Curve, 6" Spacing, Experimental Data, Test Configuration 4, 3" Deep Crack, Array Location Varied

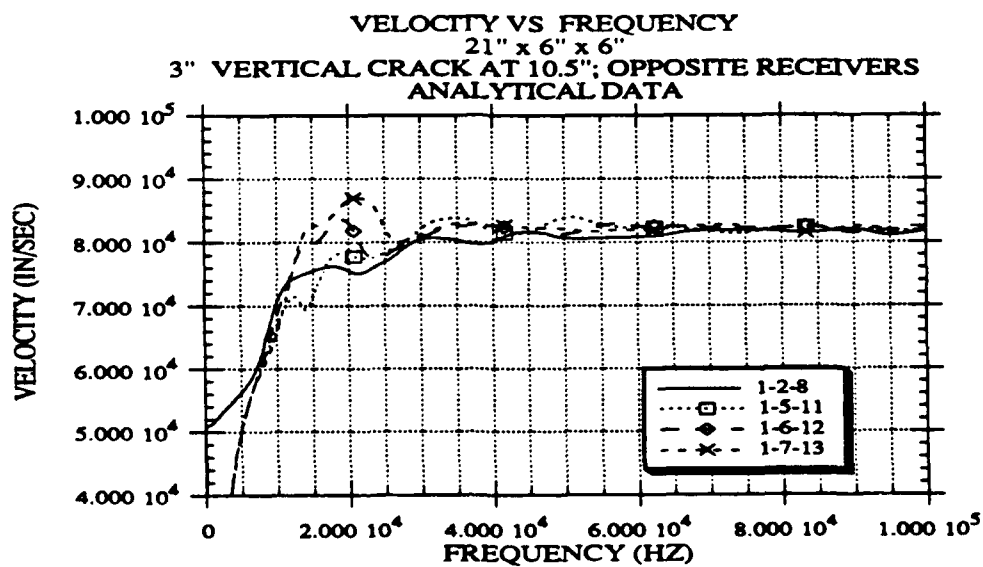


Figure 6.4 - 9 Dispersion Curve, 6" Spacing, Analytical Data, Test Configuration 4, 3" Deep Crack, Array Location Varied

6.5 LOAD AND RECEIVERS ON LATERAL SIDE OF BEAM

The load and receivers were put on the lateral side and at mid-height on the beam, as shown in Figure 6.5-1. This configuration was only investigated experimentally. For a three inch receiver spacing, the crack depth does not affect the dispersion curve. Figure 6.5 - 2 shows phase diagrams for different depths of crack and array location of 6-9-12. Figure 6.5 - 3 compares the unfolded phase diagram. Figure 6.4 shows the corresponding dispersion curve.

For a six inch receiver spacing, the phase diagrams, shown in Figure 6.5 - 5, appear to be affected. The coherence in all the records were low for all the frequencies. For reference, the no damage record from 14-8-2 is used. In the record for 1" deep crack, the phase is affected in the 25 -35 kHz range. For the 2" deep crack, the range affected is 10 -35 kHz. For the 3" deep crack, the range affected is 10-45 kHz. The higher frequencies are consistent through all levels of damage. The data was not masked and was unfolded as measured. This is shown in Figure 6.5 - 6 with the corresponding dispersion curves in Figure 6.5 - 7.

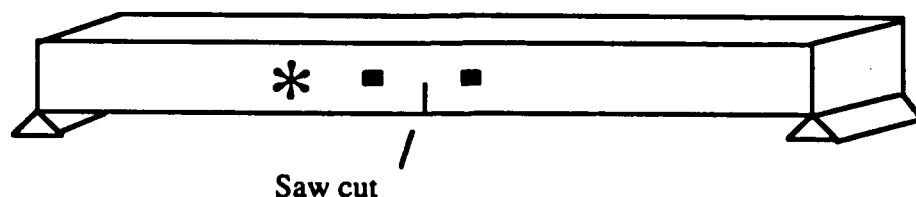


Figure 6.5 - 1 Test Configuration 5

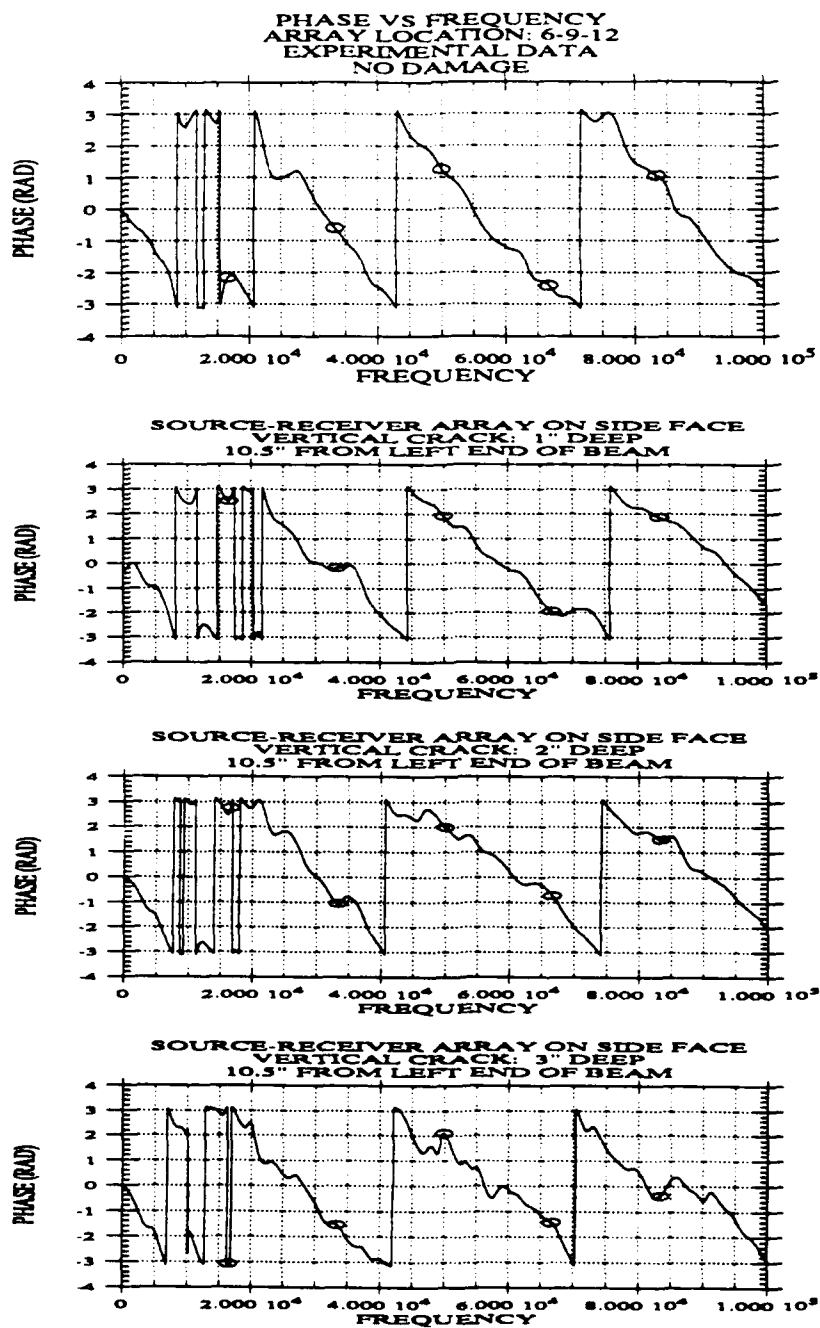


Figure 6.5 - 2 Phase Diagrams, 3" Spacing, Experimental Data, Test Configuration 5 : No Damage, 1", 2" and 3" Deep Crack

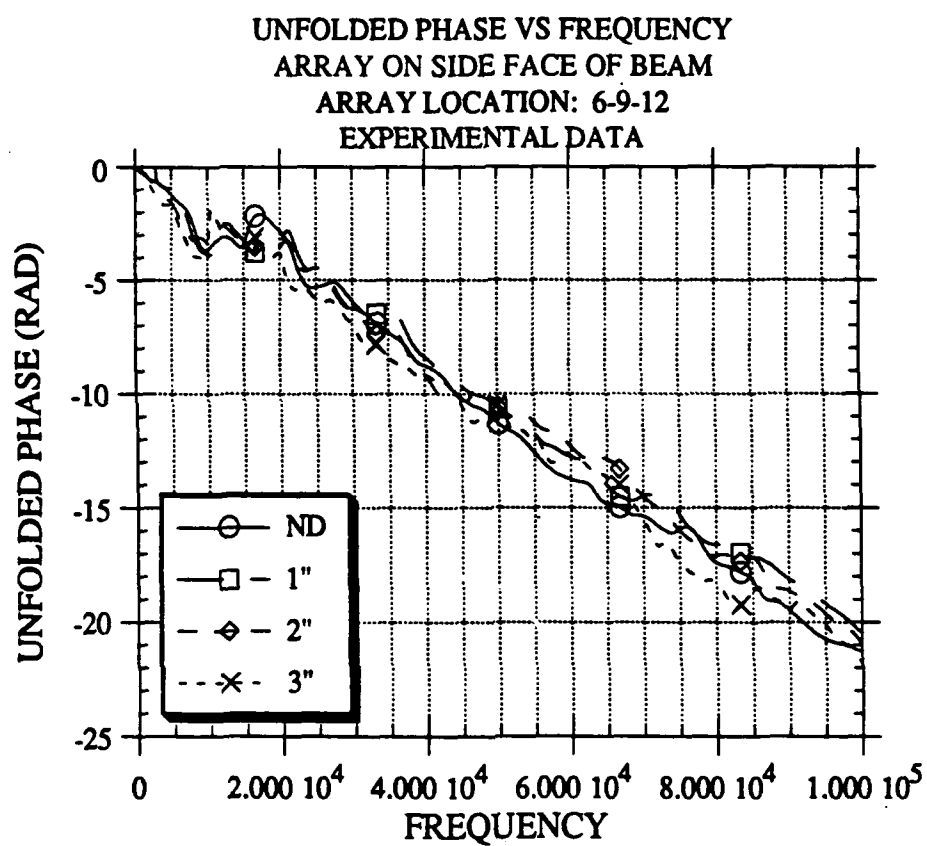


Figure 6.5 - 3 Phase Diagrams, 3" Spacing, Experimental Data, Test Configuration 5 : No Damage, 1", 2" and 3" Deep Crack

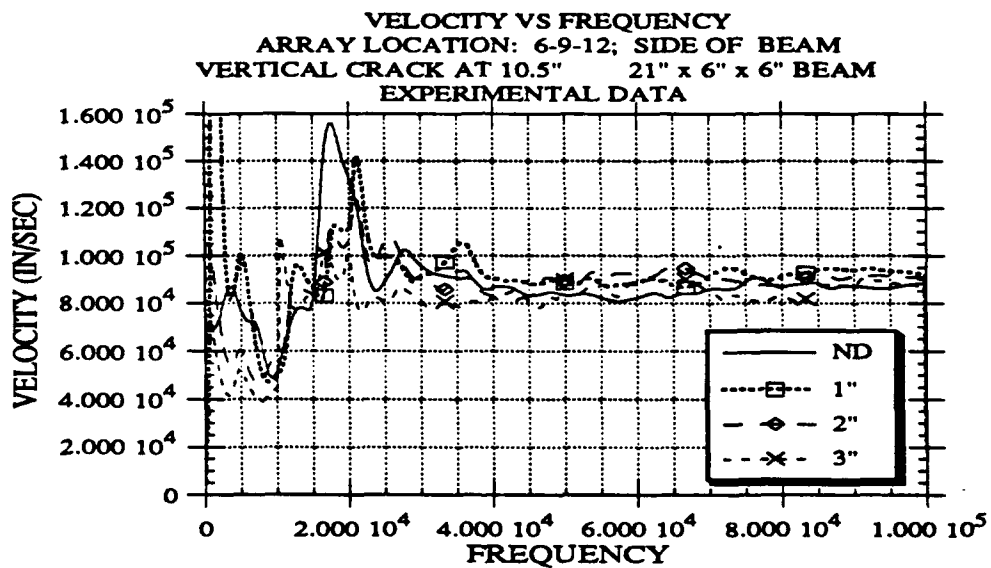


Figure 6.5 - 4 Dispersion Curve, 3" Spacing, Experimental Data, Test Configuration 5 : No Damage, 1", 2" and 3" Deep Crack

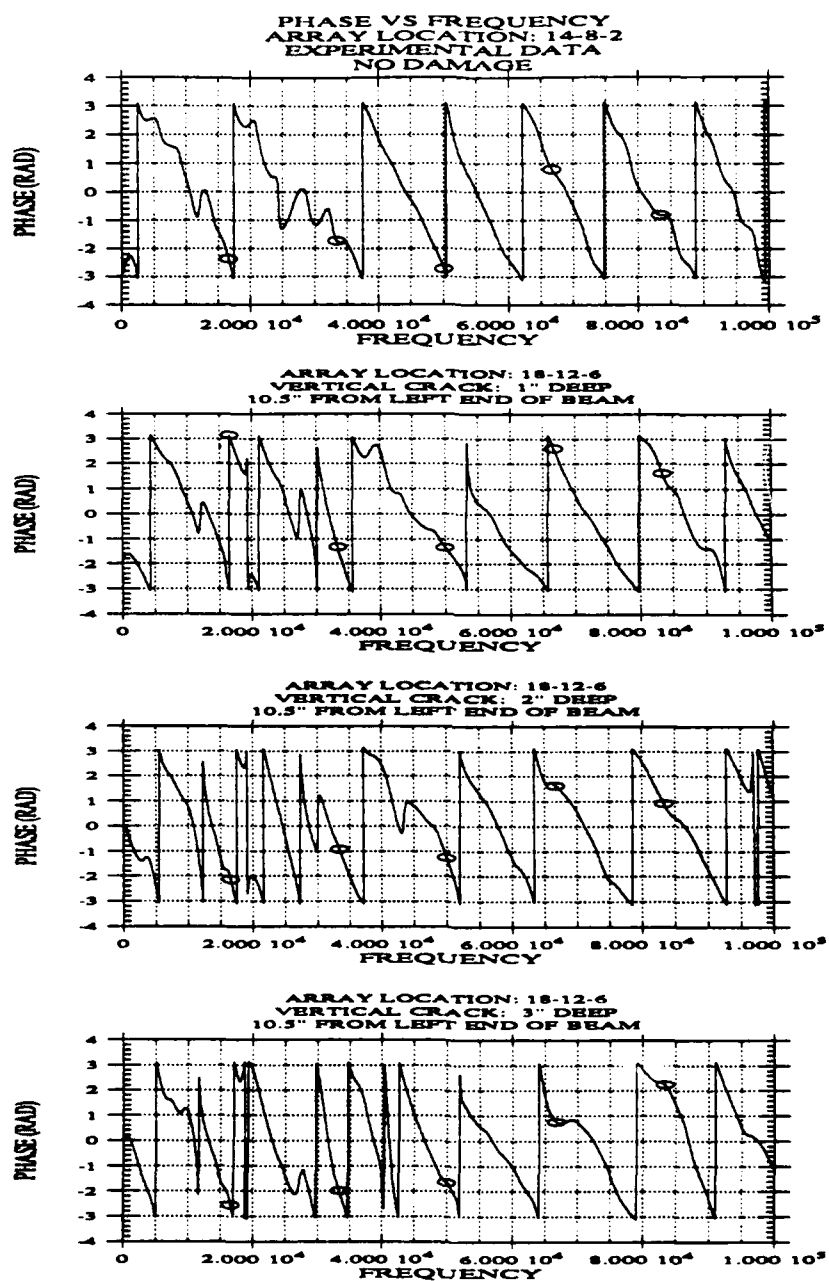


Figure 6.5 - 5 Phase Diagrams, 6" Spacing, Experimental Data, Test Configuration 5 : No Damage, 1", 2" and 3" Deep Crack

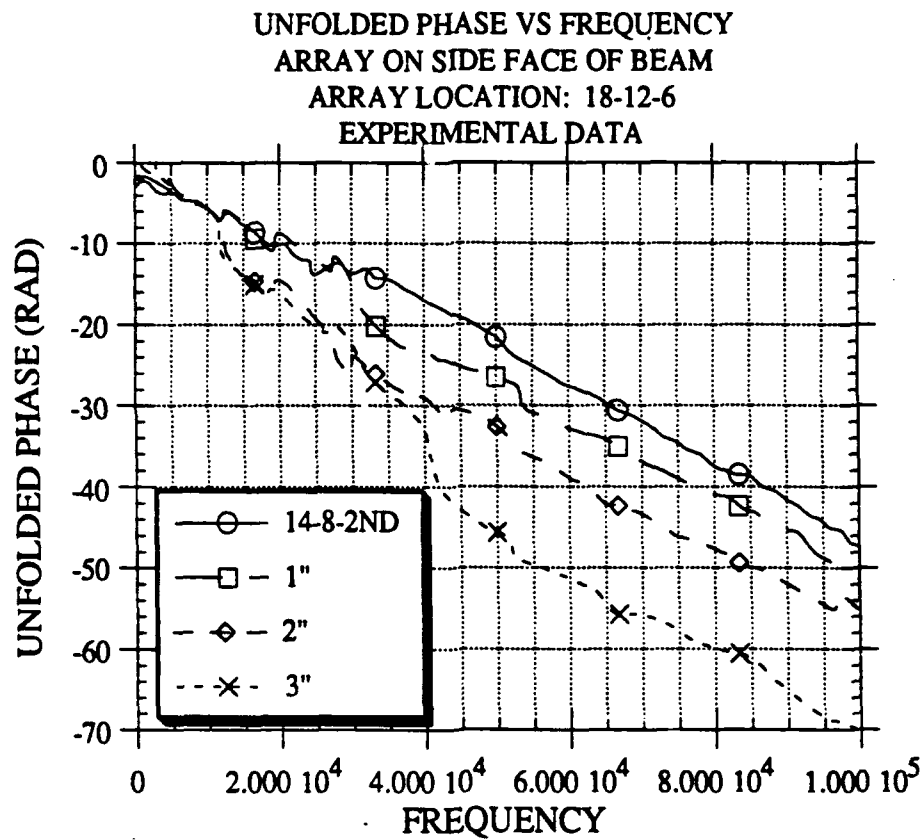


Figure 6.5 - 6 Phase Diagrams, 6" Spacing, Experimental Data, Test Configuration 5 : No Damage, 1", 2" and 3" Deep Crack

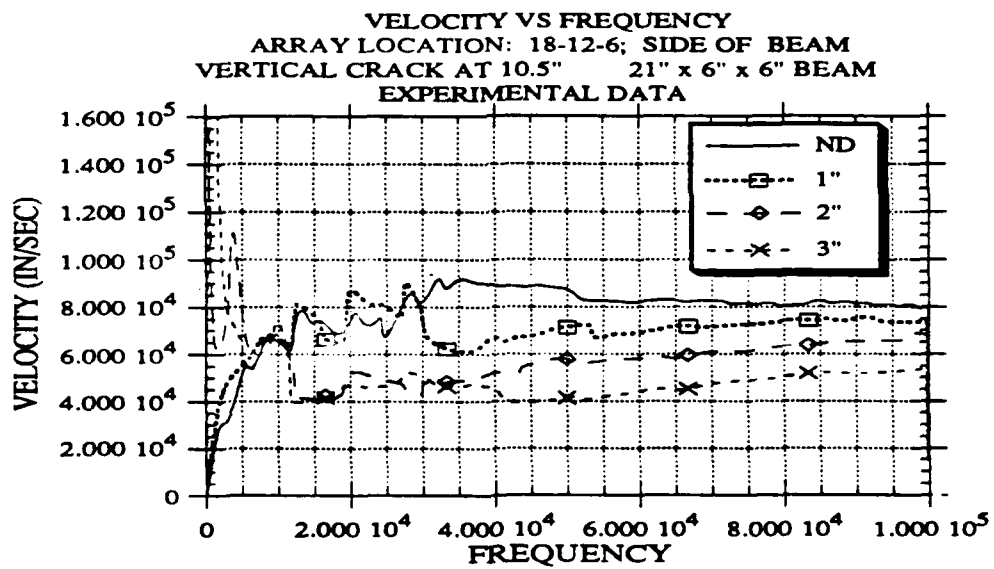


Figure 6.5 - 7 Dispersion Curve, 6" Spacing, Experimental Data, Test Configuration 5: No Damage, 1", 2" and 3" Deep Crack

CHAPTER SEVEN

SUMMARY, CONCLUSIONS AND RECOMMENDATIONS

7.1 SUMMARY

The objective of this research was to assess the ability of surface wave measurements and the SASW technique to detect crack damage in beam and column elements. Damage was detected by a change in the dispersion curve between undamaged and damaged states. The SASW (Spectral Analysis of Surface Waves) technique was used to calculate the surface wave dispersion curve (phase velocity vs frequency). The SASW method uses two simultaneous time records resulting from an impact generated surface wave and taken at a given separation. Using the time records, the phase of the cross power spectrum is calculated. The cross power spectrum phase diagram represents the phase difference between the linear spectra of the two records and is used to calculate the velocity and wavelength for each frequency. The SASW method requires the time records to be windowed (multiplied by a special function) before the cross power spectrum is calculated, the phase diagram must also be unfolded to get the unfolded phase diagram which is used in the velocity and wavelength calculations, when unfolding the phase diagram, data with low coherence must be masked.

A parametric study was run on 21" x 6" x 6" test specimens. The damage form studied was vertical cracks. Crack depths of 1", 2", and 3" were used. Two receiver spacings were used: 3" and 6". The location of the source-receiver array relative to the crack was varied, such that the crack was either outside the array, between the receivers, between the source and first receiver, or on the bottom face with the array on the top face. For each test configuration, a finite element analysis was run and experimentally acceleration measurements were made. After the cracked beams were tested, they were repaired and retested.

7.2 CONCLUSIONS

1. The SASW method is an effective way of calculating the dispersion curve for a beam or column for frequencies larger than a threshold value related to the member depth. From the dispersion curve, one can calculate the modulus of elasticity of the material.
2. Windows affect the smoothness and magnitude of the linear spectra and are needed to obtain correct phase diagrams. (Windows are special time function. The time records are multiplied by the window before the cross power spectrum is calculated.) The window length used to calculate the phase diagram should not be too long or too short. If the window is too long the cross power spectrum phase is not smooth and may be difficult to unfold. If the window is too short, higher frequency data may be eliminated giving the wrong phase diagram. The recommended length of window should be as short as possible, while the linear spectra phase is still monotonically increasing/decreasing.
3. In finite element analysis of wave propagation problems, the mesh size is important. A mesh which is too coarse, will yield an arrival time shorter than it should, lacking the proper high frequency content. The general rules of thumb relating the element size to the frequency and wavelength of interest are applicable.
4. For the beam (21" x 6" x 6") analyzed, the boundary conditions did not affect the calculated dispersion curve, when the proper window lengths were used.
5. Acceleration or displacement records should give essentially the same dispersion curve. This is a theoretical conclusion. In practice the quantity to be measured is controlled by instrumental accuracy and the ability to make the measurement.
6. The calculated dispersion curve is not sensitive to the length of the pulse used to create the stress wave as long as there is enough energy in the frequency range of interest.

7. For an intact beam, using the appropriate windows, and a three inch array spacing (half of the beam depth), the calculated dispersion curve is not sensitive to the location of the load-receiver array on the beam. For the six inch array spacing (equal to the beam depth), analytical results were indifferent to array location, but experimentally the proper phase diagram was obtained only after masking the data with low coherence.

8. For different load-receiver array spacings, there was good agreement between the calculated velocities for wavelengths less than the spacing.

9. When the load-receiver array is on the same side as the crack, a change in the dispersion curve can be used to detect cracks when the crack is between the receivers or when the crack is between the load and the receivers. Other configurations do not show a change in the dispersion curve. More studies are necessary to establish whether there is clear relationship between the changes in the dispersion curve, the length of the crack, and the receiver spacing.

10. After the cracks were repaired, there was no difference between the dispersion curve measured on the repaired cracked section and the dispersion curve measured on the intact section.

7.3 RECOMMENDATIONS FOR FUTURE RESEARCH

From this research a number of questions have been raised and identified as topics for future research.

1. In this research a clearly open crack was used. The crack was saw cut to control the depth. The width of the crack was an $1/8"$. In the future, it will be necessary to see the sensitivity of the method to the degree of crack opening and crack width.

The questions are whether hairline cracks can be detected and what happens when the crack is pushed closed by the vibration or an imposed axial force.

2. The type of repair should be varied to determine the sensitivity to the repair quality. The method shows potential as a quality control check for epoxy injection repair techniques. There are two items of interest. First is the effect of using epoxy with a stiffness significantly different than that of the concrete. The effect of the impedance mismatch must be investigated. Second, the effect of air voids in the repair, must be explored.

3. More studies are needed to correlate the size of the crack and spacing between receivers with the changes in the dispersion curve. The discrepancies between the experimental and analytical predictions in the presence of cracks must also be reconciled.

4. The effect of aggregate and reinforcement also need to be investigated.

APPENDIX A

STRESS WAVES: BASICS

Wave propagation is the passage of energy through a system. As the energy passes through the system, it causes stresses, strains, and displacements. The intent of this section is to familiarize the reader with terms, behavior, and theories which describe the energy passage through the system. For those familiar with stress wave propagation, this is a review.

This section covers the basic information about stress wave propagation. It will discuss the type of waves in a rod and a half space, phenomena such as reflections, refraction, resonance, and dispersion, and derivation of the equations of motion for a Rayleigh wave.

A.1 TERMINOLOGY

The period, T , is the time it takes a wave to travel one cycle.

The frequency, f , is defined as the number of cycles per second and is equal to $\frac{1}{T}$.

The frequency expressed in radians per second is known as the circular frequency, ω , and is equal to $2\pi f$ or $\frac{2\pi}{T}$.

The wavelength, λ , is the distance traveled in one cycle.

The wavenumber, k , is the number of radians per unit length and is equal to $\frac{2\pi}{\lambda}$.

Impedance is defined as ρV_i or the density times the velocity.

A.2 TYPES OF STRESS WAVES

There are several types of stress waves and they are related to the direction of propagation and the direction of particle motion (at a local level).

There are body waves and surface waves. There are two types of body waves, a compression and a shear wave. When the particle motion is in the same direction as the direction of propagation, the wave is called a dilatational or compressive wave. When the particle motion is in a direction perpendicular to the direction of wave propagation, the wave is called a shear wave. There are two types of shear waves, SV- and SH-waves. SV-waves are shear waves where particle motion is in a vertical plane and perpendicular to the path of wave propagation. SH-waves are shear waves where particle motion is in a horizontal plane and perpendicular to the path of wave propagation.

In a half space the surface wave is known as a Rayleigh wave. The energy propagates along the surface and the particle motion follows an elliptical path, decaying in amplitude with distance from the surface.

A.3 PHENOMENA AND DEFINITIONS

After encountering an impedance discontinuity, some energy is reflected and other transmitted. The reflected energy is returned into the body from which it came.

After encountering an impedance discontinuity, the energy transmitted has a different angle than the angle of incidence. This is referred to as refraction.

Diffraction is described as the bending of energy around a corner and described by Huygen's theorem, which states, that all points on a wave front can be considered as point sources for the production of spherical secondary wavelets. After a time, t , the new position of the wave front will be the surface of tangency to these

secondary wavelets. (Halliday and Resnick, pg 691).

Resonance is a condition encountered when the frequency of excitation is equal to the natural frequency of the vibrating system. If a system is in a free vibration condition, it will vibrate in its natural frequency.

Dispersion takes place when the stress wave velocity of propagation is frequency dependent. There are several causes for dispersion. System with viscoelastic properties are dispersive. Flexural waves are dispersive. In a system whose properties change with depth, surface waves are dispersive.

Most approaches assume a plane wave front or a close approximation. This is reasonable in the far field, but in the near field, the curvature of the wave is still important. Lysmer defined a large distance as 2.5λ from the source (Richart, Woods, Hall, pg91). Vu defines the far field as $10 - 20 \lambda$ (Vu, pg46).

A.4 STRESS WAVES IN A ROD

The equations of motion for a longitudinal (compressive) and shear rod waves are:

$$\rho \frac{\partial^2 u}{\partial t^2} = E \frac{\partial^2 u}{\partial x^2} \quad \text{where} \quad V_{\text{rod}} = \sqrt{\frac{E}{\rho}}$$

$$\rho \frac{\partial^2 u}{\partial t^2} = G \frac{\partial^2 u}{\partial x^2} \quad \text{where} \quad V_s = \sqrt{\frac{G}{\rho}}$$

The solution for each equation can be written in terms of the modes as:

$$U(x) = \sum_{n=1}^{\infty} \text{Mode Shape} [(C1)_n \cos \omega_n t + (C2)_n \sin \omega_n t]$$

where the mode shapes and natural frequencies are given in the Table A.5 - 1 for the given end conditions.

Table A.4 - 1 Wave Propagation in a Rod: Mode Shapes and Natural Frequencies

End Conditions	Mode Shapes	Natural Frequencies	
Free-Free	$\cos\left(\frac{n\pi x}{L}\right)$	$\omega_n = \frac{n\pi V_{rod}}{L}$	$n=1,2,3,\dots$
Fix-Free	$\sin\left(\frac{n\pi x}{2L}\right)$	$\omega_n = \frac{n\pi V_{rod}}{2L}$	$n=1,3,5,\dots$
Fix-Fix	$\sin\left(\frac{n\pi x}{L}\right)$	$\omega_n = \frac{n\pi V_{rod}}{L}$	$n=1,2,3,\dots$

A.5 DERIVATION OF EQUATION OF MOTION (HALF SPACE)

This section will derive the wave equations, and then imposing the boundary conditions develop the equation of motion for the Rayleigh wave. The surface wave which propagates in a half space is the Rayleigh wave and is the primary wave of interest in this study. This derivation is taken out of Soil Dynamics by Richart, Woods and Hall. Timoshenko and Goodier also develop the equation of motion in their book Theory of Elasticity.

Equilibrium of a stress block in the x-direction is:

$$\begin{aligned}
& \left(\sigma_x + \frac{\partial \sigma_x}{\partial x} \Delta x \right) \Delta y \Delta z - \sigma_x \Delta y \Delta z + \left(\tau_{xy} + \frac{\partial \tau_{xy}}{\partial y} \Delta y \right) \Delta x \Delta z \\
& - \tau_{xy} \Delta x \Delta z + \left(\tau_{xz} + \frac{\partial \tau_{xz}}{\partial z} \Delta z \right) \Delta x \Delta y - \tau_{xz} \Delta x \Delta y = 0
\end{aligned} \quad (A - 1)$$

Neglecting body forces and applying Newton's law in the x direction, equation (A - 1) leads to:

$$\rho (\Delta x \Delta y \Delta z) \frac{\partial^2 u}{\partial t^2} = \left(\frac{\partial \sigma_x}{\partial x} + \frac{\partial \tau_{xy}}{\partial y} + \frac{\partial \tau_{xz}}{\partial z} \right) \Delta x \Delta y \Delta z$$

and finally :

$$\rho \frac{\partial^2 u}{\partial t^2} = \frac{\partial \sigma_x}{\partial x} + \frac{\partial \tau_{xy}}{\partial y} + \frac{\partial \tau_{xz}}{\partial z} \quad (A - 2)$$

This is the equation of motion in terms of stress for the x direction. A similar process for the y and z direction lead to:

$$\rho \frac{\partial^2 v}{\partial t^2} = \frac{\partial \tau_{yx}}{\partial x} + \frac{\partial \sigma_y}{\partial y} + \frac{\partial \tau_{yz}}{\partial z} \quad (A - 3)$$

$$\rho \frac{\partial^2 w}{\partial t^2} = \frac{\partial \tau_{zx}}{\partial x} + \frac{\partial \tau_{zy}}{\partial y} + \frac{\partial \sigma_z}{\partial z} \quad (A - 4)$$

To solve the equations of motion, (A - 2) - (A - 4), in terms of displacement, the stress-strain relationship and strain-displacement relationship are needed.

The stress-strain relationships are:

$$\begin{aligned}
 \sigma_x &= \lambda \bar{\epsilon} + 2G\epsilon_x & \tau_{xy} &= \tau_{yx} = G\gamma_{xy} \\
 \sigma_y &= \lambda \bar{\epsilon} + 2G\epsilon_y & \tau_{xz} &= \tau_{zx} = G\gamma_{xz} \\
 \sigma_z &= \lambda \bar{\epsilon} + 2G\epsilon_z & \tau_{yz} &= \tau_{zy} = G\gamma_{yz}
 \end{aligned} \tag{A - 5}$$

$$G = \frac{E}{2(1+\nu)} \qquad \lambda = \frac{\nu E}{(1+\nu)(1-2\nu)}$$

where

E: modulus of elasticity

G: shear modulus

ν : Poisson's ratio

$\bar{\epsilon} = \epsilon_x + \epsilon_y + \epsilon_z$ = volumetric strain

ϵ : strain

γ : shear strain

The strain-displacement relationships are:

$$\begin{aligned}
 \epsilon_x &= \frac{\partial u}{\partial x} & \gamma_{xy} &= \frac{\partial u}{\partial y} + \frac{\partial v}{\partial x} & 2\bar{\omega}_x &= \frac{\partial w}{\partial y} - \frac{\partial v}{\partial z} \\
 \epsilon_y &= \frac{\partial v}{\partial y} & \gamma_{xz} &= \frac{\partial u}{\partial z} + \frac{\partial w}{\partial x} & 2\bar{\omega}_y &= \frac{\partial u}{\partial z} - \frac{\partial w}{\partial x} \\
 \epsilon_z &= \frac{\partial w}{\partial z} & \gamma_{yz} &= \frac{\partial v}{\partial z} + \frac{\partial w}{\partial y} & 2\bar{\omega}_z &= \frac{\partial v}{\partial x} - \frac{\partial u}{\partial y}
 \end{aligned} \tag{A - 6}$$

Substituting the strain-displacement equations (A - 6) into the stress-strain equations (A - 5), then substituting the stress-displacement relationship into the equations of motion, (A - 2) - (A - 4), leads to the equations of motion in terms of displacement:

$$\rho \frac{\partial^2 u}{\partial t^2} = (\lambda + G) \frac{\partial \bar{\epsilon}}{\partial x} + G \left(\frac{\partial^2 u}{\partial x^2} + \frac{\partial^2 u}{\partial y^2} + \frac{\partial^2 u}{\partial z^2} \right) \quad (\text{A - 7})$$

$$\rho \frac{\partial^2 v}{\partial t^2} = (\lambda + G) \frac{\partial \bar{\epsilon}}{\partial y} + G \left(\frac{\partial^2 v}{\partial x^2} + \frac{\partial^2 v}{\partial y^2} + \frac{\partial^2 v}{\partial z^2} \right) \quad (\text{A - 8})$$

$$\rho \frac{\partial^2 w}{\partial t^2} = (\lambda + G) \frac{\partial \bar{\epsilon}}{\partial z} + G \left(\frac{\partial^2 w}{\partial x^2} + \frac{\partial^2 w}{\partial y^2} + \frac{\partial^2 w}{\partial z^2} \right) \quad (\text{A - 9})$$

A.7 SOLUTION OF THE EQUATION OF MOTION

There are two different solutions to the equation of motion; one solution describes the dilatational (compression, P) wave, the other solution describes the distortional (shear, S) wave.

Taking the partial derivative of (A - 7) with respect to x, (A - 8) with respect to y, (A - 9) with respect to z, and then adding leads to:

$$\rho \frac{\partial^2 \bar{\epsilon}}{\partial t^2} = (\lambda + 2G) \left(\frac{\partial^2 \bar{\epsilon}}{\partial x^2} + \frac{\partial^2 \bar{\epsilon}}{\partial y^2} + \frac{\partial^2 \bar{\epsilon}}{\partial z^2} \right)$$

$$\frac{\partial^2 \bar{\epsilon}}{\partial t^2} = V_p^2 \left(\frac{\partial^2 \bar{\epsilon}}{\partial x^2} + \frac{\partial^2 \bar{\epsilon}}{\partial y^2} + \frac{\partial^2 \bar{\epsilon}}{\partial z^2} \right) \quad (\text{A} - 10)$$

where

$$V_p = \sqrt{\frac{\lambda + 2G}{\rho}}$$

Note: V_{rod} ($V_{rod} = \sqrt{\frac{E}{\rho}}$) is different from the P-wave velocity ($V_p = \sqrt{\frac{\lambda + 2G}{\rho}}$) in a half space. This is a result of the lack of lateral restraint in a bar.

The second solution is determined by taking the partial derivative of (A - 8) with respect to z , (A - 9) with respect to y , and then subtracting:

$$\rho \frac{\partial^2}{\partial t^2} \left(\frac{\partial w}{\partial y} - \frac{\partial v}{\partial z} \right) = G \left[\frac{\partial^2}{\partial x^2} \left(\frac{\partial w}{\partial y} - \frac{\partial v}{\partial z} \right) + \frac{\partial^2}{\partial y^2} \left(\frac{\partial w}{\partial y} - \frac{\partial v}{\partial z} \right) + \frac{\partial^2}{\partial z^2} \left(\frac{\partial w}{\partial y} - \frac{\partial v}{\partial z} \right) \right]$$

which leads to:

$$\rho \frac{\partial^2 \bar{\omega}_x}{\partial t^2} = G \left(\frac{\partial^2 \bar{\omega}_x}{\partial x^2} + \frac{\partial^2 \bar{\omega}_x}{\partial y^2} + \frac{\partial^2 \bar{\omega}_x}{\partial z^2} \right)$$

$$\frac{\partial^2 \bar{\omega}_x}{\partial t^2} = V_s^2 \left(\frac{\partial^2 \bar{\omega}_x}{\partial x^2} + \frac{\partial^2 \bar{\omega}_x}{\partial y^2} + \frac{\partial^2 \bar{\omega}_x}{\partial z^2} \right) \quad (\text{A} - 11)$$

where

$$V_s = \sqrt{\frac{G}{\rho}}$$

Through a similar process the distortional wave can be written for $\bar{\omega}_y$ and $\bar{\omega}_z$. Equation (A - 10) represents the P-wave and equation (A - 11) represents the shear wave.

A.7 RAYLEIGH WAVE VELOCITY

To determine the Rayleigh wave velocity a cubic equation must be solved for its roots. This section will derive the cubic equation. By assuming the potential functions Φ and Ψ and letting

$$u = \frac{\partial \Phi}{\partial x} + \frac{\partial \Psi}{\partial z} \quad (A - 12)$$

and

$$w = \frac{\partial \Phi}{\partial z} - \frac{\partial \Psi}{\partial x} \quad (A - 13)$$

The volumetric strain is

$$\bar{\epsilon} = \frac{\partial u}{\partial x} + \frac{\partial w}{\partial z} = \nabla^2 \Phi$$

and the rotation in the x-z plane is defined by:

$$2 \bar{\omega}_y = \frac{\partial u}{\partial z} - \frac{\partial w}{\partial x} = \nabla^2 \Psi$$

and substituting (A - 12) and (A - 13) into (A - 7) and (A - 9) leads to

$$\rho \frac{\partial}{\partial x} \left(\frac{\partial^2 \Phi}{\partial t^2} \right) + \rho \frac{\partial}{\partial z} \left(\frac{\partial^2 \Psi}{\partial t^2} \right) = (\lambda + 2G) \frac{\partial}{\partial x} (\nabla^2 \Phi) + G \frac{\partial}{\partial z} (\nabla^2 \Psi) \quad (\text{A - 14})$$

$$\rho \frac{\partial}{\partial z} \left(\frac{\partial^2 \Phi}{\partial t^2} \right) - \rho \frac{\partial}{\partial x} \left(\frac{\partial^2 \Psi}{\partial t^2} \right) = (\lambda + 2G) \frac{\partial}{\partial z} (\nabla^2 \Phi) - G \frac{\partial}{\partial x} (\nabla^2 \Psi) \quad (\text{A - 15})$$

Equations (A - 14) and (A - 15) are satisfied if:

$$\frac{\partial^2 \Phi}{\partial t^2} = \frac{(\lambda + 2G)}{\rho} \nabla^2 \Phi = v_p^2 \nabla^2 \Phi \quad (\text{A - 16})$$

and

$$\frac{\partial^2 \Psi}{\partial t^2} = \frac{G}{\rho} \nabla^2 \Psi = v_s^2 \nabla^2 \Psi \quad (\text{A - 17})$$

Assuming a solution for a sinusoidal wave traveling in the positive x-direction, the expressions for Φ and Ψ can be written:

$$\Phi = F(z) \exp [i (\omega t - Kx)] \quad (\text{A - 18})$$

$$\Psi = G(z) \exp [i (\omega t - Kx)] \quad (\text{A - 19})$$

where

$$K = \frac{2\pi}{\lambda}$$

Substituting (A - 18) and (A - 19) into (A - 16) and (A - 17) leads to:

$$-\frac{\omega^2}{V_p^2} F(z) = -K^2 F^2(z) + F''(z) \quad (\text{A} - 20)$$

$$-\frac{\omega^2}{V_p^2} G(z) = -K^2 G^2(z) + G''(z) \quad (\text{A} - 21)$$

Rearranging leads to:

$$F''(z) - \left(K^2 - \frac{\omega^2}{V_p^2} \right) F(z) = 0 \quad (\text{A} - 22)$$

$$G''(z) - \left(K^2 - \frac{\omega^2}{V_s^2} \right) G(z) = 0 \quad (\text{A} - 23)$$

Letting:

$$q^2 = \left(K^2 - \frac{\omega^2}{V_p^2} \right)$$

$$s^2 = \left(K^2 - \frac{\omega^2}{V_s^2} \right)$$

(A - 22) and (A - 23) become:

$$F''(z) - q^2 F(z) = 0$$

$$G''(z) - s^2 G(z) = 0$$

To solve for $F(z)$ and $G(z)$, assume a solution of the form:

$$F(z) = A_1 \exp(-qz) + B_1 \exp(qz)$$

$$G(z) = A_2 \exp(-sz) + B_2 \exp(sz)$$

Assume $B_1 = B_2 = 0$, otherwise $F(z)$ and $G(z)$ will approach infinity as z increases, and this leads to:

$$\Phi = A_1 \exp[-qz + i(\omega t - Kx)] \quad (A - 24)$$

$$\Psi = A_2 \exp[-sz + i(\omega t - Kx)] \quad (A - 25)$$

To solve for the constant A_1 and A_2 , the boundary conditions are used. The stress at the free surface must be equal to zero, which leads to

$$\sigma_z = 0 \quad \text{and} \quad \tau_{xy} = 0 \quad \text{at} \quad z = 0$$

where

$$\sigma_z = \lambda \bar{\epsilon} + 2G\epsilon_z \quad (A - 26)$$

$$\tau_{xy} = \tau_{yx} = G\gamma_{xy} \quad (A - 27)$$

Using (A - 24) and (A - 25) and the definition of u , w , and the strain displacement equation, substituting into (A - 26) and (A - 27) leads to:

$$\sigma_z (@z=0) = A_1 [(\lambda + 2G)q^2 - \lambda K^2] - 2iA_2 G K s = 0$$

$$\tau_{xy} (@z=0) = 2iA_1 K q + A_2 (s^2 + K^2) = 0$$

Solving for the ratio $\frac{A_1}{A_2}$, leads to:

$$\frac{A_1}{A_2} \frac{(\lambda + 2G)q^2 - \lambda K^2}{2iGKs} - 1 = 0$$

$$\frac{A_1}{A_2} \frac{2iKq}{(s^2 + K^2)} - 1 = 0$$

Eliminating the ratio $\frac{A_1}{A_2}$, leads to:

$$\frac{(\lambda + 2G)q^2 - \lambda K^2}{2iGKs} = - \frac{2iKq}{(s^2 + K^2)}$$

$$\therefore 4qGsK^2 = (s^2 + K^2)[(\lambda + 2G)q^2 - \lambda K^2] \quad (A - 28)$$

Substituting s, q , into (A - 28), expanding, and rearranging leads to:

$$N^6 - 8N^4 + (24 - 16\alpha^2)N^2 + 16(\alpha^2 - 1) = 0 \quad (A - 29)$$

where

$$N^2 = \frac{V_R^2}{V_S^2}$$

$$\alpha^2 N^2 = \frac{V_R^2}{V_P^2}$$

$$\alpha^2 = \frac{G}{\lambda + 2G} = \frac{1-2\nu}{2-2\nu} = \frac{V_S^2}{V_P^2}$$

Equation (A - 29) is a sixth order equation in N or a cubic equation in N^2 which must be solved to get the speed of the Rayleigh wave. The equation is a function of Poisson's ratio.

Another way to reduce Equation A - 28 is to substitute just $q^2 = \left(K^2 - \frac{\omega^2}{V_P^2}\right)$ on

the right hand side of the equation. This leads to

$$4qGsK^2 = (s^2 + K^2)[(\lambda + 2G)\left(K^2 - \frac{\omega^2}{V_p^2}\right) - \lambda K^2]$$

expanding the right side and dividing through by G leads to

$$4qsK^2 = \frac{(s^2 + K^2)}{G} \left[\lambda K^2 - \lambda \frac{\omega^2}{V_p^2} + 2GK^2 - 2G \frac{\omega^2}{V_p^2} - \lambda K^2 \right]$$

reducing leads to

$$4qsK^2 = (s^2 + K^2) \left[- \frac{\omega^2}{V_p^2} \frac{(\lambda + 2G)}{G} + 2K^2 \right]$$

substituting $\frac{\lambda + 2G}{G} = \frac{V_p^2}{V_s^2}$ leads to

$$4qsK^2 = (s^2 + K^2) \left[- \frac{\omega^2}{V_p^2} \frac{V_p^2}{V_s^2} + 2K^2 \right]$$

which leads to

$$4qsK^2 = (s^2 + K^2) \left[- \frac{\omega^2}{V_s^2} + 2K^2 \right] = (s^2 + K^2) \left[K^2 - \frac{\omega^2}{V_s^2} + K^2 \right]$$

and finally

$$4qsK^2 = (s^2 + K^2) [s^2 + K^2] = [s^2 + K^2]^2 \quad (A - 30)$$

For a half space, the Rayleigh wave speed can also be determined using equation A - 30 rather than A-29.

If instead of a half space, there is a layer of finite thickness with air on both sides the Rayleigh wave speed equation is

$$[s^2 + K^2]^4 - 8 K^2 [s^2 + K^2]^2 qs \left[\frac{C_1 C_2 - 1}{S_1 S_2} \right] + 16 q^2 s^2 K^4 = 0 \quad (\text{A} - 31)$$

where

$$\begin{aligned} C_1 &= \cosh(qh) & S_1 &= \sinh(qh) \\ C_2 &= \cosh(sh) & S_2 &= \sinh(sh) \end{aligned}$$

h is the depth of the layer

$$K = \frac{2\pi}{\lambda}$$

$$q^2 = \left(K^2 - \frac{\omega^2}{V_p^2} \right) \quad s^2 = \left(K^2 - \frac{\omega^2}{V_s^2} \right)$$

Note that as h approaches ∞ , $\left[\frac{C_1 C_2 - 1}{S_1 S_2} \right]$ approaches 1 and Equation A - 31 reduces to

$$[s^2 + K^2]^4 - 8 K^2 [s^2 + K^2]^2 qs + 16 q^2 s^2 K^4 = 0$$

which equals

$$\left[[s^2 + K^2]^2 - 4 qs K^2 \right]^2 = 0 \quad \text{which is same as a half space.}$$

Also, if plane stress is used instead of plane strain, $V_p = \sqrt{\frac{E}{\rho(1-\nu^2)}}$

instead of $V_p = \sqrt{\frac{\lambda + 2G}{\rho}}$

A.8 RAYLEIGH WAVE DISPLACEMENTS

Given :

$$\Phi = A_1 \exp [-qz + i (\omega t - Kx)]$$

$$\Psi = A_2 \exp [-sz + i (\omega t - Kx)]$$

and solving for u and w leads to:

$$u = \frac{\partial \Phi}{\partial x} + \frac{\partial \Psi}{\partial z}$$

$$u = -A_1 iK \exp [-qz + i (\omega t - Kx)] - A_2 s \exp [-sz + i (\omega t - Kx)] \quad (A - 32)$$

and

$$w = \frac{\partial \Phi}{\partial z} - \frac{\partial \Psi}{\partial x}$$

$$w = -A_1 iK \exp [-qz + i (\omega t - Kx)] - A_2 iK \exp [-sz + i (\omega t - Kx)] \quad (A - 33)$$

Given:

$$A_2 = \frac{A_1 2iKq}{(s^2 + K^2)} \quad (A - 34)$$

Substituting (A - 34) into (A - 32) and (A - 33) and solving for $u(z)$ and $w(z)$ leads to:

$$u(z) = A_1 iK \left\{ - \exp \left[- \frac{q}{K} (zK) \right] + \frac{2 \frac{q}{K} \frac{s}{K}}{\frac{s^2}{K^2} + 1} \exp \left[- \frac{s}{K} (zK) \right] \right\} \times \exp [i (\omega t - Kx)]$$

$$w(z) = A_1 K \left\{ \frac{2 \frac{q}{K}}{\frac{s^2}{K^2} + 1} \exp \left[- \frac{s}{K} (zK) \right] - \frac{q}{K} \exp \left[- \frac{q}{K} (zK) \right] \right\} \times \exp [i (\omega t - Kx)]$$

where:

$$\frac{q^2}{K^2} = 1 - \frac{\omega^2}{K^2 V_p^2} = 1 - \alpha^2 N^2$$

$$\frac{s^2}{K^2} = 1 - \frac{\omega^2}{K^2 V_s^2} = 1 - N^2$$

For a given value of Poisson's ratio, equation (A - 29) is solved for N^2 . Given N^2 , $U(z)$ and $W(z)$ can be evaluated in terms of the wave number, K , for any given value of Poisson's ratio.

A.9 VELOCITIES

This a summary of the stress wave velocities for quick reference.

	HALF SPACE	ROD
P - WAVE	$V_p = \sqrt{\frac{\lambda + 2G}{\rho}}$	$V_p = \sqrt{\frac{E}{\rho}}$
S - WAVE	$V_s = \sqrt{\frac{G}{\rho}}$	$V_s = \sqrt{\frac{G}{\rho}}$

For the Rayleigh wave, the wave speed is dependent on Poisson's ratio. The exact solution requires finding the roots of a cubic equation. Some approximation are:

$$V_R \cong (.90) V_s \text{ to } (.95) V_s$$

$$V_R \cong V_s \left[\frac{2.86 V_p^2 - 3.98 V_s^2}{3 V_p^2 - 4 V_s^2} \right] \quad (\text{Fitting, pg 86})$$

$$V_R \cong V_s \left[\frac{.87 + 1.12\nu}{(1 + \nu)} \right] \quad (\text{Vu, pg 4})$$

In Shue's dissertation, a table for $\frac{V_R}{V_s}$ is presented for a range of Poisson's ratios on pg 215.

A.10 ENERGY PARTITION

From an impact on a half space, energy is imparted into P-waves, S-waves, and Rayleigh waves, with 7% going into the P-wave, 26% into the S-wave, and 67% into the Rayleigh wave. (Richart, Hall, and Woods, pg 91)

A.11 ATTENUATION

A wave loses energy through geometric spreading or through internal damping. Geometric spreading is the spreading of the energy density as the wave propagates out from the source resulting in a reduced amplitude as shown in Table A.12 - 1. Internal damping is the result of internal friction which also causes the wave to lose energy. (Richart, Hall, and Woods, pg 91)

Table A.11 - 1 Geometric Damping

	Body	Surface
P-wave	r^{-1}	r^{-2}
S-wave	r^{-1}	r^{-2}
R-wave		$r^{-0.5}$

Some methods of measuring damping are the Logarithmic Decrement and the Half Power Bandwidth methods. Given the amplitude of displacements for the two successive peaks of free vibration response (Y_1 and Y_2), the fraction of critical damping can be calculated using the Logarithmic Decrement as:

$$\delta = \ln \left\{ \frac{Y_1}{Y_2} \right\} = \frac{2 \pi \xi}{\sqrt{1 - \xi^2}} \cong 2 \pi \xi \quad (\text{Paz, pg 30})$$

where

δ is the logarithmic decrement

ξ is the fraction of critical damping

Y_1 is maximum amplitude of the first cycle

Y_2 is maximum amplitude of the second cycle

The Half Power Bandwidth method requires the variation of the steady state response amplitude with excitation frequency. The percent of critical damping is calculated as:

$$\xi = \frac{f_2 - f_1}{f_2 + f_1}$$

where

$$f_i \text{ is taken at } \frac{1}{\sqrt{2}} \times \text{Peak Response} \quad (\text{Paz, pg 47})$$

Also at resonance,

$$\xi = \frac{1}{2 \text{ DMF}_{\max}}$$

where

$$\text{DMF}_{\max} = \frac{Y_{\max}}{Y_{\text{st}}} = \text{Dynamic Magnification Factor} \quad (\text{Paz, pg 47})$$

A.12 REFLECTIONS

A.12.1 ONE DIMENSIONAL CASE

At an interface, displacements must be compatible and equilibrium must be satisfied. When a wave encounters a discontinuity in impedance, depending on the impedance ratio between the two sides of the interface, energy is reflected and transmitted. That energy causes stresses and displacements in the materials. Table A.12.1 - 1 gives the amplitude of the transmitted and reflected waves as a fraction of the incident wave. (Short Course on Penetration Mechanics, pgs 2-28 - 2-31)

For the impedance ratio, R , there are five different possibilities. Table A.12.1 - 2 gives the values for A, B, F , and G for the different possible impedance conditions.

A.12.2 TWO DIMENSIONAL CASE

In the the two dimensional case compatibility and equilibrium must also be met, but the results are more complicated due to the existence of two sets of variables and stresses.

For a P-wave encountering an impedance discontinuity, there are four waves generated: a reflected P-wave, a reflected SV-wave, a refracted P-wave, and a refracted SV-wave. The angle of refraction is given by Snell's Law.

For the SV-wave encountering an impedance discontinuity, there are again four waves generated: a reflected P-wave, a reflected SV-wave, a refracted P-wave, and a refracted SV-wave. The angle of refraction is given by Snell's Law.

Table A.12.1 - 1 Definition for Reflected and Transmitted Amplitude Ratios

	Displacement	Stress
Reflected	$A = \frac{1-R}{1+R}$	$F = -\frac{1-R}{1+R}$
Transmitted	$B = \frac{2R}{1+R}$	$G = \frac{2R}{1+R}$

where

$$R = \frac{\rho V_2}{\rho V_1} = \text{Impedance Ratio}$$

ρ is density

V_i is velocity in "i" material

A: $\frac{\text{Reflected wave displacement amplitude}}{\text{Incident wave displacement amplitude}}$

B: $\frac{\text{Transmitted wave displacement amplitude}}{\text{Incident wave displacement amplitude}}$

F: $\frac{\text{Reflected wave stress amplitude}}{\text{Incident wave stress amplitude}}$

G: $\frac{\text{Transmitted wave stress amplitude}}{\text{Incident wave stress amplitude}}$

Table A.12.1 - 2 Displacement and Stress Amplitudes for Different Impedance Ratios

Ratio	Displacement		Stress	
	Reflected	Transmitted	Reflected	Transmitted
$R = \infty$ (fixed end)	-1	0	1	2
$R > 1$	$-1 < A < 0$	$0 < B < 1$	$0 < F < 1$	$1 < G < 2$
$R = 1$	0	1	0	1
$R < 1$	$0 < A < 1$	$1 < B < 2$	$-1 < F < 0$	$0 < G < 1$
$R = 0$ (free end)	1	2	-1	0

Another phenomenon occurs when the SV-wave encounters an impedance discontinuity. At a critical angle there is no reflected or refracted P-wave but a P-wave travelling along the interface. For angles larger than the critical angle the reflected / refracted P-wave also travels along the interface.

For an SH-wave encountering an impedance discontinuity, there are two waves generated: a reflected SH-wave and a refracted SH-wave.

For more detail on reflection and refraction in two dimensions the reader is referred to Richart, Hall, and Woods, Soil Dynamics.

APPENDIX B

FOURIER TRANSFORMS: BASICS

Another means of representing response information is in the frequency domain. This alternate representation does not provide any more or any less information than the time domain representation, but it provides an alternate means of looking at the data.

To transform time data from the time domain into the frequency domain, a Fourier transform is used as discussed in this section. Most of the information for this section was taken from class notes on "Digital Time Series Analysis and Applications" by Dr Edward J. Powers at the University of Texas at Austin.

B.1 CONTINUOUS FOURIER TRANSFORMATION

In mathematical terms, the Fourier transform is:

$$X(f) = \int_{-\text{Inf}}^{+\text{Inf}} x(t) \exp(-i 2\pi ft) dt$$

with the inverse Fourier transform as

$$x(t) = \int_{-\text{Inf}}^{+\text{Inf}} X(f) \exp(i 2\pi ft) df$$

The above two relationships are known as transform pairs.

B.2 DISCRETE FOURIER TRANSFORMATION

Most data is collected in discrete form and not found in continuous form. To deal with the discrete data, the Discrete Fourier Transform (DFT) is used.

Mathematically, the DFT is:

$$X(l) = \frac{1}{N} \sum_{n=0}^{N-1} x(n) \exp(-i 2\pi \frac{l n}{N})$$

and the inverse DFT is:

$$x(n) = \sum_{l=0}^{N-1} X(l) \exp(i 2\pi \frac{l n}{N})$$

where $l = 0, 1, 2, \dots, N-1$ and $n = 0, 1, 2, \dots, N-1$ and N is the number of points in the time record. $x(n)$ is the time domain data. $X(l)$ is the frequency domain data.

In the discrete case, both $x(n)$ and $X(l)$ are periodic.

In transition from the continuous to the discrete transform, two problems occur, aliasing and leakage. Aliasing is where high frequency components imitate low frequency components. This is a result of the sampling rate of the continuous time record. To insure aliasing is not a problem, the Sampling Theorem requires the sampling rate be twice the highest frequency represented in the time signal. The consequence of aliasing is that the original continuous time signal cannot be reproduced from the sampled signal.

The second problem is leakage. Leakage is a result of taking a finite time record (where the continuous case goes to infinity). Leakage always occurs with discrete data. The method used to minimize leakage is to multiply the sampled time record

by a special function called a window before the DFT is computed. Windows will be discussed later in this section.

The relationship between the continuous Fourier transform and the discrete Fourier transform is that the DFT (at $\text{freq} = l$) is equal to the value of the continuous transform at $(l\Delta f)$ multiplied by Δf . That is:

$$\begin{array}{ll} X(l) = & X(l\Delta f) * \Delta f \quad l = 0, 1, 2, \dots, N-1 \\ \text{DFT} & \text{Sampled Continuous Transform} \end{array}$$

Another interesting relationship is that between the DFT and a complex Fourier series expansion. A complex Fourier series can be used to represent any time data. The DFT, $X(l)$, is equal to the complex Fourier series coefficient, X_l , where X_l characterizes a sampled, periodic time series $x(t)$.

The discrete Fourier transform is calculated using an efficient algorithm called a Fast Fourier Transform (FFT). The algorithm requires the number of points in the transform to be equal to 2^N where N is an integer. In doing an FFT, there are two parameters of interest, the sampling rate, Δt between points, and the number of points in the transform, NPT . The sampling rate, Δt , controls the range of frequencies in the frequency domain, and NPT controls the resolution in the frequency domain.

$$f_{\text{upper}} = \frac{1}{\Delta t}$$

$$\Delta f = \frac{1}{\Delta t * NPT}$$

B.3 CONVOLUTION AND CORRELATION

Two other important concepts are convolution and correlation. The convolution is used to calculate the response of a system if the impulse response function and the load function are known. Convolution is defined mathematically as:

$$h(t) \text{ convoluted with } x(t) = \int_{-\text{Inf}}^{+\text{Inf}} h(\tau) x(t-\tau) d\tau$$

and is a transform pair with $H(f) * X(f)$

where

$H(f)$ is the Fourier transformation of $h(t)$

$X(f)$ is the Fourier transformation of $x(t)$

Convolution of two time records in the time domain is a transform pair with the multiplication of the Fourier transform of the individual records.

Correlation is a measure of the linear association between $y(t)$ and $x(t)$. Correlation is defined mathematically as:

$y(t)$ correlated with $x(t)$

$$= R_{yx}(\tau) = \lim_{T \rightarrow \infty} \int_{T/2}^{T/2} y(t) x(t-\tau) dt$$

and is a transform pair with $Y(f) * X^*(f)$, where
 $X^*(f)$ is complex conjugate of $X(f)$.

Correlation of two time records in the time domain is a transform pair with the multiplication of the Fourier transform of the first record and the complex conjugate of the Fourier transform of the second record.

B.4 WINDOWS

Windows are special functions used to reduce leakage. When a finite length record is used, this is the same as multiplying the infinite record with a rectangular window. As mentioned earlier a multiplication in one domain is a convolution in the other domain. As such the window multiplication in the time domain is a convolution in the frequency domain. In this research several windows were used. They include Hanning, rectangular, and exponential windows:

$$\text{Hanning:} \quad = \frac{1}{2} \left(1 - \cos \left(\frac{2\pi t}{T} \right) \right)$$

$$\begin{aligned} \text{Rectangular:} \quad &= 1 \quad 0 < t < T \\ &= 0 \quad \text{O.W.} \end{aligned}$$

$$\text{Exponential} \quad = \text{Exp} \left(-\frac{t}{\tau} \right)$$

The Hanning window is used for periodic and random data. The exponential window is used for decaying processes.

In addition to reducing leakage, windows act like a weighting function where some parts of the record are emphasized more than other. The effect of windows are discussed in section 4.3.2.

B.5 CROSS POWER SPECTRUM

The cross power spectrum of a stationary random process and the cross correlation function are transform pairs. The power spectrum is measure of the energy in the record at that frequency. The power spectrum is defined as, S_{xy} , where

$$S_{xy}(f) = \lim_{T \rightarrow \infty} \frac{1}{T} E \{ X(f) Y^*(f) \}$$

The power spectrum is a complex number and can be represented by its amplitude and phase, where

$$S_{xy}(f) = |S_{xy}(f)| \exp(i \theta_{xy}(f))$$

and

$$|S_{xy}(f)| = \sqrt{\text{Imag } S_{xy}(f)^2 + \text{Real } S_{xy}(f)^2}$$

$$\theta_{xy}(f) = \tan^{-1} \left[\frac{\text{Imag } S_{xy}(f)}{\text{Real } S_{xy}(f)} \right]$$

The phase information, $\theta_{xy}(f)$, is of interest. It tells the phase difference as a function of frequency between the two measuring points. That is

$$\theta_{xy}(f) = \theta_x(f) - \theta_y(f)$$

where $\theta_x(f)$ and $\theta_y(f)$ denote the phases of the Fourier transforms of $x(t)$ and $y(t)$ respectively.

The power spectrum is an even function. Another definition is a one sided power spectrum, $P_{xy}(l)$. In discrete form

$$P_{xy}(l) = 2 |X(l) Y^*(l)| \quad l = 1, 2, \dots, \frac{N}{2} - 1$$

$$\frac{1}{T} |X(l) Y^*(l)| \quad l = 0, \frac{N}{2}$$

B.6 COHERENCE

For a two sided power spectrum, coherence is defined as

$$\gamma_{xy}^2 = \frac{|S_{xy}|^2}{S_{xx} S_{yy}}$$

or for a one sided power spectrum as

$$\gamma_{xy}^2 = \frac{|P_{xy}|^2}{P_{xx} P_{yy}}$$

and is $0 < \gamma_{xy}^2 < 1$. Coherence is a measure of the degree of linear correlation between $x(t)$ and $y(t)$.

APPENDIX C

OTHER APPROACHES TO DAMAGE DETECTION AND CRACK SIZING

This section will provide background on other studies methods which use stress waves to detect cracking and defects. Some methods used in the past to determine the size and location of cracks are the P-wave arrival time, imaging systems, time separation of different waves (surface and mode converted), and a periodic variation in the high frequency spectrum.

C.1 P-WAVE ARRIVAL

One of the first methods used to determine cracks and crack depth, used the arrival time between a transmitter and a receiver or pulse velocity. To detect a crack, one receiver is incrementally moved away from the transmitter. Plotting separation distance vs arrival time, the plot should be a straight line until a crack is encountered at which point arrival time should increase changing the slope of the plot.

To size the crack, the receivers are put equidistant on both sides of the crack. The arrival time is measured and the depth is calculated using the formula.

$$\text{depth} = x \sqrt{\frac{T_c^2}{T_s^2} - 1}$$

where

depth = crack depth

T_c^2 = travel time around crack

T_s^2 = travel time without crack

x = distance between the crack and the receivers

C.2 IMAGING SYSTEM

C.2.1 SINGLE AND DOUBLE TRANSDUCER

Single and double transducer methods work off a reflected echo or a transmitted signal. There are three types of scanning used by this method. They are called A-scanning, B-scanning, and C-scanning.

A-scanning is where the transmitting transducer is placed directly against the object to be examined. An acoustic pulse passes into the object and is reflected by acoustic impedance discontinuities. The returned echo signal is then received by the same transducer and amplified and displayed as a function of time on the oscilloscope. (El-Sherbini, pg 8)

B-scanning, uses the return echo signal to modulate the intensity of an oscilloscope spot, while time delay is represented by horizontal position, and the mechanical position along the surface of the object is represented by the vertical position on the oscilloscope. (El-Sherbini, pg 8)

C-scanning, utilizes two focused transducers in a confocal geometry. The transmitted signal is chiefly acted upon by the small region at the focal point of the transducer. It is then received, detected and displayed as an intensity modulation of a TV monitor or recorded on paper. The transducers are scanned synchronously, in a raster mode, and the image is built up point by point. The advantage of this method is that good resolution can be achieved and a high quality transmission image of the object can be observed. (El-Sherbini, pg 10)

C.2.2 MULTIPLE TRANSDUCERS

Other means of detecting cracks are through imaging systems which require multiple transducers to record the response of the system. Given the response of

the multiple transducers, the image of the object causing the response is constructed based on an inversion process. The inversion process is not presented in this section. A good review of imaging systems is given by El-Sherbini who explains the inversion process in detail. Two methods which use this approach are holography and tomography. Tomographic systems give a picture of a cross section. A holographic system is based on the principle that when a wave, diffracted by an object, is present simultaneously with a suitable coherent reference wave on a recording medium, the recorded interference fringes form a hologram that contains the amplitude and phase of the diffracted wave. It required the invention of the laser to work.

C.3 SEPARATION OF WAVES IN WAVEFORM

Ma studied the interaction of Rayleigh waves with surface discontinuities in steel. The purpose of his research was to develop a way of separating the various components of the transmitted Rayleigh waves to find their properties and then to use them to predict the depth of a defect.

Ma suggested two methods of predicting crack depth. Both were conditioned on being able to identify parts of the transmitted wave train. The first method was based on the time separation of two different parts of the transmitted wave, which were attributable to certain interaction between the incident wave and the crack. The location of the transducers was important to be able to correctly identify each part of the record. When the transducers were not properly spaced, other interactions tended to cover up the interaction of interest.

The second method suggested was based on identifying a specific part of the wave attributable to the Rayleigh wave which is a mode converted wave from a shear wave hitting the surface, as a result of the incident Rayleigh wave interacting at the tip of the crack. This portion of the wave was Fourier transformed. The resulting transform had a distinctive cutoff frequency. An empirical equation relating the

crack depth and cutoff frequency was then developed using a least squares fit. Given this line and the experimentally determined cutoff frequency, the depth of the crack can be predicted.

C.4 PERIODIC VARIATION IN HIGH FREQUENCY SPECTRUM

Fitting also studied the interaction of Rayleigh waves with defects. He showed that in the high frequency range or short wavelength relative to the crack size the backscattered and forward scattered amplitude spectra exhibited a periodic variation. High frequency was defined as $K * d > 10$, where $K = 2\pi / \lambda$ and d is the crack depth. The periodic variation was attributed to reverberations of Rayleigh waves on the crack faces. The time spacing of reverberation depends on crack length and so the periodicity of the variation in the spectra is related to crack depth. The equation used was

$$\text{Depth} = \frac{\pi}{\Delta K} = \frac{V_R}{2 \Delta f}$$

where

V_R is the Rayleigh wave velocity

Δf is the "average" interval between peaks in the frequency spectra of the back or forward scattered fields.

BIBLIOGRAPHY

ACI Monograph No 9 "Testing Hardened Concrete: Nondestructive Methods",
Malhotra, V.M. 1976.

Agbabian, M. S., & Masri, S. F. (Eds.), Proceedings of the International Workshop on Nondestructive Evaluation for Performance of Civil Structures, Los Angeles, California: Department of Engineering, University of Southern California.

ASTM C215 - 60, Standard Test Method for Fundamental Transverse, Longitudinal, and Torsional Frequencies of Concrete Specimens.

ASTM C597-71, Standard Test Method for Pulse Velocity Through Concrete

Bedford, M. & Drumheller, D.S., (1990), "Wave Propagation ", Course Notes, EM 394V, University of Texas at Austin.

Doyle, P.A. & Scala, C.M., (1978) "Crack Depth Measurement By Ultrasonics: A Review", Ultrasonics, July, 1978, 164-170.

El-Sherbini, A.M. (May, 1983) Autoregressive Moving Average Processing for High Resolution 3-D Acoustic Imaging. (Doctoral Dissertation, Case Western Reserve University)

Fitting, D.W. (1982) Ultrasonic Spectroscopic Studies of the Interaction of Rayleigh Waves with Surface Breaking Defects. (Doctoral Dissertation, The University of Tennessee, Knoxville)

Halliday, D. & Resnick, R. (1981) Fundamentals of Physics, John Wiley & sons, Inc., New York, N.Y.

Ma, C. (1984). The Interactions of Ultrasonic Rayleigh Waves with Surface Discontinuities in Steel. (Doctoral Dissertation, Iowa State University)

Malvern, L.E. (1969). Introduction To The Mechanics of a Continuous Medium. Prentice-Hall, Inc., Englewood Cliffs, New Jersey.

Meirovitch, L., Analytical Methods in Vibrations, The Macmillan Co, New York, N.Y. 1967.

Mindess, S. & Young, J.F., Concrete, Prentice-Hall, Inc., Englewood Cliffs, New Jersey, 1981.

Nazarian, S. (1984). In Situ Determination of Elastic Moduli of Soil Deposits and Pavement Systems by Spectral-Analysis-of-Surface-Waves Method. (Doctoral Dissertation, University of Texas at Austin, 1984).

Paz, M. (1985). Structural Dynamics: Theory and Computation, Van Norstrand Reinhold Co. New York, N.Y.

Powers, E.J., (1990) "Digital Time Series Analysis and Applications", Course Note, EE381L, University of Texas at Austin.

Richart, F.E., Woods, R.D., and Hall, J.R. Vibration of Soils and Foundations. Prentice-Hall, Inc., Englewood cliffs, New Jersey, 1970.

Sansalone, M., et al. (1986). Impact-echo: A Method for Flaw Detection in Concrete Using Transient Stress Waves, (NBSIR Report No 86/3452). Gaithersburg, MD: Center for Building Technology. (NTIS No. PB87-111837).

- Shue, J. C. (1987). Applications and Limitations of The Spectral-Analysis-of-Surface-Waves Method (Doctoral dissertation, University of Texas at Austin, 1987).
- Vu, B.Q., (1981). Scattering of Rayleigh Surface Waves in a Half-Space. (Doctoral dissertation, University of Colorado)
- Wilbeck, J.S., et al, "A Short Course on Penetration Mechanics", Course Notes, Southwest Research Institute, San Antonio, Texas.

VITA

Britt Roderick Bowen was born, the son of Barbara and Ronald Bowen, in Silver City, New Mexico, on 30 July, 1962. He grew up in Fort Defiance and Coolidge, Arizona. He graduated from Coolidge High School in 1980. Since high school, he has received a Bachelor of Science in Civil Engineering from the Air Force Academy in 1984 and a Master of Science degree from Columbia University in 1985. From 1985 to 1988, he managed government research contracts, while stationed at Tyndall AFB, Florida. In September 1988, he entered the Graduate School of The University of Texas. After graduation for the Air Force Academy, he has served as a commissioned officer in the U.S. Air Force.

Permanent address: 281 S. 7th St.
Coolidge, Arizona
85228

This dissertation was typed by the author.